*Acoustical Physics, Vol. 50, No. 2, 2004, pp. 115–120. Translated from Akusticheskiĭ Zhurnal, Vol. 50, No. 2, 2004, pp. 149–155.*


# Sensing Properties of Normal Oscillatory Modes of Quartz Plates

**I. V. Anisimkin**†

*Institute of Radio Engineering and Electronics, Russian Academy of Sciences, Mokhovaya ul. 11 (stroenie 7), Moscow, 125009 Russia*

*e-mail: ivanis@cplire.ru*

Received March 18, 2003

**Abstract**—The responses (relative velocity variations $\Delta v/v$ of normal (symmetric or asymmetric) Lamb and shear-horizontal modes of ST-cut quartz plates, whose thickness is comparable with the wavelength, is studied. Since modes of different orders $n$ belonging to these two families have different propagation velocities $v_n$, polarizations $u_i$, and displacement distributions in depth $H$, they exhibit different responses to variations in the parameters of the plate (density, elastic moduli, thickness, and temperature) and to the loading of its surface by thin films (i.e., to surface adsorption). Results of numerical calculation of the responses to these parameters are corroborated by experiments on the effect of the plate temperature variation and the effect of adsorption of water vapor onto the plate surface. © *2004 MAIK "Nauka/Interperiodica".*

## INTRODUCTION

In recent years, an explosion has been observed in research into external effects, processes, and media at solid–gas and solid–liquid interfaces. These problems have much in common with gas and liquid detection and recognition problems. The interest in these studies is caused by the necessity to develop new means for environmental monitoring, biological shielding, analytical chemistry, biology, medicine, and other fields of science and engineering.

Application of surface acoustic waves (SAW) for these purposes has a number of advantages over methods based on other physical principles. Therefore, the sensing properties of waves of different types propagating in various kinds of structures have been studied for more than 15 years.

These studies were traditionally limited to the use of Rayleigh waves [1, 2], surface waves [3], leaky surface acoustic waves [4], and shear horizontal waves [5]. However, until now, the detection properties of normal oscillatory modes of thin plates were only studied for several lowest-order waves [6–8]. At the same time, it would be natural to assume that, because modes of different orders $n$ excited in plates differ in the propagation velocity $v_n$, polarization $u_i$, and displacement distribution over the depth $H$, they must exhibit different responses to external actions.

This paper studies the differences in the responses of Lamb and shear horizontal (SH) modes of different orders $n$ to the same variations in the parameters of the plate and to the same external actions.

† Deceased.

## PROPERTIES OF PLATE MODES VERSUS PLATE PARAMETERS

The sensing properties of the modes were studied with the use of software [9] that solves wave equations with appropriate boundary conditions by the numerical method of multilayer matrices.

For quartz plates with relative thicknesses of $H/\lambda$ = 0.6, 1.0, and 1.2755, where $H$ is the plate thickness and $\lambda$ is the wavelength, the relative variation in the velocity of the plate modes, $\Delta v_n/v_n$, was calculated as a function of the plate density $\rho$, elasticity $c_{ij}$, and thickness $H/\lambda$. Each parameter was progressively varied within ±1% near its nominal value (i.e., the value under normal conditions) at nominal values of the remaining parameters, and three velocities $v_n^{+1}$, $v_n^0$, and $v_n^{-1}$ of each $n$th mode were calculated for the parameter values, respectively, 1% greater than, equal to, and 1% lower than its nominal value. The value $\Delta v_n/v_n$ (response of the $n$th mode to the change in the parameter) was defined as $\Delta v_n/v_n = (v_n^{+1} - v_n^{-1})/v_n^0$. As a result, we obtained the curves representing $\Delta v_n/v_n$ versus $n$ for various parameters and mode types. Results of similar calculations for temperature coefficients of delay (TCD) of SH modes are reported in [10]. The corresponding results for Lamb waves are presented below. As an example, Fig. 1 shows the data for Lamb waves in a plate with $H/\lambda = 0.6$ (at $H/\lambda = 1.0$ and 1.2755 the behavior is similar). The symmetric and asymmetric modes are numbered sequentially. The behavior of $\Delta v_n/v_n$ for Lamb waves differs from that for SH waves: it depends nonmonotonically on the mode index $n$ (the value of $\Delta v_n/v_n$ is different for each subsequent mode), no tendency to

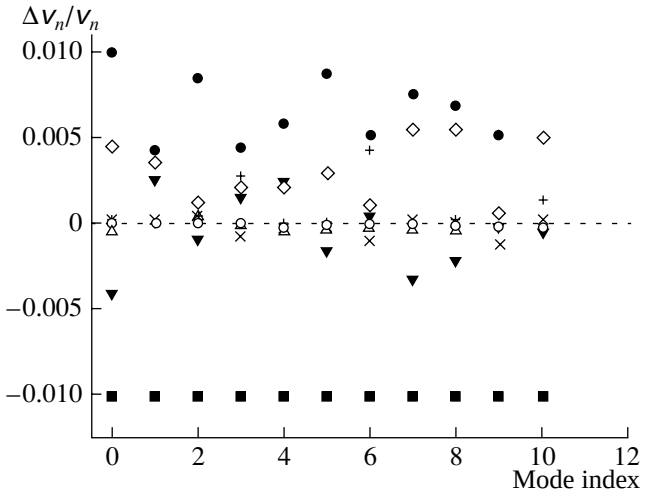


**Fig. 1.** Sensitivity of Lamb modes to individual parameters of the ST,X quartz plate at $H/\lambda = 0.6$: (■) $\Delta\rho$, (●) $\Delta C_{11}$, (△) $\Delta C_{12}$, (×) $\Delta C_{13}$, (▼) $\Delta C_{14}$, (+) $\Delta C_{33}$, (◇) $\Delta C_{44}$, and (○) $\Delta H/\lambda$.

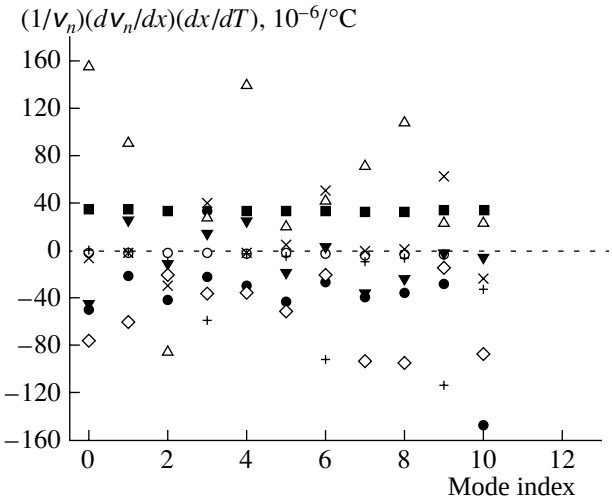


**Fig. 2.** Partial contributions to the TCD of Lamb modes due to the temperature variations in the parameters of the ST,X quartz plate at $H/\lambda = 0.6$: (■) $\Delta\rho$, (●) $\Delta C_{11}$, (△) $\Delta C_{12}$, (×) $\Delta C_{13}$, (▼) $\Delta C_{14}$, (+) $\Delta C_{33}$, (◇) $\Delta C_{44}$, and (○) $\Delta H/\lambda$.

saturation of $\Delta v_n/v_n$ at large $n$ is observed, and the sensitivity of Lamb modes to variations in the density of the plate is the same and slowly varies when $H/\lambda$ decreases from 1.2755 to 0.6. Both Lamb and SH modes exhibit the highest sensitivity to $\rho$, $C_{11}$, $C_{14}$, and $C_{44}$. Accordingly, the velocity of Lamb modes decreases ($\Delta v_n/v_n < 0$) with increasing density $\rho$ and increases ($\Delta v_n/v_n > 0$) with increasing $C_{11}$ and $C_{44}$.

These results show that both the Lamb and SH modes of different orders $n$ exhibit different sensitivities to the parameters of the plate, and, for some modes, the difference occurs in both the magnitude and sign of the response $\Delta v_n/v_n$. For each mode type, there exist elastic moduli of the plate whose variations cause no velocity changes for any of the modes. For modes of both types, there are parameters to which all modes of the type exhibit a high, though different, sensitivity. A 1% change in these parameters may cause a response as high as 1%.

## PROPERTIES OF PLATE MODES VERSUS TEMPERATURE

As is known, the temperature sensitivity of acoustic waves of any type is characterized by the temperature coefficient of delay (TCD). For thin plates, a change in temperature $T$ in general causes changes in all parameters of the plate: thickness $H$, density $\rho$, and elasticity $C_{ij}$. Each of these parameters causes a particular change in the velocity of a mode and its $\mathrm{TCD}_n$. We calculated the $\mathrm{TCD}_n$ for different Lamb modes in ST,X quartz near room temperature by a technique similar to that used earlier in [10]. This technique represents the TCD as a total differential with respect to the variables $x = \rho$, $c_{ij}$, and $H/\lambda$:

$$\mathrm{TCD}_n = \alpha_{\mathrm{pl}} - \frac{1}{v_n}\frac{dv_n}{dT} = \alpha_{\mathrm{pl}} - \frac{1}{v_n}\frac{dv_n}{\partial(H/\lambda)}\frac{\partial(H/\lambda)}{\partial T} - \frac{1}{v_n}\frac{\partial v_n}{\partial\rho}\frac{\partial\rho}{\partial T} - \frac{1}{v_n}\frac{\partial v_n}{\partial c_{ij}}\frac{\partial c_{ij}}{\partial T}, \quad (1)$$

where $\alpha_{\mathrm{pl}}$ is the plate linear expansion coefficient in the mode propagation direction. Representation (1) allows one to analyze partial contributions to $\mathrm{TCD}_n$ from each plate parameter separately and find the values of $\mathrm{TCD}_n$ for various plate modes that propagate in the same direction. The contributions of the dielectric and piezoelectric moduli of quartz to $\mathrm{TCD}_n$ are small and can be neglected.

Figure 2 shows the TCD for the Lamb modes calculated at $H/\lambda = 0.6$. It can be seen that, unlike SH modes [10], Lamb modes feature a nonmonotonic behavior of all $(1/v_{no})(\Delta v_n/\Delta x)$, and $(dx/dt)$ functions versus the mode index $n$ (except for the density dependence), because the partial contribution to $\mathrm{TCD}_n$ is different for almost each subsequent Lamb mode. No tendency to saturation with increasing $n$ can also be observed. The sensitivity of Lamb modes to the plate density $\rho$ is the same as for SH modes and slowly varies with $n$ for $H/\lambda$ decreasing from 1.2755 to 0.6. The contribution of the temperature variation in $H/\lambda$ to $\mathrm{TCD}_n$ is negligible for all modes, while the contributions of variations in other parameters are nonzero: either positive ($\rho$), or negative ($C_{11}$, $C_{33}$, $C_{44}$), or they differ in sign for modes of different orders ($C_{12}$, $C_{13}$, $C_{14}$).

Note that, although (as we found out above) the effect of elastic moduli $C_{12}$, $C_{13}$, and $C_{33}$ on the velocities $v_n$ of plate modes is small, the effect of the temper-

ature variation in these moduli on the velocity and $TCD_n$ is high and is comparable with that of other elastic moduli. This result is associated with a rather strong temperature dependence of the coefficients themselves. In other words, modes can generally exhibit a widely different sensitivity to the elastic moduli and their temperature variations.

Next, we analyze the values of $TCD_n$ calculated as a sum of contributions according to Eq. (1). As can be seen from Fig. 3, for Lamb modes, the dependence of $TCD_n$ on the mode index $n$ is nonmonotonic. At the same plate thickness and propagation direction, modes exist whose TCDs are positive, negative, or zero. There is no universal dependence of $TCD_n$ on the plate thickness $H/\lambda$ in the thickness range under study.

It should be particularly noted that, according to our calculations, the temperature sensitivity of the plate modes can vary over a wide range for the same propagation direction and reach high values even for quartz, which is usually regarded as a thermally stable material. It therefore seems incorrect to apply the term "thermally stable" to any material, because the thermal stability implied refers to a wave of a particular type alone and only near a particular temperature. In the cases considered above, the temperature sensitivity of Lamb modes at room temperature was in the range of –170 to $+250 \times 10^{-6}$ /°C. For comparison, the highest sensitivity of a Rayleigh wave ({100}, ⟨110⟩ $Bi_{12}GeO_{20}$ single crystal) is $+120 \times 10^{-6}$ /°C [11].

## PROPERTIES OF PLATE MODES IN THE PRESENCE OF SURFACE ADSORPTION

To study the sensitivity of Lamb modes and SH modes to a surface load, we calculated the relative changes in their velocities, $\Delta v/v_n$, which occurred as a result of applying a thin film of another material to one of the plate surfaces. In order to cover the maximum possible number of film and plate material combinations, we analyzed all materials listed in the data base of program [9]. Similar to paper [12], in which the acoustic properties of layered structures in the form of a layer overlying a half-space were analyzed, I choose film materials with Rayleigh and SH wave velocities lower, approximately equal, or higher than those in ST,X quartz and ST,X + 90° quartz. As in [12], I will call these films slow-wave, neutral, or fast-wave films, respectively. For SH-polarized modes propagating in the X + 90° direction, the materials selected were gold (Au), yttrium gallium garnet ($Y_3Ga_5O_{12}$), and silicon (Si); for Lamb modes propagating along the $X$ axis of ST-cut quartz, gold (Au), europium iron garnet ($Eu_3Fe_5O_{12}$), and diamond (C) were used. The short-circuiting effect of metal films was eliminated by appropriately choosing the operating conditions of the program [9]. The relative film thicknesses $h/\lambda$ (where $h$ is the film thickness) were varied over a range of 0.00–0.01. The plate thickness was $H/\lambda = 0.6$ and

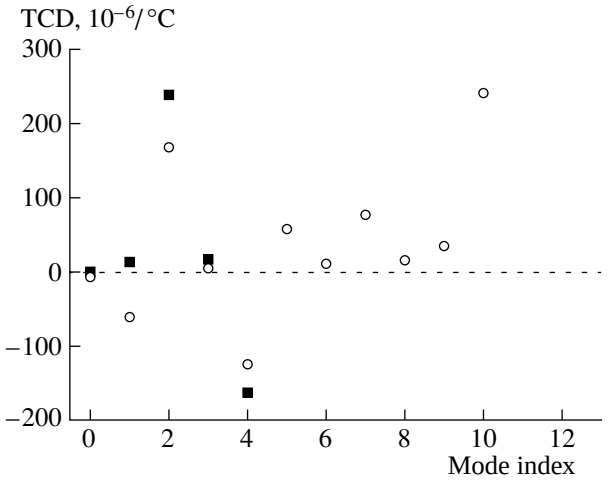


**Fig. 3.** TCD of Lamb modes in an ST,X quartz plate with $H/\lambda = 0.6$ at room temperature (TCD = 0 is the TCD of the Rayleigh wave in ST,X quartz at the same temperature): (■) experiment and (○) theory.

1.2755. For typical wavelengths of acoustic modes $\lambda$ = 100–500 μm, the values of $h$ were within 0.01–5.00 μm, which corresponds to the typical biochemical monolayer thickness (0.1 μm [13]) and is therefore realistic for modeling the process of surface adsorption.

Our calculations show that, for SH modes, the slow-wave film expectedly reduces the velocities of all modes, i.e., the responses $\Delta v_n/v_n$ are negative. The relative velocity variation $\Delta v_n/v_n$ versus mode index $n$ reaches its maximum at a certain $n$, which depends on the film thickness, and exhibits saturation at large $n$. Responses of all mode orders increase with the relative thickness (mass) of the slow-wave film, $h/\lambda$. The minimum response is exhibited by either the 0th-order mode ($h/\lambda$ = 0.0001–0.001) or the 1st-order mode ($h/\lambda$ = 0.005–0.01). The neutral film (yttrium gallium garnet) produces a similar effect on the SH modes.

The mass-elastic action of the fast-wave film leads to a different behavior of the dependence of $\Delta v_n/v_n$ on $n$ and $h/\lambda$ (Fig. 4). In this case, the responses of the 0th- and 1st-order modes become positive (the mass-elastic load increases the velocities of these modes), the responses of the 2nd- and 3rd-order modes become close to zero (these modes are almost insensitive to the load), and the responses of higher-order modes are again negative and almost equal to each other. In my opinion, the fast-wave film reduces the velocities of higher-order modes, because these velocities are high and the film actually becomes a slow-wave structure for them.

A common effect of the mass-elastic loading of the plate surface by the slow-wave, neutral, and fast-wave films is that the responses of SH modes $\Delta v_n/v_n$ depend on the mode index $n$, they are approximately equal for high-order modes and grow with increasing load. The

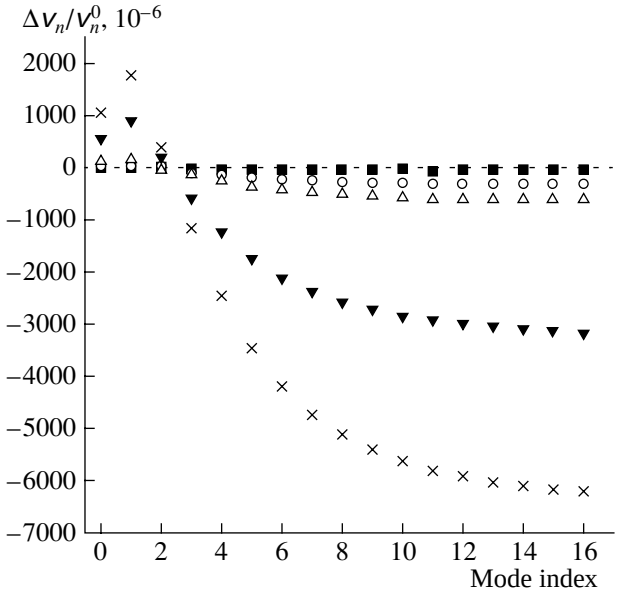


**Fig. 4.** SH modes in an ST,X + 90° quartz plate with $H/\lambda$ = 1.2755 covered with a fast-wave ⟨001⟩, ⟨100⟩ Si film of thickness $h$ = (■) 0.0001, (○) 0.0005, (△) 0.001, (▼) 0.005, and (×) 0.01.

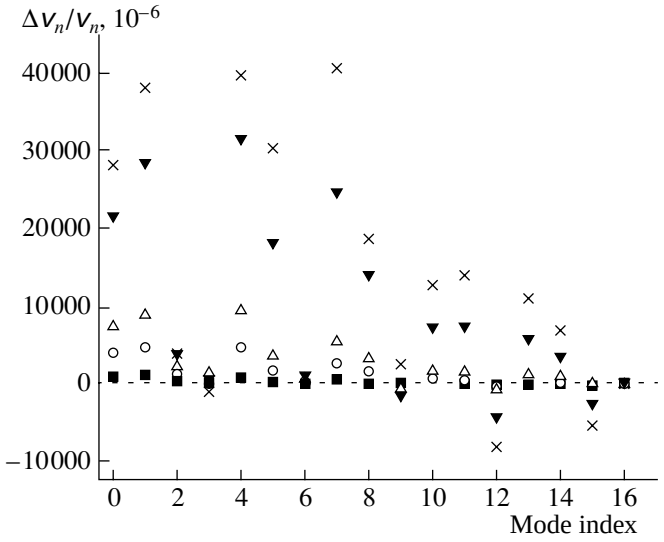


**Fig. 5.** Lamb modes in an ST,X quartz plate with $H/\lambda$ 1.2755 covered with a fast-wave ⟨001⟩, ⟨100⟩ diamond film with $h$ = (■) 0.0001, (○) 0.0005, (△) 0.001, (▼) 0.005, and (×) 0.01.

ranges of responses for the minimal and maximal thicknesses of loading films are given in Table 1.

For the Lamb modes, the mass-elastic loading of the plate surface leads to a more complex behavior. The response $\Delta v_n/v_n$ changes for almost every subsequent mode $n$, taking on negative values for the slow-wave and neutral films and predominantly positive values for the fast-wave film. An increase in the load (film thickness $h/\lambda$) does not necessarily enhance the response of the modes (2nd, 3rd, and 6th modes, Fig. 5). Such an increase may even cause the acoustic response to change its sign (3rd and 9th modes, Fig. 5). Because $\Delta v_n/v_n$ is a nonmonotonic function of $n$, the number of modes that are insensitive to the mass-elastic load increases. The fast-wave film increases the velocity of the major part of the modes, including the higher-order ones, although their velocities in the film material are higher than the velocity of the Rayleigh wave. The ranges of responses for Lamb modes at the minimal and maximal thicknesses of the loading film are given in Table 2.

The above features of Lamb and SH modes in a quartz plate with a relative thickness of $H/\lambda$ = 1.2755 and with a mass-elastic load persist when the plate thickness decreases. Thus, the effect produced by the mass-elastic load on the velocity of normal oscillatory modes of the quartz plate is different for different modes.

## EXPERIMENTAL

Parameters of the ST-cut quartz plates used in our experimental study of the sensitivity of the plate modes to temperature and gas adsorption are summarized in Table 3. Samples 2 and 3 had one surface ground and one surface polished, on which receiving and transmitting 100-nm-thick transducers made of Al/Cr or Au/Cr were positioned. Both surfaces of samples 1 and 4 were optically polished. The Lamb modes were excited to travel in the direction of the $X$ crystallographic axis; the SH modes, perpendicular to this axis, for which purpose pairs of interdigital transducers were placed on the samples at an angle of 90° to one another. The experi-

**Table 1.** Response ranges of SH modes in ST,X + 90° quartz for the minimal and maximal thicknesses of the loading films

| Material \ Velocity | $\Delta v_n/v_n$, $10^{-6}$ ($h/\lambda$ = 0.0001) | $\Delta v_n/v_n$, $10^{-6}$ ($h/\lambda$ = 0.01) |
|---|---|---|
| Au (slow-wave) | –277…–569 | –2281…–123319 |
| $Y_3Ga_5O_{12}$ (neutral) | –31…–164 | –3776…–14292 |
| Si (fast-wave) | +18…–119 | +1780…–6228 |

**Table 2.** Response ranges of Lamb modes for the minimal and maximal thicknesses of the loading films

| Material \ Velocity | $\Delta v_n/v_n$, $10^{-6}$ ($h/\lambda$ = 0.0001) | $\Delta v_n/v_n$, $10^{-6}$ ($h/\lambda$ = 0.01) |
|---|---|---|
| Au (slow-wave) | –203…–788 | –21744…–98695 |
| $Eu_3Fe_5O_{12}$ (neutral) | +17…–169 | –1469…–15891 |
| C (diamond) (fast-wave) | +1000…–84 | +40733…–8211 |

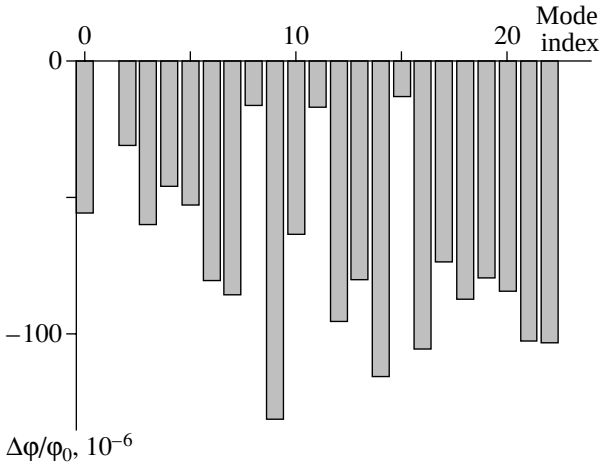


**Fig. 6.** Relative phase change (response) of SH modes in an ST,X + 90° quartz plate with $H/\lambda = 1.4855$, with water vapor adsorbed on its clean surface at room temperature and a relative air humidity of 80%.

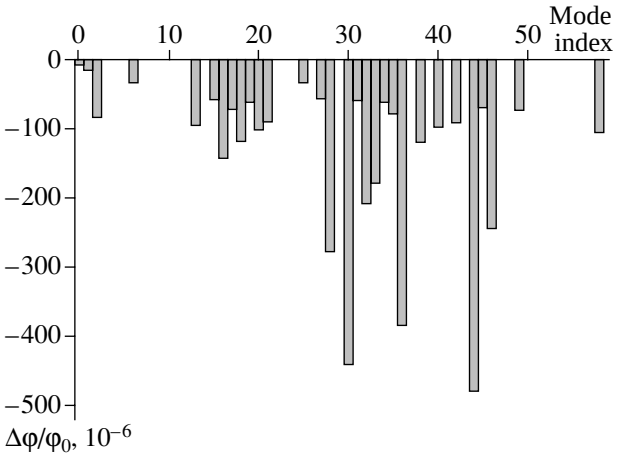


**Fig. 7.** Relative phase change (response) of Lamb modes in an ST,X quartz plate with $H/\lambda = 1.4855$, with water vapor adsorbed on its clean surface at room temperature and a relative air humidity of 80%.

mental technique and the procedures for the spatial mode resolution and identification by the velocity and by the electromechanical coupling coefficient are identical to those used in [10].

The experimental TCD values for the Lamb modes are in good agreement with the theoretical values: the magnitude and sign of the TCD practically change for each subsequent mode $n$; the TCD of the 2nd-order mode at a temperature of $T = 20°C$ and a relative plate thickness of $H/\lambda = 0.6$ reaches a high value of $180 \times 10^{-6}/°C$ (Fig. 3). Thus, the plate modes demonstrate a variety of temperature-dependent properties, which include negative and zero TCD values, as well as record high positive and negative values in the temperature range of $T = 2$–$92°C$. To obtain a further increase in the temperature sensitivity of acoustic oscillations while keeping the TCD values stable over a wide temperature range, one should search among the plate oscillatory modes by simultaneously optimizing the material, crystallographic cut, and thickness of the plate.

The sensitivity of the plate modes to gas adsorption was studied in water vapor. Because gas adsorption on a clean plate surface is generally accompanied by changes in the mass, elasticity, conductivity, and temperature of the boundary region, the resulting change in the mode propagation velocity is caused by the combined effect of the mass, elastic, electric, and thermal loading of the surface. The samples were exposed to a flow of humid air (with a relative humidity of 10 to 85%) in a chamber with a volume of 250 ml. The response of the sample treated with a nitrogen flow was used as a reference. The responses were measured by an HP 8753A network analyzer operated in the phase mode. The temperature and humidity in the chamber were measured independently by a commercially available IVTM-7 probe, within ±0.1°C and ±0.1% of the relative humidity, respectively. Other features of the experiment are detailed in [10]. The experimental results are shown in Figs. 6 and 7.

As can be seen from Fig. 6, the responses $\Delta\varphi/\varphi_0$ of SH modes to the adsorption of gas with a constant relative humidity of 80% change with the mode number $n$. For plates of thickness $H/\lambda = 1.4855$, the highest sensitivity is observed for the 9th, 14th, 16th, 21st, and 22nd modes; the lowest, for the 8th, 11th, and 15th modes. Unlike the cases when the samples were subjected to one type of the surface load, which we studied numerically, the combined action of the mass, elastic, electric, and thermal surface loads leads to a more complex nonmonotonic behavior of $\Delta\varphi/\varphi_0$ versus $n$ (Fig. 6).

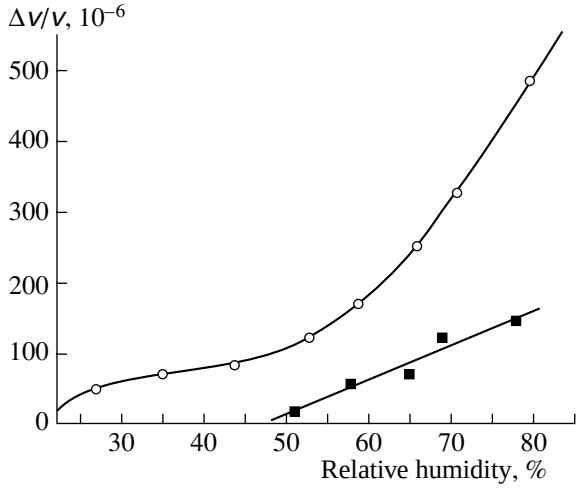


**Fig. 8.** Concentration curves of the 16th- and 44th-order Lamb mode responses for an ST,X quartz plate with $H/\lambda = 1.4855$, with water vapor adsorbed on its surface at room temperature: (dots) experiment, (lines) approximation curves, (■) 16th-order mode, and (○) 44th-order mode.

**Table 3.** Parameters of experimental samples

| Sample | $H$, mm | $\lambda$, μm | $H/\lambda$ | $N$ | $2a$, mm | $L$, mm | $\varphi_0$, deg |
|---|---|---|---|---|---|---|---|
| 1 | 0.3 | 500 | 0.6 | 20 | 20 | 30 | 21600 |
| 2 | 0.5 | 500 | 1.0 | 20 | 20 | 30 | 21600 |
| 3 | 0.5 | 392 | 1.2755 | 20 | 16 | 24.1 | 22130 |
| 4 | 0.3 | 202 | 1.4855 | 16 | 12 | 26.2 | 46693 |

Note: $H$ is the plate thickness; $\lambda$, $N$, and $2a$ are the period, number of electrode pairs, and aperture of the transducers; and $L$ and $\varphi_0$ are the distance and the total phase advance of the plate mode (initial phase of the mode) between the transducers.

The responses $\Delta\varphi/\varphi_0$ of Lamb modes to the adsorption of gas with a constant relative humidity of 80% also change with the mode number $n$ (Fig. 7). For plates with $H/\lambda = 1.4855$, the highest sensitivity is observed for the 28th, 30th, 36th, 44th, and 46th modes; the lowest, for the 0th, 1st, and 29th modes. Under the combined action of the mass, elastic, electric, and thermal surface loads, $\Delta\varphi/\varphi_0$ exhibits complex and nonmonotonic behavior as a function of $n$, the same as under the individual action of each of these loads.

For both SH modes and Lamb modes, the behavior of $\Delta\varphi/\varphi_0$ versus the relative humidity (concentration dependences) is different for modes of different orders $n$. This is exemplified in Fig. 8 by the 16th- and 44th-order Lamb modes. As can be seen, at the same number of water molecules adsorbed by the plate surface (at the same relative humidity), the concentration curves differ in both magnitude and shape. Note that the response of Rayleigh SAWs in quartz of the same cut to the adsorption of 80% water vapor is an order of magnitude smaller, $\Delta\varphi/\varphi_0 \sim 10 \times 10^{-6}$ [14].

## CONCLUSIONS

Our experimental studies corroborate the conclusions drawn from numerical results: plate modes of different orders and types exhibit different responses to external actions. In each mode family, there are both highly sensitive and insensitive modes to a particular action. For a uniform thermal action, modes are found with a record-high sensitivity to temperature as well as those insensitive to it over a wide temperature range. When water molecules are adsorbed on a clean surface of the quartz plate, the Lamb modes whose sensitivity is an order of magnitude higher than that of Rayleigh waves are found, as well as modes that are insensitive to adsorption of these molecules. In my opinion, this situation is typical of plate modes in general and will be observed under any other external actions. The high propagation velocity of the plate modes, which is an order of magnitude higher than the velocity of Rayleigh waves propagating in the same direction, makes it possible to achieve an order of magnitude higher operating frequencies with the same period of interdigital transducers without using ultraviolet or electron lithography.

## ACKNOWLEDGMENTS

This work was supported by the INTAS, project no. 2001-0257.

## REFERENCES

1. H. Wohltjen and R. Dessy, Anal. Chem., No. 51, 1458 (1979).
2. A. Bryant, M. Poirier, G. Riley, *et al.*, Sens. Actuators, No. 4, 105 (1983).
3. S. J. Martin, A. J. Ricco, and R. C. Hughes, in *Proceedings of 4th International Conference on Solid-State Sensors and Actuators* (1987), p. 478.
4. T. Moriizumi, Y. Unno, and S. Shiokawa, in *Proceedings of IEEE Ultrasonics Symposium* (1987), p. 579.
5. Z. Shana and F. Josse, in *Proceedings of IEEE Ultrasonics Symposium* (1990), p. 123.
6. C. Caliendo, A. D'Amico, P. Verardi, and E. Verona, in *Proceedings of IEEE Ultrasonics Symposium* (1990), p. 383.
7. D. Rebiere, J. Pistre, M. Hoummady, *et al.*, Sens. Actuators B, No. 6, 274 (1992).
8. G. McHale, F. Martin, and M. I. Newton, J. Appl. Phys. **92** (6), 3368 (2002).
9. E. L. Adler, J. K. Slaboszewicz, G. W. Farnell, and C. K. Jen, IEEE Trans. Ultrason. Ferroelectr. Freq. Control **37**, 215 (1990).
10. I. V. Anisimkin, V. I. Anisimkin, Yu. V. Gulyaev, and E. Verona, Akust. Zh. **48**, 12 (2002) [Acoust. Phys. **48**, 8 (2002)].
11. A. J. Slobodnik, Jr., in *Acoustic Surface Waves*, Ed. by A. A. Oliner (Springer, New York, 1978; Mir, Moscow, 1981), pp. 270–286.
12. G. W. Farnell and E. L. Adler, in *Physical Acoustics*, Ed. by W. P. Mason and R. N. Thurston (Academic, New York, 1972), Vol. 9, pp. 35–57.
13. G. Kovacs, G. W. Lubking, M. J. Vellekoop, and A. Venema, in *Proceedings of IEEE Ultrasonics Symposium* (1992), p. 281.
14. V. I. Anisimkin, S. A. Maksimov, C. Caliendo, and E. Verona, Poverkhnost, No. 3, 73 (1998).

*Translated by A. Khzmalyan*

*Acoustical Physics, Vol. 50, No. 2, 2004, pp. 121–125. Translated from Akusticheskiĭ Zhurnal, Vol. 50, No. 2, 2004, pp. 156–160.*


# Low-Frequency Shear Parameters of Liquid Viscoelastic Materials

**B. B. Badmaev[1], B. B. Damdinov[1, 2], and D. S. Sanditov[1]**

[1] *Department of Physical Problems, Buryat Scientific Center, Siberian Division, Russian Academy of Sciences, ul. Sakh'yanovoi 6, Ulan-Ude, 670047 Russia*

*e-mail: lmf@ofpsrv.bsc.buryatia.ru*

[2] *Andreev Acoustics Institute, Russian Academy of Sciences, ul. Shvernika 4, Moscow, 117036 Russia*

*e-mail: dababa@rambler.ru*

Received March 31, 2003

**Abstract**—An experimental study of the shear parameters of viscoelastic liquids is carried out by the acoustic resonance method based on the changes in the natural frequency and *Q* factor of a piezoelectric quartz resonator. The liquid to be studied is placed between a stationary quartz strap and the piezoelectric quartz crystal vibrating at the resonance frequency. For a set of drilling muds, the values of the real and imaginary shear moduli are obtained at a frequency of 74 kHz. The measurements are performed with a liquid layer thickness much smaller than the shear wavelength. It is shown that the shear modulus decreases with increasing strain amplitude. A cluster model based on the Isakovich–Chaban nonlocal diffusion theory is proposed for explaining the low-frequency viscoelastic relaxation process. © *2004 MAIK "Nauka/Interperiodica"*.

## INTRODUCTION

Many liquids are known to change their viscosity and exhibit viscoelastic properties under an external load. These are the so-called non-Newtonian liquids. Viscoelastic materials with non-Newtonian behavior have attracted the attention of researchers [1–3]. For studying the mechanical properties of viscoelastic liquids, different acoustic methods were developed. A review of the acoustic methods used for measuring the viscoelastic properties of materials can be found in [4]. Earlier, we performed experimental studies of the low-frequency shear properties of viscoelastic liquids at a constant strain by the acoustic resonance method with the use of a piezoelectric quartz resonator [5].

In the present experiment, we use a method of measuring the complex shear moduli of liquids to study the shear properties of drilling muds depending on the vibration amplitude of the resonator.

## METHOD

An acoustic resonance method of measuring the complex shear modulus of liquid was described in [6]. This method is basically identical to that proposed by Mandel'shtam [7] and applied by Khaĭkin [8] to study the nature of interaction forces between two contacting solid bodies. In a piezoelectric quartz crystal *1* shaped as a rectangular bar (Fig. 1), length vibrations are excited at the fundamental resonance frequency. On the crystal, a second solid body *3* (a strap) is placed, and the character of the interaction of these two bodies is studied by the changes in the parameters of the vibrations. Using this method, it was shown [8] that friction forces are of an elastic nature when the vibration amplitudes are small. In the resonance method of measuring viscoelastic properties of liquids, a thin layer *2* of the liquid under investigation is placed between the quartz crystal and the strap. The working surface of the piezoelectric quartz crystal is its horizontal face perpendicular to the optical axis. When the quartz crystal vibrates, the strap is practically at rest, because the coupling through the liquid layer is weak and cannot transmit the acceleration of the quartz crystal to the strap. The piezoelectric quartz crystal is fixed by steel needles at points lying on the nodal line. The voltage from the output of an oscillator is supplied to the first pair of electrodes positioned at one end of the quartz crystal on its two lateral faces. Under the effect of the alternating electric field, the quartz crystal performs forced vibrations of the compression–extension type. The alternating emf arising due to the piezoelectric effect is applied

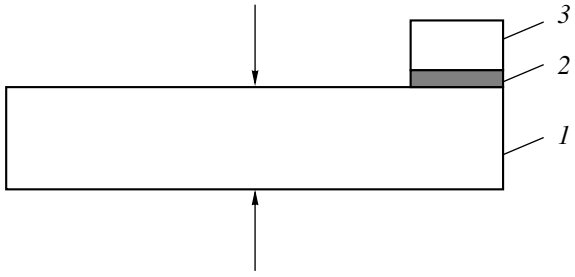


**Fig. 1.** (*1*) Piezoelectric quartz crystal with (*2*) a liquid layer and (*3*) a quartz strap.

1063-7710/04/5002-0121$26.00 © 2004 MAIK "Nauka/Interperiodica"

to the second pair of electrodes symmetrically positioned at the other end of the lateral faces. Vibrations of the quartz crystal are controlled by an oscilloscope. The resonance frequency of the quartz crystal is determined with an accuracy of ±1 Hz. By smoothly varying the modulation frequency, it is possible to make one of the side frequencies equal to the natural frequency of the quartz crystal. In this case, the vibration amplitude of the latter increases, reaching its maximum. Correspondingly, the voltage supplied to a millivoltmeter also increases. A voltmeter is used to measure the voltage across the quartz crystal, which usually does not exceed several hundreds of millivolts. The resonance frequency shift of the piezoelectric quartz crystal is measured for different thicknesses of the liquid film. The increase observed in the resonance frequency of the vibratory system proves that the liquid layer exhibits not only viscous but also elastic properties. If only dissipative forces are present, e.g., internal friction, the resonance frequency can only decrease. The experiments were performed with an 18.5° *X*-cut quartz crystal whose Poisson ratio was zero. The dimensions of the crystal were $36 \times 12 \times 5$ mm$^3$, and its resonance frequency was 74 kHz. From the changes in the acoustic parameters of the piezoelectric quartz crystal (the resonance frequency and the width of the resonance curve), the real $G'$ and imaginary $G''$ shear moduli of the viscoelastic liquid were determined.

The measuring procedure was as follows. The liquids under investigation and the surfaces of both the quartz and the strap were carefully cleaned. Immediately after cleaning, the piezoelectric quartz crystal was mounted on the sample holder and the liquid under study was placed on the quartz surface and covered with the strap. The film thickness was determined and monitored by the interference method [6]. After this, the resonance frequency of the vibratory system and the width of the resonance curve were measured.

The theory of the resonance method [9] yields the following formulas for the real and imaginary shear moduli of the liquid layer:

$$G' = \frac{4\pi^2 M f_0 \Delta f' H}{S}, \quad (1)$$

$$G'' = \frac{4\pi^2 M f_0 \Delta f'' H}{S}, \quad (2)$$

where $M$ is the mass of the piezoelectric quartz crystal, $\Delta f'$ is the resonance frequency shift of the piezoelectric quartz crystal, $\Delta f''$ is the change in the half-width of the resonance curve of the quartz crystal, $f_0$ is its natural resonance frequency, $H$ is the thickness of the liquid layer, and $S$ is the area of the strap. Formulas (1) and (2) are valid under the following conditions:

$$m/M \ll 1, \quad H/\lambda \ll 1, \quad f_1/f_0 \ll 1, \quad (3)$$

where $m$ is the mass of the strap, $\lambda$ is the wavelength of the shear wave propagating in the liquid layer of thickness $H$ under the effect of the quartz crystal vibrations, and $f_1$ is the natural frequency of the strap, which is determined by the elastic coupling with the quartz surface through the liquid layer. In the experiment, to satisfy conditions (3), we used $M = 7.04$ g and $m = 0.4$ g. The shear wavelength was of an order of 100 μm at the given frequency, and the values of the film thickness $H$ were usually no greater than several microns [10]. The behavior of a viscoelastic liquid at low frequencies of external actions can be described by the simple Maxwell rheological model [11]. The shear viscosity $\eta$ is calculated by the formula

$$\eta = \frac{G'^2 + G''^2}{2\pi f_0 G''}. \quad (4)$$

From Eqs. (1), (2), and (4), one can calculate the main shear parameters of liquids.

## EXPERIMENTAL RESULTS AND DISCUSSION

We studied the shear viscoelastic properties of a set of drilling muds with different dynamic viscosities. The drilling muds were chosen as liquids that exhibit a non-Newtonian behavior under a shear external action. A drilling mud is a water solution of silicates (clays). Drilling muds with different dynamic viscosities were given different numbers: 1, 2, 3, etc. For all the liquids studied, linear dependences of the frequency shifts on the inverse thickness of the liquid layer were obtained at a constant vibration amplitude of the piezoelectric quartz crystal. Figure 2 shows the dependences of the real resonance frequency shift of the quartz crystal on the thickness of the liquid layer for drilling muds 2 and 3. One can see that the dependences are linear in the whole thickness range under study. From formulas (1), (2), and (4), we determine the real and imaginary parts of the complex shear modulus and the viscosity of the liquids under investigation. The results of the measurements are presented in the table. The last column shows the values of dynamic viscosity $\eta_d$, which are given for comparison.

Earlier, in [6] it was shown that the shear elasticity of liquids is of a nonlinear character, i.e., depends on the amplitude of the external action. We performed a study of the drilling muds under increasing angles of shear. Figure 3 presents the experimental dependences of the real resonance frequency shift on the vibration amplitude of the piezoelectric quartz crystal for several drilling muds. The abscissa axis represents the ratio $A/H$ as a measure of the angle of shear, where $A$ is the vibration amplitude of the quartz crystal in microns. The amplitude was determined by the method described in [12]. One can see that, up to a certain value of the angle of shear, the real frequency shift (and, hence, the shear modulus) has a constant value; as the angle of shear increases further, the real frequency shift decreases. Based on this observation, we can assume

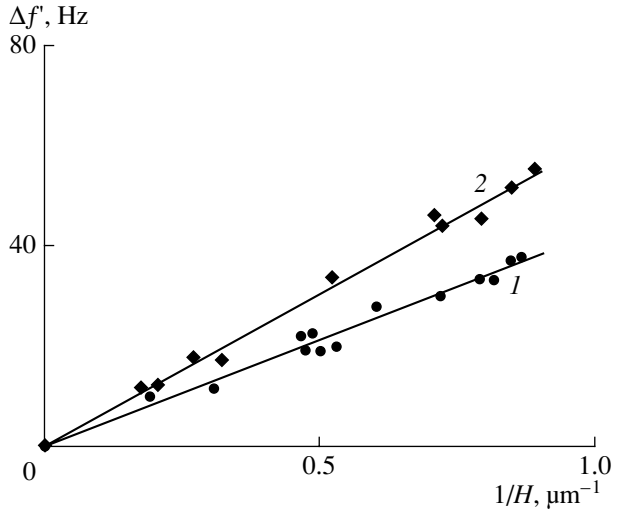


**Fig. 2.** Dependences of the real frequency shift of the resonator on the inverse thickness of the liquid layer for drilling muds (*1*) 3 and (*2*) 2.

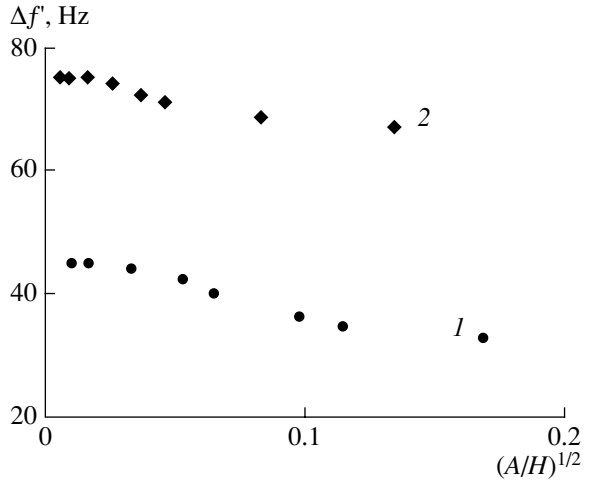


**Fig. 3.** Dependences of the real frequency shift of the resonator on the vibration amplitude of piezoelectric quartz crystal for drilling muds (*1*) 3 and (*2*) 2.

that, in equilibrium, the liquid possesses some equilibrium structure, which is retained in the presence of small strains; as the shear strain increases, the structure is destroyed, which leads to a decrease in the real shear modulus.

Thus, the study of drilling muds showed that they possess a complex shear modulus. This means that, in these liquids, a low-frequency viscoelastic process due to the interactions of large groups of molecules, i.e., clusters, takes place.

According to the Isakovich–Chaban model [13], a highly viscous liquid can be considered as a microinhomogeneous medium consisting of two dynamic components: ordered microregions, i.e., clusters, in a loosely packed disordered matrix. Under external actions, the clusters are rearranged. We assume that such a dynamic structural microinhomogeneity is a characteristic structural feature of all liquids. No fundamental qualitative difference exists between highly viscous and slightly viscous liquids. Only a quantitative difference can be found between them, namely: the cluster lifetime in ordinary liquids is much smaller than that in highly viscous liquids. In terms of this model, the low-frequency viscoelastic relaxation of liquids is caused by the decay and recovery of such fluctuation clusters, i.e., dynamic microinhomogeneities of the structure.

Let us assume that a cluster is a quasi-closed system consisting of $z$ identical kinetic units (atoms or groups of atoms). The cluster lifetime is determined by the equation [14]

$$\tau = B\exp[(U - TS)/kT]. \quad (5)$$

The thermodynamic probability $W$ of the cluster presence in the Boltzmann equation $S = k\ln W$ is higher the greater the number of particles in the cluster is, $W = cz$. Then, we have

$$\tau = czB\exp(U/kT). \quad (6)$$

The proportionality coefficient $c$ is equal to unity, because at $z = 1$, when the cluster consists of one kinetic unit, the quantity $\tau$ is determined from the known Frenkel formula [15]:

$$\tau = B\exp(U/kT), \quad (7)$$

where the pre-exponential factor $B$ means the period of particle oscillations about the equilibrium position $\tau_0$:

$$B \approx \tau_0 \approx 10^{-12}\ \text{s}. \quad (8)$$

Therefore the equation for the relaxation time takes the form

$$\tau = B_\lambda\exp(U/kT), \quad (9)$$

where the pre-exponential factor $B_\lambda$ for the low-frequency relaxation process proves to be $z$ times greater than for the high-frequency relaxation process associated with the mobility of a single particle: $B_\lambda = zB$. Amorphous polymers [16] have a wide variety of ordered microregions, which play the role of microvolume physical λ-nodes. Therefore, in these materials, a

Shear viscoelastic properties of liquids

| Liquids | $G'\times10^{-5}$, Pa | $G''\times10^{-5}$, Pa | η, Pa s | $\eta_d$, Pa s |
|---|---|---|---|---|
| Drilling mud no. 1 | 1.353 | 0.271 | 1.528 | 0.0192 |
| Drilling mud no. 2 | 0.334 | 0.072 | 0.353 | 0.0128 |
| Drilling mud no. 3 | 0.201 | 0.063 | 0.153 | 0.0085 |
| Drilling mud no. 4 | 0.442 | 0.099 | 0.451 | 0.0156 |

group of λ-transitions arises with identical activation energies but with different coefficients $B_\lambda$.

In the temperature dependence of the mechanical loss tangent measured for petroleum jelly at a frequency of $\nu_1$ = 40 kHz in the temperature interval within 300–340 K, two peaks were observed at temperatures of 303 and 323 K. At another frequency $\nu_2$ = 74 kHz, in the temperature interval within 263–303 K, one peak was observed at a temperature of about 283 K [17]. Presumably, at this frequency, the second peak should appear above 303 K. By analogy with polymers, one can assume that, in petroleum jelly within 300–340 K at $\nu_1$ = 40 kHz, two λ-relaxation processes, $\lambda_1$ and $\lambda_2$, corresponding to two different types of physical nodes, i.e., clusters, take place.

We substitute the condition of maximal mechanical loss [16], $\omega\tau = 2\pi\nu\tau = c$, into Eq. (9) to obtain the relation between frequency and temperature:

$$\nu = \nu_0 \exp(-U/kT), \tag{10}$$

$$\nu_0 = \frac{c}{2\pi B_\lambda}. \tag{11}$$

Here the constant $c$ for small-scale transitions is equal to unity, $c \approx 1$, which corresponds to the Debye equation for dielectric relaxation in liquids. For a number of the relaxation transitions that occur in amorphous organic polymers due to the mobility of macromolecule segments, the quantity $c$ is close to $c \approx 10$ [16].

Writing formula (10) for the dependence $\nu(T)$ at frequencies $\nu_1$ = 40 kHz and $\nu_2$ = 74 kHz and substituting the $\lambda_1$-transition temperatures $T_1$ = 303 K and $T_2$ = 283 K into it at these frequencies, we obtain the following approximate estimate for the activation energy of the low-frequency viscoelastic relaxation transition ($\lambda_1$-process) in petroleum jelly:

$$U = \left(R\ln\frac{\nu_1}{\nu_2}\right)\left(\frac{1}{T_1} - \frac{1}{T_2}\right)^{-1} \approx 21.6\ \frac{\text{kJ}}{\text{mol}}. \tag{12}$$

This estimate is close to the energy of the hydrogen bond ($U \approx 5$ kcal/mol).

Knowing $U$, we can estimate the pre-exponential factor

$$B_\lambda = \frac{c}{2\pi\nu_0} \approx 2 \times 10^{-9}\ \text{s},$$

where the values $c$ = 10 and $\nu_0 = \nu_1 \exp(U/kT_1) \approx 7 \times 10^8$ Hz are used. Assuming that $B = 10^{-12}$ s for one particle, we estimate (in order of magnitude) the number of particles in a cluster of petroleum jelly:

$$z = B_\lambda/B \approx 10^3.$$

At $c$ = 1, we have $z = 10^2$. For a SKMS-10 butadiene-methylstyrene elastomer, the following estimate was obtained [14, 16]:

$$z = B_\lambda/B \approx 10^4\text{–}10^6.$$

The segment volume is about $V \approx 10^{-21}$ cm$^3$, which yields a cluster volume of $zV = 10^{-17}$–$10^{-15}$ cm$^3$. This value corresponds to a linear size of $l \approx 10^{-6}$–$10^{-5}$ cm, which agrees well with the direct estimates of the size of ordered microregions of the elastomer structure [16]. A close value was obtained for the cluster size in glycerol by Isakovich and Chaban [13]:

$$l = (2D\tau)^{1/2} \approx 10^{-7}\ \text{cm},$$

where $D$ is the self-diffusion coefficient and $\tau$ is the relaxation time.

Thus, in terms of the proposed cluster model, the low-frequency shear elasticity of liquids is caused by the presence of relatively long-lived clusters of a fluctuation nature: they arise and decay with time. Their lifetime is long because of the great number of bound molecules forming a cluster rather than because of the large-size particles. The decay of a cluster occurs through the bound molecule-to-free molecule transition, which resembles the decay of a liquid drop due to the evaporation of individual molecules. Such a multistep process is characterized by a long relaxation time $\tau$.

## CONCLUSIONS

(i) By the acoustic resonance method with the use of a piezoelectric quartz resonator, we obtained the values of the real and imaginary shear moduli and mechanical loss tangent of drilling muds at a constant vibration amplitude of the quartz crystal. We showed that all liquids studied possess measurable values of the complex shear modulus.

(ii) The study of shear parameters under an increasing vibration amplitude of the quartz crystal showed that the shear modulus of the objects studied decreases with increasing angle of shear.

(iii) We proposed a cluster model of liquids on the basis of the Isakovich–Chaban nonlocal diffusion theory. In the framework of the model, we estimated the activation energy of the viscoelastic relaxation process.

## ACKNOWLEDGMENTS

This work was supported by the Russian Foundation for Basic Research, project nos. 02-02-16453 and 02-01-00007. We are grateful to P.A. Pyatakov and I.B. Esipov for discussing the results of this study.

## REFERENCES

1. J. D. Ferry, *Viscoelastic Properties of Polymers* (Wiley, New York, 1961; Inostrannaya Literatura, Moscow, 1963).
2. K. Hyun, S. H. Kim, K. H. Ahn, and S. J. Lee, J. Non-Newtonian Fluid Mech. **107**, 51 (2002).
3. I. B. Esipov, in *Acoustics of Inhomogeneous Media: Proceedings of Professor S. A. Rybak's Scientific School* (Mosk. Fiz.–Tekh. Inst., Moscow, 2000), No. 1, pp. 51–57.

4. G. Mac-Skeeman, in *Physical Acoustics: Principles and Methods*, Ed. by W. P. Mason (Academic, New York, 1964; Inostrannaya Literatura, Moscow, 1966), Vol. 1, Part A, pp. 327–397.
5. B. B. Badmaev and B. B. Damdinov, Akust. Zh. **47**, 561 (2001) [Acoust. Phys. **47**, 487 (2001)].
6. U. B. Bazaron, B. V. Deryagin, and A. V. Bulgadaev, Dokl. Akad. Nauk SSSR **166**, 639 (1966).
7. L. I. Mandel'shtam, *Collected Works* (Akad. Nauk SSSR, Moscow, 1955).
8. S. É. Khaĭkin, L. P. Lisovskiĭ, and A. E. Salomonovich, Dokl. Akad. Nauk SSSR **24**, 134 (1939).
9. U. B. Bazaron, B. V. Deryagin, and O. R. Budaev, Dokl. Akad. Nauk SSSR **205**, 1324 (1972) [Sov. Phys. Dokl. **17**, 769 (1972)].
10. B. B. Badmaev, O. R. Budaev, and T. S. Dembelova, Akust. Zh. **45**, 610 (1999) [Acoust. Phys. **45**, 541 (1999)].
11. V. N. Alekseev and S. A. Rybak, in *Acoustics of Inhomogeneous Media: Proceedings of Professor S. A. Rybak's Scientific School* (Mosk. Fiz.–Tekh. Inst., Moscow, 2001), No. 2, pp. 115–126.
12. U. B. Bazaron, *Low-Frequency Shear Elasticity of Liquids* (Buryat. Nauchn. Tsentr Sib. Otd. Ross. Akad. Nauk, Ulan-Ude, 2000).
13. M. A. Isakovich and I. A. Chaban, Zh. Éksp. Teor. Fiz. **50**, 1343 (1966) [Sov. Phys. JETP **23**, 893 (1966)].
14. D. S. Sanditov, Dokl. Sib. Otd. Akad. Nauk Vyssh. Sh., No. 2 (4), 1 (2001).
15. Ya. I. Frenkel', *Kinetic Theory of Liquids* (Nauka, Leningrad, 1975; Clarendon, Oxford, 1946).
16. G. M. Bartenev and D. S. Sanditov, *Relaxation Processes in Glass-Like Systems* (Nauka, Novosibirsk, 1986).
17. B. B. Badmaev, M. N. Ivanova, and S. A. Bal'zhinov, *The I Conference on Basic and Applied Problems of Physics: Abstracts of Papers* (Buryat Scientific Center, Siberian Division, Russian Academy of Sciences, Ulan-Ude, 1999), p. 62.

*Translated by E. Golyamina*

*Acoustical Physics, Vol. 50, No. 2, 2004, pp. 126–133. Translated from Akusticheskiĭ Zhurnal, Vol. 50, No. 2, 2004, pp. 161–169.*


# Stoneley Wave Generation by an External Seismic Point Source in an Infinite Fluid-filled Borehole Embedded in a Transversely Isotropic Formation: Basic Relationships

**P. M. Bokov and A. M. Ionov**

*Moscow State Engineering Physics Institute (State University), Kashirskoe sh. 31, Moscow, 115409 Russia*
*e-mail: aionov@hotmail.com*

Received August 22, 2002

**Abstract**—The method of integral transformations is used to obtain a long-wave solution to the problem of tube wave excitation by an external point source in an infinite fluid-filled borehole embedded in a transversely isotropic formation. The external field that occurs in the formation gives rise to waves in the borehole fluid.The waves generated in the borehole include the lowest mode of the Stoneley wave (tube wave), which is the borehole eigenmode, and the *qP*- and *qSV*-waves. It is shown that the Stoneley wave is determined by the contributions of two poles in the complex plane of horizontal slowness. According to the asymptotic solution, the Stoneley wave can be described by one of three different waveforms depending on the relationship between the elastic parameters of the surrounding anisotropic formation and the borehole fluid. An analysis of the results of calculations shows that the shape and polarity of the Stoneley wave strongly depend on the sign of the nonellipticity parameter of the elastic medium, which offers a possibility of estimating the anisotropy of the borehole environment from observations of the waveform of the Stoneley wave. *© 2004 MAIK "Nauka/Interperiodica".*

## INTRODUCTION

The excitation and propagation of tube waves generated in fluid-filled boreholes by both external and internal seismic sources are the subject of numerous publications [1–4], because the characteristics of the borehole wave field carry valuable information about the properties of the borehole environment. Some efficient algorithms were designed to simulate the behavior of tube waves in a borehole embedded in both isotropic and anisotropic layered formations [3, 4]. A reasonably complete theory of tube wave propagation was developed for boreholes embedded in isotropic elastic surroundings. In the case of a pulsed source located within a fluid-filled borehole, this theory may allow one to obtain a solution to the problem of tube wave propagation for an arbitrary relationship between the wavelength and the borehole radius. In the seismic frequency range, the wavelength usually far exceeds the borehole radius. For this reason, the advisable approach consists in investigating the problem in the long-wave approximation, which considerably simplifies the formulation and solution of the problem and the analysis of the generated wave field. In the case of tube wave excitation by an external pulsed source, the analysis of the dynamic field generated in the borehole becomes much more complex even in the long-wave approximation. It is well known [1] that plane elastic *P*- and *SV*-waves incident on a fluid-filled borehole generate only *P*- and *SV*-waves in the borehole, but not the borehole eigenmode (the Stoneley wave). The Stoneley wave is generated in the borehole by an external dynamic action if the incident wave front has a nonzero curvature. An expression for the Stoneley wave excited in an infinite rectilinear borehole embedded in an isotropic elastic formation by an external isotropic point source was obtained only recently [5].

Actual geological formations often show prominent anisotropy. For this reason, much attention has been paid by researchers to studying the dynamic characteristics of tube waves in anisotropic formations and, in particular, in formations with a vertical symmetry axis, which are also called transversely isotropic formations (see, e.g., [6, 7]). In the latter, an isotropic point source excites both quasi-longitudinal *qP*-waves and quasi-transverse *qSV*-waves [1]. They considerably complicates the asymptotic analysis of the generated tube wave field even in the long-wave approximation. In addition, the geometric properties of wave fronts of the quasi-longitudinal and quasi-transverse waves incident on the borehole from the surrounding formation depend on the parameters of anisotropy and can be rather complex, which makes the complete investigation even more difficult [8].

In this paper, an exact solution is obtained to the problem of tube wave excitation by an external point source in a fluid-filled borehole embedded in a transversely isotropic formation. The solution is obtained with the use of the method of integral transformations. Asymptotically, the wave field excited in the borehole fluid can be divided into quasi-longitudinal (*qP*) and quasi-transverse (*qSV*) waves, whose waveforms coincide with those of incident waves in the surrounding

1063-7710/04/5002-0126$26.00 © 2004 MAIK "Nauka/Interperiodica"

formation, and the Stoneley wave. The emphasis is on investigating the dynamic characteristics of the Stoneley wave and their dependence on the anisotropy of the surrounding formation.

## TUBE WAVE PROPAGATION IN A BOREHOLE EMBEDDED IN A TRANSVERSELY ISOTROPIC MEDIUM

The statement of the problem under consideration is as follows. An isotropic pulsed point source is located at a distance $r$ from a fluid-filled borehole embedded in a transversely isotropic elastic formation whose symmetry axis coincides with the borehole axis. Figure 1 shows the geometry of the problem. We desire to find the dynamic pressure field produced in the borehole fluid under the action of seismic waves generated by the source. The problem is solved in the long-wave approximation, i.e., we assume that the characteristic wavelength of the source far exceeds the borehole radius. The field in the borehole must satisfy the Sommerfeld radiation condition [9] for distant portions of the borehole ($z \longrightarrow \pm\infty$).

A transversely isotropic medium has a distinguished symmetry axis, and, in the plane perpendicular to this axis, elastic properties are independent of direction. Since the symmetry axis and the borehole axis coincide, Hooke's law for this medium has the following form (in the cylindrical coordinate system) [1, 10]:

$$\begin{aligned}\sigma_{rr} &= (\lambda_\parallel + 2\mu_\parallel)\varepsilon_{rr} + \lambda_\parallel\varepsilon_{\theta\theta} + \lambda_\perp\varepsilon_{zz};\\ \sigma_{\theta\theta} &= \lambda_\parallel\varepsilon_{rr} + (\lambda_\parallel + 2\mu_\parallel)\varepsilon_{\theta\theta} + \lambda_\perp\varepsilon_{zz};\\ \sigma_{zz} &= \lambda_\perp\varepsilon_{rr} + \lambda_\perp\varepsilon_{\theta\theta} + (\lambda_\perp + 2\mu_\perp)\varepsilon_{zz};\\ \sigma_{r\theta} &= 2\mu_\parallel\varepsilon_{r\theta};\quad \sigma_{\theta z} = 2\mu_*\varepsilon_{\theta z};\quad \sigma_{zr} = 2\mu_*\varepsilon_{zr},\end{aligned} \tag{1}$$

where $\sigma_{ik}$ is the stress tensor, $\varepsilon_{ik}$ is the strain tensor, $\lambda_\perp$ and $\mu_\perp$ are the Lamé coefficients along the symmetry axis ($z$ axis), $\lambda_\parallel$ and $\mu_\parallel$ are the Lamé coefficients in the plane perpendicular to the symmetry axis, and $\mu_*$ is the shear modulus independent of other elastic constants. The components of the strain tensor are expressed through the displacement components according to the formulas

$$\begin{aligned}\varepsilon_{rr} &= \frac{\partial u_r}{\partial r};\quad \varepsilon_{\theta\theta} = \frac{u_r}{r};\quad \varepsilon_{zz} = \frac{\partial u_z}{\partial z};\quad \varepsilon_{z\theta} = 0;\\ \varepsilon_{r\theta} &= 0;\quad \varepsilon_{rz} = \frac{1}{2}\left(\frac{\partial u_r}{\partial r} + \frac{\partial u_z}{\partial z}\right).\end{aligned} \tag{2}$$

Below, it will be convenient to use the propagation velocities of elastic waves instead of the Lamé coefficients. We denote the density of the elastic medium as $\rho_s$ and introduce the velocities of the corresponding

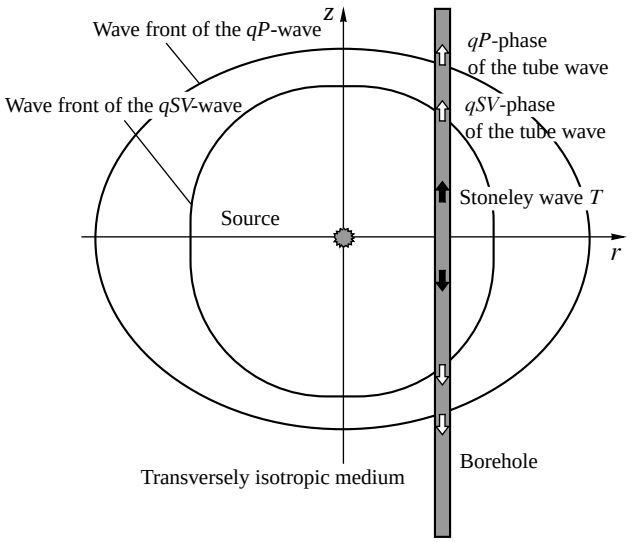


**Fig. 1.** Geometry of the problem.

longitudinal and transverse waves according to [10]:

$$\begin{aligned}\alpha_\parallel &= \sqrt{\frac{\lambda_\parallel + 2\mu_\parallel}{\rho_s}};\quad \alpha_\perp = \sqrt{\frac{\lambda_\perp + 2\mu_\perp}{\rho_s}};\\ \alpha_* &= \sqrt{\frac{\lambda_\perp + 2\mu_*}{\rho_s}};\quad \beta_\parallel = \sqrt{\frac{\mu_\parallel}{\rho_s}};\quad \beta_* = \sqrt{\frac{\mu_*}{\rho_s}}.\end{aligned} \tag{3}$$

Here, $\alpha_\perp$ is the velocity of the longitudinal wave in the direction of the symmetry axis, $\alpha_\parallel$ is the velocity of the longitudinal wave in the plane perpendicular to the symmetry axis, $\beta_*$ is the velocity of the transverse wave in any of these two mutually orthogonal directions, and $\beta_\parallel$ is the velocity of transverse *SH*-waves in the plane perpendicular to the symmetry axis.

According to the theory of excitation and propagation of tube waves, pressure at every point of the liquid inside the borehole is formed by the combined contributions of secondary sources distributed along the borehole surface. Physically, these sources are formed by the local compression of the borehole wall induced by seismic waves propagating in the surrounding medium. In the long-wave approximation, the following wave equation describes the propagation of waves in the fluid of a vertical straight borehole embedded in a transversely isotropic medium with a vertical symmetry axis [2]:

$$\frac{\partial^2 P}{\partial z^2} - \frac{1}{c_{\text{tw}}^2}\frac{\partial^2 P}{\partial t^2} = -2\rho_\text{f}\frac{\partial^2}{\partial t^2}\left[\frac{(\sigma_{rr}^{\text{ext}} + \sigma_{\theta\theta}^{\text{ext}})}{E_h} - \frac{\nu_z\sigma_{zz}^{\text{ext}}}{E_z}\right], \tag{4}$$

where $P(z, t)$ is the dynamic pressure in the borehole; $c_{\text{tw}}$ is the tube wave velocity; $\rho_\text{f}$ is the fluid density; $t$ is the time; $\sigma_{rr}^{\text{ext}}(r, z, t)$, $\sigma_{\theta\theta}^{\text{ext}}(r, z, t)$, and $\sigma_{zz}^{\text{ext}}(r, z, t)$ are the dynamical stresses in the formation at the borehole axis; $E_z$ and $E_h$ are the effective Young's moduli in the

vertical and horizontal directions; and $\nu_z$ is the effective Poisson's ratio for the vertical uniaxial stress state. One can show that the effective elastic constants involved in Eq. (4) are expressed in terms of parameters (3) according to the formulas

$$\frac{\nu_z}{E_z} = \frac{(\alpha_*^2 - 2\beta_*^2)^2}{2\rho_s[(\alpha_\parallel^2 - \beta_\parallel^2)\alpha_\perp^2 - (\alpha_*^2 - 2\beta_*^2)^2]};$$

$$E_h^{-1} = \frac{[\alpha_\parallel^2\alpha_\perp^2 - (\alpha_*^2 - 2\beta_*^2)^2]}{4\rho_s\beta_\parallel^2[(\alpha_\parallel^2 - \beta_\parallel^2)\alpha_\perp^2 - (\alpha_*^2 - 2\beta_*^2)^2]}, \quad (5)$$

$$c_{tw} = c_f\sqrt{\mu_\parallel/(\mu_\parallel + \rho_f c_f^2)}.$$

It is well known [1] that the fundamental solutions to the wave equation in a transversely isotropic medium are quasi-longitudinal (*qP*) and quasi-transverse (*qSV*) waves. Using the cylindrical coordinate system $(r, \theta, z)$, we introduce the potentials $\phi(r, z, t)$ and $\psi(r, z, t)$ of elastic displacements in *qP*- and *qSV*-waves propagating in the formation, so that these potentials are related to the displacement components by the formulas

$$u_r = \frac{\partial\phi}{\partial r} + \frac{\partial^2\psi}{\partial r\partial z}; \quad u_z = \frac{\partial\phi}{\partial z} - \Delta_r\psi, \quad (6)$$

where $\Delta_r = \frac{1}{r}\frac{\partial}{\partial r}\left(r\frac{\partial}{\partial r}\right)$ is the radial part of the Laplacian $\Delta = \Delta_r + \partial^2/\partial z^2$ in the cylindrical coordinate system. Expressing the components of strain tensor (2) of the medium in terms of the elastic displacement potentials (6), we obtain

$$\varepsilon_{rr}^{ext} + \varepsilon_{\theta\theta}^{ext} = \Delta_r\left(\phi + \frac{\partial\psi}{\partial z}\right); \quad \varepsilon_{zz}^{ext} = \frac{\partial^2\phi}{\partial z^2} - \Delta_r\frac{\partial\psi}{\partial z}. \quad (7)$$

Using Hooke's law (1), we represent Eq. (4) in the form

$$\frac{\partial^2 P}{\partial z^2} - \frac{1}{c_{tw}^2}\frac{\partial^2 P}{\partial t^2} = -\frac{\rho_f}{\beta_\parallel^2}\frac{\partial^2}{\partial t^2}\left\{\left[\alpha_\parallel^2\Delta_r\phi + (\alpha_*^2 - 2\beta_*^2)\frac{\partial^2\phi}{\partial z^2}\right] + [\alpha_\parallel^2 - \alpha_*^2 + 2\beta_*^2]\Delta_r\frac{\partial\psi}{\partial z}\right\}. \quad (8)$$

Note that the radial coordinate *r* is a fixed parameter in Eq. (8).

After a double Fourier transformation of Eq. (8) with respect to time *t* and the vertical coordinate *z*, we obtain a formal solution to Eq. (8) in the form of the Fourier integral

$$\bar{P}(r, z, \omega) = -\frac{\rho_f\omega^2}{\beta_\parallel^2}\int_{-\infty}^{+\infty} dk\exp(-ikz) \times \frac{(\mathbf{L}_1\bar{\phi}(r, k, \omega) + \mathbf{L}_2\bar{\psi}(r, k, \omega))}{k^2 - \omega^2/c_{tw}^2}, \quad (9)$$

where $\omega$ is the angular frequency and *k* is the wave number. In Eq. (9), we introduced differential operators $\mathbf{L}_1 \equiv \alpha_\parallel^2\Delta_r - (\alpha_*^2 - 2\beta_*^2)k^2$ and $\mathbf{L}_2 \equiv -ik[\alpha_\parallel^2 - \alpha_*^2 + 2\beta_*^2]\Delta_r$; the overbar means the Fourier transform with respect to time.

Further calculation requires that the behavior of the elastic displacement potentials in the formation along the borehole axis be known as explicit functions of the coordinates and time. Here, we assume that seismic waves are generated by an isotropic point source. Potentials $\phi$ and $\psi$ of seismic waves generated by such a source are determined in the Appendix in the form of an integral with respect to the ray parameter (the horizontal slowness) *p*.

Equation (9) depends on the Fourier transforms of the potentials $\bar{\phi}(r, k, \omega)$ and $\bar{\psi}(r, k, \omega)$. Performing the Fourier transformation of the potentials (A1) with respect to *z* and changing the integration order, we encounter the necessity of calculating the Fourier transforms of the functions $\exp(-i\omega\xi_j(p)|z|)$ and $\exp(-\omega p|z|)$ for the potential $\bar{\phi}(r, k, \omega)$ and the functions $\mathrm{sgn}(z)\exp(-i\omega\xi_j(p)|z|)$ and $\mathrm{sgn}(z)\exp(-i\omega p|z|)$ for the potential $\bar{\psi}(r, k, \omega)$ (here, $j = 1, 2$).

To calculate the Fourier transform with respect to *z*, we use the residue theorem. The contour integration is performed as in [11] when obtaining the solutions for the field potentials $\bar{\phi}$ and $\bar{\psi}$ in the formation. The correct choice of poles follows from the principle of ultimate absorption and the condition at infinity (only outgoing waves are present at infinity) [9]. The calculation of integrals with allowance for the principle of ultimate absorption gives the following expressions for the Fourier transforms of the potentials:

$$\begin{pmatrix}\bar{\phi}(r, q, \omega)\\ \bar{\psi}(r, q, \omega)\end{pmatrix} = \frac{i\bar{A}(\omega)}{\pi}\begin{pmatrix}-1\\ q\omega^{-1}\end{pmatrix}\int_0^{+\infty} dp\frac{pJ_0(\omega pr)}{\Phi(p)} \times\left[\frac{1}{q^2 + p^2}\begin{pmatrix}pa_0(p)\\ b_0(p)\end{pmatrix} + \sum_{j=1}^{2}\frac{1}{(q^2 - \xi_j^2(p))}\begin{pmatrix}i\xi_j(p)a_j(p)\\ b_j(p)\end{pmatrix}\right], \quad (10)$$

where the integration variable *k* was replaced according to $k = \omega q$. Substituting the Fourier transforms of potentials $\bar{\phi}(r, q, \omega)$ and $\bar{\psi}(r, q, \omega)$ in Eq. (9), we obtain the desired representation of the solution in the form of the double integral with respect to *p* and *q*. The integral can

be simplified by changing the integration order and integrating with respect to the variable $q$.

The contributions of the first terms in potentials (10) (with pole singularities at $q = \pm ip$) to the pressure field (9) in the borehole can be calculated by the residue theorem:

$$\bar{P}^{\mathrm{tw}}_{inh}(z, \omega) = -\alpha_{\|}^2 \sigma_1 c_{\mathrm{tw}} \frac{\rho_{\mathrm{f}}}{\beta_{\|}^2} i\omega^3 \bar{A}(\omega) \times \exp\left(-i\frac{\omega}{c_{\mathrm{tw}}}|z|\right) \int_0^{\infty} dp \frac{p^5 J_0(\omega p r)}{\Phi(p)}, \tag{11}$$

where $\sigma_1$ is a constant determined in the Appendix.

Substituting the remaining terms in the potentials (10) (with pole singularities at $q = \pm\xi_j(p)$) in Eq. (9) and integrating with respect to the variable $q$, we obtain that the dynamic pressure field in the borehole fluid is the sum of two components: $\bar{P}(z, \omega) = \bar{P}^{\mathrm{tw}}(z, \omega) + \bar{P}^{\mathrm{ext}}(z, \omega)$. The first term $\bar{P}^{\mathrm{tw}}(z, \omega)$ describes the Stoneley wave propagating along the borehole with velocity $c_{\mathrm{tw}}$, and the second term $\bar{P}^{\mathrm{ext}}(z, \omega)$ describes the contribution of the quasi-longitudinal $qP$- and quasi-transverse $qSV$-waves. The terms $\bar{P}^{\mathrm{tw}}(z, \omega)$ and $\bar{P}^{\mathrm{ext}}(z, \omega)$ are given by the formulas

$$\bar{P}^{\mathrm{tw}}(z, \omega) = i\omega^3 \bar{A}(\omega) c_{\mathrm{tw}} \frac{\rho_{\mathrm{f}}}{\beta_{\|}^2} \exp\left(-i\frac{\omega}{c_{\mathrm{tw}}}|z|\right) \times \int_0^{+\infty} dp \frac{p J_0(\omega p r)}{\Phi(p)} \sum_{j=1}^{2} (\xi_j^2(p) - c_{\mathrm{tw}}^{-2})^{-1} [\xi_j(p) \times a_j(p)(\alpha_{\|}^2 p^2 + \sigma_3 c_{\mathrm{tw}}^{-2}) + \sigma_4 c_{\mathrm{tw}}^{-2} p^2 b_j(p), \tag{12a}$$

$$\bar{P}^{\mathrm{ext}}(z, \omega) = -i\omega^3 \bar{A}(\omega) c_{\mathrm{tw}} \frac{\rho_{\mathrm{f}}}{\beta_{\|}^2} \int_0^{+\infty} dp \frac{p J_0(\omega p r)}{\Phi(p)} \times \sum_{j=1}^{2} \exp(-i\omega\xi_j(p)|z|)\xi_j^{-1}(p)(\xi_j^2(p) - c_{\mathrm{tw}}^{-2})^{-1} \times [\xi_j(p) a_j(p)(\alpha_{\|}^2 p^2 + \sigma_3 \xi_j^2(p)) + \sigma_4 p^4 b_j(p)\xi_j^2(p)], \tag{12b}$$

where $\sigma_3 = \alpha_*^2 - 2\beta_*^2$ and $\sigma_4 = \alpha_{\|}^2 - \sigma_3$.

Now, we rearrange Eq. (12a) for the Stoneley wave. As follows from Eq. (12a), the integrand has singular points (as will be shown below, these are power singularities) determined by the implicit equations $p^2 + c_{\mathrm{tw}}^{-2} - c_{1,2}^{-2}(p) = 0$. Reducing the sum in braces in Eq. (12a) to a common denominator and performing relatively cumbersome algebraic transformations, we obtain that the quantity $\bar{P}^{\mathrm{tw}}(z, \omega)$ can be represented as the sum of two terms: the first term $\bar{P}_1^{\mathrm{tw}}(z, \omega)$ retains the aforementioned singularities and the second term $\bar{P}_2^{\mathrm{tw}}(z, \omega)$ is free of them. The second term $\bar{P}_2^{\mathrm{tw}}(z, \omega)$ coincides to a sign with the term $\bar{P}_{inh}^{\mathrm{tw}}(z, \omega)$ given by Eq. (11), so that their combined contribution to the field of the Stoneley wave is zero. Hence, the total field of the Stoneley wave is only determined by the term $\bar{P}_1^{\mathrm{tw}}(z, \omega)$:

$$\bar{P}^{\mathrm{tw}}(z, \omega) = \bar{P}_1^{\mathrm{tw}}(z, \omega) = -i\omega^3 \bar{A}(\omega) c_{\mathrm{tw}} \frac{\rho_{\mathrm{f}}}{\beta_{\|}^2} \times \exp\left(-i\frac{\omega}{c_{\mathrm{tw}}}|z|\right) \int_0^{+\infty} dp \frac{p J_0(\omega p r)}{\Phi(p)} \times \left\{ \frac{[1 - \beta_*^2(p^2 + c_{\mathrm{tw}}^{-2})][\alpha_{\|}^2 p^2 + \sigma_3 c_{\mathrm{tw}}^{-2}] + c_{\mathrm{tw}}^{-2}\Delta_\alpha p^2}{c_1^2(p)c_2^2(p)(p^2 + c_{\mathrm{tw}}^{-2} - c_1^{-2}(p))(p^2 + c_{\mathrm{tw}}^{-2} - c_2^{-2}(p))} \right\}, \tag{13}$$

where $\Delta_\alpha = [\alpha_{\|}^2(\alpha_{\perp}^2 - \alpha_*^2) + (\alpha_*^2 - \alpha_{\|}^2)(\alpha_*^2 - \beta_*^2)]$.

Let us show that the poles determined by zeros of the fourth-order polynomial $\Phi(p)$ contribute nothing to the field of the Stoneley wave given by Eq. (13). Using Eq. (A2) for the velocities of $qP$- and $qSV$-waves as functions of parameter $p$, we rearrange the denominator of Eq. (13) to the form

$$c_1^2 c_2^2 (p^2 + c_{\mathrm{tw}}^{-2} - c_1^{-2})(p^2 + c_{\mathrm{tw}}^{-2} - c_2^{-2}) = \alpha_{\|}^2 \beta_*^2 (p^2 - p_1^2)(p^2 - p_2^2)/\Phi(p). \tag{14}$$

Here, $p_1$ and $p_2$ are the roots of biquadratic equation with real coefficients

$$\Phi(p) - B(p)(p^2 + c_{\mathrm{tw}}^{-2}) + \alpha_{\perp}^2 \beta_*^2 (p^2 + c_{\mathrm{tw}}^{-2})^2 = 0. \tag{15}$$

These roots are given by the formula

$$p_{1,2}^2 = -\frac{1}{c_{\mathrm{tw}}^2} + \frac{1}{2}\left(\frac{1}{\alpha_{\|}^2} + \frac{1}{\beta_*^2}\right) - \frac{1}{c_{\mathrm{tw}}^2}\left(\frac{\alpha_*^2}{\alpha_{\|}^2} - 1\right) + \frac{1}{2c_{\mathrm{tw}}^2}\left(\frac{\alpha_{\perp}^2}{\beta_*^2} - \frac{\alpha_*^4}{\alpha_{\|}^2\beta_*^2}\right) \mp \frac{1}{2}\left\{\left[\frac{1}{\alpha_{\|}^2} - \frac{1}{\beta_*^2}\right]^2 - \frac{2}{c_{\mathrm{tw}}^2}\left[\left(\frac{1}{\alpha_{\|}^2} + \frac{1}{\beta_*^2}\right)\left(2\left(\frac{\alpha_*^2}{\alpha_{\|}^2} - 1\right) + \left(\frac{\alpha_{\perp}^2}{\beta_*^2} - \frac{\alpha_*^4}{\alpha_{\|}^2\beta_*^2}\right)\right) - \frac{2}{\beta_*^2}\left(\frac{\alpha_{\perp}^2}{\alpha_{\|}^2} - 1\right)\right] + \frac{1}{c_{\mathrm{tw}}^4}\left[\left(\frac{\alpha_{\perp}^2}{\beta_*^2} - \frac{\alpha_*^4}{\alpha_{\|}^2\beta_*^2}\right)^2 + 4\left(\frac{\alpha_*^4}{\alpha_{\|}^4} - \frac{\alpha_{\perp}^2}{\alpha_{\|}^2}\right)\left(1 - \frac{\alpha_*^2}{\beta_*^2}\right)\right]\right\}^{1/2}, \tag{16}$$

where the minus sign (root $p_1^2$) corresponds to the *qP*-wave and the plus sign (root $p_2^2$), to the *qSV*-wave.

Substituting expression (14) for the denominator in Eq. (13), we obtain the Stoneley wave in the form

$$\bar{P}^{\text{tw}}(z, \omega) = -i\omega^3 \bar{A}(\omega) \frac{\rho_f c_{\text{tw}}}{\alpha_\parallel^2 \beta_\parallel^2 \beta_*^2} \exp\left(-i\frac{\omega}{c_{\text{tw}}}|z|\right)$$

$$\times \int_0^{+\infty} dp\, p J_0(\omega p r) \tag{17}$$

$$\times \left\{ \frac{[1 - \beta_*^2(p^2 + c_{\text{tw}}^{-2})][\alpha_\parallel^2 p^2 + \sigma_3 c_{\text{tw}}^{-2}] + c_{\text{tw}}^{-2}\Delta_\alpha p^2}{(p^2 - p_1^2)(p^2 - p_2^2)} \right\}.$$

In this form, the integral can be easily calculated with the use of the residue theorem. Before we represent the borehole pressure field in final form, let us analyze the possible values of the roots $p_1^2$ and $p_2^2$, because, as will be shown below, they may determine different shapes and amplitudes of the Stoneley wave. Since quadratic equation (15) has real coefficients, it may have in the general case either two real roots (positive or negative), or one multiple real root, or two complex conjugate roots.

*Two real roots.* A quadratic equation with real coefficients may have two positive roots, two negative roots, or one positive root and one negative root. In an isotropic medium, $p_1^2 \longrightarrow \alpha^{-2} - c_{\text{tw}}^{-2}$ and $p_2^2 \longrightarrow \beta^{-2} - c_{\text{tw}}^{-2}$ (here, $\alpha$ and $\beta$ are the velocities of longitudinal and transverse waves in the isotropic medium, respectively). It is known that, in the case of an isotropic medium, the difference $\alpha^{-2} - c_{\text{tw}}^{-2}$ is almost always negative (an opposite case also may occur, but very seldom [12]). Conversely, the difference $\beta^{-2} - c_{\text{tw}}^{-2}$ can be both positive (in low-velocity media for which the inequality $\beta < c_f\sqrt{1 - \rho_f/\rho_s}$ holds) and negative (in high-velocity media for which the inverse inequality holds).

In obtaining the final result, we assume that only two situations can take place for transversely isotropic media: the existence of either two negative roots $p_1^2$, $p_2^2$ or two roots of different signs. We supported this assumption by multiple calculations for actual media, whose elastic parameters were published in the literature.

Consider first the case of two negative roots and find the expression for the Stoneley wave. With this goal in mind, we calculate the integral with respect to the horizontal slowness in Eq. (17). Using the relationship $J_0(\omega pr) = [H_0^{(2)}(\omega pr) - H_0^{(2)}(-\omega pr)]/2$ for the Bessel function, we represent Eq. (17) in the form $\int_0^{+\infty} p\,dp J_0(\omega pr)F(p^2) = \frac{1}{2}\int_0^{+\infty} p\,dp\, H_0^{(2)}(\omega pr)F(p^2)$. Here, $H_0^{(2)}(\omega pr)$ is a zero-order Hankel function of the second kind and $F(p^2)$ denotes the expression in braces. Consider this integral in the complex plane of variable $p$. To calculate the integral, we use the closed contour shown in Fig. 2 and the residue theorem. Because we assume that the roots $p_1^2$ and $p_2^2$ are negative, the pole positions $p_{1,2} = \pm\sqrt{p_{1,2}^2}$ appear to be purely imaginary in this case. Figure 2 shows that, in the case under consideration, we must use residues at the poles lying in the lower half-plane, i.e., $-i\sqrt{-p_1^2}$ and $-i\sqrt{-p_2^2}$.

Using the definition of the zero-order Macdonald function of a real argument $K_0(x) = -i\pi H_0^{(2)}(-ix)/2$, we represent the Stoneley wave in the following final form:

$$\bar{P}^{\text{tw}}(z, \omega) = \frac{\rho_f c_{\text{tw}}}{\alpha_\parallel^2 \beta_\parallel^2 \beta_*^2} \frac{i\omega^3 \bar{A}(\omega)}{(p_2^2 - p_1^2)} \exp\left(-\frac{i\omega|z|}{c_{\text{tw}}}\right)$$

$$\times \sum_{j=1}^{2} (-1)^{j+1} K_0(\omega\sqrt{-p_j^2}\, r)\{[1 - \beta_*^2(p_j^2 + c_{\text{tw}}^{-2})] \tag{18}$$

$$\times [\alpha_\parallel^2 p_j^2 + \sigma_3 c_{\text{tw}}^{-2}] + c_{\text{tw}}^{-2} p_j^2 \Delta_\alpha\}.$$

As follows from Eq. (18), in the case under consideration, the Stoneley wave consists of two components, the first of which can be interpreted as the Stoneley wave excited by the *qP*-wave propagating in the formation and the second, by the *qSV*-wave. For an isotropic medium, $\alpha_\perp = \alpha_\parallel = \alpha_* = \alpha$, $\beta_\parallel = \beta_* = \beta$, and $\Delta_\alpha \longrightarrow 0$, so that only the first component remains nonzero in Eq. (18) and this component coincides with the expression for the Stoneley wave in an isotropic medium [5].

Consider now the case with roots of different signs and assume that root $p_2^2$ is positive. This case is realized in media in which the velocity of transverse waves $\beta_\parallel$ is smaller than the velocity of tube waves, this situation being possible when the inequality $\beta_\parallel < c_f\sqrt{1 - \rho_f/\rho_s}$ is satisfied. Under these conditions, the argument of the Macdonald function in the second term appears to be purely imaginary, so that a Hankel function of the second kind appears instead of it. In calculating the integral, the problem of choosing the rule of bypassing the poles on the real axis arises. This rule follows from the asymptotic behavior of the solution at $r \longrightarrow \infty$, where only the outgoing wave is present. Correspondingly, we should encircle only the pole lying on the positive half-axis. The first term in Eq. (18) related to the Stoneley wave excitation by the *qP*-wave remains intact. Regarding the second term in Eq. (18), this case corresponds to a qualitatively different solution, because it includes the Hankel function instead of the Macdonald function. This fact noticeably changes both

the shape of the Stoneley wave and its amplitude attenuation with distance. The Macdonald and Hankel functions exhibit essentially different asymptotic behavior for large arguments. The amplitude of the solution described by the function $K_0(x)$ attenuates with the borehole–source distance much faster that the amplitude of the solution described by the function $H_0^{(2)}(x)$. Hence, one can expect that, in the latter case, the wave will have a higher amplitude. In addition, the widths of wave packets described by the first and second terms can be different, because the characteristic width of the wave described by the Macdonald function is determined by the argument, which results in a broadening of the wave with increasing distance $r$ between the source and the borehole axis. Conversely, the wave described by the Hankel function is characterized by the width of about the characteristic wavelength of the wave generated by the source.

Physically, the reason for the difference in the behavior of the Stoneley waves excited by the *qSV*-waves in these two cases follows from the relationship between the propagation velocity of the external disturbance along the borehole and the velocity of the Stoneley wave [12]. In the first case, the propagation velocity of the *qSV*-wave propagating in the formation along the borehole always exceeds the velocity of the Stoneley wave. In the second case, beginning from a certain borehole–source distance, the velocity of the Stoneley wave exceeds the apparent propagation velocity of the external *qSV*-wave propagating in the formation, so that the external action lags behind the Stoneley wave excited by this very action. In this case, the Stoneley wave is a conic wave (Mach wave) [12].

*Complex conjugate roots.* It can be shown that there are some formations whose elastic parameters give rise to complex conjugate roots of the quadratic equation. In this case, we can use considerations similar to those used in the derivation of the expression for the Stoneley wave in the case of two negative roots. In the case of complex conjugate roots, the expression for $P_1^{\text{tw}}$ coincides with the above expression, in which the sign of the roots $p_{1,2} = \pm\sqrt{p_{1,2}^2}$ is chosen according to the rule of path tracing in such a way as to make the imaginary part negative.

## EFFECT OF THE ANISOTROPIC PARAMETERS OF THE FORMATION ON THE AMPLITUDE AND SHAPE OF THE STONELEY WAVE

Let us analyze the effect of the elastic parameters of an anisotropic formation surrounding the borehole on the amplitude and shape of the excited Stoneley wave. An exhaustive analysis and a general interpretation (in multidimensional space of parameters describing the elastic properties of the borehole environment and fluid) seem to be too difficult. In addition, such modeling requires the consideration for all possible restrictions imposed on the parameters of the elastic medium and, in particular, the restrictions imposed by thermodynamic conditions [8, 13]. For this reason, we performed our calculations for actual transversely isotropic media whose parameters are cited in the literature [14, 15]. All calculation assumed that the borehole fluid was water (with density $\rho_f = 1.0$ g/cm$^3$, sound velocity $c_f = 1500$ m/s).

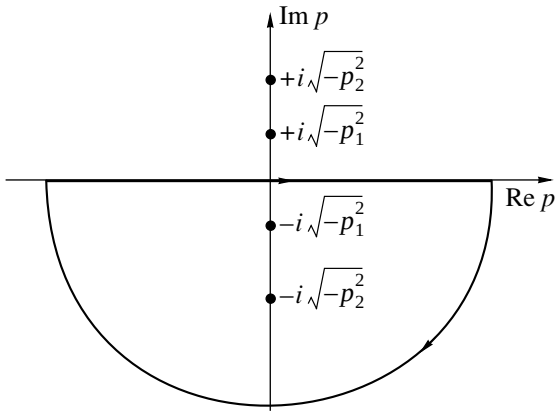


**Fig. 2.** Integration contour bypassing the poles in the case of $p_1^2$, $p_2^2 < 0$.

In the general case, five independent parameters are sufficient to completely describe a transversely isotropic medium. Currently, the parameters most commonly used are referred to as the Thomsen notation, which includes the velocities of longitudinal and transverse waves along the symmetry axis, $V_{P0}$ and $V_{S0}$, and three dimensionless parameters describing the deviation of the medium from an isotropic one, $\varepsilon$, $\delta$, and $\gamma$ [15]. These parameters are related to the parameters used in this paper by the formulas:

$$V_{P0} = \alpha_\perp, \quad V_{S0} = \beta_*, \quad \varepsilon = \frac{1}{2}\left(\frac{\alpha_\parallel^2}{\alpha_\perp^2} - 1\right),$$

$$\delta = \frac{(\alpha_*^2 - \beta_*^2) - (\alpha_\perp^2 - \beta_*^2)^2}{2\alpha_\perp^2(\alpha_\perp^2 - \beta_*^2)}, \quad \gamma = \frac{\beta_\parallel^2 - \beta_*^2}{2\beta_*^2}.$$

The velocity of transverse waves in the vertical direction $V_{S0}$ is often replaced by another parameter, $f$, defined by the formula $f = 1 - V_{S0}^2/V_{P0}^2 = 1 - \beta_*^2/\alpha_\perp^2$. Parameter $\gamma$ characterizes the anisotropy of transverse velocities in the transversely isotropic medium. For *qP*- and *qSV*-waves polarized in the vertical plane that contains the symmetry axis, this parameter does not appear in the defining equations [11]. Nevertheless, the parameters of the Stoneley wave depend on all three anisotropy parameters $\varepsilon$, $\delta$, and $\gamma$, because the effective

Young's moduli and the effective Poisson's ratio $z$ (see Eqs. (5)) of an anisotropic medium depend on $\beta_{\square}$.

Let us analyze the waveforms of the Stoneley wave for actual transversely isotropic media from paper [14]. As was shown earlier, the shape and amplitude of the Stoneley wave depends on the roots $p_{1,2}^2$ in Eq. (18). Among high-velocity media, one can select a group of media for which roots $p_{1,2}^2$ are negative and, hence, the field of the Stoneley wave is described by the sum of two terms with the Macdonald functions of real argument (see Eq. (18)). This group includes media with $(\varepsilon - \delta) > 0$. Other high-velocity media with $(\varepsilon - \delta) < 0$ correspond to the case of complex conjugate roots $p_{1,2}^2$. As is known [13], the case $\varepsilon = \delta$ corresponds to transversely isotropic media with an elliptic anisotropy, when the wave front of the quasi-longitudinal *qP*-wave has the shape of an ellipsoid of revolution. Thus, since the nonellipticity parameter $(\varepsilon - \delta)$ describes the deviation of the anisotropic properties of an elastic medium from the elliptic anisotropy, we can assume that, in high-velocity media, the type of solution (and, consequently, the shape of the Stoneley wave) depends on the sign of this parameter.

The low-velocity media that we have considered were characterized by the roots $p_{1,2}^2$ of different signs. As will be shown below, the value of the parameter $(\varepsilon - \delta)$ of the elastic medium also strongly affects the shape, amplitude, and polarity of the Stoneley wave.

To justify the above statements, additional calculations were carried out for 44 transversely isotropic elastic media whose parameters were taken from [15]. The calculations showed that, for all anisotropic media specified in [15], the type of solution determined in accordance with the roots $p_{1,2}^2$ is reduced to the cases considered above.

In this paper, we present the calculated profiles of the Stoneley waves for elastic media with transverse isotropy specified in [14]. In the waveform calculations, we used the seismic source function $\Psi_S(t)$ in the form of the Berlague potential

$$\dot{\Psi}_S(t) = [(1 + B_0^2)/B_0]2\pi^2 f_0^2 \Psi_\infty t \exp(-\Omega t) \times \sin(2\pi f_0 t)\Theta(t),$$

where $\Psi_\infty$ is the statical value of the volume displaced due to explosion, $f_0$ is the characteristic frequency of the source, $B_0 = \Omega/(2\pi f_0)$, and $\Theta(t)$ is the Heaviside step function. For the source, we used the parameters: $\Psi_\infty = 3 \times 10^{-4}$ m$^3$, $f_0 = 50$ Hz, and $B_0 = 0.5$.

In the calculations, we assumed that the source is positioned at the origin of the cylindrical coordinate system $(r, z, \varphi)$ and that a vertical borehole with a receiver at a depth of $z = 250$ m is located at a horizontal distance $r = 80$–$120$ m from the source.

Figures 3 and 4 show the Stoneley wave profiles calculated for low-velocity and high-velocity formations, respectively. These results are typical of the media under consideration, including the media from [15]. The following inferences can be made from our analysis.

First, the Stoneley wave is characterized by a single-peak profile, similar to that shown in Fig. 3a, for all high-velocity media with a positive nonellipticity parameter $(\varepsilon - \delta) > 0$. Second, for low-velocity media with $(\varepsilon - \delta) < 0$, the Stoneley wave is also characterized by a single-peak profile if the nonellipticity parameter is small. As the absolute value of the nonellipticity parameter increases, the wave slowly transforms to a two-peak profile (Fig. 3b).

Third, in the case of low-velocity formations with a sufficiently great nonellipticity parameter $(\varepsilon - \delta)$, the polarity of the first arrival of the Stoneley wave coincides with the sign of the nonellipticity parameter (Fig. 4).

The dependence of the Stoneley wave profile on the nonellipticity parameter obtained for actual formations was tested by numerical simulation. The inference that the nonellipticity parameter governs the Stoneley wave profile (single-peak or two-peak) remains valid. Note that variation of the magnitude and sign of the nonellipticity parameter results in a continuous transformation of the Stoneley wave profile from one type to another.

To verify the statement that the Stoneley wave retains its shape when the source–borehole distance varies, we performed special calculations, whose results are shown in Fig. 5. The gray color marks the results for which asymptotic approximation is formally inapplicable. The analysis of calculated results shows that, regardless of the fact that interference between partial contributions of *qP*- and *qSV*-waves to the Stoneley wave seemingly increases with increasing horizontal distance, the duration of these contributions decreases, which preserves the shape of the Stoneley wave in the parameter range under consideration.

## CONCLUSIONS

(1) In this paper, we obtained the long-wave solution to the problem of tube wave excitation by an external point source in an infinite fluid-filled borehole embedded in a transversely isotropic formation with the help of the method of integral transformations. Asymptotically, the wave field in the fluid can be separated into the *qP*- and *qSV*-waves, which represent the local response of the borehole fluid to the quasi-longitudinal and quasi-transverse waves in the formation, and the lowest borehole eigenmode, i.e., the Stoneley wave (tube wave).

(2) The Stoneley wave is shown to be determined by the contributions of two poles in the complex plane of horizontal slowness. Depending on the anisotropy parameters of the medium, these poles either lie on the real axis or are complex conjugate. The expression

obtained for the Stoneley wave allows an asymptotic analysis of the Stoneley wave characteristics for a high-velocity medium, in which the apparent velocity of the quasi-transverse *qSV*-wave propagating in the formation along the borehole exceeds the velocity of the Stoneley wave, and for a low-velocity medium as well. It is shown that the solutions for the Stoneley wave are essentially different in these cases.

(3) Our investigation shows that certain correlation exists between the shape and amplitude of the Stoneley wave and the nonellipticity parameter $(\varepsilon - \delta)$ of the borehole environment for both low-velocity and high-velocity formations. In high-velocity formations, the Stoneley wave behaves as a single-peak impulse for $(\varepsilon - \delta) > 0$, while for $(\varepsilon - \delta) < 0$ it exhibits a two-peak shape under the condition that the nonellipticity is considerable. In low-velocity media, the polarity of the first arrival of the Stoneley wave coincides with the sign of the nonellipticity parameter when the latter is sufficiently large. In addition, the Stoneley wave amplitude strongly depends on the parameters $\varepsilon$ and $\delta$.

The results of this investigation offer a possibility of estimating the anisotropy parameters of the borehole environment from the amplitude and shape of the excited Stoneley wave.

## *APPENDIX*

The solution to the problem of radiation of a point source in a transversely isotropic medium was considered in many papers. In the form convenient for our analysis of the dynamic pressure field in the borehole fluid, such a solution for elastic potentials is given, for example, in [11]. In a compact notation, it can be written as follows:

$$\begin{pmatrix}\bar{\phi}(r,z,\omega)\\ \bar{\psi}(r,z,\omega)\end{pmatrix} = \bar{A}(\omega)\begin{pmatrix}-i\omega\\ \mathrm{sgn}(z)\end{pmatrix}\int_0^{+\infty} dp\frac{pJ_0(\omega pr)}{\Phi(p)} \times\left[\begin{pmatrix}a_0(p)\\ b_0(p)\end{pmatrix}\exp(-\omega p|z|) + \sum_{j=1}^{2}\begin{pmatrix}a_j(p)\\ b_j(p)\end{pmatrix}\exp(-i\omega\xi_j(p)|z|)\right], \quad \text{(A1)}$$

where $j = 1, 2$,

$$a_j(p) = \frac{1-\beta_*^2/c_j^2(p)-\sigma_1 p^2(1-p^2c_j^2(p))}{\xi_j(p)(c_2^2(p)-c_1^2(p))},$$

$$b_j(p) = (-1)^{j+1}\frac{\sigma_1 c_j^2(p)p^2+\sigma_2}{c_2^2(p)-c_1^2(p)},$$

$$a_0(p) = ip^3\sigma_1, \quad b_0(p) = p^2\sigma_1,$$

$$\sigma_1 = \alpha_\perp^2+\alpha_\parallel^2-2\alpha_*^2, \quad \sigma_2 = \alpha_*^2-\alpha_\perp^2.$$

Here, $\bar{A}(\omega) = \bar{\Psi}_S(\omega)\alpha_0^2$, where $\bar{\Psi}_S(\omega)$ is the spectrum of the seismic source function $\Psi_S(t)$ (the spectrum of the potential of elastic displacements at the source), $\alpha_0$ is the normalizing constant with the dimension of velocity, and $J_0(x)$ is the zero-order Bessel function. The velocities of the quasi-longitudinal (*qP*) and quasi-transverse (*qSV*) waves, $c_1(p)$ and $c_2(p)$, are the roots of the biquadratic dispersion equation [11]:

$$\Phi(p)c^4(p) - 2\alpha_\perp\beta_* B(p)c^2(p) + \alpha_\perp^2\beta_*^2 = 0 \quad \text{(A2)}$$

whose coefficients are

$$\Phi(p) = 1 + (\alpha_\perp^2-\alpha_\parallel^2)p^2 + [(\alpha_*^2-\alpha_\parallel^2)(\alpha_\perp^2-\beta_*^2) + (\alpha_*^2-\alpha_\perp^2)(\alpha_*^2-\beta_*^2)]p^4,$$

$$B(p) = (\alpha_\perp^2+\beta_*^2-[(\alpha_\perp^2-\alpha_*^2)(\alpha_*^2-2\beta_*^2) + (\alpha_\parallel^2-\alpha_*^2)\alpha_\perp^2]p^2)/(2\alpha_\perp\beta_*).$$

The parameters $\xi_{1,2}(p) = \sqrt{c_{1,2}^{-2}(p)-p^2}$ correspond to the vertical slowness of the *qP*- and *qSV*-waves.

## REFERENCES


1. J. E. White, *Underground Sound, Application of Seismic Waves* (Elsevier, Amsterdam, 1983; Nedra, Moscow, 1986).
2. W. Dong and M. N. Toksöz, Geophysics **60**, 29 (1995).
3. W. Dong and M. N. Toksöz, Geophysics **60**, 748 (1995).
4. A. M. Ionov and G. A. Maximov, Geophys. J. Int. **124**, 888 (1996).
5. A. M. Ionov and G. A. Maksimov, Akust. Zh. **45**, 354 (1999) [Acoust. Phys. **45**, 311 (1999)].
6. T. Alkhalifah, Geophysics **65**, 1316 (2000).
7. M. Jacobsen and T. A. Johansen, Geophysics **65**, 1711 (2000).
8. G. I. Petrashen', *Wave Propagation in Anisotropic Elastic Media* (Nauka, Leningrad, 1984).
9. V. S. Vladimirov, *Equations of Mathematical Physics*, 4th ed. (Nauka, Moscow, 1981; Marcel Dekker, New York, 1971).
10. R. Sheriff and L. Geldart, *Exploration Seismology* (Cambridge Univ. Press, Cambridge, UK, 1982; Mir, Moscow, 1987).
11. P. M. Bokov and A. M. Ionov, Akust. Zh. **47**, 304 (2001) [Acoust. Phys. **47**, 253 (2001)].
12. J. A. Meredith, M. N. Toksöz, and C. H. Cheng, Geophys. Prospect. **41** (3), 287 (1993).
13. I. D. Tsvankin, Geophysics **61** (2), 467 (1996).
14. A. J. Seriff and K. P. Siriam, Geophysics **56**, 1271 (1991).
15. S. Ryan-Grigor, Geophysics **62**, 1359 (1997).


*Translated by A. Vinogradov*

*Acoustical Physics, Vol. 50, No. 2, 2004, pp. 134–139. Translated from Akusticheskiĭ Zhurnal, Vol. 50, No. 2, 2004, pp. 170–176.*


# Rotationally Invariant Theory of Magnetoacoustic Wave Attenuation in Cubic Ferromagnets

**R. M. Vakhitov* and V. R. Khusainova****

** Bashkortostan State University, ul. Frunze 32, Ufa, 450074 Bashkortostan, Russia*
*e-mail: vakhitovrm@bsu.bashedu.ru*
*** Bashkortostan State Pedagogical University, ul. Oktyabr'skoi Revolyutsii 3a, Ufa, 450000 Bashkortostan, Russia*

Received May 14, 2002

**Abstract**—Rotationally invariant theory is used to study the effect of magnetization relaxation on the spectrum of magnetoacoustic waves propagating in a cubic ferromagnet with an induced uniaxial anisotropy along the [011] direction. It is found that the inclusion of rotationally invariant terms leads to certain contributions to the propagation velocity and rate of attenuation of magnetoelastic waves, thus increasing the degree of anisotropy of these characteristics. Among different types of coupled waves, only quasi-sound modes exhibit a relaxation nature in the region of magnetic phase stability loss. The introduction of dissipation and rotational invariance affects the acoustic birefringence, while the latter gives rise to an additional term in the expression for the phase shift. © *2004 MAIK "Nauka/Interperiodica".*

Many magnetoelastic (ME) effects are considerably enhanced as a magnet approaches a spin-reorientation phase transition (SRPT) [1, 2]. In particular, investigations have shown that, when dissipation processes in the magnetic subsystem of a magnet are taken into account, all types of ME waves, including quasi-magnon and quasi-phonon ones, are weakly attenuating. At the same time, in the vicinity of the SRPT, they may turn into purely relaxation waves [3]. To some extent, this may explain the absence of experimental evidence for the phenomenon of complete softening of quasi-sound near the SRPT [4], which was predicted theoretically in [1]. On the other hand, from a number of publications [2, 5], it follows that the presence of rotationally invariant contributions leads to an additional manifestation of ME coupling, and the latter, in turn, gives rise to new magnetoacoustic effects. From this point of view, it is of interest to consider the effect of ME wave attenuation in the framework of the rotationally invariant theory.

Let us consider the propagation of ME waves in a cubic ferromagnet with an induced uniaxial anisotropy when the easy axis of this anisotropy coincides with the [011] direction (a (011) plate). Such a situation is rather common and may occur in (011) epitaxial iron garnet films [6, 7], in $DyFe_2$-type intermetallic compound films [8], etc. In the magnet under consideration, the induced uniaxial anisotropy can be separated into two components: a perpendicular component ($K_u$) and a rhombic one ($K_p$), which complicates the SRPT pattern [9]. In particular, from the orientational phase diagram of a (011) plate, it follows that this plate may contain nine magnetic phases: three symmetric ($\Phi_{[011]}$, $\Phi_{[001]}$, $\Phi_{[01\bar{1}]}$) and six disymmetric [10], five of the latter being angular and the sixth being a general-type phase. In this paper, we consider the magnet states corresponding to symmetric phases.

(i) $\mathbf{M}_0 \parallel \mathbf{H} \parallel [011]$. The stability condition for this phase is determined by the relations [11]

$$\begin{aligned} &2K_1^* - 2(K_u - 2\pi M_s^2) - 2K_p - M_s H \le 0, \\ &K_1^* + \frac{1}{2}K_2 + 2(K_u - 2\pi M_s^2) + M_s H \ge 0, \end{aligned} \tag{1}$$

where

$$K_1^* = K_1 + \frac{B_1^2}{C_2} - \frac{B_2^2}{2C_{44}}. \tag{2}$$

The corresponding thermodynamic potential of the problem with allowance for rotationally invariant terms has the form [2]

$$\begin{aligned} E = {} & A\left(\frac{\partial \mathbf{m}}{\partial x_i}\right)^2 - (\mathbf{MH}) + \frac{1}{8\pi}H_{\text{dip}}^2 + H_1 m_y^2 + H_2 m_x^2 \\ & + 2B_{me1} m_y \varepsilon_{yz} + 2B_{me2} m_x \varepsilon_{xz} - 2H_{me1} m_y \omega_{yz} \\ & - 2H_{me2} m_x \omega_{xz} + H_{e1}\omega_{yz}^2 + H_{e2}\omega_{xz}^2 + H_{e3}\omega_{yx}^2 \\ & + \frac{1}{2}C_{11}\varepsilon_{xx}^2 + \frac{1}{2}C_1\varepsilon_{yy}^2 + \frac{1}{2}C_4\varepsilon_{zz}^2 + 2C_{44}\varepsilon_{yx}^2 + 2C_2\varepsilon_{yz}^2 \\ & + 2C_5\varepsilon_{xz}^2 + C_3\varepsilon_{yy}\varepsilon_{zz} + C_6\varepsilon_{xx}\varepsilon_{yy} + C_7\varepsilon_{xx}\varepsilon_{zz} \\ & - 2C_8\varepsilon_{yx}\omega_{yx} - 2B_{e1}\varepsilon_{yz}\omega_{yz} - 2B_{e2}\varepsilon_{xz}\omega_{xz}, \end{aligned} \tag{3}$$

where $H_1 = -K_1^* + (K_u - 2\pi M_s^2) + K_p + M_s H/2 + B_1^2/C_2$, $H_2 = (2K_1^* + K_2)/4 + (K_u - 2\pi M_s^2) + M_s H/2 + B_2^2/(2C_{44})$; $A$, $B_i$, and $C_{ij}$ are the exchange interaction constant, the ME coupling constant, and the elastic constant, respectively; $K_1$ and $K_2$ are the first and second cubic anisotropy constants; $m_i$ are the components of the unit magnetization vector **m** (**m** = **M**/$M_s$, where $M_s$ is the saturation magnetization); **H** is the external magnetic field; and $\mathbf{H}_{\text{dip}}$ is the demagnetizing field, which is determined from the magnetostatic equations

$$\operatorname{div}(\mathbf{H}_{\text{dip}} + 4\pi\mathbf{M}) = 0, \quad \operatorname{curl}\mathbf{H}_{\text{dip}} = 0. \tag{4}$$

Here,

$$\left.\begin{matrix}\varepsilon_{ij}\\ \omega_{ij}\end{matrix}\right\} = \frac{1}{2}\left[\frac{\partial u_i}{\partial x_j} \pm \frac{\partial u_j}{\partial x_i}\right] \tag{5}$$

are the strain tensor and the local rotation tensor. For a homogeneous state of the magnet, the strain tensor components take the form

$$\varepsilon_{xx}^0 = \frac{B_1 C_{12}^0}{D}, \quad \varepsilon_{yy}^0 = \frac{B_2}{4C_{44}^0} - \frac{B_1 C_{11}^0}{2D}, \quad \varepsilon_{zz}^0 = -\frac{B_2}{4C_{44}^0} - \frac{B_1 C_{11}^0}{2D}, \tag{6}$$

where

$$D = C_2^0(C_{11}^0 + 2C_{12}^0), \quad C_2^0 = (C_{11}^0 - C_{12}^0),$$

$$B_{me1} = B_1[1 + (\varepsilon_{yy}^0 + \varepsilon_{zz}^0)/2],$$

$$B_{me2} = B_2[1 + (\varepsilon_{xx}^0 + \varepsilon_{zz}^0)/2],$$

$$H_{me1} = H_1 - B_1(\varepsilon_{yy}^0 - \varepsilon_{zz}^0)/2,$$

$$H_{me2} = H_2 - B_2(\varepsilon_{xx}^0 - \varepsilon_{zz}^0)/2,$$

$$H_{e1} = H_1 - B_1(\varepsilon_{yy}^0 - \varepsilon_{zz}^0) + C_2^0(\varepsilon_{yy}^0 - \varepsilon_{zz}^0)^2/2,$$

$$H_{e2} = H_2 - B_2(\varepsilon_{xx}^0 - \varepsilon_{zz}^0) + C_{44}^0(\varepsilon_{xx}^0 - \varepsilon_{zz}^0)^2/2,$$

$$H_{e3} = C_{44}^0(\varepsilon_{xx}^0 - \varepsilon_{yy}^0)/2,$$

$$C_{11} = C_{11}^0(1 + \varepsilon_{xx}^0)^2, \quad C_1 = 2C_1^0(1 + \varepsilon_{yy}^0)^2,$$

$$C_1^0 = (C_{11}^0 + C_{12}^0 + 2C_{44}^0)/4, \quad C_4 = 2C_1^0(1 + \varepsilon_{zz}^0)^2,$$

$$C_{44} = C_{44}^0[1 + (\varepsilon_{xx}^0 + \varepsilon_{yy}^0)/2]^2,$$

$$C_2 = C_2^0[1 + (\varepsilon_{yy}^0 + \varepsilon_{zz}^0)/2]^2/2,$$

$$C_5 = C_{44}^0[1 + (\varepsilon_{xx}^0 + \varepsilon_{zz}^0)/2]^2,$$

$$C_3 = C_3^0(1 + \varepsilon_{yy}^0)(1 + \varepsilon_{zz}^0),$$

$$C_3^0 = (C_{11}^0 + C_{12}^0 - 2C_{44}^0)/2,$$

$$C_6 = C_{12}^0(1 + \varepsilon_{xx}^0)(1 + \varepsilon_{yy}^0),$$

$$C_7 = C_{12}^0(1 + \varepsilon_{xx}^0)(1 + \varepsilon_{zz}^0),$$

$$C_8 = C_{44}^0(\varepsilon_{xx}^0 - \varepsilon_{yy}^0)[1 + (\varepsilon_{xx}^0 + \varepsilon_{yy}^0)/2],$$

$$B_{e1} = [B_1 - C_2^0(\varepsilon_{yy}^0 - \varepsilon_{zz}^0)][1 + (\varepsilon_{yy}^0 + \varepsilon_{zz}^0)/2],$$

$$B_{e2} = [B_2 - C_{44}^0(\varepsilon_{xx}^0 - \varepsilon_{zz}^0)][1 + (\varepsilon_{xx}^0 + \varepsilon_{zz}^0)/2],$$

and $C_{ij}^0$ are the equilibrium values of the elastic constants [2].

From the analysis of dispersion relations describing coupled oscillations of the elastic and spin subsystems [1], it follows that, in the long-wave approximation when the wave vector is **k** ∥ [011], we have

$$\begin{aligned}
\omega_1 &= \omega_{11}, \quad \omega_2 = \{[\omega_s^2 - r^2(\omega_{s1} - \omega_{s2})^2/4]^{1/2} \\
&\quad + ir(\omega_{s1} + \omega_{s2})/2\}/(1 + r^2), \\
\omega_3 &= \omega_{t1}\sqrt{1 - \xi_1} + ir\omega_{t1}^2\{\omega_{s1}\xi_1(1 - \xi_1)(s_{t1}^2 - s_{t2}^2) \\
&\quad + \omega_{s2}(\xi_1 - \xi_2)[s_{t1}^2(1 - \xi_1) - s_{t2}^2]\}/\{2\omega_s^2 \\
&\quad \times [s_{t1}^2(1 - \xi_1)\ s_{t2}^2(1 - \xi_2)]\}, \quad \text{and} \\
\omega_4 &= \omega_{t2}\sqrt{1 - \xi_2} + ir\omega_{t2}^2\{\omega_{s2}\xi_2(1 - \xi_2)(s_{t2}^2 - s_{t1}^2) \\
&\quad + \omega_{s1}(\xi_2 - \xi_1)[s_{t2}^2(1 - \xi_2) - s_{t1}^2]\}/\{2\omega_s^2 \\
&\quad \times [s_{t2}^2(1 - \xi_2)\ s_{t1}^2(1 - \xi_1)]\},
\end{aligned} \tag{7}$$

where $\omega_{l1} = s_{l1}k$, $s_{l1} = \sqrt{C_4/\rho}$, $\omega_s = \sqrt{\omega_{s1}\omega_{s2}}$, $\omega_{s1} = 2\gamma H_1/M_s + \omega_k$, $\omega_{s2} = 2\gamma H_2/M_s + \omega_k$, $\omega_k = 2\gamma A k^2/M_s$, $\omega_{t1}^2 = \omega_{t1}'^2 + \omega_{t1}''^2$, $\omega_{t1}'^2 = [H_{e1} - 2B_{e1}]k^2/(2\rho)$, $\omega_{t1}''^2 = C_2 k^2/\rho$, $\omega_{t2}^2 = \omega_{t2}'^2 + \omega_{t2}''^2$, $\omega_{t2}'^2 = [H_{e2} - 2B_{e2}]k^2/(2\rho)$, $\omega_{t2}''^2 = C_5 k^2/\rho$, $\xi_1 = \gamma[H_{me1} - B_{me1}]^2/(\rho M_s s_{t1}^2 \omega_{s1})$, $\xi_2 = \gamma[H_{me2} - B_{me2}]^2/(\rho M_s s_{t2}^2 \omega_{s2})$, $s_{t1} = \omega_{t1}/k$, $s_{t2} = \omega_{t2}/k$, $\gamma$ is the gyromagnetic ratio, $r$ is the dimensionless damping parameter of the magnetic subsystem, and $\rho$ is the density of the crystal.

It should be noted that each solution corresponds to two types of waves, which have identical frequencies but propagate in opposite directions. As seen from the relations derived above, longitudinal elastic vibrations do not interact with spin waves, and only transverse vibrations prove to be coupled. The velocities of these waves are renormalized as a result of taking into

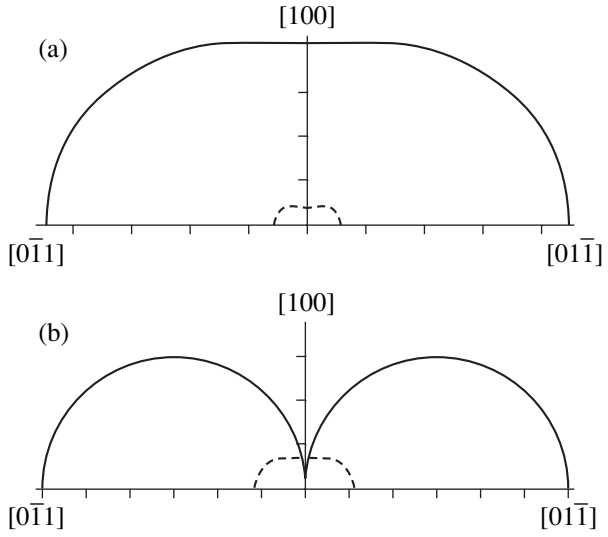


**Fig. 1.** Cross section of the velocity surface of quasi-elastic waves in $Sm_3Fe_5O_{12}$ [19] (a) away from the SRPT and (b) at the SRPT point coinciding with the compensation point; the solid line corresponds to the real part, and the dashed line, to the imaginary part.

account the rotational invariance in energy, in accordance with [2]; here the frequencies $\omega_{l1}$, $\omega''_{t1}$, and $\omega''_{t2}$ characterize longitudinal and transverse sound and are independent of how close the system is to the point of stability loss. The first solution ($\omega_1$) corresponds to a longitudinal wave, the second ($\omega_2$) describes quasi-magnon oscillations, and the third and fourth ($\omega_{3,4}$) describe quasi-phonon oscillations, where the imaginary part is associated with the relaxation component of frequency.

At the point of SRPT ($\xi_{1,2} \longrightarrow 1$), $\omega_2$ corresponds to damped oscillations of the magnetization vector and the two other modes are quasi-elastic waves of a purely relaxation nature and are described by the expressions

$$\omega_3 = ir(\omega'^2_{t1} + \omega''^2_{t1})\frac{1}{2\omega_{s1}}, \quad \omega_4 = ir(\omega'^2_{t2} + \omega''^2_{t2})\frac{1}{2\omega_{s2}}. \quad (8)$$

In the following calculations, we neglect the corrections to elastic and ME constants of the order of $B/C \approx 10^{-5}$–$10^{-6}$ that appear because of the magnetostrictive strain. This allows us to deal with the terms caused by rotational invariance only. Then, the frequencies $\omega_{l1}$, $\omega''_{t1}$, and $\omega''_{t2}$ will correspond to purely elastic vibrations [12] and the frequencies $\omega'_{t1}$ and $\omega'_{t2}$ will represent the contribution of the rotationally invariant theory. The latter two frequencies decrease as the system approaches the SRPT point. Thus, the inclusion of rotational invariance in the consideration leads to the appearance of additional terms in the relaxation component of frequency ($\mathrm{Im}\,\omega_{3,4}$) of quasi-elastic modes, and these terms lead to an increase in the rate of attenuation of ME waves. In addition, the rotational invariance makes a contribution to the ME coupling constant; however, at the SRPT point, this contribution becomes negligibly small ($\xi_{1,2} \longrightarrow 1$).

The spectrum of ME waves propagating in the (011) plane has the form

$$\begin{aligned}\omega_{1,2}\{[\omega_{\mathrm{I}}^2 + \omega_{\mathrm{II}}^2 \\ \pm\sqrt{(\omega_{\mathrm{I}}^2 - \omega_{\mathrm{II}}^2)^2 + 4C_{11}C_{44}k^4\sin^2 2\alpha/\rho^2}]/2\}^{1/2}, \\ \omega_4 = \sqrt{\omega_{t\mathrm{I}}^2(1-\tilde{\xi}_1)\sin^2\alpha + \omega_{t\mathrm{II}}^2(1-\tilde{\xi}_2)\cos^2\alpha} \\ + ir(\omega_{t\mathrm{I}}^2\tilde{\xi}_2\tilde{\omega}_{s2}\sin^2\alpha + \omega_{t\mathrm{II}}^2\tilde{\xi}_1\tilde{\omega}_{s1}\cos^2\alpha)/(2\tilde{\omega}_s^2),\end{aligned} \quad (9)$$

where $\omega_{\mathrm{I}}^2 = (C_{11}\cos^2\alpha + [H_{e3} + 2C_8 + 2C_{44}]\sin^2\alpha/2)k^2/\rho$, $\omega_{\mathrm{II}}^2 = ([H_{e3} - 2C_8 + 2C_{44}]\cos^2\alpha/2 + C_1^0\sin^2\alpha)k^2/\rho$, $\omega_{t\mathrm{I}}^2 = \omega'^2_{t\mathrm{I}} + \omega''^2_{t1}$, $\omega'^2_{t\mathrm{I}} = [H_{e1} + 2B_{e1}]k^2/(2\rho)$, $\omega_{t\mathrm{II}}^2 = \omega'^2_{t\mathrm{II}} + \omega''^2_{t2}$, $\omega'^2_{t\mathrm{II}} = [H_{e2} + 2B_{e2}]k^2/(2\rho)$, $\tilde{\omega}_s = \sqrt{\tilde{\omega}_{s1}\tilde{\omega}_{s2}}$, $\tilde{\omega}_{s1} = \omega_{s1} + 4\pi\gamma M_s\sin\alpha$, $\tilde{\omega}_{s2} = \omega_{s2} + 4\pi\gamma M_s\cos\alpha$, $\tilde{\xi}_1 = \gamma[H_{me1} + B_{me1}]^2/(\rho M_s s_{t\mathrm{I}}^2\tilde{\omega}_{s1})$, $\tilde{\xi}_2 = \gamma[H_{me2} + B_{me2}]^2/(\rho M_s s_{t\mathrm{II}}^2\tilde{\omega}_{s2})$, $s_{t\mathrm{I}} = \omega_{t\mathrm{I}}/k$, $s_{t\mathrm{II}} = \omega_{t\mathrm{II}}/k$, and $\alpha$ is the angle between vector **k** and the [100] axis.

Here and below, the frequencies $\omega_{1,2}$ correspond in character to ME waves of a mixed type representing a hybrid of longitudinal and transverse vibrations. Only when the propagation occurs along a certain crystallographic axis do these waves fall into purely longitudinal and purely transverse waves, which are independent of the spin subsystem. The frequency $\omega_3$ corresponds to the quasi-magnon mode for the case of $\mathbf{M}_0 \parallel \mathbf{H} \parallel \mathbf{k} \parallel [011]$ with the substitution $\omega_s \longrightarrow \tilde{\omega}_s$, $\omega_{s1,2} \longrightarrow \tilde{\omega}_{s1,2}$, and $\xi_{1,2} \longrightarrow \tilde{\xi}_{1,2}$. The solution $\omega_4$ is a soft quasi-elastic mode by which the given SRPT occurs.

Figure 1 shows the dependence of the velocity of ME waves on the direction of their propagation. One can see that the velocity of quasi-phonons is anisotropic due to the difference in the contributions of the elastic and ME interactions in different crystallographic directions. The mode softening for the real and imaginary parts (here, the imaginary part of velocity is interpreted as the rate of attenuation of quasi-phonons) is maximal in the direction of the [100] axis (Fig. 1a). As the line of stability loss of the phase next to the angular phase $\Phi_<^{\mathrm{I}}$ [9] is approached, the degree of anisotropy increases and, in the vicinity of the SRPT, the maximal softening of quasi-sound occurs in the [100] direction. (In this case, a complete softening of quasi-sound, i.e., $\mathrm{Re}\,\omega_{5,6} = 0$, as well as the greatest increase in attenua-

tion (Fig. 1b) [13], will only be observed in magnets whose SRPT point coincides with the compensation point [15].) If a magnet is in other conditions, i.e., in the vicinity of an SRPT between some other phases (in particular, $\Phi_{[011]}$ and $\Phi_{<}^{III}$), the softening of sound in the [100] direction will be minimal while the symmetry of the anisotropy of attenuation will remain invariable. In this connection, it should be noted that the plots in Fig. 1 were obtained for $Sm_3Fe_5O_{12}$ under the aforementioned specific conditions (the coincidence of the compensation point with the SRPT line), which can be satisfied in this material if we additionally assume that the uniaxial anisotropy is induced by external elastic stresses [16]. For plates of this type with an induced uniaxial anisotropy falling into two components, the anisotropy of attenuation in the film plane was revealed experimentally by the angular dependence of the parallel external magnetic field [7]. The broadening of the ferromagnetic resonance line was determined by the dependence of the attenuation parameter on the effective magnetic anisotropy field. Here, it is necessary to mention the study of Mn–Zn spinel crystals with (011) orientation [17]: it revealed a strong anisotropy of the propagation velocity and attenuation of sound because of the elastic and ME interactions. The difference (~40%) in the velocities of quasi-transverse waves of different polarization is explained by the strong elastic anisotropy of the crystal. In other experiments [18, 19] with the same materials, it was found that the maximal attenuation of ultrasound is observed in the region of the SRPT. In these experiments, the attenuation of longitudinal and transverse acoustic waves with frequencies of 5–30 MHz was studied. In [18], temperature dependences of the attenuation coefficient were obtained and maximal sound attenuation was found to occur along the [100] and [011] crystallographic directions. In [19], crystals of the same composition, but grown by two different methods, were used to reveal a sharp increase in the attenuation of longitudinal ultrasonic waves in the [100] and [111] directions.

In the case under consideration, the inclusion of rotationally invariant terms in the thermodynamic potential also leads to an anisotropy of ME wave propagation in the magnet (Fig. 2). According to the calculations, the maximal manifestation of this effect occurs in the direction of the [100] axis and the minimal, in the direction of the $[01\bar{1}]$ axis. At the same time, from Fig. 2, one can see that, for yttrium iron garnet–type magnets, the contribution of the rotational invariance is small; it may be considerable only in materials with a giant magnetostriction [20, 21].

In this situation, the following effect should also take place: the effect related to the change of polarization of a transverse ME wave from linear to elliptic when the wave is transmitted through a sample placed in a magnetic field **H** oriented normally to the propagation direction and at an angle $\varphi = \pi n/2$ ($n \in Z$) to the

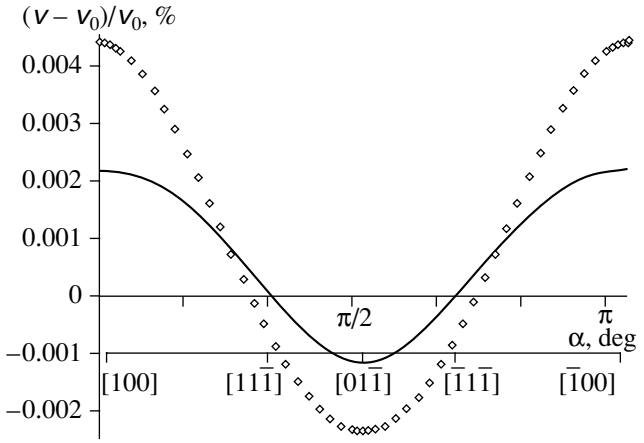


**Fig. 2.** Contribution of the rotational invariance to the propagation velocity and rate of attenuation of quasi-elastic waves in $Sm_3Fe_5O_{12}$ [19]; $v_0$ is the velocity of quasi-sound without considering rotationally invariant terms, and $v$, with allowance for rotational invariance; the solid and dotted lines represent the real and imaginary parts, respectively.

wave polarization plane; i.e., the effect of acoustic birefringence [22]. In this case, a transverse elastic wave can be represented as a sum of two components with displacements along each of the two directions (perpendicular and parallel to the field **H**). The wave polarized along the [011] direction does not interact with the spin mode, while the wave polarized along $[01\bar{1}]$ is coupled with the spin mode. This leads to a phase shift whose value per unit length is determined by the formula

$$\psi = \psi_1 + \psi_2, \tag{10}$$

where $\psi_1 = \omega(s_{t2}^{-1} - s_{t1}^{-1})$ and $\psi_2 = \dfrac{\omega\xi_2}{2s_{t2}}\dfrac{\omega_s^2}{\omega_s^2 - (1+r^2)\omega^2}$.

Without considering the rotational invariance, we have $\psi_1 = 0$ and the expression for $\psi$ coincides with that given in [12]. If we assume that the attenuation is small, i.e., $r \ll 1$, the expression for $\psi$ will coincide with the results obtained in [23].

(ii) $\mathbf{M}_0 \parallel \mathbf{H} \parallel [100]$. The stability condition for this phase has the form [11]

$$\begin{gathered} K_1^* - 2(K_u - 2\pi M_s^2) + M_s H \geq 0, \\ 2K_1^* + 2K_p + M_s H \geq 0. \end{gathered} \tag{11}$$

The corresponding thermodynamic potential is expressed as

$$E = A\left(\frac{\partial \mathbf{m}}{\partial x_i}\right)^2 - (\mathbf{MH}) + \frac{1}{8\pi}H_{\text{dip}}^2 + H_1' m_z^2 + H_2' m_y^2 + 2B_{me2}(m_y\varepsilon_{xy} + m_z\varepsilon_{zx}) - 2H_{me1}' m_z\omega_{zx}$$

$$-2H'_{me2}m_y\omega_{yx} + H'_{e1}\omega_{zx}^2 + H'_{e2}\omega_{yx}^2 + \frac{1}{2}C_{11}\varepsilon_{xx}^2 \quad (12)$$

$$+\frac{1}{2}C_1(\varepsilon_{yy}^2 + \varepsilon_{zz}^2) + 2C_5(\varepsilon_{xy}^2 + \varepsilon_{xz}^2) + 2C_2\varepsilon_{yz}^2$$

$$+ C_3\varepsilon_{yy}\varepsilon_{zz} + C_7\varepsilon_{xx}(\varepsilon_{yy} + \varepsilon_{zz}) - 2B'_{e2}(\varepsilon_{xy}\omega_{yx} + \varepsilon_{xz}\omega_{zx}),$$

where $H'_1 = 2\pi M_s^2 - K_u + M_sH/2 + K_1^* + B_2^2/(2C_{44})$, $H'_2 = K_p + M_sH/2 + K_1^* + B_2^2/(2C_{44})$, $H'_{me1} = H'_1 - B_2(\varepsilon_{yy}^0 - \varepsilon_{xx}^0)/2$, $H'_{me2} = H'_2 - B_2(\varepsilon_{yy}^0 - \varepsilon_{xx}^0)/2$, $H'_{e1} = H'_1 - B_2(\varepsilon_{yy}^0 - \varepsilon_{xx}^0) + C_{44}^0(\varepsilon_{yy}^0 - \varepsilon_{xx}^0)^2/2$, $H'_{e2} = H'_2 - B_2(\varepsilon_{yy}^0 - \varepsilon_{xx}^0) + C_{44}^0(\varepsilon_{yy}^0 - \varepsilon_{xx}^0)^2/2$, $B'_{e2} = [B_2 - C_{44}^0(\varepsilon_{yy}^0 - \varepsilon_{xx}^0)][1 + (\varepsilon_{yy}^0 + \varepsilon_{xx}^0)/2]$.

For this case, in the ground state of the magnet, the components of the strain tensor have the form

$$\varepsilon_{xx}^0 = -\frac{B_1(C_{11}^0 + C_{12}^0)}{D}, \quad \varepsilon_{yy}^0 = \varepsilon_{zz}^0 = \frac{B_1C_{12}^0}{D}. \quad (13)$$

A study of the dispersion relation for the direction of $\mathbf{k} \parallel [100]$ shows that this situation is similar to the case of $\mathbf{M}_0 \parallel \mathbf{H} \parallel [011]$ ($\mathbf{k} \parallel [011]$); i.e., $\omega_1 = \omega_{l2}$ and $\omega_2$, $\omega_3$, and $\omega_4$ correspond to the solutions for the case of $\mathbf{M}_0 \parallel \mathbf{H} \parallel \mathbf{k} \parallel [011]$ with the substitution $\omega_s \longrightarrow \omega'_s$, $\omega_{s1,2} \longrightarrow \omega'_{s1,2}$, $\xi_{s1,2} \longrightarrow \xi'_{s1,2}$, $\omega_{t1} \longrightarrow \omega_{t3}$, $\omega_{t2} \longrightarrow \omega_{t4}$, where $\omega_{l2} = \sqrt{C_{11}/\rho}k$, $\omega_{t3}^2 = \omega_{t3}'^2 + \omega_{t2}''^2$, $\omega_{t3}'^2 = [H'_{e1} - 2B'_{e2}]k^2/(2\rho)$, $\omega_{t4}^2 = \omega_{t4}'^2 + \omega_{t2}''^2$, $\omega_{t4}'^2 = [H'_{e2} - 2B'_{e2}]k^2/(2\rho)$, $\xi'_1 = \gamma[H'_{me1} - B_{me2}]^2/(\rho M_s s_{t3}^2\,\omega'_{s1})$, $\xi'_2 = \gamma[H'_{me2} - B_{me2}]^2/(\rho M_s s_{t4}^2\,\omega'_{s2})$, $s_{t3} = \omega_{t3}/k$, and $s_{t4} = \omega_{t4}/k$.

From the relations obtained above, it follows that the longitudinal mode is independent while the two transverse modes are coupled. At the SRPT point, quasi-elastic waves turn into purely relaxation waves.

When ME waves propagate in the (100) plane, the spectrum is described by the following expressions:

$$\omega_{1,2} = \{[\omega_{\mathrm{III}}^2 + \omega_{\mathrm{IV}}^2 \pm \sqrt{(\omega_{\mathrm{III}}^2 - \omega_{\mathrm{IV}}^2)^2 + (C_1 + C_3)^2k^4\sin^2 2\alpha'/\rho}]/2\}^{1/2}, \quad (14)$$

and $\omega_3$ and $\omega_4$ correspond to the solutions for the case of $\mathbf{k} \perp [011]$, $\mathbf{M}_0 \parallel \mathbf{H} \parallel [011]$ with the substitution $\tilde{\omega}_s \longrightarrow \tilde{\omega}'_s$, $\tilde{\omega}_{s1,2} \longrightarrow \tilde{\omega}'_{s1,2}$, $\tilde{\xi}_{s1,2} \longrightarrow \tilde{\xi}'_{s1,2}$, $\omega_{t\mathrm{I}} \longrightarrow \omega_{t\mathrm{III}}$, and $\omega_{t\mathrm{II}} \longrightarrow \omega_{t\mathrm{IV}}$, where $\omega_{\mathrm{III}}^2 = [C_2\cos^2\alpha' + C_1\sin^2\alpha']k^2/\rho$, $\omega_{\mathrm{IV}}^2 = [C_1\cos^2\alpha' + C_2\sin^2\alpha']k^2/\rho$, $\omega_{t\mathrm{III}}^2 = \omega_{t\mathrm{III}}'^2 + \omega_{t2}''^2$, $\omega_{t\mathrm{III}}'^2 = [H'_{e1} + 2B'_{e2}]k^2/(2\rho)$, $\omega_{t\mathrm{IV}}^2 = \omega_{t\mathrm{IV}}'^2 + \omega_{t2}''^2$, $\omega_{t\mathrm{IV}}'^2 = [H'_{e2} + 2B'_{e2}]k^2/(2\rho)$, $\tilde{\omega}'_s = \sqrt{\tilde{\omega}'_{s1}\tilde{\omega}'_{s2}}$, $\tilde{\omega}'_{s1} = \omega'_{s1} + 4\pi\gamma M_s\cos\alpha'$, $\tilde{\omega}'_{s2} = \omega'_{s2} + 4\pi\gamma M_s\sin\alpha'$, $\tilde{\xi}'_1 = \gamma[H'_{me1} + B'_{me2}]^2/(\rho M_s s_{t\mathrm{III}}^2\tilde{\omega}'_{s1})$, $\tilde{\xi}'_2 = \gamma[H'_{me2} + B'_{me2}]^2/(\rho M_s s_{t\mathrm{IV}}^2\tilde{\omega}'_{s2})$, $s_{t\mathrm{III}} = \omega_{t\mathrm{III}}/k$, $s_{t\mathrm{IV}} = \omega_{t\mathrm{IV}}/k$, and $\alpha'$ is the angle between the vector $\mathbf{k}$ and the $[01\bar{1}]$ axis.

In this case, we also have a hybridization of longitudinal and transverse vibrations not coupled with the spin subsystem while the SRPT occurs by the other coupled quasi-elastic branch. At the point of the phase stability loss, a complete softening of quasi-sound and the maximal increase in attenuation (under the specific conditions considered in the previous case) will occur in the $[01\bar{1}]$ direction, but the birefringence will be absent.

For the magnet under consideration in the $\Phi_{[01\bar{1}]}$ phase, the spectrum of ME waves is similar to that in the case of $\mathbf{M}_0 \parallel [011]$. This is explained by the fact that phases $\Phi_{[01\bar{1}]}$ and $\Phi_{[011]}$ are identical, because they correspond to the directions of $\mathbf{M}_0$ that coincide with the axes of the induced uniaxial anisotropy. The latter axes (i.e., [011] and $[01\bar{1}]$) are interchangeable from the point of view of magnetic symmetry of the crystal [9].

Thus, taking into account the rotational invariance because of the magnetic crystallographic anisotropy, we obtain an additional term in the acoustic birefringence and a renormalization of the velocities of transverse and longitudinal sound and the ME coupling constant, which is in good agreement with the results reported in [2, 5]. In addition, calculations show that the rotationally invariant terms in the expression for energy make a contribution to the relaxation component of quasi-elastic waves. A specific feature of the situation under study is that, when attenuation is taken into account, quasi-elastic waves are weakly attenuating away from the SRPT, while near the SRPT they become relaxation waves, this effect being possible only when $\mathbf{k} \parallel \mathbf{M}_0$, which is in good agreement with [3]. However, unlike the cited publication [3] where the appearance of relaxation quasi-magnon waves at the SRPT point was predicted, no such modes were revealed in the (011) plate. An anisotropy of the propagation velocity and rate of attenuation of sound was revealed, which qualitatively agrees with the experiment.

## ACKNOWLEDGMENT

This work was supported in part by the Federal Target Program “Integratsiya” (project no. BOO65).

## REFERENCES


1. E. A. Turov and V. G. Shavrov, Usp. Fiz. Nauk **140**, 429 (1983) [Sov. Phys. Usp. **26**, 593 (1983)].
2. V. G. Bar'yakhtar and E. A. Turov, in *Electronic Structure and Electronic Properties of Metals and Alloys*, Ed. by V. G. Bar'yakhtar (Naukova Dumka, Kiev, 1988), p. 39.
3. V. D. Buchel'nikov and V. G. Shavrov, Pis'ma Zh. Éksp. Teor. Fiz. **60**, 534 (1994) [JETP Lett. **60**, 548 (1994)].
4. I. M. Vitebskiĭ, N. K. Dan'shin, A. I. Izotov, *et al.*, Zh. Éksp. Teor. Fiz. **98**, 334 (1990) [Sov. Phys. JETP **71**, 187 (1990)].
5. E. A. Turov and I. A. Kaĭbichev, Fiz. Tverd. Tela (Leningrad) **31** (9), 138 (1989) [Sov. Phys. Solid State **31**, 1554 (1989)].
6. A. M. Zyuzin and V. V. Radaĭkin, Zh. Tekh. Fiz. **67** (8), 131 (1997) [Tech. Phys. **42**, 974 (1997)].
7. V. V. Randoshkin, V. M. Kozlov, V. Yu. Mochar, *et al.*, Fiz. Tverd. Tela (St. Petersburg) **41**, 1254 (1999) [Phys. Solid State **41**, 1144 (1999)].
8. V. Oderno, C. Dufour, K. Dumesnil, *et al.*, Phys. Rev. B **54**, R17375 (1996).
9. R. M. Vakhitov, Fiz. Met. Metalloved. **89** (6), 16 (2000).
10. Yu. A. Izyumov and V. N. Syromyatnikov, *Phase Transitions and the Crystal Symmetry* (Nauka, Moscow, 1984).
11. R. M. Vakhitov, V. V. Grinevich, and M. M. Vakhitova, Zh. Tekh. Fiz. **72** (5), 42 (2002) [Tech. Phys. **47**, 555 (2002)].
12. R. M. Vakhitov and V. R. Khusainova, in *Structural and Dynamic Effects in Ordered Media* (Bashk. Gos. Univ., Ufa, 2001), p. 57.
13. V. D. Buchel'nikov and V. G. Shavrov, Fiz. Met. Metalloved. **68** (3), 421 (1989).
14. *Physical Quantities: A Handbook*, Ed. by I. S. Grigor'ev and E. Z. Meĭlikhov (Énergoatomizdat, Moscow, 1991).
15. A. I. Belyaeva, V. P. Yur'ev, and V. A. Potakova, Zh. Éksp. Teor. Fiz. **83**, 1104 (1982) [Sov. Phys. JETP **56**, 626 (1982)].
16. V. D. Buchel'nikov and V. G. Shavrov, Fiz. Tverd. Tela (Leningrad) **23**, 1296 (1981) [Sov. Phys. Solid State **23**, 760 (1981)].
17. S. G. Abarenkova, S. Sh. Gendelev, L. K. Zarembo, *et al.*, Fiz. Tverd. Tela (Leningrad) **27**, 2450 (1985) [Sov. Phys. Solid State **27**, 1467 (1985)].
18. M. V. Bazhenov and L. N. Kotov, Akust. Zh. **43**, 744 (1997) [Acoust. Phys. **43**, 646 (1997)].
19. L. N. Kotov and S. N. Karpachev, Pis'ma Zh. Tekh. Fiz. **28** (3), 49 (2002) [Tech. Phys. Lett. **28**, 105 (2002)].
20. A. E. Clark, H. T. Savage, and O. D. McMasters, in *Proceedings of International Conference on Magnetism'76* (Amsterdam, 1976), p. 131.
21. Z. J. Guo, S. C. Busbridge, Z. D. Zhang, *et al.*, J. Magn. Magn. Mater. **239**, 554 (2002).
22. V. V. Lemanov, in *Physics of Magnetic Dielectrics*, Ed. by G. A. Smolenskiĭ (Nauka, Leningrad, 1974).
23. V. V. Grinevich and R. M. Vakhitov, in *XV All-Russian School–Seminar on New Magnetic Materials of Microelectronics: Abstracts of Papers* (Moscow, 1996), p. 251.


*Translated by E. Golyamina*

*Acoustical Physics, Vol. 50, No. 2, 2004, pp. 140–145. Translated from Akusticheskiĭ Zhurnal, Vol. 50, No. 2, 2004, pp. 177–183.*


# Focusing and Dispersion of a Plane Wave by Transversally Isotropic Elastic Lenses

**V. I. Gulyaev* and G. M. Ivanchenko****

** National Transport University, ul. Suvorova 1, Kiev, 01010 Ukraine*
*e-mail: gulyayev@mail.kar.net*
*** Kiev National University of Construction and Architecture,*
*Vozdukhoflotskii pr. 31, Kiev, 01037 Ukraine*
*e-mail: ivlena@ukr.net*

Received January 5, 2003

**Abstract**—Transformation of a plane longitudinal wave front at the surfaces of a transversely isotropic elastic lens is considered. Nonlinear Snell equations are solved using an approach that combines Newton's method and the algorithm of solution continuation with respect to a parameter. The cases of focusing and divergence of rays passing through a convex lens are investigated. Numerical examples are given for different relationships between the parameters of the elastic medium. *© 2004 MAIK "Nauka/Interperiodica".*

The investigation of singularities and rearrangements of caustics and phase fronts in geometrical optics is an example of using the theory of differentiable mappings in physics [1–4]. The singularities become clearly apparent even in a simplest optical system that consists of homogeneous media separated by a curvilinear boundary. The description of such a system requires only two consequences of Fermat's principle of least time, namely: (i) for light incident on a reflecting surface, the angle of incidence is equal to the angle of reflection, and (ii) for light transmitted through an interface, the angles of incidence and refraction obey the refraction law. Since light rays are focused at the ray envelope (caustic), the light field intensity along the caustics becomes infinitely large (within the framework of the geometrical optics) and singularities appear on the phase front. In the course of the motion of the front, these singularities glide along the caustics and, at certain instants related to the appearance of singularities on caustics as well, become rearranged.

The types of caustics and phase front singularities were studied and classified by Arnol'd [1–3]. Kravtsov and Orlov [5] used these results to analyze physical phenomena in optics, acoustics, and radio-wave physics.

The approaches developed in these studies appear to be efficient for investigating the propagation of discontinuous strain waves in elastic media. In this case, the problems of primary interest are related to the geometrical construction of moving surfaces of discontinuity for the first derivatives of field functions (these surfaces are often called shock waves) and to the calculation of the magnitude of these discontinuities, which provide the most important information about the wave front and the intensity of the main portion of the momentum carried by the wave at every point of the wave front. For formulating and solving such problems in the theory of elasticity, the methods of geometrical optics are quite important; in particular, the zero-order approximation of the ray method proves to be sufficient for an adequate quantitative description of many wave phenomena of different physical natures [5, 6].

The ray method selects the function of the optical path of a wave, which is also called eikonal, and uses the eikonal equation to construct the system of rays and fronts of a shock wave. This problem can be solved relatively easily for isotropic media; however, even in this case, some difficulties arise when the problem concerns the interaction of a wave with an interface between media with different mechanical properties (elastic reflectors, lenses, etc.), because such an interaction causes the formation of caustics at which energy is focused and the field intensity grows without limit (within the framework of the ideal theory of elasticity and the ray method).

The physical pattern of dynamic phenomena becomes much more complicated if the study concerns the propagation of elastic waves in anisotropic media [7–9]. In this case, the field function appears to be a vector function and three wave types of different polarizations exist for every direction. The phase velocities of waves depend on both wave polarization and propagation direction. In the general case, rays are not orthogonal to the wave front surfaces, and the velocity of wave propagation along the ray differs from the phase velocity. The phenomenon of wave diffraction by interfaces between media also becomes more complicated, because the corresponding Snell relationships appear to be strongly nonlinear, which is a consequence of the lack of preliminary information about the phase velocities of reflected and transmitted waves. For this reason,

the determination of the directions of outgoing rays from boundary surfaces requires solving nonlinear systems of equations. The possible nonuniqueness of their solutions may be an additional reason for the appearance of caustics even in the case of a regular shock wave incident on a plane interface boundary [10], and give rise to a variety of qualitatively different phenomena in the reflection–refraction processes.

Commonly, problems on the interaction of an incident wave with a boundary between anisotropic media are solved by constructing the curves of refraction vectors [11, 12], which is, in essence, a graphic method. In this paper, we solve the problem using the method of solution continuation with respect to a parameter [13–15], which is the simplest way of identifying bifurcation states.

Note that the solutions found below may be useful in the problems of seismology and prospecting seismology, as well as in designing explosive technologies.

## RAY METHOD IN THE THEORY OF ELASIC WAVES

The dynamic equilibrium of particles of a transversely isotropic medium in which an elastic nonstationary wave propagates is described by the following equations in the Cartesian coordinate system $x_1$, $x_2$, $x_3$:

$$\sum_{k,p,q=1}^{3} \frac{c_{ik,pq}}{\rho}\frac{\partial^2 u_q}{\partial x_k \partial x_p} - \frac{\partial^2 u_i}{\partial t^2} = 0, \quad i = 1, 2, 3, \quad (1)$$

where $\rho$ is the density of the medium; $u_1$, $u_2$, and $u_3$ are elastic displacements; $t$ is time; and $c_{ik,pq}$ are the components of the tensor of elastic parameters of the medium. Due to the symmetry of this tensor with respect to the $Ox_2$ axis and the fact that it has only five irreducible parameters, it can be reduced to a two-dimensional form

$$\|C_{\alpha\beta}\| = \left\| \begin{array}{cc} C_1 & 0 \\ 0 & C_2 \end{array} \right\|,$$

$$C_1 = \left\| \begin{array}{ccc} \lambda+2\mu & \lambda-l & \lambda \\ \lambda-l & \lambda+2\mu-p & \lambda-l \\ \lambda & \lambda-l & \lambda+2\mu \end{array} \right\|, \quad (2)$$

$$C_2 = \left\| \begin{array}{ccc} \mu-m & 0 & 0 \\ 0 & \mu & 0 \\ 0 & 0 & \mu-m \end{array} \right\|,$$

where $\lambda$ and $\mu$ are the Lamé coefficients and $l$, $m$, and $p$ are the anisotropy parameters, which distinguish the medium under consideration from the isotropic one.

We represent the solutions to system (1) in the form of a plane monochromatic wave

$$\mathbf{u} = \mathbf{A} \cdot e^{ik(\mathbf{n}\cdot\mathbf{r} - vt)} \quad (3)$$

with a phase number $k$ and a phase velocity $v$. The phase fronts of this wave will be surfaces of constant phase $\mathbf{n}\cdot\mathbf{r} - vt = \text{const}$ locally perpendicular to unit vector $\mathbf{n}$ and traveling with velocity $\mathbf{v} = v\cdot\mathbf{n}$.

The magnitude of the phase velocity $v$ and the vector of wave polarization $\mathbf{A}$ are determined from the homogeneous system of algebraic equations [10, 11]

$$\sum_{k,p,q=1}^{3} \frac{c_{ik,pq}}{\rho} n_k n_p A_q - v^2 A_i = 0, \quad i = 1, 2, 3, \quad (4)$$

as eigenvalues and eigenvectors of the symmetric and positively defined Christoffel matrix $\Lambda_{iq} = \sum_{k,p=1}^{3} c_{ik,pq}\rho^{-1} n_k n_p$, where $i, q = 1, 2, 3$.

The condition of existence of a nonzero solution for the system of three equations (4) is written in the form of a cubic equation in the squared phase velocity:

$$\left\| \sum_{k,p=1}^{3} \frac{c_{ik,pq}}{\rho} n_k n_p - v^2 \delta_{iq} \right\| = 0. \quad (5)$$

For any preliminarily chosen direction of the normal $\mathbf{n}$ to the front, the roots of this equation are three positive numbers that allow the determination of the phase velocity magnitudes and their arrangement in descending order: $v_1(\mathbf{n}) > v_2(\mathbf{n}) \geq v_3(\mathbf{n}) > 0$. The maximum propagation velocity corresponds to the quasi-longitudinal wave, while the remaining velocities correspond to two quasi-transverse waves with different polarizations.

The polarization vector $\mathbf{A}^{(r)}$ for each of the three ($r$ = 1, 2, 3) waves possible in anisotropic media can be found by substituting the corresponding squared phase velocity into system (4) and determining the eigenvector of the matrix of coefficients of the system of equations

$$\sum_{k,p,q=1}^{3} \frac{c_{ik,pq}}{\rho} n_k n_p A_q^{(r)} - [v^{(r)}]^2 A_i^{(r)} = 0, \quad i = 1, 2, 3. \quad (6)$$

The time-dependent phase front surface of an elastic wave is described by the relationship

$$\tau(x_1, x_2, x_3) - t = 0, \quad (7)$$

where $\tau$ is some function satisfying the first-order partial differential equation [11]

$$\sum_{i,k,p,q=1}^{3} \frac{c_{ik,pq}}{\rho}\frac{\partial\tau}{\partial x_k}\frac{\partial\tau}{\partial x_p} A_q^{(r)} A_i^{(r)} = 1, \quad (8)$$

which extends the eikonal equation of geometrical optics to elastic waves in anisotropic media.

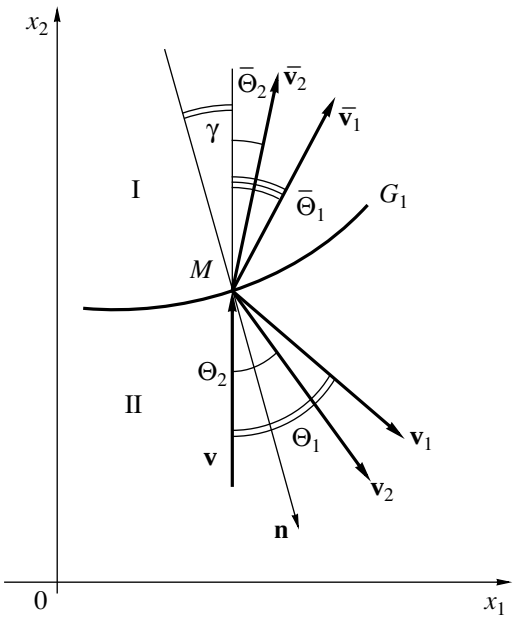


**Fig. 1.** Schematic diagram of orientation of the phase velocity vectors of nonstationary waves ($G_1$ is the boundary between media I and II).

Partial derivatives of the function $\tau$ with respect to the Cartesian coordinates are the components of the refraction vector **p** and are determined by the formulas

$$p_k \equiv \partial\tau/\partial x_k = \mathbf{n}/V_r(\mathbf{n}), \quad k = 1, 2, 3.$$

To construct the frontal surfaces (7) of an elastic nonstationary wave in a homogeneous anisotropic medium ($\rho$ = const, $c_{ik,\,pq}$ = const), we must find solutions to Eq. (8) that can be reduced to a system of ordinary differential equations by using the method of characteristics:

$$\frac{dx_k}{d\tau} = \xi_k = \frac{1}{\rho}\sum_{i,\,p,\,q\,=\,1}^{3} c_{ik,\,pq}p_pA_q^{(r)}A_i^{(r)},$$
$$\frac{dp_k}{d\tau} = 0, \quad k = 1, 2, 3. \tag{9}$$

In system (9), three first equations allow the determination of three components of the ray velocity vector $\boldsymbol{\xi} = \boldsymbol{\xi}^{(r)}(\mathbf{n}, x_k)$, along which the wave travels. Another group of equations shows that these rays are rectilinear in a homogeneous anisotropic medium.

Hence, the kinematic problem of constructing the evolving front of a nonstationary shock wave in a homogeneous anisotropic medium is reduced to the construction of a system of rectilinear rays whose directions satisfy Eq. (9) and correspond to a given sequence of normals **n** to the wave front. For a certain $t$ = const, the locus of the points lying on these rays and located at a distance $\xi(\mathbf{n}) \cdot t$ from the elastic wave source forms the front surface.

The interaction of rays and wave fronts with the boundaries between anisotropic media with different physical parameters makes their geometries much more complicated. In the general case, the front incident on the boundary generates three refracted and three reflected fronts of differently polarized elastic waves.

## METHOD OF SOLUTION

Consider a plane shock wave traveling along the $Ox_2$ axis and passing through a convex anisotropic lens, and assume that the $Ox_2$ axis coincides with the symmetry axes of both transversely isotropic medium and lens. This is a special direction in which the vectors of the ray and phase velocities coincide, so that the wave appears purely longitudinal. Because of the axial symmetry of the problem, an investigation of the behavior of traces of front surfaces in some plane containing the $Ox_2$ axis appears to be sufficient for the solution. We distinguish two transversely isotropic media with different elastic parameters: the initial medium (with the incident wave), whose parameters are marked with subscript I, and the internal medium of the lens marked with subscript II (Fig. 1). At every point $M$ of the first boundary surface of the lens (boundary $G_1$ between elastic media I and II), the incident ray produces a beam of two refracted and two reflected rays whose directions and phase velocities satisfy Snell's law [11]

$$\frac{\sin(\gamma)}{V} = \frac{\sin(\Theta_\nu - \gamma)}{V_\nu(\Theta_\nu)} = \frac{\sin(\bar{\Theta}_\mu + \gamma)}{\bar{V}_\mu(\bar{\Theta}_\mu)}, \tag{10}$$
$$\nu, \mu = 1, 2,$$

where $\gamma$ is the angle of inclination of the tangent to the surface $G_1$ at the point $M$ of ray incidence; $\Theta_1$ and $\Theta_2$ are the angles between the $Ox_2$ axis and the directions of the phase velocity vectors of the quasi-longitudinal *qP* and quasi-transverse *qS* waves reflected in medium I; $\bar{\Theta}_1$ and $\bar{\Theta}_2$ are the corresponding angles for waves refracted in medium II (in the lens); and $V$, $V_\nu$, and $\bar{V}_\mu$ are the phase velocities of the incident longitudinal wave and reflected and refracted waves (subscripts 1 and 2 correspond to quasi-longitudinal and quasi-transverse waves, respectively).

The characteristic feature of Snell's law (10) for anisotropic media is that the denominators $V_\nu$ and $\bar{V}_\mu$ are explicit functions of the corresponding angles $\Theta_\nu$ and $\bar{\Theta}_\mu$ and implicit functions of the angle $\gamma$ as are the numerators. The refraction and reflection angles $\Theta_\nu$ and $\bar{\Theta}_\mu$ ($\nu$, $\mu$ = 1, 2) at a point $M$ of boundary $G_1$ are obtained from the nonlinear system of equations (10), which is solved using the Newton method combined with the algorithm of solution continuation with respect to a parameter [14]. The angle of inclination of the tangent $\gamma$ appears to be a convenient choice for the leading parameter. With such a choice, for the first equation of system (10) with certain known parameter $\gamma = \gamma^n$ and

vectors $\mathbf{v}_\nu^n$, a small increment of the leading parameter $\Delta\gamma^n$ will cause the following increments of the pointing angles of elastic waves reflected in medium I:

$$\Delta\Theta_\nu^n = \frac{\cos\gamma\, v_\nu(\Theta_\nu^n) + \cos(\Theta_\nu^n - \gamma)\, v}{\cos(\Theta_\nu^n - \gamma)\, v - \sin(\gamma)\partial v_\nu(\Theta_\nu^n)/\partial\Theta_\nu}\Delta\gamma + r_\nu, \quad (11)$$

where $r_\nu = \sin(\Theta_\nu^n - \gamma)\, v - \sin\gamma v_\nu(\Theta_\nu^n)$ are the residuals at the considered step of the solution construction.

Rays of quasi-longitudinal and quasi-transverse waves outgoing from point $M$ are incident on the boundary surface $G_2$. At the points $M_P$ and $M_S$ of incidence on surface $G_2$, each wave produces new beams of quasi-longitudinal and quasi-transverse waves refracted in medium I and reflected in the lens (medium II). Phase velocities and vector directions of the rays of every beam again satisfy Snell's equations, which now have the form

$$\frac{\sin(\Theta - \varphi)}{v(\Theta)} = \frac{\sin(\Theta_\nu + \varphi)}{v_\nu(\Theta_\nu)} = \frac{\sin(\bar{\Theta}_\mu - \varphi)}{\bar{v}_\mu(\bar{\Theta}_\mu)}, \quad (12)$$

$$\nu, \mu = 1, 2.$$

The solution of system (12) is also performed according a step-by-step procedure. By way of example, a small variation $\Delta\varphi^n$ of the angle of inclination of the tangent to surface $G_2$ will cause increments of the pointing angles of phase velocity vectors of the refracted waves of both types:

$$\Delta\Theta_\nu^n = \frac{f_1\Delta\Theta + f_2\Delta\varphi}{f_3} + r_\nu^n. \quad (13)$$

Here, we introduced the functions

$$f_1 = \sin(\Theta_\nu^n + \varphi)\frac{dv(\Theta)}{d\Theta} - \cos(\Theta - \varphi)\, v_\nu^n,$$

$$f_2 = \cos(\Theta - \varphi)\, v_\nu^n(\Theta_\nu^n) + \cos(\Theta_\nu^n + \varphi)\, v,$$

$$f_3 = \sin(\Theta - \varphi)\frac{dv_\nu^n(\Theta_\nu^n)}{d\Theta_\nu^n} - \cos(\Theta_\nu^n + \varphi)\, v(\Theta)$$

and the residual of Eqs. (12) is $r_\nu^n = \sin(\Theta_\nu^n + \gamma)\, v - \sin(\Theta - \gamma)\, v_\nu^n(\Theta_\nu^n)$.

The implementation of successive calculations by formulas like (11) and (13) requires the knowledge of some initial state $\gamma$, $v$, $\Theta_\nu^0$, and $v_\nu(\Theta_\nu^0)$. In the case of the axially symmetric lens under consideration, a convenient choice of the initial direction is $\gamma = 0$, which corresponds to constructing a family of reflected and refracted rays beginning with the ray directed along the $Ox_2$ axis, because this ray produces rays directed along this very axis at both lens surfaces. For nonzero denominators, formulas like (11) and (13) allow the determination of a unique set of increments for pointing angles of all phase velocity vectors of both types of waves at both lens surfaces. Angles $\gamma$ for which the denominator on the right-hand side of Eqs. (11) and (13) vanishes,

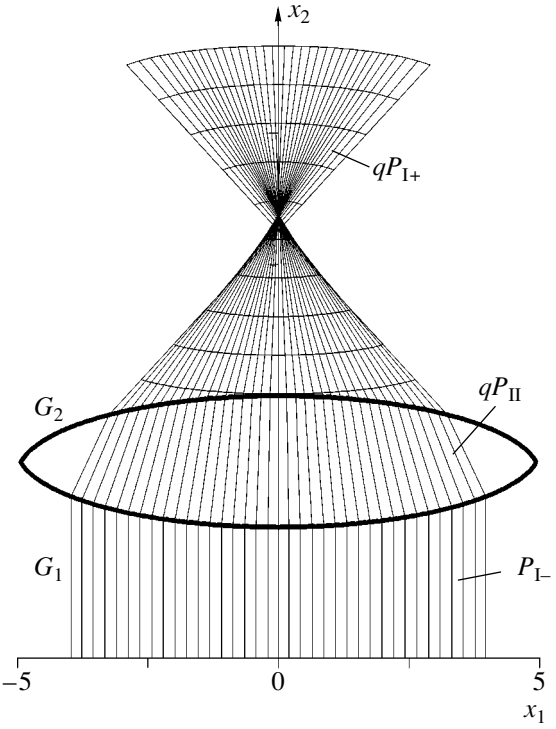


**Fig. 2.** Focusing of the rays of a longitudinal wave by a convex ellipsoidal lens.

$$\cos(\Theta_\nu^n - \gamma)\, v - \sin(\gamma)\frac{\partial v_\nu(\Theta_\nu^n)}{\partial\gamma} = 0,$$

$$\sin(\Theta - \varphi)\frac{dv_\nu^n(\Theta_\nu^n)}{d\Theta_\nu^n} - \cos(\Theta_\nu^n + \varphi)\, v(\Theta) = 0, \quad (14)$$

$$\nu = 1, 2$$

are the conditions of bifurcation for the solution. The solution continuation through this state requires that the terms of the second (third, and so on as required) order should be added to these equations [13].

Condition (14) of a possible nonuniqueness of the solutions to system (11), (13) corresponds to the convergence (contact) and intersection of reflected and refracted rays on one lens surface. These effects can be accompanied by the phenomenon of quasi-total internal reflection [16].

Moving away from lens surfaces, rays can touch and cross one another forming the envelopes of ray families called caustics. Since the singularities of the wave front appear on caustics, the focusing occurs at them and is accompanied by an infinite growth of the stress field intensity at the points of geometric singularities.

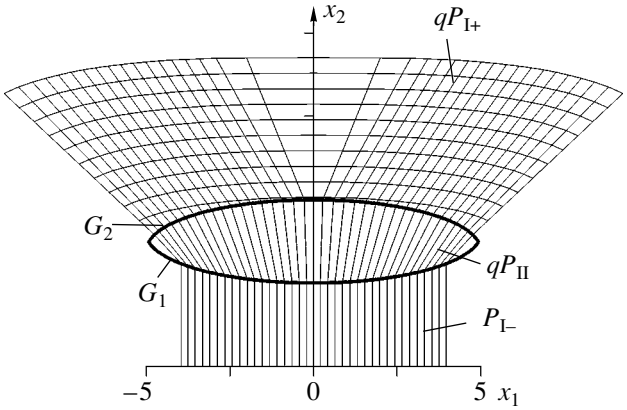


**Fig. 3.** Divergence of the rays of a longitudinal wave by a convex ellipsoidal lens.

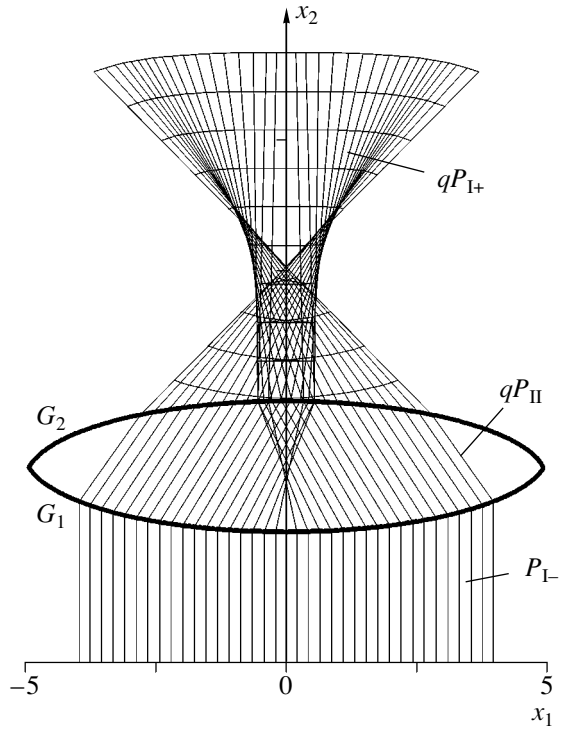


**Fig. 4.** Focusing of the rays of a longitudinal wave within a convex ellipsoidal lens.

The variation of the strain discontinuity at the moving front behaves depending on the geometry of the front surface and is characterized by the geometric divergence of rays, which is a function of **n** for anisotropic media. The geometric divergence of rays can be determined by the formula [11]

$$L = L(\alpha, \beta, \tau) = c(\alpha, \beta)\sqrt{\frac{|J(\alpha, \beta, \tau)|}{\xi(\alpha, \beta, \tau)}}, \qquad (15)$$

where $c(\alpha, \beta)$ is a constant coefficient and $J(\alpha, \beta, \tau)$ is the Jacobian of the transformation of the ray coordinate system to the Cartesian coordinate system. The Jacobian is calculated by the formula

$$J(\alpha, \beta, \tau) = (\mathbf{z}_1[\mathbf{z}_2 \times \mathbf{z}_3]) = \begin{bmatrix} z_{11} & z_{12} & z_{13} \\ z_{21} & z_{22} & z_{23} \\ z_{31} & z_{32} & z_{33} \end{bmatrix}, \qquad (16)$$

where $\mathbf{z}_1 = \sum_{k=1}^{3} \frac{\partial x_k}{\partial \alpha}\mathbf{i}_k$, $\mathbf{z}_2 = \sum_{k=1}^{3} \frac{\partial x_k}{\partial \beta}\mathbf{i}_k$, and $\mathbf{z}_3 = \sum_{k=1}^{3} \frac{\partial x_k}{\partial \tau}\mathbf{i}_k$ are the coordinate vectors of the curvilinear ray coordinate system $\alpha$, $\beta$, and $\tau$ determined numerically by using the difference scheme for calculating partial derivatives.

## RESULTS

The algorithm suggested above was used to investigate the diffraction of a plane longitudinal wave by a convex axially symmetric anisotropic lens bounded by ellipsoidal surfaces whose traces on the symmetry plane $Ox_1x_2$ are

$$G_1: \left(\frac{x_1}{5}\right)^2 + \left(\frac{x_2 - 4}{1.5}\right)^2 = 1;$$
$$G_2: \left(\frac{x_1}{5}\right)^2 + \left(\frac{x_2 - 3.5}{1.5}\right)^2 = 1. \qquad (17)$$

The problem was solved for anisotropic media with the following physical and mechanical parameters: $\rho_1 = 2.650 \times 10^3$ kg/m$^3$, $\lambda_1 = 4.972 \times 10^{10}$ Pa, $\mu_1 = 3.906 \times 10^{10}$ Pa, $\rho_2 = 2.650 \times 10^3$ kg/m$^3$, $\lambda_2 = 2.486 \times 10^{10}$ Pa, and $\mu_2 = 1.953 \times 10^{10}$ Pa. For the anisotropy coefficients $l_i = -0.1\lambda_i$, $m_i = 0.3\mu_i$, and $p_i = 0.5(\lambda_i + 2\mu_i)$, where $i = 1, 2$, Fig. 2 shows the system of rays belonging to the longitudinal incident wave $P_{I-}$, rays of quasi-longitudinal wave $qP_{II}$ refracted into the lens, and rays of quasi-longitudinal wave $P_{I+}$ produced by the latter in medium I (behind the lens). In Fig. 2, we did not show quasi-longitudinal rays reflected from both lens surfaces, all quasi-transverse rays, and evolutions of fronts (excluding the fronts of the quasi-longitudinal wave behind the lens). It is seen that initially parallel rays of an elastic wave are focused after their passage through an acoustically softer lens in the same way as light rays in geometrical optics. However, focuses of anisotropic lenses with ellipsoidal surfaces are not points in the general case; instead, each pair of symmetric rays has its own point of intersection at the symmetry axis, and these intersection points form a focusing zone. The sizes and location of such a zone depend on the lens geometry and the physical parameters of both anisotropic media.

As was described in [17], in the case of isotropic lenses and surrounding media, the ability of a biconvex lens to cause convergence or divergence of rays depends on the refractive index $n = c_1/c_2$, where $c_1$ and $c_2$ are the velocities of waves in the surrounding medium and in the lens material, respectively. When $n > 1$, the lens is convergent, and when $n < 1$, it is divergent. If we interchange the places of the elastic media with the parameters used above, the lens under consideration will become divergent (Fig. 3). The divergence degree and the uniformity of doubly refracted rays depends on the elastic characteristics of media and on the geometry of the surfaces $G_1$ and $G_2$.

Because of anisotropy, variation of some elastic characteristics of one of the media may considerably complicate the pattern of rays and fronts under consideration. By way of example, using the lens with the Lamé coefficients $\lambda_2 = 5.682 \times 10^9$ Pa and $\mu_2 = 2.273 \times 10^{10}$ Pa, for the first case we obtain that some rays of the elastic wave $qP_{II}$ intersect within the lens (Fig. 4). This fact causes rather complicated focusing of these rays behind the second boundary between the media and noticeably changes the stress field in medium II.

## REFERENCES


1. V. I. Arnol'd, *Singularities of Caustics and Wave Fronts* (Fazis, Moscow, 1996).
2. V. I. Arnol'd, Usp. Mat. Nauk **29** (4), 153 (1974).
3. V. I. Arnol'd, A. N. Varchenko, and S. M. Gusseĭn-Zade, *Singularities of Differentiable Maps* (Nauka, Moscow, 1982; Birkhauser, Boston, 1984).
4. T. Poston and I. Stewart, *Catastrophe Theory and Its Applications* (PITMAN, London, 1978; Mir, Moscow, 1980).
5. Yu. A. Kravtsov and Yu. I. Orlov, *Geometrical Optics of Inhomogeneous Media* (Nauka, Moscow, 1980).
6. Yu. N. Podil'chuk and Yu. K. Rubtsov, *Ray Methods in the Theory of Wave Propagation and Scattering* (Naukova Dumka, Kiev, 1988).
7. V. M. Byrdin, Akust. Zh. **49**, 284 (2003) [Acoust. Phys. **49**, 236 (2003)].
8. D. D. Zakharov, Akust. Zh. **48**, 205 (2002) [Acoust. Phys. **48**, 171 (2002)].
9. G. Busse, I. Yu. Solodov, R. Stoessel, and Yu. Schuetz, Akust. Zh. **48**, 22 (2002) [Acoust. Phys. **48**, 18 (2002)].
10. V. I. Gulyaev, P. Z. Lugovoĭ, G. M. Ivanchenko, and E. V. Yakovenko, Prikl. Mat. Mekh. **64** (3), 394 (2000).
11. G. I. Petrashen', *Propagation of Waves in Anisotropic Elastic Media* (Nauka, Leningrad, 1980).
12. F. I. Fedorov, *Theory of Elastic Waves in Crystals* (Nauka, Moscow, 1965; Plenum, New York, 1968).
13. M. M. Vaĭnberg and V. A. Trenogin, *Theory of Bifurcation of Solutions of Nonlinear Equations* (Nauka, Moscow, 1969; Noordhoff, Leyden, 1974).
14. V. I. Gulyaev, V. A. Bazhenov, and E. A. Gotsulyak, *Stability of Nonlinear Mechanical Systems* (Vyshcha Shkola, Lvov, 1982).
15. P. Z. Lugovoy and V. I. Gouliaev, in *Proceedings of the Conference of the American Physical Society on Shock Compression of Condensed Matter, Snowbird, Utah, USA, 1999*, Ed. by M. D. Furnish, L. C. Chhabildas, and R. S. Nixon (1999), p. 1287.
16. I. I. Anik'ev, V. I. Gulyaev, G. M. Ivanchenko, *et al.*, Prikl. Mekh. Tekh. Fiz. **41** (1), 21 (2000).
17. I. N. Kanevskiĭ, *Focusing of Sonic and Ultrasonic Waves* (Nauka, Moscow, 1977).


*Translated by A. Vinogradov*

*Acoustical Physics, Vol. 50, No. 2, 2004, pp. 146–153. Translated from Akusticheskiĭ Zhurnal, Vol. 50, No. 2, 2004, pp. 184–192.*


# Mechanism of Erythrocyte Aggregation Enhancement by Ultrasonic Field

**V. A. Dubrovskiĭ, K. N. Dvoretskiĭ, and A. É. Balaev**

*Department of Medical and Biological Physics, Saratov State Medical University, Bol'shaya Kazach'ya ul. 112, Saratov, 410710 Russia*

*e-mail: biophys@med.sgu.ru*

Received March 17, 2003

**Abstract**—Effect of a standing ultrasonic wave on the spontaneous and induced (specific, immune) processes of erythrocyte aggregation is studied *in vitro* on the basis of the data obtained from the elastic scattering of light. The effect of the time of ultrasonic action and the concentration of the initial reagents on the enhancement of these processes is analyzed. An approximate theoretical model is developed to describe the mechanism of the enhancement of erythrocyte aggregation by an ultrasonic field and the observation of the process of interest by the turbidimetric optical method. The model provides a good agreement between theory and experiment. The results of the study are used to derive recommendations as to how to increase the resolving power of the turbidimetric method of immunoanalysis with the aid of ultrasound. *© 2004 MAIK "Nauka/Interperiodica".*

## INTRODUCTION

Ultrasonic waves have found wide application in clinical medicine. Examples of such applications include ultrasonic therapy and surgery, Doppler spectroscopy, and ultrasonic testing. The possibilities of using ultrasound in biomedical technologies and in laboratory diagnostics have also been investigated. For example, experiments on ultrasonic manipulation of suspended particles [1–3] and cells [3–6] as well as filtration of bacteria [7–9] and their separation by ultrasound [10] have been described in the literature. A promising area of ultrasound application is biomedical immunology [11–18]. Note that immunological methods based on a specific interaction of antigenes and antibodies *in vitro* with the subsequent observation of the resulting immune complexes (induced formation of complexes) lie at the heart of many diagnostic tests used in laboratory medical diagnostics.

In [14–18] it was shown that the application of ultrasound accelerates the process of the induced formation of complexes, leads to an increase in the size of erythrocyte complexes, and accelerates their sedimentation. As a result, the resolving power of the method of detecting the immune complex formation increases and the time required for diagnostic testing is reduced. Note that the resolving power of the method characterizes the difference between the signals (e.g., optical signals [14–18]) recorded for the induced and spontaneous processes of complex formation (without specifying the interaction between the reagents). Naturally, an increase in the resolving power of the method makes the results of diagnostic testing more reliable and allows one to detect microscopic concentrations of the reagents of interest, which is important for, e.g., early diagnostics of diseases. In this paper, as in [14–18], we determine the resolving power of the method used for detecting the process of complex formation as the ratio of two optical signals: $K = I_{ind}/I_{sp}$, where $I_{ind}$ is the optical signal level obtained in the case of the induced formation of erythrocyte complexes (the agglutination reaction) and $I_{sp}$ is the optical signal level in the case of the spontaneous formation of complexes.

The subject of this paper is an analysis of the mechanism of induced and spontaneous processes of erythrocyte aggregation *in vitro* in the presence of an ultrasonic wave and an analysis of the optical (turbidimetric) response to these processes. For this purpose, we developed an approximate theoretical model, which described the immune processes *in vitro* under the action of ultrasound, as well as the changes in the optical signals obtained when probing these processes by a light beam. The study is carried out with a view to optimizing the parameters of the biological object under investigation, the time of the ultrasonic action on this biological object, and the experimental technique, so as to increase the resolving power of the method of detecting the induced immune process and, hence, the reliability of the diagnostic test. The results of theoretical calculations are compared with the experimental data obtained by the authors.

## 1. IRRADIATION OF A SUSPENSION WITH ULTRASOUND

The object of investigation was a mixture of dilute human blood with isohemagglutinating serum, i.e., a mixture similar to that used in the standard medical procedure for blood group determination. If the blood group of the specimen under investigation immunolog-

1063-7710/04/5002-0146$26.00 © 2004 MAIK "Nauka/Interperiodica"

ically fits the isohemagglutinating serum, erythrocyte complexes of large mass are formed and intensely sediment (precipitate). This process corresponds to the induced formation of complexes unlike the spontaneous process, which occurs when the erythrocytes of the blood did not fit the serum. In the latter case, erythrocyte complexes are practically not formed and the sedimentation of free erythrocytes proceeds at a low rate.

Naturally, the reliability of blood group determination (errors should be completely ruled out) is better the higher the resolving power with which the induced and spontaneous processes of complex formation are resolved.

The solvent used for the whole blood and the isohemagglutinating serum was an isotonic solution of sodium chloride with a concentration of 0.85%. Blood dilutions were within 1–6% of the whole blood. The standard isohemagglutinating serum was diluted by the same solvent to a concentration of 33%.

The mixture under study was incubated and then exposed to ultrasound. When the ultrasonic field was turned off, the destruction of spontaneously formed erythrocyte complexes was observed and, hence, the erythrocyte sedimentation process was slow. In the case of induced aggregation of erythrocytes (the erythrocyte agglutination reaction), the rate of sedimentation of the complexes and its depth were much greater.

As a source of ultrasound, we used an ultrasonic generator and a piezoceramic transducer, which was 30 mm in diameter and 1 mm in thickness. The frequency of the generator was 2.64 MHz ± 20%, and its rated output power was no greater than 1 W. The voltage applied to the transducer was limited so as to prevent the hemolysis (disruption) of erythrocytes and was approximately 6 V. The voltage and the frequency of ultrasonic oscillations were constant in all experiments.

A dish with the blood–serum solution under investigation was positioned on the piezoceramic transducer. The latter was wet with water to improve its acoustic matching with the glass dish. The length, thickness, and height of the dish were 20, 3, and 40 mm, respectively. The time of the ultrasonic action on the object varied from 20 to 160 s with the aim to determine the optimal conditions of irradiation of the biological object from the viewpoint of obtaining the maximal resolution $K$.

Under irradiation, a standing ultrasonic wave was formed in the dish. This wave caused the separation of erythrocytes and erythrocyte complexes by way of their grouping near the nodes of the standing wave. The separation of the cells and their complexes could easily be observed visually. Erythrocytes coming closer to each other at the nodes caused an increase in the probability of an induced immune interaction and, hence, an increase in the rate of the agglutination reaction. In addition, the effect of ultrasound caused an increase in the size of the erythrocyte complexes and, hence, accelerated their sedimentation after the ultrasonic field was switched off.

## 2. PRINCIPLES OF CONSTRUCTING THE THEORETICAL MODEL

The processes under study were modeled according to the following scheme.

Calculations performed for the motion of erythrocytes in the ultrasonic field with their grouping in the nodal zones of the standing wave made it possible to determine the concentration of cells in these zones. In its turn, the concentration of erythrocytes served as the starting data for calculating the kinetics of the formation of erythrocyte complexes in the nodal zones. The next step was the evaluation of the amount of erythrocytes and their complexes after switching off the ultrasonic field with the sedimentation of cells and their complexes being taken into account. Finally, the knowledge of the concentration of erythrocytes and light complexes that did not have enough time for their sedimentation allowed the determination of the optical response to the processes of interest when studied by the turbidimetric method.

It should be noted that the modeling of the processes considered above was performed for both the spontaneous and induced formation of complexes with a subsequent comparison of the results.

The motion of erythrocytes in the field of a standing ultrasonic wave was analyzed with allowance for the dynamics of the spatial variation of viscosity in the solution. Erythrocytes were approximated by spherical particles. It was assumed that the formation of spontaneous and immune erythrocyte complexes occurred only after the erythrocytes gathered in the zone of a certain given thickness near a node of the standing ultrasonic wave. The analysis was performed for the conditions of a continuous influx of erythrocytes into this zone under the effect of the radiation pressure forces of the standing ultrasonic wave. The sedimentation of erythrocyte complexes was analyzed with allowance for their distribution in size.

The calculation of the concentration of erythrocyte complexes in a given zone with their subsequent sedimentation made it possible to determine the level of a probing optical signal transmitted through the mixture under study. The results obtained by calculating the cell concentrations in the given zone for the cases of spontaneous and induced aggregation of erythrocytes were compared. In addition, a similar comparison was performed for the corresponding optical signals. The theoretical results were compared with the experimental data obtained by the authors.

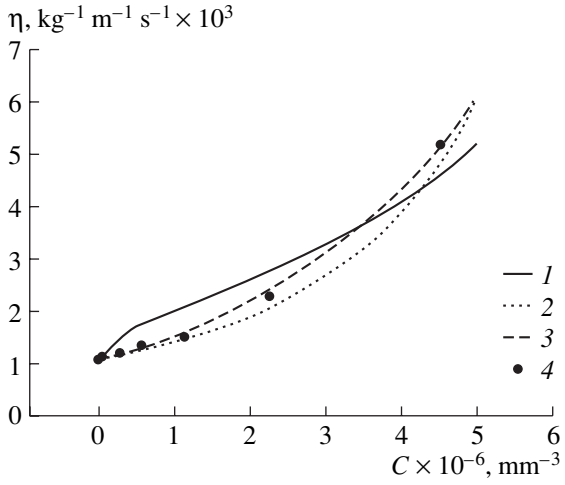


**Fig. 1.** Dependence of the structural viscosity of the blood solution on the erythrocyte concentration.

## 3. MOTION OF AN ERYTHROCYTE IN THE SOLUTION IN THE PRESENCE OF AN ULTRASONIC WAVE

The radiation pressure forces of the standing ultrasonic wave cause a separation of the cell suspension between the nodes of the pressure field, which occur at half-wavelength intervals. Since the total volume of erythrocytes in blood is approximately 50 times greater than the total volumes of other blood-forming elements [19], it is possible to simplify the calculations by considering blood as a homogeneous solution of erythrocytes. The motion of a body in the field of an ultrasonic wave is mainly determined by the size and shape of this body. In normal conditions (*in vivo*), erythrocytes of human blood have the form of biconcave disks with diameters varying from 5.7 (microcytes) to 9.35 μm (macrocytes). The majority of red cells (68%) have diameters within 7.0–8.0 μm (normocytes) [20] with the ratio of diameter to maximal thickness being approximately equal to 4 [21]. However, in experimental conditions (*in vitro*) without changes in volume, erythrocytes gradually transform to echinocytes (the cell surface develops thorns), stomacytes (disks that are concave on one side), spherocytes, etc. [19]. An exact calculation of the motion of such particles in the ultrasonic field presents a difficult problem. Therefore, to simplify the description of the cell motion, we approximate an erythrocyte with a sphere. Since the volume of an average erythrocyte is about 87 femtoliters [22], its radius should be about 2.75 μm.

The motion of an erythrocyte in the field of an ultrasonic wave is determined by such parameters as the densities of the cell and the surrounding medium, their compressibilities, and the structural viscosity of the medium surrounding the erythrocyte. The structural viscosity of the liquid under study is understood as the viscosity of the plasma solution with allowance for the effect of the surrounding erythrocytes on the motion of a given erythrocyte. In the process of cell separation under the action of the ultrasonic field, the cell concentration and, hence, the structural viscosity cease being uniform over the whole dish volume and become dependent on the distance to the nodal plane and on the time of ultrasonic action. This fact should be taken into account in considering the cell motion under the effect of the radiation pressure force of the standing ultrasonic wave. For high erythrocyte concentrations, high levels of cell concentrations are characteristic of the regions near the nodal planes of the ultrasonic field. With the accumulation of blood cells in these regions, the determination of the structural viscosity becomes rather difficult. Therefore, in practice, at high erythrocyte concentrations, numerous empirical relations are used. For example, $\eta/\eta_0 = (1 - H^{1/3})^{-1}$ [23] or $\eta/\eta_0 = (1 - H)^{-2.5}$ [24], where $\eta/\eta_0$ represents the dependence of the relative structural viscosity on the hematocrit index $H$ (the relative volume of blood-forming elements), $\eta_0$ is the viscosity of the plasma solution ($1.072 \times 10^{-3}$ kg/(m s)), and $\eta$ is the structural viscosity of blood. The above empirical dependences of $\eta$ on erythrocyte concentration are plotted in Fig. 1 (curves *1* and *2*, respectively).

Using a capillary viscometer (for low concentrations) and an AKR-2 rotational viscometer (for concentrations from 5% to whole blood), we measured the blood viscosity. The results of these measurements are also shown in Fig. 1 (dots *4*).

The approximation of these experimental results was realized with the following empirical relation:

$$\eta = \eta_0 e^{kC}. \quad (1)$$

Here, $C$ is the number of erythrocytes per 1 mm$^3$ and $k$ is a coefficient chosen so as to provide the best agreement of the approximation with the experimental data; this coefficient proved to be equal to $3.4805 \times 10^{-7}$. The form of approximation (1) is shown in Fig. 1 (curve *3*). One can see a good agreement of empirical dependence (1) with the dependences described earlier, as well as with the results of our measurements. Therefore, in what follows, we use relation (1) to describe the spatial changes in the resistance to cell motion in the presence of the ultrasonic field.

The motion of a cell is determined by the radiation force $F_r$ and the Stokes force $F_S$. The radiation force $F_r$ has the form [25]

$$F_r = -\left[\frac{P_m^2 V \beta_m}{2\lambda}\right]\left[\frac{5\rho - 2\rho_m}{2\rho + \rho_m} - \frac{\beta}{\beta_m}\right]\sin\left(\frac{4\pi Z}{\lambda}\right), \quad (2)$$

where $P_m$ is the sound pressure amplitude, $V$ is the volume of the moving particle, $\lambda$ is the ultrasound, wavelength $\rho$ and $\rho_m$ are the densities of the cell and the surrounding medium, and $\beta$ and $\beta_m$ are their compressibilities. The Stokes force $F_S$ is determined as

$$F_S = 6\pi\eta\rho v, \quad (3)$$

where $\eta$ is the structural viscosity of the medium, $r$ is the radius of the particle, and $v$ is the velocity of its motion.

Hence, a spherical particle moves under the action of the resulting force $F$:

$$F = ma = F_r - F_S, \quad (4)$$

where $m$ is the mass of the moving particle and $a$ is its acceleration. Note that, according to estimates, the gravity and buoyancy forces acting on an erythrocyte can be neglected in comparison with the sound pressure force acting on the cell even in the region of the nodal plane of a standing ultrasonic wave.

Since the grouping of erythrocytes in the zones of pressure nodes of the standing ultrasonic wave proceeds relatively slowly, we can neglect the acceleration of the cell (by analogy with [8]). Then, we have

$$0 = F_r - F_S. \quad (5)$$

From this relation, we easily obtain the expression for the instantaneous velocity of the particle at a point located at a distance $Z$ from a pressure node of the ultrasonic wave:

$$v(Z) = -\left[\frac{P_m^2 r^2 \beta_m}{9\lambda\eta}\right]\left[\frac{5\rho - 2\rho_m}{2\rho + \rho_m} - \frac{\beta}{\beta_m}\right]\sin\left(\frac{4\pi Z}{\lambda}\right). \quad (6)$$

Since the distance between neighboring nodes of the pressure field is equal to a half-wavelength of the ultrasonic wave, the cells located within a quarter-wavelength from a node should gather near this node within a certain time. The time required for a particle to reach a node depends on the initial position of the particle. As the particle approaches the node, the velocity of its motion drastically decreases. This occurs because, first, the radiation force (2) of the standing ultrasonic wave, which moves the particle, decreases near the node, and, second, the structural viscosity of the medium increases with an increasing concentration of erythrocytes gathering in this zone. Therefore, one should not consider the time within which a particle exactly reaches the node. In the literature, the usual practice is to consider the time within which the particles gather in a certain zone near the node [8]. We choose the zone with the boundaries at approximately $\pm\lambda/80$ from a node, where $\lambda$ is the wavelength of ultrasound. The choice of the width of the zone is determined by the fact that, for the experimental solutions of human blood [17, 18], all erythrocytes lying at distances up to $\lambda/4$ from the nodal plane of the ultrasonic wave may group into a zone of approximately this width. For $\lambda = 0.576$ mm, this value is about 7 μm. The time that is necessary for the cells lying at a distance $Z$ from the node to reach the boundary of the chosen zone can be estimated by the formula

$$T = \int_Z^{\lambda/80} \frac{dz}{v(z)}. \quad (7)$$

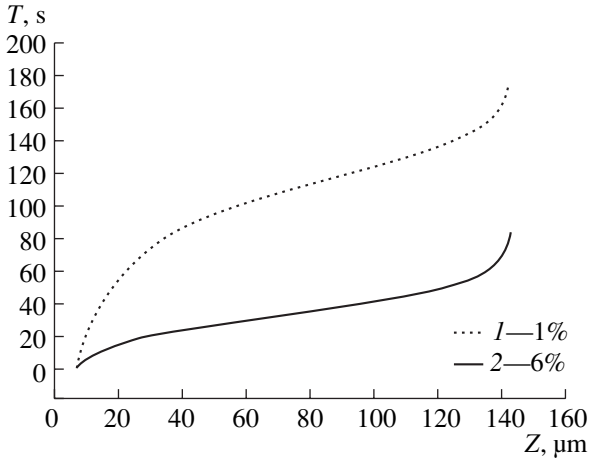


**Fig. 2.** Time that is necessary for erythrocytes to gather in the zone lying within $\pm\lambda/80$ from the nodal plane of the ultrasonic wave versus their initial position with respect to this plane.

The results of numerical integration by formula (7) can be used to analyze the variation of the number of cells in a given volume with time. For suspensions containing 1 and 6% of erythrocytes, the results of calculations are presented in Fig. 2. In the calculations, the following initial parameters were used: $P_m = 250$ kPa, $\rho \approx 1.092 \times 10^3$ kg/m$^3$ [19], $\rho_m = 1.0045 \times 10^3$ kg/m$^3$ [26], $\beta_m = 4.58 \times 10^{-10}$ Pa$^{-1}$ [8], and $\beta = 3.48 \times 10^{-10}$ Pa$^{-1}$ [27]. One can easily see that the time within which all erythrocytes will gather near the node (in the zone of width $\pm\lambda/80$) strongly depends on their initial concentration. For 1 and 6% solutions of blood, this time is about 60 and 160 s, respectively, which agrees well with the experimental results presented below.

Figure 3 shows the dependence of the erythrocyte concentration in the given zone near the nodal plane of the ultrasonic wave on the time of ultrasonic action. These results were used to determine the concentration of immune erythrocyte complexes and their distribution in size.

## 4. INDUCED AGGREGATION OF ERYTHROCYTES IN THE ULTRASONIC FIELD

An increase in the concentration of blood cells near the nodal plane leads to an increase in the probability of intercellular interactions. Depending on the group of blood and on the type of isohemagglutinating serum, these interactions may be of a spontaneous or induced (specific immune) character [16, 18]. The kinetics of the formation of erythrocyte complexes can be described using the system of ordinary differential

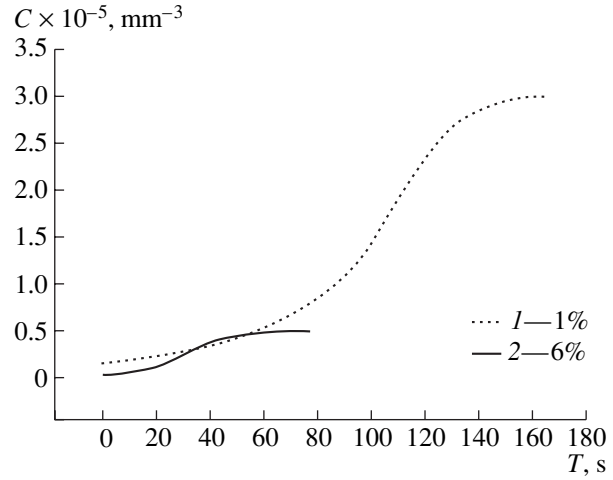


**Fig. 3.** Dependence of the concentration of blood cells near the nodal plane on the time of ultrasonic action.

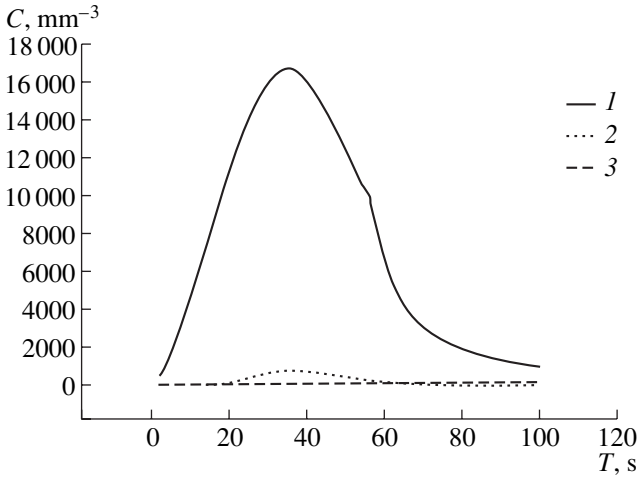


**Fig. 4.** Concentration of erythrocyte complexes as a function of the time of ultrasonic action: (*1*) single erythrocytes, (*2*) four-cell complexes, and (*3*) eight-cell complexes.

equations of the first order [28]:

$$\frac{dC_{AB}}{dt} = k_{AB}C_AC_B, \quad (8)$$

where $C_A$, $C_B$, and $C_{AB}$ are the concentrations of the initial reagents A and B and their product AB; $k_{AB}$ is the association constant, which depends on the mobility of the reagents and on the steric factor (the probability of the formation of a complex at the collision of the reaction products).

For spontaneous processes, the association constants are much smaller than those for induced processes [29]. In our study, the best agreement between theory and experiment was achieved under the condition that the association constant for the induced agglutination reaction was approximately 10 times as great as the corresponding constant for the spontaneous aggregation process.

Using this condition, we determined the dependence of the size distribution of erythrocyte complexes on the time of ultrasonic action by solving the system of differential equations in the framework of the first three stages of complex formation [28]. The time dependences of the concentrations of free erythrocytes and complexes consisting of 4 and 8 erythrocytes is shown in Fig. 4. The time of the characteristic break in curve *1* corresponds to the accumulation of all erythrocytes near the nodal plane, after which only the process of transformation of free erythrocytes into complexes due to their interaction takes place. The bell-shaped run of the curve is explained as follows: at small times of ultrasonic action, an increase in $T$ leads to an increase in the concentration of complexes as free erythrocytes arrive at the given zone $\pm\lambda/80$; however, at greater times, the erythrocyte inflow into this zone slows down while the complexes are transformed to larger ones with a simultaneous decrease in their number.

## 5. TURBIDIMETRY OF THE BIOLOGICAL OBJECT UNDER STUDY

To estimate the optical response to the induced aggregation of erythrocytes, one should take into account that the object under study is a dynamic one: the formation of erythrocyte complexes is accompanied by a simultaneous sedimentation of erythrocytes and their complexes.

It is well known that the agglutination of erythrocytes accelerates the sedimentation process, because the rate of sedimentation depends on the mass of particles sedimented. Therefore, the sedimentation of heavy erythrocyte complexes proceeds faster than that of light complexes or single cells. An exact modeling of the sedimentation process in a dynamically varying polydisperse medium is a rather complicated problem. Therefore, to simplify the calculations, we assumed that heavy erythrocyte complexes leave the zone of observation fast, so that after the ultrasonic field is switched off, only free erythrocytes and light erythrocyte complexes remain in this zone.

The observation of the dynamics of sedimentation in a red cell suspension allows one to judge the intensity of the agglutination process. Among the methods used for such observations, the most informative and most used ones are the optical methods, such as photometry [30], nephelometry [31], and fluorescence measurements [32]. In [16–18], we used an optical method that was a combination of the photometric and nephelometric ones, namely, the turbidimetric method. Since the object under investigation was a highly concentrated suspension of particles varying widely in size, the existing theories of single scattering of light provided no

adequate solution to the problem. The use of the theory of multiple scattering of light by disperse systems in the general form requires cumbersome mathematics and physical data that are not easily accessible. For the transmission of normally incident light through an erythrocyte suspension on the assumption that almost all radiation is scattered into the front half-plane, after some additional simplifications, the general theory yields the expression [33]

$$I/I_0 = \exp(-C\sigma_a d) \times \{\exp(-C\sigma_s d) + q[1 - \exp(-C\sigma_s d)]\}, \quad (9)$$

where $I$ and $I_0$ are the intensities of the transmitted and incident light beams, $C$ is the concentration of scatterers, $\sigma_a$ and $\sigma_s$ are the absorption and scattering cross sections, $d$ is the thickness of the scattering layer, and $q$ describes the total power fraction scattered in the solid angle of reception from a single scatterer. For the theoretical calculation of $q$, it is necessary to know the geometry of the experiment and the dependence of the scattered light intensity on the observation angle. The latter cannot be easily determined for erythrocytes with allowance for their distribution in size, shape, and orientation. Therefore, in modeling, the value of $q$ was chosen empirically, proceeding from the values of photocurrents at the initial instant of time (when the concentration of particles was known) and at the terminal instant (when the concentration of cells in the volume under observation was equal to zero as a result of their sedimentation). The value of $q$ proved to be approximately equal to $10^{-4}$. With this value, the time dependence obtained above for the concentration of blood cells with allowance for its variation under the effect of the ultrasonic field (Fig. 3) and sedimentation was substituted into Eq. (9). This allowed us to estimate the dynamics of the clarification of the medium with time and to compare the results with experimental data.

## 6. COMPARISON OF THEORETICAL AND EXPERIMENTAL RESULTS

Theoretical results and experimental data for the case when the intercellular interaction is not of a specific immune character are shown in Fig. 5. Curve *1* and dots *3* represent the theoretical and experimental results, respectively, for the 1% solution of blood, and curve *2* and dots *4*, for the 6% solution. One can see that, up to certain values of the time of ultrasonic action, the medium is clarified weakly, after which the clarification proceeds much faster. This may be explained as follows. The probability of the spontaneous formation of a strong large erythrocyte complex is fairly small, but it increases with increasing concentration of cells in the zones of nodal planes of the ultrasonic standing wave because of the increase in the probability of cell membrane contacts. The comparison of the results shown in Figs. 5 and 3 suggests that the characteristic instant of time at which the clarification of the medium is drastically enhanced corresponds to the instant when almost all cells gather near the nodal planes of the standing ultrasonic wave. Further action of the ultrasonic field leads to a still denser packing of cells and, hence, to an increase in the number of large cell complexes, whose fast sedimentation leads to the clarification of the medium observed in the experiment. It should be noted that the time within which the red cells gather near the nodal planes strongly depends on the initial concentration of erythrocytes in the solution. As one can see from the experiment (Fig. 5), the characteristic pre-clarification times for the 1 and 6% concentrations of blood differ by approximately a factor of 2.5, which agrees well with the results of theoretical modeling (Figs. 3 and 5).

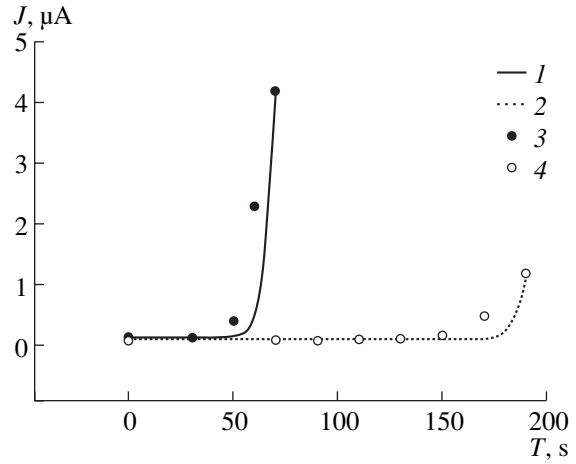


**Fig. 5.** Dependence of the photocurrent on the time of ultrasonic action in the case of the spontaneous formation of erythrocyte complexes.

Similar results for the agglutination reaction (specific immune intercellular interaction) are presented in Fig. 6. Their comparison with the results displayed in Fig. 5 shows that, in this case, the characteristic time of the beginning of the fast clarification process is much smaller than the corresponding time in the case of the spontaneous formation of erythrocyte complexes. This difference can be explained as follows. Unlike the spontaneous process, induced agglutination actively proceeds during both incubation of the specimens and ultrasonic action on the specimens. In the field of the ultrasonic wave, the velocity of erythrocytes and their complexes strongly depends on the size of the biological objects (see Eq. (6)). This leads to a decrease in the time within which most erythrocytes gather near the nodal planes of the ultrasonic wave, as compared to the spontaneous process. A rigorous description of this process presents a difficult problem. Therefore, we use the approximation in which all complexes have a single effective size (the radius of an effective sphere). An estimate of this size by the least squares method yields approximately 5 μm, which approximately corresponds to a complex consisting of six erythrocytes.

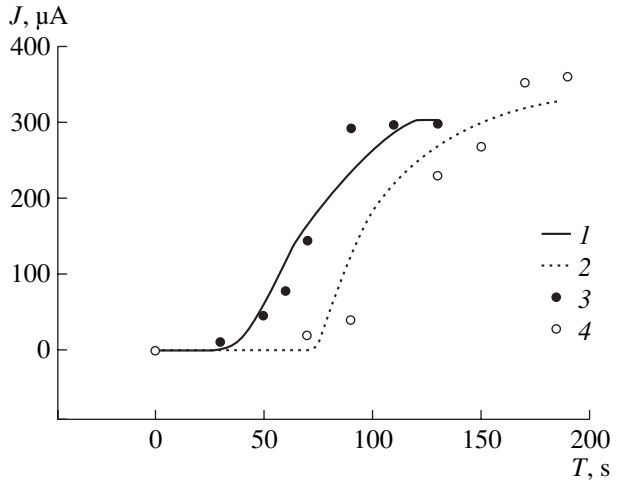


**Fig. 6.** Dependence of the photocurrent on the time of ultrasonic action in the case of the induced formation of erythrocyte complexes.

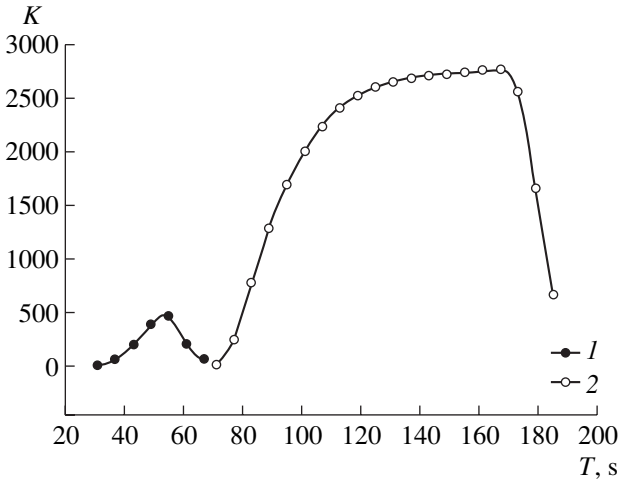


**Fig. 7.** Dependence of the resolving power of the immunoanalysis method on the time of ultrasonic action.

Naturally, in the case of agglutination, the induced complex formation and, hence, the sedimentation proceed more actively than in the case of the spontaneous process, which manifests itself in the observed degree of clarification of the medium. From Fig. 6, one can see that it reaches values that are hundreds of times greater than in the previous case (Fig. 5). It should be noted that, eventually, all curves (Figs. 5 and 6) exhibit saturation, which is explained by the sedimentation of practically all cells.

Figure 7 presents the resolving power $K$ for 1 and 6% solutions of blood. The curves are bell-shaped because, for the induced and spontaneous processes of complex formation, the clarification of the medium occurs with different rates (see Figs. 5 and 6). This difference is determined by two components: first, by the aforementioned difference in the association constants for the spontaneous and induced erythrocyte agglutination reactions, and, second, by the aforementioned decrease in the time within which the erythrocyte suspension undergoes separation due to the effect of the standing ultrasonic wave. These two components can be manipulated. The rate of the induced agglutination of erythrocytes can be increased by choosing the optimal concentration ratio of the isohemagglutinating serum and the blood cells. As the time of incubation of the erythrocyte suspension increases, the depth of the agglutination reaction grows. This leads to an increase in the fraction of large erythrocyte complexes. As a result, the time of separation of the medium decreases and, hence, the clarification process is accelerated. However, the dependence of the gain in the resolution of the method on the time of incubation has the form of a saturation curve [17, 18]. The latter is explained by the fact that an increase in the incubation time may lead to the state when the agglutination reaction almost completely terminates and a further increase in the incubation time does not lead to any considerable change in the size distribution of erythrocyte complexes. In its turn, this situation leads to a smaller variation in the time of separation of the medium and to a saturation of the gain in resolving power $K$ as a function of the time of incubation.

A decrease in the resolving power of the method for large times of ultrasonic action (Fig. 7) is also caused by the difference in the rates of the complex formation and sedimentation processes. In the case of the agglutination reaction, practically all blood cells are sedimented within a certain time and, hence, the observed clarification of the medium reaches its maximum (Fig. 6). In the case of the spontaneous formation of complexes, the signal continues to grow (Fig. 5). In the limit, the ratio of the two signals tends to unity, which corresponds to the case of a complete sedimentation of the cells and complexes in both cases. Therefore, to obtain the maximal resolving power, one has to choose the optimum time of ultrasonic action. From Fig. 7, one can also see that this optimum strongly depends on the initial concentration of erythrocytes. When the initial concentration of blood cells changes from 1 to 6%, the resolving power of the method increases by approximately a factor of 5. Simultaneously, the time of ultrasonic action that corresponds to the maximal resolving power increases by approximately a factor of 3.

## CONCLUSIONS

In this paper, the mechanism of erythrocyte agglutination enhancement by a standing acoustic wave was studied on the basis of a specially developed approximate theoretical model and the theoretical results were compared with experimental data. This study allowed us to reveal ways to increase the resolving power of the method of immunoanalysis. They include the optimization of both the initial erythrocyte concentration and the ratio between this concentration and the concentration

of the isohemagglutinating serum. In addition, the resolving power of the method may be considerably increased by choosing the optimal time of incubation of the biological object and the time of ultrasonic action. With these recommendations, one can increase the maximal resolving power of the method by a factor of 4 for the case of a 1% solution of blood and by a factor of 1.5 for a 6% solution, compared with the data shown in Fig. 7. It should be noted that an increase in the resolving power of the method of analyzing the induced aggregation of cells is an important problem, for example, in the case of determining the group of blood with a reduced agglutination ability of erythrocytes, when the standard methods lead to a high probability of error while the procedure of the blood group determination is rather laborious.

On the whole, the study described above should be useful for understanding the processes that occur in an immune biological medium in the presence of an ultrasonic wave. It also demonstrates the prospects of ultrasound application in the development of methods and instruments for biomedical immunological studies and diagnostics.

## REFERENCES


1. G. Whitworth, M. A. Grundy, and W. T. Coakley, Utrasonics **29**, 439 (1991).
2. C. J. Schram, Adv. Sonochem. **2**, 293 (1991).
3. W. T. Coakley, G. Whitworth, M. A. Grundy, *et al.*, Bioseparation **4**, 73 (1994).
4. W. T. Coakley, D. W. Bardsley, M. A. Grundy, *et al.*, J. Chem. Technol. Biotechnol. **44**, 43 (1989).
5. D. G. Kilburn, D. J. Clarke, W. T. Coakley, and D. W. Bardsley, Biotechnol. Bioeng. **34**, 559 (1989).
6. O. Doblhoff-Dier, Th. Gaida, H. Katinger, *et al.*, Biotechnol. Prog. **10**, 428 (1994).
7. J. J. Hawkes and W. Goakley, Enzyme Microb. Technol. **19**, 57 (1996).
8. J. J. Hawkes, M. S. Limaye, and W. T. Coakley, J. Appl. Microbiol. **82**, 39 (1997).
9. F. Trampler, S. A. Sonderhoff, P. W. S. Pui, *et al.*, Biotechnology (N.Y.) **12**, 281 (1994).
10. C. A. Miles, M. J. Morley, W. R. Hudson, and B. M. Mackey, J. Appl. Bacteriol. **78**, 47 (1995).
11. M. A. Grundy, W. E. Bolek, W. T. Coakley, and E. Benes, J. Immunol. Methods **165**, 57 (1993).
12. M. A. Grundy, K. Moore, and W. T. Coakley, J. Immunol. Methods **176**, 169 (1994).
13. E. T. Nerys and W. T. Coakley, Ultrasound Med. Biol. **22**, 1277 (1996).
14. V. A. Dubrovskiĭ and L. B. Denisov, in *Proceedings of IV All-Union School on Laser Applications in Biology* (Chisinau, 1986), p. 64.
15. V. A. Dubrovskiĭ, L. B. Denisov, and V. V. Gusev, in *Proceedings of All-Union Conference on Measurements in Medicine and Their Metrological Provision* (Moscow, 1986), p. 69.
16. V. A. Doubrovski, V. F. Kirichuk, and I. V. Sherbakova, in *Proceedings of Symposium on Biomedical Optics, Europe 1994, Lille, France* (1994), p. 60.
17. V. A. Dubrovskiĭ and K. N. Dvoretskiĭ, Opt. Spektrosk. **89**, 109 (2000) [Opt. Spectrosc. **89**, 99 (2000)].
18. V. A. Doubrovski and K. N. Dvoretski, Ultrasound Med. Biol. **26**, 655 (2000).
19. V. A. Levtov, S. A. Regtrer, and N. Kh. Shadrina, *Reology of Blood* (Meditsina, Moscow, 1982), p. 272.
20. D. I. Gol'dberg and E. D. Gol'dberg, *Handbook on Hematology* (Tomsk Gos. Univ., Tomsk, 1980), p. 267.
21. A. L. Chizhevskiĭ, *Biophysical Mechanisms of Erythrocyte Sedimentation* (Nauka, Novosibirsk, 1980), p. 178.
22. D. H. Tycko, M. N. Metz, E. A. Epstein, and A. Grinbaum, Appl. Opt. **24**, 1355 (1985).
23. S. E. Charm and G. S. Kurland, *Blood Flow and Microcirculation* (Wiley, New York, 1974).
24. G. R. Cokelet, in *Microcirculation* (New York, 1976), Vol. 1, p. 9.
25. W. L. Nyborg, *Ultrasound: Its Application in Medicine and Biology* (Elsevier, New York, 1978).
26. E. C. Everbach and R. E. Apfel, J. Acoust. Soc. Am. **98**, 3428 (1995).
27. K. K. Shung, B. A. Krisko, and J. O. Ballard, J. Acoust. Soc. Am. **72**, 1364 (1982).
28. V. A. Doubrovski, K. N. Dvoretski, V. F. Kirchuk, and I. V. Scherbakova, Proc. SPIE **3053**, 18 (1997).
29. M. I. Levi, Zh. Obshch. Biol. **40**, 423 (1979).
30. P. Latimer, Appl. Opt. **22**, 1136 (1983).
31. E. Muralidharan, N. Tateishi, and N. Maeda, Biochim. Biophys. Acta **1194**, 255 (1994).
32. G. Serman, M. Purmasir, and D. Glencross, Cytometry **34**, 43 (1998).
33. V. J. Twerrsky, J. Opt. Soc. Am. **60**, 1084 (1970).


*Translated by E. Golyamina*

*Acoustical Physics, Vol. 50, No. 2, 2004, pp. 154–157. Translated from Akusticheskiĭ Zhurnal, Vol. 50, No. 2, 2004, pp. 193–197.*


# Averaged Response of a Horizontal Linear Antenna in a Shallow Sea

**V. A. Eliseevnin**

*Andreev Acoustics Institute, Russian Academy of Sciences, ul. Shvernika 4, Moscow, 117036 Russia*
*e-mail: bvp@akin.ru*

Received October 21, 2002

**Abstract**—Response of a horizontal linear receiving antenna combining the powers of incident normal waves in a shallow sea is studied. The acoustic field is produced by an omnidirectional monochromatic point source. The antenna aperture is comparable to or smaller than the sea depth. © *2004 MAIK "Nauka/Interperiodica".*

At present, linear antennas are widely used in applied hydroacoustics [1]. The acoustic field in underwater acoustic waveguides can be characterized in terms of its intensity averaged over the propagation path [2–4], which is calculated by a noncoherent summation of individual normal modes or beams, so that the interference structure of the field proves to be smeared. The cited publications consider omnidirectional transmission or reception. Averaged characteristics of the acoustic field produced by a vertical transmitting antenna in a waveguide are addressed in [5–8]. The present paper studies the shape of the response of a horizontal linear antenna in an underwater acoustic waveguide with uniform sound velocity (a shallow sea model) when the responses of the antenna to individual normal waves are combined disregarding their phases; i.e., the antenna combines the powers of normal waves.

The acoustic field in a waveguide excited by a point source can be represented as a superposition of normal waves [9]. Consider the reception by a horizontal linear antenna with an aperture $L$ and with an electronic compensator, which allows the rotation of the antenna phase front about the center through a given compensation angle $\beta$ in the horizontal plane. Assume that the source is in the far field (Fraunhofer region) of the antenna. A definition of the far-field region for a horizontal antenna in a waveguide can be found in [10].

Directional characteristics of hydroacoustic antennas in a homogeneous unbounded medium (free space) are studied in sufficient detail [11, 12]. It seems reasonable to evaluate the directional properties of the same antennas operating in a waveguide in terms of similar characteristics but with an allowance made for specific features of the waveguide propagation. Therefore, we define the antenna response in a waveguide as the output signal intensity, normalized by its maximum, versus the angle $\alpha$ between the source direction and the normal to the antenna in the horizontal plane and the compensation angle $\beta$ [13–16]:

$$B(\alpha, \beta) = \frac{u_a u_a^*}{\max\{u_a u_a^*\}}, \tag{1}$$

$$u_a u_a^* = \sum_{l=1}^{m}\sum_{q=1}^{m} D_l(\alpha, \beta) D_q(\alpha, \beta) \exp[j(\xi_l - \xi_q)R]$$

$$= \sum_{l=1}^{m} D_l^2(\alpha, \beta) \tag{2}$$

$$+ 2\sum_{l=1}^{m-1}\sum_{q=l+1}^{m} D_l(\alpha, \beta) D_q(\alpha, \beta) \cos[(\xi_l - \xi_q)R],$$

$$D_l(\alpha, \beta)$$

$$= A_l(\xi_l, b_l, Z_0, Z) \frac{\sin\left[\frac{L}{2}(\xi_l \sin\alpha - k\sin\beta)\right]}{\frac{L}{2}(\xi_l \sin\alpha - k\sin\beta)}. \tag{3}$$

Here, the quantity $D_l(\alpha, \beta)$ is the response of the antenna to the first normal wave alone, and $B(\alpha, \beta)$ is the superposition of individual responses to each of the rest of the normal waves, when considered in the horizontal plane. At a certain fixed $\beta$, $B(\alpha)$ is the directional pattern of the antenna in the horizontal plane, and $B(\beta)$ at a certain fixed $\alpha$ is the scanogram of the horizontal linear antenna in the waveguide. These functions are analogs of the antenna pattern and scanogram in free space; $u_a$ is the signal at the antenna output; $m$ is the number of normal waves, which propagate in the waveguide without attenuation; $\xi_l$ and $b_l$ are the horizontal and vertical components of the wave vector $k$ of the first normal wave; $Z_0$ and $Z$ are the transmission and reception depths, respectively; $R$ is the horizontal distance between the source and the antenna center; and $A_l$ characterizes the intensity of the $l$th normal wave. The compensator introduces linear phase delays in each

receiving channel of the antenna in accordance with the phase velocity $C$ of sound in water ($k = \omega/C$ is the wave number and $\omega$ is the circular frequency).

The first term on the right-hand side of expression (2) (single sum) is a superposition of responses to individual normal waves without taking into account phases, i.e., a sum of their powers (the power-related part of the response $B_p$). The second term on the right-hand side of expression (2) (double sum) characterizes the interference between normal waves with different indices at the antenna aperture (the interference-related part of the response). The antenna response $B(\alpha, \beta)$ in a waveguide for different parameters of the problem was studied in [13–16]. The attention was focused mostly at the low-frequency region, in which a small number of normal waves (a few or few tens) propagate in the waveguide, and at long linear antennas whose length may be greater (sometimes considerably) than the sea depth. Below, we analyze a distribution of the power-related part of the response of an antenna whose aperture is comparable to or smaller (or even much smaller) than the waveguide depth. The waveguide may allow the propagation of a great number (hundreds) of normal waves, so that the geometrical acoustics approximation becomes valid. Our calculations are performed for a waveguide of uniform sound velocity with a soft surface and rigid bottom, with $A_l = \cos(b_l Z_0)\cos(b_l Z)/\sqrt{\xi_l}$.

According to Eqs. (1)–(3), the parameters that determine the response of the antenna include the number of normal waves propagating in the waveguide. While, in free space, a decrease in the wavelength $\lambda$ (an increase in the frequency $\omega$) increases the antenna dimension in terms of the wavelength, $L/\lambda$ in the waveguide. Simultaneously, the ratio $H/\lambda$ increases and, therefore, the number $m$ of propagating waves also increases. This situation must be taken into account when interpreting the results presented below.

As is known, the directional pattern of a continuous linear antenna in free space has the form of one main lobe and a number of small side lobes, which move along the axis of angles $\alpha$ when the compensation angle $\beta$ is varied [11, 12]. A similar behavior is observed in the scanogram, but the lobes move along the axis of angles $\beta$ when the angle $\alpha$ is varied. It has been shown [13–16] that, when the antenna is placed in the waveguide horizontally, its pattern or scanogram retains one main lobe only when $\beta = 0°$ or $\alpha = 0°$, respectively. Otherwise ($\beta > 0°$ or $\alpha > 0°$), the energy is distributed in the response over a wide angular range from 0° to 90°. (A symmetric situation observed in the angular range from 90° to 180° is not considered here.) While the interference-related part of the response is oscillatory and these oscillations are random, the power-related part of the response is smooth and has a specific shape. The number of oscillations increases with the number of normal waves.

Our further discussion will be illustrated by calculations performed for particular examples. Figure 1

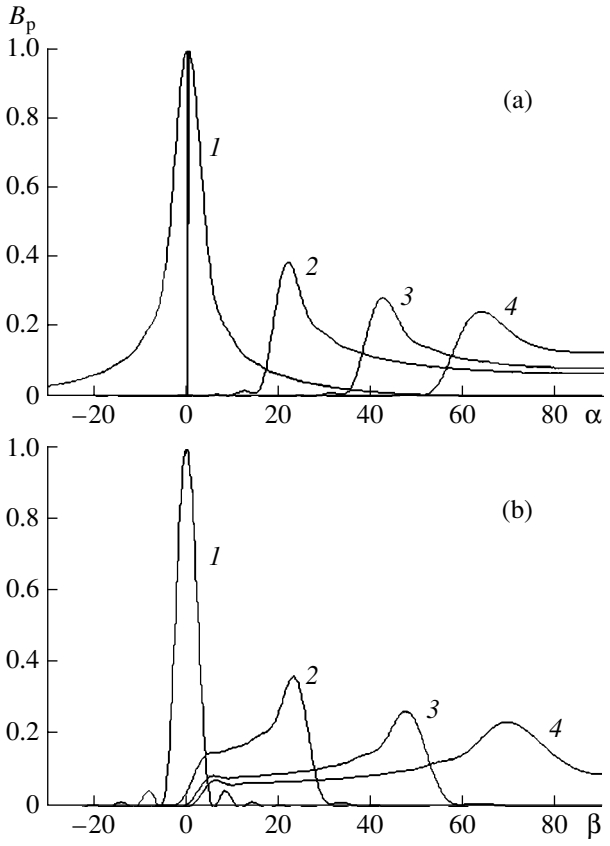


**Fig. 1.** (a) Patterns and (b) scanograms for different angles (a) $\beta_c$ = (*1*) 0°, (*2*) 20°, (*3*) 40°, and (*4*) 60° and (b) $\alpha_s$ = (*1*) 0°, (*2*) 25°, (*3*) 50°, and (*4*) 75° at $H = 50\lambda$, $m = 100$, $L = 10\lambda$, and $Z_0 = Z = 0$.

shows the power-related part of the response of a horizontal linear antenna with an aperture $L = 10\lambda$ in a waveguide with a depth of $H = 50\lambda$ at different compensation angles $\beta_c$ (patterns, Fig. 1a) and directions to the source characterized by the angle $\alpha_s$ (scanograms, Fig. 1b). In this waveguide, $m = 100$ normal waves can propagate without attenuation. Here and below, the source and the antenna reside on the bottom: $Z_0 = Z = 0$. All curves in each of these figures are normalized by the same maximum value. Figures 1a and 1b show that, as we noted above, it is only at $\beta_c = 0°$ or $\alpha_s = 0°$ that the response curve has the form of one symmetric main lobe whose amplitude is greater than the amplitudes of all the other curves. With an increase in the compensation angle $\beta_c$ (Fig. 1a) or the angle $\alpha_s$, which characterizes the direction to the source (Fig. 1b), the curves of the power-related part of the response acquire a flat shape in their central part with a smooth plateau on their left-hand side at $\alpha = \beta_c$ for patterns (Fig. 1a) or right-hand side at $\beta = \alpha_s$ for scanograms (Fig. 1b). For the above parameters, these maxima are approximately three times lower than the maximum of the response at $\beta_c = 0°$ or $\alpha_s = 0°$.

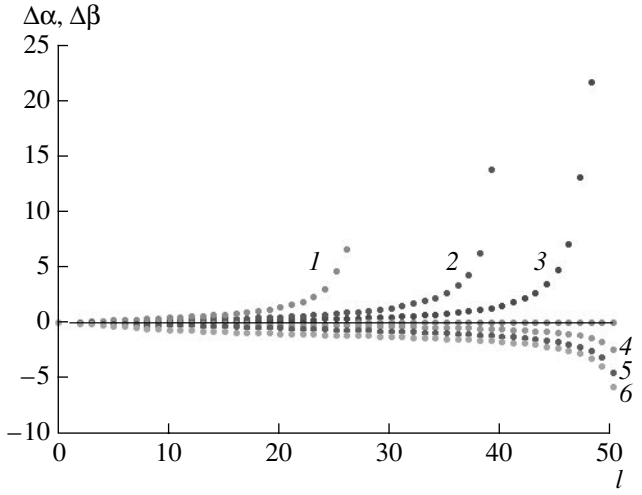


**Fig. 2.** Differences (*1–3*) Δα and (*4–6*) Δβ versus the normal wave index $l$ for $\beta_c$ = (*1*) 20°, (*2*) 40°, and (*3*) 60° and $\alpha_s$ = (*4*) 25°, (*5*) 50°, and (*6*) 75°.

According to (1)–(3), the power-related part of the response is a sum of the responses $D_l$ to individual normal waves shifted in the axis of angles α to the right at $\beta_c \neq 0°$ (Fig. 1a) or in the axis of angles β to the left at $\alpha_s \neq 0°$ (Fig. 1b). The shift of the response $D_l$ increases with the index of the normal wave in a nonlinear manner. This is illustrated in Fig. 2, which shows the differences $\Delta\alpha = \alpha^l_{\max} - \alpha^{l-1}_{\max}$ (curves *1–3*) and $\Delta\beta = \beta^l_{\max} - \beta^{l-1}_{\max}$ (curves *4–6*) versus the index of normal wave $l$ = 2–100. The angles $\alpha^l_{\max}$ and $\beta^l_{\max}$ are the angular positions of the maxima of the responses to the $l$th normal waves. As can be seen from the figure, the rate at which these differences increase with the index of the normal wave $l$ is small for normal waves with small indices, which gives rise to the maxima in the curves in Figs. 1a and 1b. The rate at which the differences increase is more or less constant for medium normal wave indices, which provides a relatively constant level of response within the rest of the range.

We should emphasize the following feature of the curve obtained for the power-related part of the response of the antenna operated in the waveguide. If the dimension $L/\lambda$ of the antenna is comparable to or less than the depth $H/\lambda$ of the waveguide, the shape of the curve remains almost unchanged with an increase in $H/\lambda$ or, which is the same, with an increase in number $m$ of normal waves propagating in the waveguide if other parameters ($L/\lambda$, $Z_0$, $Z$, and angles $\beta_c$ for patterns or $\alpha_s$ for scanograms) are constant. Figure 3 shows the power-related part of the pattern (Fig. 3a) and scanogram (Fig. 3b) for the antenna with an aperture of $L = 10\lambda$ in waveguides with depths of $H = 10\lambda$, $50\lambda$, $100\lambda$, and $250\lambda$ ($m$ = 20, 100, 200, and 500) at $\beta_c = 20°$ and $\alpha_s = 60°$. Each curve is normalized by its maximum value. The curves for $H = 50\lambda$, $100\lambda$, and $250\lambda$ coincide

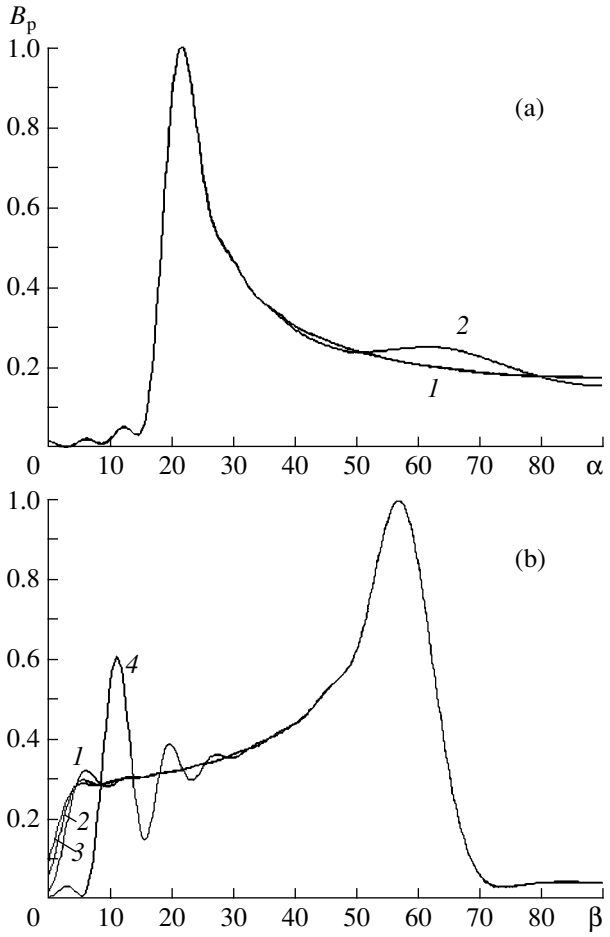


**Fig. 3.** (a) Patterns and (b) scanograms for different numbers of waves propagating in the waveguide at $L = 10\lambda$ and $Z_0 = Z = 0$: (a) $\beta_c = 20°$ and $m$ = (*1*) 100, 200, and 500 and (*2*) 20 and (b) $\alpha_s = 60°$ and $m$ = (*1*) 100, (*2*) 200, (*3*) 500, and (*4*) 20.

for patterns (curve *1* in Fig. 3a) and actually coincide in their main part for scanograms (curves *1–3* in Fig. 3b). The latter curves differ insignificantly in their left part. A minor difference in the right-hand parts of the patterns (curve *2* in Fig. 3a) and a noticeable difference in the left-hand parts of the scanograms (curve *4* in Fig. 3b) are observed at $H = 10\lambda$ and $m = 20$. In this case, the antenna aperture $L/\lambda$ is equal to the waveguide depth $H/\lambda$.

If the aperture size $L/\lambda$ is comparable to or greater than the waveguide depth $H/\lambda$, under certain conditions (large angles $\beta_c$ for the pattern or $\alpha_s$ for the scanogram), part or all of the normal waves can be separated in the form of clear-cut maxima in the curve of the antenna response as a whole and in the curve of its power-related part as well [13–16]. The height of these maxima and their angular positions can be used to calculate the parameters of these normal waves. If the antenna aperture is comparable to or smaller than the waveguide depth, a small number of normal waves, if any, can separate. Figure 3 illustrates this very case, when one or two normal waves become separated.

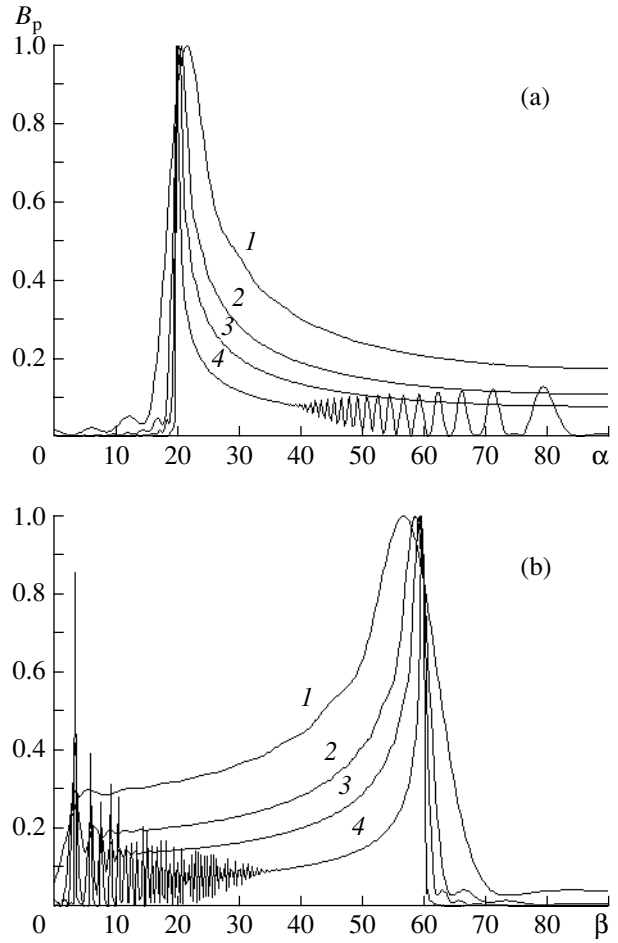


**Fig. 4.** (a) Patterns and (b) scanograms for different antenna apertures at $H = 100\lambda$, $m = 200$, $Z_0 = Z = 0$, and $L = (1)\ 10\lambda$, $(2)\ 25\lambda$, $(3)\ 50\lambda$, and $(4)\ 200\lambda$; (a) $\beta_c = 20°$ and (b) $\alpha_s = 60°$.

Now, let us consider the effect of the aperture length on the behavior of the energy-related part of the response, the remaining parameters of the problem being unchanged. Figure 4 shows the energy-related part of the pattern (Fig. 4a) and scanogram (Fig. 4b) for antennas with apertures $L = 10\lambda$, $25\lambda$, $50\lambda$, and $200\lambda$ (curves *1–4* in Figs. 4a and 4b) operating in a waveguide of depth $H = 100\lambda$ at $m = 200$, $\beta_c = 20°$, and $\alpha_s = 60°$. Each curve is normalized by its maximum value. As can be seen from the figure, an increase in the aperture length narrows the maximum on the left-hand side of the pattern and on the right-hand side of the scanogram and also lowers their central plateau-shaped parts. If the antenna aperture is larger than the waveguide depth, individual maxima appear in the patterns and scanograms (curves *4* in Figs. 4a and 4b), which are associated with normal waves with the greatest indices; in the case under study, the antenna aperture $L = 200\lambda$ is twice as large as the waveguide depth $H = 100\lambda$. As was noted above, these waves are separated from the curves.

Thus, at low frequencies as well as at high frequencies, when a few (tens) or hundreds of normal waves, respectively, propagate in the waveguide, the energy in the antenna response appears to be distributed in the general case (at nonzero angles $\beta_c$ and $\alpha_s$) over a wide range of angles $\alpha$ (pattern) and $\beta$ (scanogram). This fact degrades the directional characteristics of the antenna operated in the waveguide (decreases its concentration factor and reduces its noise immunity) and makes it more difficult to determine the exact direction of the source. To solve these and a number of other problems of applied hydroacoustics, a usual compensator, which introduces a linear phase delay into each receiving channel, proves to be inefficient, so that a special processing of the signal over the antenna aperture is necessary.

The use of a waveguide model with a lossy impedance bottom instead of an ideal waveguide leads to the attenuation of normal waves with large indices and a change in the behavior of the response curve. Its plateau-shaped part becomes shorter on the right (for patterns) or left (for scanograms), the effect being stronger the higher the attenuation of the normal waves is. It should also be noted that, if various averaging procedures (over space or time) or the power summation of normal waves are used, it is necessary to perform a comparative analysis of the results obtained.

## REFERENCES

1. M. R. Dungan and D. R. Dowling, J. Acoust. Soc. Am. **112**, 1842 (2002).
2. L. M. Brekhovskikh, Akust. Zh. **10**, 114 (1964) [Sov. Phys. Acoust. **10**, 89 (1964)].
3. L. M. Brekhovskikh, Akust. Zh. **11**, 148 (1965) [Sov. Phys. Acoust. **11**, 126 (1965)].
4. D. E. Weston, J. Acoust. Soc. Am. **68**, 282 (1980).
5. D. I. Abrosimov, Akust. Zh. **29**, 309 (1983) [Sov. Phys. Acoust. **29**, 181 (1983)].
6. M. S. Vinogradov and V. A. Eliseevnin, Akust. Zh. **38**, 855 (1992) [Sov. Phys. Acoust. **38**, 467 (1992)].
7. Yu. A. Kravtsov and V. M. Kuz'kin, Akust. Zh. **33**, 261 (1987) [Sov. Phys. Acoust. **33**, 156 (1987)].
8. V. M. Kuz'kin and T. A. Frolova, Akust. Zh. **34**, 891 (1988) [Sov. Phys. Acoust. **34**, 515 (1988)].
9. L. M. Brekhovskikh, *Waves in Layered Media* (Nauka, Moscow, 1973; Academic, New York, 1980).
10. V. A. Eliseevnin, Akust. Zh. **39**, 172 (1993) [Acoust. Phys. **39**, 88 (1993)].
11. M. D. Smaryshev, *Directivity of Hydroacoustic Antennas* (Sudostroenie, Leningrad, 1973).
12. M. D. Smaryshev and Yu. Yu. Dobrovol'skiĭ, *Hydroacoustic Antennas* (Sudostroenie, Leningrad, 1984).
13. V. A. Eliseevnin, Akust. Zh. **25**, 227 (1979) [Sov. Phys. Acoust. **25**, 123 (1979)].
14. V. A. Eliseevnin, Akust. Zh. **29**, 44 (1983) [Sov. Phys. Acoust. **29**, 25 (1983)].
15. V. A. Eliseevnin, Akust. Zh. **35**, 468 (1989) [Sov. Phys. Acoust. **35**, 274 (1989)].
16. V. A. Eliseevnin, Akust. Zh. **42**, 208 (1996) [Acoust. Phys. **42**, 182 (1996)].

*Translated by A. Khzmalyan*

*Acoustical Physics, Vol. 50, No. 2, 2004, pp. 158–162. Translated from Akusticheskiĭ Zhurnal, Vol. 50, No. 2, 2004, pp. 198–203.*


# Imaging with Acoustic Antenna Array through a Thick Layer of Large-Scale Inhomogeneities

**V. A. Zverev**

*Institute of Applied Physics, Russian Academy of Sciences, ul. Ul'yanova 46, Nizhni Novgorod, 603600 Russia*
*e-mail: zverev@hydro.appl.sci-nnov.ru*

Received August 28, 2002

**Abstract**—The problem of determining the positions and levels of signals by an array in a thick layer of large-scale inhomogeneities is considered. The problem is solved in two steps. At the first step, the method of wave front inversion is used to find the fractions of the spatial spectra at which one of the signals predominates. At the second step, within each spectral fraction, the signal is processed by using both the method [5] of taking the logarithms of complex functions with a subsequent filtering and the method of parameter estimation. The results of numerical modeling are presented. © *2004 MAIK "Nauka/Interperiodica".*

Media in which one can acoustically locate an object in the absence of inhomogeneities can be in practice so inhomogeneous that classical acoustic imaging proves to be unfeasible. Inhomogeneities in solids, and sometimes in liquids (in the absence of currents and within the time of a two-way sound propagation), are stationary to an extent that allows one to use the method of wave front inversion (WFI) to suppress the effects of inhomogeneities [1]. In [2], the WFI method was used to exclude the influence of strong inhomogeneities occupying a thin layer. The method used in [2] has two significant limitations. First, it cannot be used when the inhomogeneous layer is so thick that the signals from the objects corresponding to different angles relative to the array (and to the layer) have different distortions. Second, this method allows one to determine the positions and strengths of objects in a relative form, with respect to the strongest object: the coordinate and the level of this strongest object remain unknown.

In further studies, both the aforementioned limitations of the method used in [2] were overcome. The objective of the present study is to show that one can determine the positions and levels of all objects when the inhomogeneous layer is rather thick, so that each object to be located undergoes its own distortions. The problem was solved by imposing an additional restriction on the properties of the inhomogeneities, namely, the inhomogeneities should be large-scale ones. The method described in [2] is free of such a restriction. Here, we assume that only the inhomogeneities themselves should be large-scale. This restriction does not refer to the phase distribution over the antenna array under the influence of the inhomogeneities: the phase distribution can have a broad spatial spectrum resulting in strong interference.

There are also two restrictions on the shape and positions of the objects for the WFI method to be feasible [1]. The objects to be located must reradiate a spherical wave in response to a wave of arbitrary shape incident on it. In addition, the objects should be arranged in space so that they can be reliably separated from each other by the same array in a homogeneous medium.

The problem is solved in two steps. At the first step, the WFI method is used to separate signals from different objects. First, the strongest signal is separated by multiply repeated wave front inversion [1]. This strongest signal is fixed. Then, at the array, a signal is formed that makes the strongest signal equal to zero or close to zero. Now, by repeating the WFI procedure, one separates the next strongest signal from the remaining ones. This signal is fixed again, and a signal is emitted that suppresses almost to zero the signal scattered by the second object. The procedure lasts until all signals of interest are found. At the second step, each of the detected signals is separately processed to specify the angle at which the object is located and the level of the signal scattered by it. The latter can be accomplished in two different ways: by the procedure of parameter estimation [3, 4] or by filtering. In this work, both methods are used.

Filtering is performed by the method that was proposed and put into practice in [5]. Before filtering, the signal phase is extracted without the $2\pi$-periodic jumps. For this purpose, the logarithm of the complex signal is taken [6]. As a result, the spectra of the signal and interfering noise prove to be separated, just as in the cepstral analysis [5, 7]. After that, the noise is filtered out and one obtains a pure signal whose parameters (the angular position and level) are to be determined.

Let us consider an example to show how the signal parameters can be determined by using an extended array in a thick inhomogeneous layer.

Consider a linear array that consists of $L$ receiving (and transmitting) elements spaced at $\lambda/2$, where $\lambda$ is

1063-7710/04/5002-0158$26.00 

the wavelength. The array is placed into a stationary inhomogeneous medium. The transmitted and received signals are pulses with a monochromatic carrier and a duration sufficient for the signals to be treated as monochromatic. The signal received by the array can be written as

$$S(k) = \sum_n A_n(k)\exp(iF_n(k)). \quad (1)$$

Here, $A_n(k)$ represents the signals received by the array in the medium without inhomogeneities and $F_n(k)$ represents the phase changes caused by the medium. These changes are supposed to be much greater than $\pi$. Let us assume that the signal sources are in the far field of the array, where the signals received by the array in the homogeneous medium can be represented as plane waves [8]:

$$A_n(k) = W_n\exp\left(i\frac{2\pi}{L}kU_n\right). \quad (2)$$

Here, $W_n$ is the wave amplitude and $U_n$ is the spatial frequency. The angle $\theta_n$ corresponding to the wave can be determined as [8]

$$\arcsin(\theta_n) = \frac{\lambda}{L}U_n. \quad (3)$$

In our example, we consider the case of three signals whose parameters are summarized in the table.

The signal levels are specified in advance to differ substantially in their values; otherwise too many WFI repetitions would be required in the numerical simulation. The array consists of 1024 receiving elements spaced at $0.5\lambda$.

According to the WFI procedure [1], the observations begin with the emitting of a pulse from one element of the array. This pulse undergoes strong distortions in propagating through the medium. However, in spite of the distortions, each object reradiates a spherical wave [1]. These waves, propagating through the inhomogeneous medium again, reach the array to form the field of the form given by Eq. (1). The distortions of the wave field are so strong that the signal processing used in the homogeneous medium (Fourier spectral analysis of the array signal) leads to the result shown in Fig. 1a. The Fourier spectrum of the array signal can be represented in the form

$$P1(u) = W_1 ua(u) + W_2 ub(u) + W_3 uc(u), \quad (4)$$

where

$$ua(u) = \Phi\left[\frac{A_1(k)}{W_1}\exp(iF_1(k))\right], \quad (5)$$

$$ub(u) = \Phi\left[\frac{A_2(k)}{W_2}\exp(iF_2(k))\right], \quad (6)$$

$$uc(u) = \Phi\left[\frac{A_3(k)}{W_3}\exp(iF_3(k))\right]. \quad (7)$$

Here, $\Phi$ denotes the Fourier transform of the square-bracketed function.

Figure 1a shows the modulus of the spatial spectrum for the signal received by the array, as given by Eqs. (5), (6), and (7). Figure 2a presents the result of such a signal processing for the homogeneous medium. This figure shows the levels of all three signals and their positions on the axis of spatial frequencies. These quantities, in turn, determine the signal amplitude values $U_n$ related by Eq. (3) to the angles $\theta_n$, at which the objects are observed. In the homogeneous medium, no additional processing is required.

However, from Fig. 1a, which is all we have at our disposal, no pattern characterizing the position of the objects is apparent. To extract such information, one needs to perform additional signal processing. At the first stage, this processing procedure consists in separating the signals from different scattering objects. First, we separate the strongest signal from all other signals. To do so, we fix the field at the array and then transmit a complex-conjugate signal with the opposite sign of time from the same array. As a result, the array will emit the WFI signal. Upon propagating through the same inhomogeneities, this signal will take the form of a spherical wave in the vicinity of the object. The amplitude of this wave will correspond to the value of $W_n$ for each given object. Being scattered by an object, the wave acquires an additional factor $W_n$.

For the received wave that was emitted as the WFI one, the spatial spectrum at the array takes the form

$$P2(u) = W_1^2 ua(u) + W_2^2 ub(u) + W_3^2 uc(u). \quad (8)$$

As a result, the first signal becomes much greater than the other signals. This result is illustrated by Fig. 1b. For free space, the same procedure yields Fig. 2b.

Now the signal that is next in amplitude should be separated. To do so, one should exclude the first signal. This is accomplished by emitting the following WFI signal:

$$PA(k) = P1(k)\mathrm{NA} - P2(k), \quad (9)$$

where NA is a factor fitted to minimize the signal scattered by the first located object.

To select the value of NA, one should use signals that are received by the array after transmitting the sig-

**Table**

| $n$ | 1 | 2 | 3 |
|---|---|---|---|
| $W_n$ | 6 | 2 | 0.5 |
| $U_n$ | 50 | 150 | 250 |

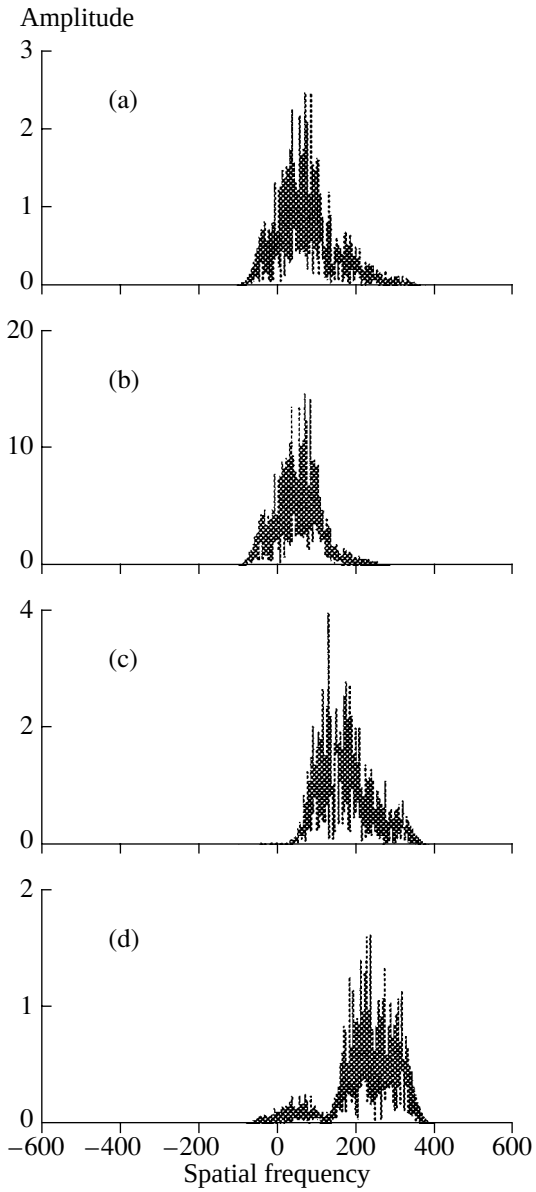


**Fig. 1.** Angular spectra of signals (a) before and (b–d) after their separation by the WFI method.

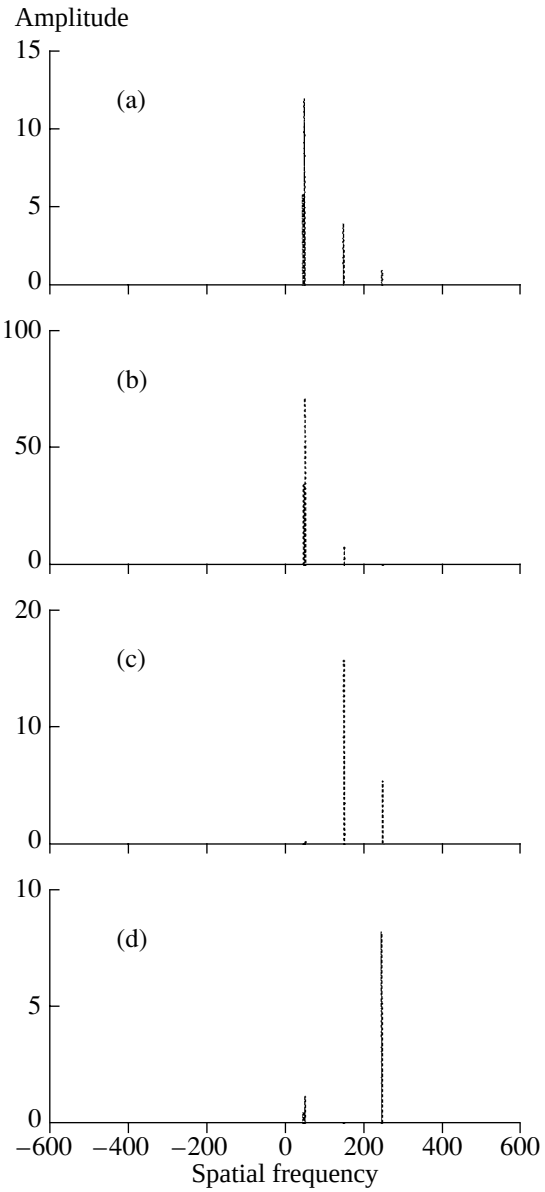


**Fig. 2.** Angular spectra of signals in free space (a) before and (b–d) after their separation by the WFI method.

nals of form (9) with different values of NA. Actually, by substituting Eqs. (4) and (8) into Eq. (9), we obtain:

$$\begin{aligned} P4(u) &= (W_1\mathrm{NA} - W_1^2)ua(u)W_1 \\ &+ (W_2\mathrm{NA} - W_2^2)ub(u)W_2 \\ &+ (W_3\mathrm{NA} - W_3^2)uc(u)W_3. \end{aligned} \tag{10}$$

From Eq. (10) it follows that the signal scattered by the first strongest object becomes equal to zero when

$$\mathrm{NA} = W_1. \tag{11}$$

However, one cannot directly use condition (11), because the level of the first signal is unknown. Then, one can make use of the fact that the excluded signal is the strongest one, and its absence should substantially change the level of signal (10), which is available for observation. The minimum must occur in the signal at the array but not in its spectrum. Therefore, one should search for the minimum in the inverse Fourier transform of Eq. (10). The value NA = 5.975 corresponds to the minimum of the integral of the squared inverse Fourier transform of Eq. (10). By comparing this value with the value $W_1 = 6$ presented in the table, we arrive at the conclusion that the estimate is biased. In further processing, this estimate can be refined. Signal (10) with the value NA = 5.975 substituted into it can be treated as the second selected signal. This signal should be recorded. The modulus of the spatial spectrum of this signal is shown in Fig. 1c. The corresponding spectrum

in free space is presented in Fig. 2c. One can see from Fig. 2c that the second signal is actually the maximal one in the case at hand.

By repeating the procedure described above, we eliminate the second signal. For this purpose, we emit a signal constructed by analogy with Eq. (9):

$$PB(k) = PA(k)\mathrm{NB} - P4(k). \quad (12)$$

Here, $PA(k)$ is determined by Eq. (9) with NA being replaced by its value determined above, and the term $P4(k)$ represents the inverse Fourier transform of Eq. (10) with NA being replaced by the aforementioned value. Let us omit here the full lengthy expression for the received signal. We rather mention the fact that the coefficient of $ua(u)$ contains the factor $\mathrm{NA} - W_1$ and consider the coefficient $ub(u)$ of the signal second in intensity:

$$Kb = (W_2\mathrm{NA} - W_2^2)(\mathrm{NB} - W_2). \quad (13)$$

From Eq. (13) it follows that the second signal becomes equal to zero when

$$\mathrm{NB} = W_2. \quad (14)$$

Since the value of $W_2$ is unknown, condition (14) can be determined by minimizing the result of WFI for signal (12) by varying the value of NB. In this way, we arrive at a value of NB = 1.993. Figure 1d shows the modulus of the spatial spectrum of this signal for the inhomogeneous medium, and Fig. 2d, for the homogeneous medium. In Figs. 1d and 2d, one can see traces of the first signal. These traces are the consequence of the fact that the value of NA was determined with an error. The error can be substantially decreased by varying the value of NA so as to minimize the traces of the first signal in Fig. 1d. I performed such a procedure. As a result, the value NA = 6 was obtained to an accuracy of $10^{-4}$.

At the second stage of the processing procedure, pure signals are extracted from the medium-caused interference by way of sequential elimination of the strongest signals. In the case at hand, the technique described in [5, 9] was used. This technique for signal extraction is based on the fact that only one monochromatic signal in the form of one summand of Eq. (1) is known to be present. By taking the logarithm of this expression without the $2\pi$-periodic phase jumps, according to [6], we obtain the pure expression for the signal phase with a minimal spectrum width. To separate the spectra of signal and noise, we use the method that is considered in detail in [5]. Prior to extracting the signal phase free of the $2\pi$-periodic jumps, the signal is multiplied by the factor

$$M(k) = \exp\left(i\frac{2\pi}{L}kQ_n\right) + 0.5. \quad (15)$$

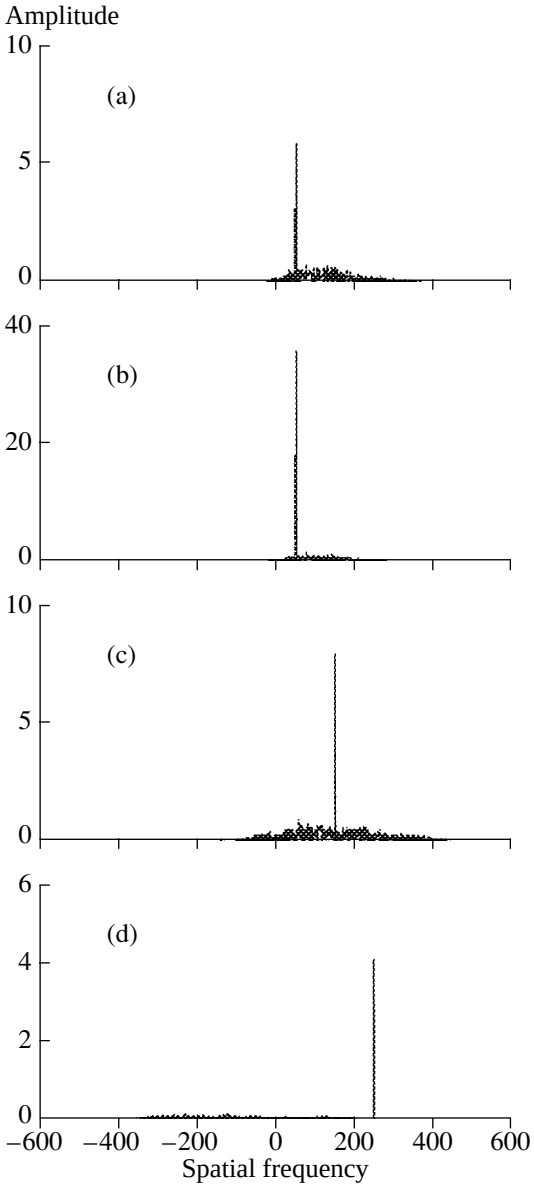


**Fig. 3.** Angular spectra of signals filtered out by taking the complex logarithm (a) before and (b–d) after the separation of signals by the WFI method.

The value of $Q_n$ is selected in view of the condition of minimal spectral width for the product of factor $M(k)$ with the signal extracted by the WFI procedure.

The fitting of $U_n$ is performed by multiplying the signal that was obtained using the WFI by factor (15) (without adding the term 0.5 to the exponential). Varying the quantity $Q_n$, one can obtain a minimal variance of the extracted phase. Figure 4 shows the resulting dependences of the phase variance on the value of $Q_n$. In separating the signals of individual objects, the values NA = 5.975 and NB = 1.993, obtained experimentally, were used. The minimal values of the phase variances in Figs. 4a and 4c coincide with the specified val-

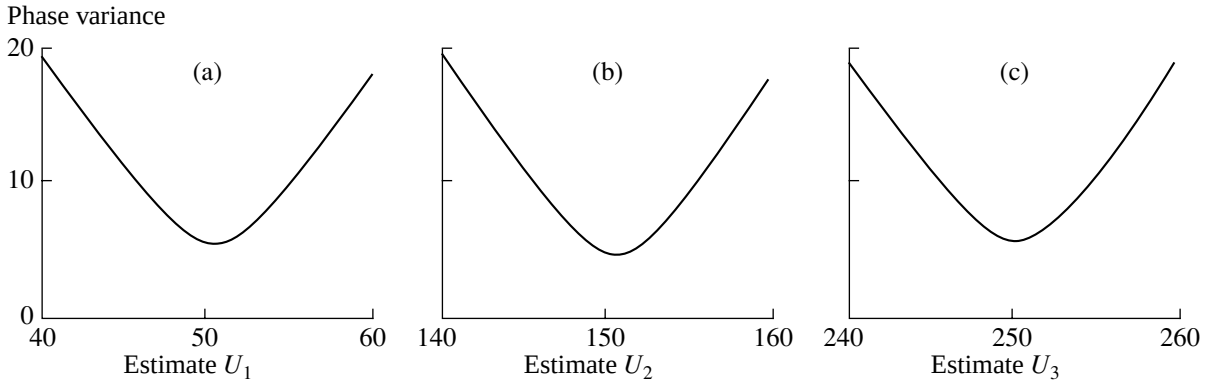


**Fig. 4.** Estimations of the spatial frequencies (angles) of the objects by minimizing the phase variance. Estimates for the (a) first, (b) second, and (c) third signals.

ues of spatial frequencies. The minimal value in Fig. 4b is 151 instead of the specified value of 150. The difference corresponds to a single element of the array resolution. This difference is caused by the interfering noise, which was not suppressed in this processing procedure.

Note that the estimates obtained are quite sufficient to determine the coordinates of the objects, and one can do so without filtering to separate the signals. Such a procedure of determining the signal parameters without filtering admits a broader band of spatial frequencies of the inhomogeneities, compared to the method with filtering.

The results obtained by filtering the signals are presented in Fig. 3. This figure illustrates both the positions of the signals on the frequency axis and their amplitudes. Let us make use of these data to determine the level of the third weakest signal, whose parameters remain unknown. According to Eq. (12), the amplitude of the third signal *Kc* (in Fig. 3d) must have the following value:

$$Kc = \mathrm{NB}W_3(\mathrm{NA} - W_3) - W_3(W_3\mathrm{NA} - W_3^2). \quad (16)$$

To obtain the estimate from Eq. (16), one should solve the cubic equation. We proceeded in another way. If we substitute all true values from the table into Eq. (16), we obtain the value $Kc = 4.087$. In Fig. 3d, the corresponding value of the signal amplitude is 4.086. The closeness of these values confirms that the estimate of the signal level obtained from Fig. 3d is close to the true value.

The method of signal separation with the use of WFI can be also applied to a focusing array. However, the method of filtering is not applicable in this case, and the estimation procedure has some specific features. Such a situation will be analyzed in a next paper.

## ACKNOWLEDGMENTS

This work was supported by the Russian Foundation for Basic Research (project no. 02-02-17036) and the Ministry of Industry and Science of Russian Federation (project no. NSh-1644.2003.2).

## REFERENCES

1. M. Fink, D. Cassereau, A. Derode, *et al.*, Rep. Prog. Phys. **63**, 1933 (2000).
2. V. A. Zverev, Akust. Zh. **50**, 158 (2004) [Acoust. Phys. **50**, 52 (2004)].
3. Y. Bard, *Nonlinear Parameter Estimation* (Academic, New York, 1974; Mir, Moscow, 1979).
4. V. A. Zverev, Akust. Zh. **46**, 796 (2000) [Acoust. Phys. **46**, 676 (2000)].
5. V. A. Zverev and A. A. Pavlenko, Akust. Zh. **47**, 355 (2001) [Acoust. Phys. **47**, 297 (2001)].
6. V. A. Zverev and A. A. Pavlenko, Izv. Vyssh. Uchebn. Zaved., Radiofiz. **43** (7), 652 (2000).
7. A. V. Oppenheim, R. W. Schafer, and T. G. Stockham, IEEE Trans. Audio Electroacoust. **16** (3), 437 (1968).
8. V. A. Zverev, *Physical Foundations of Imaging by Wave Fields* (Inst. Prikl. Fiz., Ross. Akad. Nauk, Nizhni Novgorod, 1998).
9. V. A. Zverev and A. A. Stromkov, *Signal Extraction from Noise by Numerical Methods* (Inst. Prikl. Fiz., Ross. Akad. Nauk, Nizhni Novgorod, 2001).

*Translated by E. Kopyl*

*Acoustical Physics, Vol. 50, No. 2, 2004, pp. 163–168. Translated from Akusticheskiĭ Zhurnal, Vol. 50, No. 2, 2004, pp. 204–209.*


# Controlled Excitation of Resonance Self-Oscillations in One-Dimensional Distributed Systems

**M. Ya. Izrailovich**

*Blagonravov Institute of Mechanical Engineering, Russian Academy of Sciences, Malyi Khariton'evskii per. 4, Moscow, 101990 Russia*

*e-mail: vibris@interface.ru*

Received February 5, 2003

**Abstract**—On the basis of the method of equivalent linearization combined with the method of moments, laws of self-oscillation excitation are obtained that provide the modes with maximum intensity of resonance (or quasi-resonance) oscillations in one-dimensional systems with distributed parameters. A restriction of a general type is imposed on the law of excitation. In the particular case of an integral quadratic restriction, the law of excitation leads to the generation of purely harmonic self-oscillations. The use of an extended (multiplicatively stabilizing) control provides the uniqueness and stability of the quasi-optimal mode of self-oscillation. © *2004 MAIK "Nauka/Interperiodica".*

This paper considers the problem of constructing the law of self-oscillation excitation in a one-dimensional linear system with distributed parameters. Such a problem is of interest, in particular, for designing ultrasonic machine systems. Below, the problem of synthesizing the law of excitation is solved with the use of methods of the optimum control theory. A restriction of a general type is imposed on the law of excitation $u$:

$$\left(\int_0^{2\pi/\omega} |u|^g dt\right)^{\frac{1}{g}} \le U_g,$$

where $U_g$ represents the limiting values of the excitation resource, $1 \le g < \infty$, and $\omega$ is the predefined frequency of self-oscillation. It is shown that a quadratic restriction ($g = 2$) imposed on the excitation law $u$ results in the generation of purely harmonic self-oscillations.

Problems of self-oscillation excitation in distributed systems are urgent for many fields of engineering. In particular, ultrasonic vibrations are widely used for ultrasonic treatment of different materials. The excitation and stabilization of the corresponding self-oscillation modes are among the principal issues in the design of machines for these purposes [1, 2]. By now, the methods of analyzing self-oscillatory systems are completely developed for systems with both lumped [3] and distributed [4] parameters. The most used scheme of designing self-oscillatory systems is based on presetting a possible structure of the excitation law and then analyzing the dynamics of the system [1, 2, 5].

As regards the development of regular methods for synthesizing self-oscillatory systems (SOS), only a few publications have been concerned with this problem. In monograph [6], which is the only Russian book entirely dedicated to this topic, such problems are completely solved in detail for objects belonging to a specific class by using the criterion of maximum speed of operation; the solutions are based on the Pontryagin maximum principle and on the analysis of phase trajectories. In paper [7], the problem of SOS synthesis is also solved for a specific object: a wind-driven powerplant. The cited paper [7] points out the urgency of using the methods of optimum control theory in solving the problems of SOS synthesis.

Since self-oscillatory systems usually operate in resonance or quasi-resonance modes, which means that the harmonic approximation is quite adequate for describing these modes of operation, the combination of the method of harmonic (equivalent) linearization with the methods of the optimum control theory (in particular, with the method of moments) should be the most efficient approach to the SOS synthesis. The corresponding procedures can be found in papers [8–10].

It is known that nonlinear systems, which include SOSs and, specifically, SOSs whose excitation laws were synthesized with the use of such procedures, are characterized by multiple periodic modes. For the problems of our concern, this means that some other modes can appear in addition to the designed optimum mode of maximum intensity and predefined frequency. Moreover, the designed (rated) mode may appear unstable. To eliminate the multiple mode feature and stabilize the rated mode, the principle of extended (multiplicatively stabilizing) control was proposed in [11, 12]. This principle consists in introducing an additional factor into the primarily synthesized excitation law, so that this factor ensures the feature of an artificial attractor whose degree of attraction to the rated limiting cycle can be as high as desired. On the basis of this principle, the law

1063-7710/04/5002-0163$26.00 © 2004 MAIK "Nauka/Interperiodica"

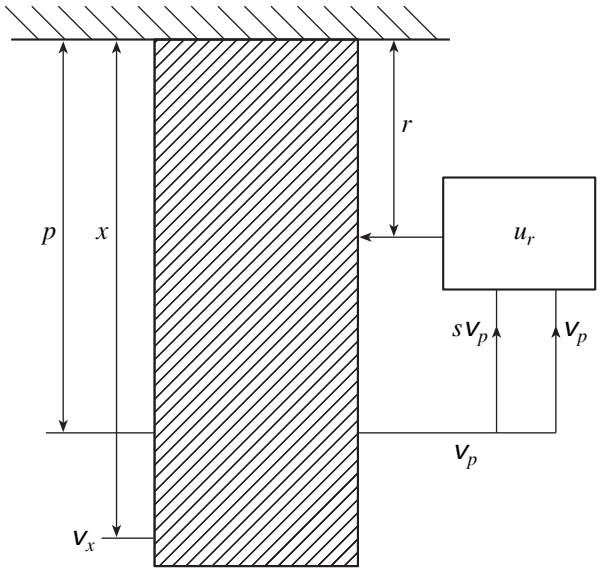


**Figure.**

of excitation of purely harmonic self-oscillations was synthesized for a system with a linear passive part [13].

The results of papers [8–13] refer to systems with finite numbers of degrees of freedom. The present paper extends them to one-dimensional distributed systems. In addition, unlike [8–13], this paper presents a general procedure for constructing an excitation source in the class of functions defined either in space $L^g(0; 2\pi/\omega)$, $1 \le g < \infty$ or in space $M(0; 2\pi/\omega)$.

Consider the one-dimensional distributed system (in this particular case, a bar system) shown in the figure. It is assumed that a force acts on the system at a point with coordinate $r$ and that this force is formed by the combination of a current displacement $v_p$ and displacement derivative $sv_p$ at a point with coordinate $p$. The excitation law of self-oscillations, $u_r^*(v_p, sv_p)$, should be synthesized so as to excite self-oscillations with maximum amplitude of the steady-state mode at a point with coordinate $x$.

Displacement $v_x$ at this point is related to the exciting force through the dynamic compliance operator:

$$v_x = L_{xr}(s)u_r, \tag{1}$$

where $L_{xr}(s)$ is a linear differential operator describing the response at a point in the section with coordinate $x$ to a force acting in the section with coordinate $r$. The function $u_r$ can be considered as an unknown function of quantities $v_x$ and $sv_x$.

Additionally, we assume that the specified angular frequency $\omega$ of self-oscillation excitation is close to (or coincides with) one of the natural frequencies of the system. Then, the total contribution of higher harmonics of steady-state oscillations excited in the distributed system is small. It should be noted that this assumption is equivalent to the existence of resonant (or filtering) properties in the system [14] and does not mean that higher harmonics $u_r$ are small in the general case.

Taking into account the above assumptions, we apply the procedure of harmonic linearization [14] to Eq. (1) to obtain

$$v_x = L_{xr}(s)\left(u_{r1} + \frac{s}{\omega}u_{r2}\right)v_x, \tag{2}$$

where $u_{r1}$ and $u_{r2}$ are the coefficients of harmonic linearization of the sought-for quantity $u_r$:

$$u_{r1} = \frac{1}{\pi A_x}\int_0^{2\pi} u_t \sin\psi d\psi, \quad u_{r2} = \frac{1}{\pi A_x}\int_0^{2\pi} u_r \cos\psi d\psi. \tag{3}$$

Here, $A_x$ is the amplitude of the harmonic component of steady-state oscillations at point $x$ and $\psi = \omega t$. Replacing operator $s$ in the characteristic equation corresponding to Eq. (2) by the product $j\omega$, which corresponds to the steady-state mode with frequency $\omega$, we obtain the equation in $u_{r1}$ and $u_{r2}$:

$$1 - L_{xr}(j\omega)(u_{r1} + u_{r2}) = 0. \tag{4}$$

Separating real and imaginary parts in Eq. (4), we obtain the system of two linear algebraic equations in $u_{r1}$ and $u_{r2}$:

$$L_{xr}u_{r1} - L_{xr2}u_{r2} = 1, \quad L_{xr2}u_{r1} + L_{xr1}u_{r2} = 0, \tag{5}$$

where $L_{xr1} = \mathrm{Re}L_{xr}(j\omega)$ and $L_{xr2} = \mathrm{Im}L_{xr}(j\omega)$. From Eqs. (5), we obtain

$$u_{r1} = \frac{L_{xr1}}{|L_{xr}|^2}, \quad u_{r2} = -\frac{L_{xr2}}{|L_{xr}|^2}, \tag{6}$$

where $|L_{xr}| = |L_{xr}(j\omega)|$.

Equations (3) and (6) determine the isoperimetric conditions (moment conditions) imposed on the sought-for function $u_r$:

$$\begin{aligned}\int_0^{2\pi} u_r \sin\psi d\psi &= \alpha_1(A, \omega),\\ \int_0^{2\pi} u_r \cos\psi d\psi &= \alpha_2(A, \omega),\end{aligned} \tag{7}$$

where $\alpha_1(A, \omega) = \pi A_x L_{xr1}/|L_{xr}|^2$ and $\alpha_2(A, \omega) = -\pi A_x L_{xr2}/|L_{xr}|^2$.

The restriction imposed on the excitation law is specified in the form

$$\left(\int_0^{2\pi/\omega} |u_r|^g dt\right)^{\frac{1}{g}} \le U_g, \quad 1 \le g < \infty. \tag{8}$$

Such a definition of the restriction covers different particular cases: for $g = 1$, we have a restriction on the

impulse of the exciting force; for $g = 2$, a restriction on the integral value; and for $g \longrightarrow \infty$, a restriction on the magnitude of the maximum value of $u_r$.

To determine the function $u_r^*$ that provides the maximum value of $A_x$ under restriction (8), we first consider the following auxiliary problem, which can be of interest by itself. Let $A_x$ be a given quantity and we seek a function $u_{0r}(\psi)$ satisfying conditions (7) and corresponding to the minimal intensity

$$J_g = \left(\int_0^{2\pi} |u_r|^g d\psi\right)^{\frac{1}{g}}. \tag{9}$$

In accordance with [15], the solution to this problem exists; it is unique and representable in the form

$$u_\gamma^0 = \frac{1}{l^q}\left|\varepsilon_1^0 \sin\psi + \varepsilon_2^0 \cos\psi\right|^{q-1} \times \operatorname{sgn}(\varepsilon_1^0 \sin\psi + \varepsilon_2^0 \cos\psi), \tag{10}$$

where $\frac{1}{q} + \frac{1}{g} = 1$; the numbers $\varepsilon_1^0$ and $\varepsilon_2^0$ are determined from the solution to the extremum problem

$$\min_{\varepsilon_1, \varepsilon_2}\left(\int_0^{2\pi} |\varepsilon_1 \sin\psi + \varepsilon_2 \cos\psi|^q d\psi\right)^{\frac{1}{q}} = \frac{1}{l} \tag{11}$$

under the condition that $\alpha_1\varepsilon_1 + \alpha_2\varepsilon_2 = 1$; and $l^{-1}$ is the minimum value of norm (9):

$$l^{-1} = J_g(u_r^0) = J_g^0.$$

After the transformation of the left-hand side of Eq. (11)

$$\min_{\varepsilon_1, \varepsilon_2}\sqrt{\varepsilon_1^2 + \varepsilon_2^2}\left[\int_0^{2\pi} |\sin(\psi + \psi_1)|^q d\psi\right]^{\frac{1}{q}} = \min_{\varepsilon_1, \varepsilon_2}\sqrt{\varepsilon_1^2 + \varepsilon_2^2} M_q, \tag{12}$$

where $M_q = \left[\int_0^{2\pi} |\sin(\psi + \psi_1)|^q d\psi\right]^{\frac{1}{q}} = \left(\int_0^{2\pi} |\sin\psi|^q d\psi\right)^{\frac{1}{q}}$ and $\psi_1 = \arg\cos\frac{\varepsilon_1}{\sqrt{\varepsilon_1^2 + \varepsilon_2^2}}$, the minimizing values of numbers $\varepsilon_1^0$ and $\varepsilon_2^0$ can be found by the formulas

$$\varepsilon_1^0 = \frac{\alpha_1}{\alpha_1^2 + \alpha_2^2}, \quad \varepsilon_2^0 = \frac{\alpha_2}{\alpha_1^2 + \alpha_2^2}. \tag{13}$$

From Eqs. (11)–(13) and expressions (7) for $\alpha_1$ and $\alpha_2$, one can determine the relationship between the amplitude $A_x$ and the minimum intensity of exciting action:

$$A_x = |L_{xr}|\frac{(M_q J_g^0)}{\pi}. \tag{14}$$

From Eq. (14) it follows that $A_x$ is a monotonically increasing function of intensity $J_g^0$. Therefore, the maximum value $A_x^*$ of amplitude $A_x$ is achieved at the limiting value of intensity specified by restriction (8):

$$A_x^* = \frac{|L_{xr}|}{\pi}\left(M_q \omega^{\frac{1}{g}} U_g\right). \tag{15}$$

From Eqs. (13) with $A_x = A_x^*$ determined by Eq. (15), we obtain $\varepsilon_1^* = \frac{L_{xr1}}{\pi A_x^*}$, $\varepsilon_2^* = -\frac{L_{xr2}}{\pi A_x^*}$.

Then, according to Eq. (10), we obtain that the excitation law corresponding to the value of $A_x$ is determined as the following function of $\psi$:

$$u_r^*(\psi) = \left(\omega^{\frac{1}{g}} U_g\right)^q (\pi A_x^*)^{-(q-1)} \times |L_{xr1}\sin\psi - L_{xr2}\cos\psi|^{q-1} \times \operatorname{sgn}(L_{xr1}\sin\psi - L_{xr2}\cos\psi). \tag{16}$$

To form the control action $u_r^*$ in the form of a function of $v_p$ and $sv_p$, we need to determine the response of the system at a point of section $p$ to the action $u_r^*(\psi)$ given by Eq. (16). The exact expression for this response has the form

$$v_p = L_{pr}(s)u_r^*(\psi), \tag{17}$$

where $L_{pr}(s)$ is the operator of dynamic compliance from point $r$ to point $p$. Since the problem is considered in the first harmonic approximation (by virtue of the smallness of the total contribution of higher harmonics, which was mentioned earlier), we can calculate the first harmonic of function $v_p$ in Eq. (17) using only the first harmonic of function (16) rather then the exact expression. The coefficients of the first harmonic of the Fourier series of this function are determined by formulas (6) and (7). Then, from Eq. (17), we have

$$v_p(\psi) = L_{pr}(s)A_x^*(u_{r1}\sin\psi + u_{r2}\cos\psi). \tag{18}$$

From Eqs. (18) and (6), we obtain

$$v_p(\psi) = A_p^*(\sin\psi\cos\varphi + \cos\psi\sin\varphi), \quad sv_p(\psi) = \omega A_p^*(-\sin\psi\sin\varphi + \cos\psi\cos\varphi), \tag{19}$$

where $A_p^* = \frac{|L_{pr}|}{|L_{xr}|}A_x^*$, $\cos\varphi = -\frac{L_{pr1}L_{xr1} + L_{pr2}L_{xr2}}{|L_{xr}||L_{pr}|}$, $\sin\varphi = \frac{L_{pr1}L_{xr2} - L_{pr2}L_{xr1}}{|L_{xr}||L_{pr}|}$,

$$L_{pr1} = \mathrm{Re}L_{pr}(j\omega), \quad L_{pr2} = \mathrm{Im}L_{pr}(j\omega),$$
$$|L_{pr}| = |L_{pr}(j\omega)|.$$

Using system (19), the functions $\sin\psi$ and $\cos\psi$ can be expressed in terms of $v_p(\psi)$ and $sv_p(\psi)$:

$$\sin\psi = \frac{1}{A_p^*}\left(\cos\varphi v_p - \sin\varphi\frac{sv_p}{\omega}\right),$$
$$\cos\psi = \frac{1}{A_p^*}\left(\sin\varphi v_p + \cos\varphi\frac{sv_p}{\omega}\right). \quad (20)$$

Substituting Eqs. (20) into the program law $u_k^*(\psi)$ given by Eq. (16), we determine the structure of the excitation law with a feedback:

$$u_r^*(v_p, sv_p) = \left(\omega^{\frac{1}{g}}U_g\right)^q \pi^{q-1}A_p^{*-2(q-1)} \times \left|L_{pr2}\frac{sv_p}{\omega} - L_{pr1}v_p\right|^{q-1}\mathrm{sgn}\left(L_{pr2}\frac{sv_p}{\omega} - L_{pr1}v_p\right). \quad (21)$$

The Dynamic properties of the system with the source of self-oscillation excitation in the form of Eq. (21) are determined, according to Eq. (17), by the equation

$$v_p = L_{pr}(s)u_r^*(v_p, sv_p). \quad (22)$$

In the harmonic approximation, the analysis of the dynamics of a closed system is performed using the equivalent linearization of Eq. (22):

$$v_p = L_{pr}(s)\left(w_1^* + \frac{s}{\omega_1}w_2^*\right)v_p, \quad (23)$$

where $w_1^*$ and $w_2^*$ are the coefficients of harmonic linearization of the nonlinear function $u_r^*(v_p, sv_p)$ given by Eq. (21):

$$w_1^*(A_p, \omega_1) = \frac{1}{\pi A_p}\int_0^{2\pi}u_r^*(A_p\sin\psi, \omega_1 A_p\cos\psi)\sin\psi d\psi = \lambda_q A_p^{q-2}\eta_1(\omega_1),$$

$$w_2^*(A_p, \omega_1) = \frac{1}{\pi A_p}\int_0^{2\pi}u_r^*(A_p\sin\psi, \omega_1 A_p\cos\psi)\cos\psi d\psi = \lambda_q A_p^{q-2}\eta_2(\omega_1),$$

$$\lambda_q = \left(\omega^{\frac{1}{g}}U_g\right)^q \pi^{q-2}A_p^{*-2(q-1)},$$

$$\eta_1(\omega_1) = \int_0^{2\pi}\left|L_{pr2}\frac{\omega_1}{\omega}\cos\psi - L_{pr1}\sin\psi\right|^{q-1} \times \mathrm{sgn}\left(L_{pr2}\frac{\omega_1}{\omega}\cos\psi - L_{pr1}\sin\psi\right)\sin\psi d\psi,$$

$$\eta_2(\omega_1) = \int_0^{2\pi}\left|L_{p\gamma 2}\frac{\omega_1}{\omega}\cos\psi - L_{p\gamma 1}\sin\psi\right|^{q-1} \times \mathrm{sgn}\left(L_{p\gamma 2}\frac{\omega_1}{\omega}\cos\psi - L_{p\gamma 1}\sin\psi\right)\sin\psi d\psi.$$

Here, $A_p$ and $\omega_1$ are the values of modes of closed system (22); in the general case, these values are different from the calculated values of $A_p^*$ and $\omega$. From the definition of the structure of function $u_r^*(v_p, sv_p)$, Eq. (21), it follows that

$$w_1^*(A_p^*, \omega) = u_{r1}, \quad w_2^*(A_p^*, \omega) = u_{r2}, \quad (24)$$

where $u_{r1}$ and $u_{r2}$ (6) defined in Eqs. (6) are the given values of the harmonic linearization coefficients used in the construction of the program law $u_r^*(\psi)$, Eq. (16).

The characteristic equation corresponding to Eq. (23) has the form

$$1 - L_{pr}(s)\left(w_1^* + \frac{s}{\omega_1}w_2^*\right) = 0. \quad (25)$$

Substituting $s = j\omega_1$ in Eq. (25) and separating the real and imaginary parts, we obtain a system of two equations in two unknowns, $A_p$ and $\omega_1$:

$$X(A_p, \omega_1) = 1 - L_{pr1}(\omega_1)\lambda_q\eta_1(\omega_1)A_p^{q-2} + L_{pr2}(\omega_1)\lambda_q\eta_2(\omega_1)A_p^{q-2} = 0, \quad (26)$$

$$Y(A_p, \omega_1) = L_{pr2}(\omega_1)\lambda_q\eta_1(\omega_1)A_p^{q-2} + L_{pr1}(\omega_1)\lambda_q\eta_2(\omega_1)A_p^{q-2} = 0, \quad (27)$$

where $L_{pr1}(\omega_1) = \mathrm{Re}L_{pr}(j\omega_1)$ and $L_{pr2}(\omega_1) = \mathrm{Im}L_{pr}(j\omega_1)$.

The system of equations (26), (27) has the solution $A_p = A_p^*$, $\omega_1 = \omega$. However, this solution is not unique in the general case. From Eq. (27), one can derive the following equation in frequency:

$$L_{pr2}(\omega_1)\eta_1(\omega_1) + L_{pr2}(\omega_1)\eta_2(\omega_1) = 0. \quad (28)$$

If Eq. (28) has positive solutions $\omega_1 \neq \omega$, the corresponding amplitudes $A_p$ can be found from Eq. (26):

$$A_p = \{\lambda_1[L_{pr1}(\omega_1)\eta_1(\omega_1) - L_{pr2}(\omega_1)\eta_2(\omega_1)]\}^{\frac{1}{2-q}}. \quad (29)$$

The stability of the modes of closed system (22) is analyzed on the basis of the criterion suggested in paper [16]. According to this criterion, the mode $A_p$, $\omega_1$ is stable when

$$\frac{d}{dA_p}Y(A_p, \omega_1) > 0, \tag{30}$$

where $Y(A, \omega_1)$ is the imaginary part of characteristic equation (25) and $\omega_1 = \omega_1(A)$, i.e., the frequency is determined in the general case as the function inverse of function (29). As shown in [16], criterion (30) is equivalent to the energy condition of stability.

For the rated mode $A_p = A_p^*$, $\omega_1 = \omega$, by virtue of identity (24), and stability condition (30) has the form

$$(q-2)A_p^{*q-3}(L_{pr2}u_{r1} + L_{pr1}u_{r2}) > 0. \tag{31}$$

In the general case, modes $A_p$, $\omega_1$ different from the rated mode $A_p^*$, $\omega$ and the instability of the rated mode $A_p^*$, $\omega$ may occur. In particular, for $g = 2$, which corresponds to an integral quadratic restriction imposed on the excitation law, the law $u_r^*$ Eq. (21), appears to be linear:[1]

$$u_r^*(v_p, sv_p) = \omega U_2^2 \frac{\pi|L_{xr}|}{|L_{pr}|}\left(L_{pr2}\frac{sv_p}{\omega} - L_{pr1}v_p\right). \tag{32}$$

In this case, the mode $A_p^*$, $\omega$ in system (22) is unstable, because the left-hand side of inequality (31) vanishes at $q = 2$.

To make the rated mode stable and to eliminate unwanted modes, according to [11, 12], we replace the law $u_r^*$ given by Eq. (21) by the extended control

$$u_{rmc}^* = \chi(A_p, A_p^*)u_r^*(v_p, sv_p), \tag{33}$$

where $\chi(A_p, A_p^*) = [1 + \rho\sigma(A_p, A_p^*)]^m$, $\sigma(A_p, A_p^*)$ is a function that is continuous together with its derivatives as functions of the current value of $A_p$ (this value is calculated through $v_p$ and $sv_p$: $A_p = \left[v_p^2 + \left(\frac{sv_p}{\omega_1}\right)^2\right]^{\frac{1}{2}}$[2] and the rated value of $A_p^*$, and $\rho$ and $m$ are constant parameters; this function must satisfy the following conditions: $\sigma(A_p^*, A_p^*) = 0$ and $\frac{\partial}{\partial A_p}\sigma(A_p^*, A_p^*) \neq 0$.

Thus, for $A_p = A_p^*$ $u_{rmc}^*$, the control law $u_{rmc}^*$ given by Eq. (33) coincides with the previously defined law (21), and when $A_p$ differs from $A_p^*$, these functions can take different values. Since, by virtue of (33), the coefficients of harmonic linearization of function $u_{rmc}^*$ are determined by the formulas

$$w_{rmc}^* = \chi(A_p, A_p^*)w_{r1}^*, \quad w_{rmc2}^* = \chi(A_p, A_p^*)w_{r2}^*,$$

where $w_{r1}^*$ and $w_{r2}^*$ are the coefficients of harmonic linearization of function $u_r^*$, Eqs. (26) and (27) for the system with exciting action $u_{rmc}^*$ given by Eq. (33) will take the form

$$X(A_p, \omega_1) = 1 - \chi(A_p, A_p^*)\lambda_q A_p^{q-2} \times \lfloor L_{pr1}(\omega_1)\eta_1(\omega_1) - L_{pr2}(\omega_1)\eta_2(\omega_1)\rfloor = 0, \tag{34}$$

$$Y(A, \omega_1) = \chi(A_p, A_p^*)\lambda_q A_p^{q-2} \times [L_{pr2}(\omega_1)\eta_1(\omega_1) + L_{pr1}(\omega_1)\eta_2(\omega_1)] = 0. \tag{35}$$

From Eq. (35) it follows that the values of frequency are determined, as before, by Eq. (28). If this equation has positive roots $\omega_1 \neq \omega$, the corresponding amplitudes $A_p$ are determined, according to Eq. (35), from the equation

$$\lambda_q\chi(A_p, A_p^*)A^{q-2} = [L_{pr1}(\omega_1)\eta_1(\omega_1) - L_{pr2}(\omega_1)\eta_2(\omega_1)]^{-1} = f(\omega_1). \tag{36}$$

Equation (36) involves an arbitrary function $\sigma(A_p, A_p^*)$ and two parameters $\rho$ and $m$. They can be defined in such a way that Eq. (36) will have no positive solutions $A_p$, excluding $A_p = A_p^*$. In particular, when $g = q = 2$, which corresponds to linear law (32), and when $\sigma(A_p, A_p^*) = (A_p^{*2} - A_p^2)$, the solution to Eq. (36) is determined by the formula

$$A_p = \left[A_p^{*2} - \frac{f^m(\omega_1) - 1}{\rho}\right]^{\frac{1}{2}}. \tag{37}$$

For $|\rho|A_p^{*2} < |f^m(\omega_1) - 1|$, the radicand in Eq. (37) is negative, which ensures the uniqueness of the rated mode $A_p^*$, $\omega$. The condition of stability of mode $A_p^*$, $\omega$ given by Eq. (30) for the system with excitation law (33) takes on the following form by virtue of Eq. (35):

$$\left\{\left[1 + \rho\frac{\delta}{\delta A_p}\sigma(A_p^*, A_p^*)\right]^{m-1}A_p^{*q-2} + (q-2)A_p^{*q-1}\right\} \times (L_{p\gamma 2}u_{\gamma 1} + L_{p\gamma 1}u_{\gamma 2}) > 0. \tag{38}$$

[1] Because $u_p^*(\psi)$ is a purely harmonic function, law (32) corresponds to the excitation of purely harmonic self-oscillations. A similar solution for systems with finite numbers of degrees of freedom is given in paper [13].

[2] Formally, the current value of frequency $\omega_1$ appearing in this expression must be measured in the process of the system operation; however, in practice, as follows from numerical experiments [12, 13], the given frequency $\omega$ can be used instead of $\omega_1$.

The first factor of inequality (38) contains three parameters: $\frac{\partial}{\partial A_p}\sigma(A_p^*, A_p^*)$, $\rho$, and $m$. They can always be chosen so as to satisfy inequality (38). This way, we ensure the stability of the mode $A_p^*$, $\omega$.

## REFERENCES


1. V. K. Astashev and M. E. Gerts, Akust. Zh. **22**, 192 (1976) [Sov. Phys. Acoust. **22**, 108 (1976)].
2. V. K. Astashev, V. I. Babitskiĭ, and M. E. Gerts, Nauchn. Tr. Vyssh. Uchebn. Zaved. Lit. SSR, Vibrotekh., No. 3 (20), 253 (1973).
3. P. S. Landa, *Self-Oscillation in Systems with Finite Number of Degress of Freedom* (Nauka, Moscow, 1980).
4. P. S. Landa, *Auto-Oscillations in Distributed Systems* (Nauka, Moscow, 1983).
5. M. E. Gerts, Mashinovedenie, No. 6, 3 (1979).
6. A. V. Repnikov, *Oscillations in Optimal Automated Control Systems* (Mashinostroenie, Moscow, 1968).
7. A. A. Krasovskiĭ, Izv. Ross. Akad. Nauk, Tekh. Kibern., No. 6, 5 (1994).
8. M. Ya. Izrailovich, Probl. Mashinostr. Nadezhnosti Mash., No. 6, 76 (1993).
9. M. Ya. Izrailovich, Izv. Ross. Akad. Nauk, Teor. Sist. Upr., No. 6, 56 (1995).
10. M. Ya. Izrailovich, Dokl. Akad. Nauk **367**, 606 (1999).
11. M. Ya. Izrailovich, Dokl. Akad. Nauk **377**, 25 (2001).
12. M. Ya. Izrailovich, Probl. Mashinostr. Nadezhnosti Mash., No. 4, 3 (2001).
13. M. Ya. Izrailovich, Dokl. Akad. Nauk **380**, 465 (2001).
14. E. P. Popov, *Applied Theory of Control Processes in Nonlinear Systems* (Nauka, Moscow, 1973).
15. A. G. Butkovskiĭ, *Theory of Optimal Control of Systems with Distributed Parameters* (Nauka, Moscow, 1965).
16. V. I. Babitskiĭ, *Theory of Vibration Shock Systems* (Nauka, Moscow, 1978).


*Translated by A. Vinogradov*

*Acoustical Physics, Vol. 50, No. 2, 2004, pp. 169–176. Translated from Akusticheskiĭ Zhurnal, Vol. 50, No. 2, 2004, pp. 210–219.*


# Space–Frequency Dependence of the Horizontal Structure of a Sound Field in the Presence of Intense Internal Waves

**B. G. Katznel'son and S. A. Pereselkov**

*Voronezh State University, Universitetskaya pl. 1, Voronezh, 394893 Russia*

*e-mail:katz@phys.vsu.ru*

Received November 20, 2002

**Abstract**—Sound propagation in a shallow sea is considered in the presence of a packet of intense internal waves. It is shown that horizontal refraction caused by these packets can lead to noticeable changes in the spectrum and spatial intensity distribution of a signal propagating approximately parallel to the wave fronts of internal wave packets. © *2004 MAIK "Nauka/Interperiodica".*

The present state of the art in studying the ocean in general and the shelf zone (shallow sea) in particular by acoustic methods is such that researchers now pass from relatively simple experiments on acoustic probing along single tracks to the realization of tomographic schemes. In the latter case, a set of sources and receiving arrays of different configurations is used that can probe simultaneously in different directions with signals of different duration and spectral composition (broadband and narrowband signals) for quite a long time. For example, such experiments are the SWARM [1, 2] and PRIMER [3] ones, in which intersecting acoustic tracks covered certain regions of the ocean. These kinds of ocean studies allow one to detect rather fine acoustic effects caused by various oceanic phenomena. However, in explaining many of the experimental results, one should take into account the anisotropy that appears in the horizontal plane due to various ocean motions (internal waves, tides, and the motion of frontal zones). To a great extent, such an anisotropy manifests itself for internal waves (IWs) in shallow water. As is known, the IWs propagate toward the beach with an almost plane wave front whose length can reach several tens of kilometers. The amplitude of oscillations of the constant density surface can reach 5–10 m. In this case, if the sound velocity gradient along the wave front (or in the absence of IWs) is on the order of $0.001\ s^{-1}$, it may be $0.1\ s^{-1}$ along the propagation direction (across the wave front). This value is comparable with the vertical gradient. Moreover, the sound velocity field in this direction has a quasi-periodic structure. Observations [4, 5] show that a packet may contain ten or more individual IWs for a total length of the packet of up to 10 km. In this case, the propagation medium is similar to a diffraction lattice covering a considerable area of about $10 \times 20\ km^2$. If we take into account the presence of a noticeable geometric (waveguide) dispersion, we obtain a periodic inhomogeneous anisotropic dispersive medium. It is important to note that, in studying the propagation of broadband signals (short pulses), the predominance of intermode dispersion (the difference in the group velocities for different vertical modes) has been conventionally recognized. This allows one to perform a reliable mode selection (mode filtering) by the arrival times of the corresponding signals. Usually, the difference in the group velocities of waveguide modes is several tens of meters per second, which for typical tracks (>10 km) gives a quite observable difference of more than 0.1 s in the arrival times. As for intramode dispersion (i.e., the frequency dependence of the group velocity of a single mode and, hence, the deformation of pulses corresponding to individual modes), its manifestation has been much weaker until now. However, as will be shown below, the manifestation of the intramode dispersion in the aforementioned anisotropic waveguide medium is noticeable.

As is shown in [6], space anisotropy manifests itself as a noticeable horizontal refraction caused by IWs, up to the formation of a waveguide in the horizontal plane for acoustic tracks that are almost parallel to internal wave fronts (see also the numerical modeling of this situation in [7]). It is also noted that, using the approach of "vertical modes and horizontal rays," the influence of anisotropy on the three-dimensional structure of the sound field has a selective character in modes. In other words, the structure of horizontal rays may be qualitatively different for different vertical modes. Since the vertical modes depend on frequency (in general, in a rather complicated way), one should expect that the structure of horizontal rays (and, hence, the three-dimensional field structure) will also depend on frequency. This frequency dependence in the case of a horizontal refraction is studied in the present paper. The dependence may be of resonance character and manifest itself in the propagation of broadband signals.

1063-7710/04/5002-0169$26.00 

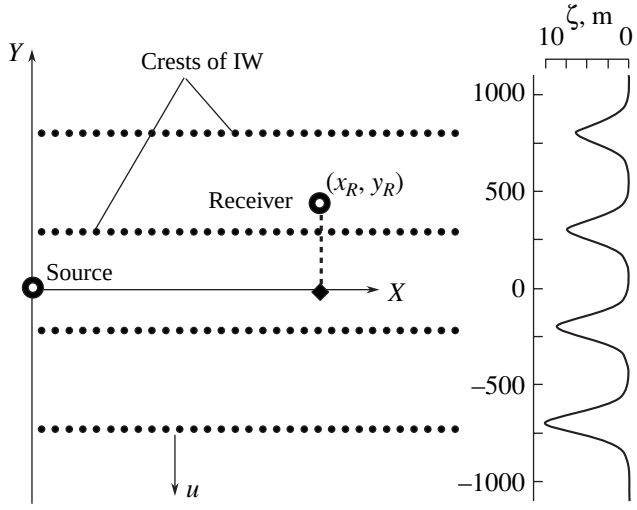


**Fig. 1.** Statement of the problem. Dotted lines denote the wave fronts of a packet of internal waves (the lines of maximum amplitude ζ). The location of the IW packet, whose form corresponds to a chosen model at a given moment, is shown on the right.

The spectral characteristics of sound signals in the presence of internal waves attracted some interest previously. In particular, the presence of a frequency dependence of a resonance character was detected in the known experimental work [8], where the propagation of broadband (explosive) signals crossing the internal wave fronts was studied. The authors of [8] stated that the measured difference in the sound level at a fixed frequency reached 25 dB depending on the direction of sound propagation. They (as did the authors of [9]) interpreted such a behavior of the frequency dependence as a result of a selective interaction of modes because of the sound velocity perturbation by IWs. This interaction steeply increases at the coincidence of the spatial period (quasi-period) of the IW packet with the spatial scale of beatings of interacting modes at some resonance frequency.[1] Note that, in this work, some features (dips and peaks) are observed in the frequency dependence of the signals for another orientation of the acoustic track. However, for this case, the authors do not suggest any interpretation.

In the present paper, the frequency dependence of signal characteristics is considered in the course of signal propagation in the medium described above. In particular, it will be shown that different features, among them resonance-like ones, can occur due to horizontal refraction when the acoustic track is oriented at a relatively small angle to the shoreline (to the wave fronts of IWs).

Let us consider the propagation of a signal along the acoustic track in a shallow-water sound channel in the presence of internal waves propagating almost normally to this track. Otherwise, we consider the sound field in the region corresponding to rather small azimuth angles with respect to the *X* axis (Fig. 1).

We represent a shallow-water ocean medium as the three-dimensional waveguide in the system of coordinates *X*, *Y*, *Z*. The waveguide is formed by a water layer with squared refractive index

$$n^2(\mathbf{r}, z) = n^2(z) + \mu(\mathbf{r}, z, t), \quad (1)$$

where $n^2(z)$ corresponds to some average equilibrium stratification of the layer (the profiles of the sound velocity and density are denoted by $c(z)$ and $\rho(z)$, respectively), $\mu(\mathbf{r}, z, t)$ is the fluctuation of its acoustic properties caused by the packet of the internal waves, and $\mathbf{r} = (x, y)$ is the radius vector in the horizontal plane. The water layer is bounded in depth by the free surface $z = 0$ and a homogeneous absorbing half-space (bottom) $z = H$ with a density $\rho_1$ and squared refractive index $n_1^2(1 + i\alpha)$, where $n_1 = c(H)/c_1$ and $\alpha$ is determined by the absorbing properties of the bottom.

According to [10], the expression for $\mu(\mathbf{r}, z, t)$ is determined by the parameters of the packet of internal waves

$$\mu(\mathbf{r}, z, t) = -\frac{2\delta c(\mathbf{r}, z, t)}{c(z)} = -2QN^2(z)\zeta(\mathbf{r}, z, t). \quad (2)$$

Here, $\delta c$ is the sound velocity variation caused by the displacement of the surface of constant density, $N(z) = \left(\frac{g}{\rho}\frac{d\rho}{dz}\right)^{1/2}$ is the buoyancy frequency determined by the density stratification of the water layer, $g$ is the gravitational acceleration, $Q \approx 2.4$ s$^2$/m is the constant determined by the physical properties of water, and ζ is the vertical displacements of the water layers. Taking into account that the first gravitational mode $\Phi(z)$ predominates in the vertical distribution, these displacements can be written as

$$\zeta(\mathbf{r}, z, t) = \Phi(z)\zeta_s(\mathbf{r} - \mathbf{u}t), \quad (3)$$

where $\mathbf{u} = (u_x, u_y)$ is the velocity of an internal wave in the horizontal plane. In general, $u$ depends on the coordinates, which causes, in particular, a possible distortion of the wave front. The function $\Phi(z)$ is normalized by its maximum value, and $\zeta_s$, which represents the displacement of the surface where the gravitational mode equals unity, can be called the envelope of the IW packet. For numerical modeling, it is assumed that the speed of the packet motion is directed along the *Y* axis ($u_x = 0$) and the wave fronts in the packet are rectilinear and parallel to the *X* axis.

In [6, 7] it was shown that, if the IW packets propagate along an acoustic track that is roughly parallel to the IW front (i.e., roughly parallel to the shoreline), there is a significant horizontal refraction of the sound rays propagating from the source to the receiver. This

[1] A direct comparison with [8] is difficult, because detailed data on IWs are absent in [8].

refraction may form a waveguide in the horizontal plane, which generates noticeable field fluctuations in time at the receiver. This issue has been analyzed in detail in [6]. Here, we consider possible space–frequency fluctuations in the spectrum of the sound field at the point of reception in our conditions.

Our problem is to determine the three-dimensional field structure of a monochromatic point source for the waveguide model described above. We need to solve the equation

$$\Delta\Psi(\mathbf{r}, z) + k^2 n^2(\mathbf{r}, z)\Psi(\mathbf{r}, z) = 0 \quad (4)$$

with the boundary conditions for the function $\Psi(\mathbf{r}, z)$ at the bottom and the sea surface and with the conditions that determine the omnidirectional point source.[2] We seek the solution to Eq. (4) as an expansion in the modes of the reference waveguide, $\psi_l(\mathbf{r}; z)$, which depend on the horizontal coordinate $\mathbf{r}$ as a parameter:

$$\Psi(\mathbf{r}, z) = \sum_l P_l(\mathbf{r})\psi_l(\mathbf{r}; z). \quad (5)$$

In the adiabatic approximation (neglecting the interaction of vertical modes) for the function $P_l(\mathbf{r})$, we obtain the equation

$$\nabla_r^2 P_l(\mathbf{r}) + \xi_l^2(\mathbf{r})P_l(\mathbf{r}) = 0, \quad (6)$$

where $\nabla_r = \left(\frac{\partial}{\partial x}, \frac{\partial}{\partial y}\right)$ and $\xi_l(\mathbf{r}) = q_l(\mathbf{r}) + i\frac{\gamma_l(\mathbf{r})}{2}$ are the eigenvalues of the Sturm problem in the given cross-section of the waveguide. These eigenvalues are complex quantities because of the absorption and they also depend on the horizontal coordinate as a parameter.

The three-dimensional field structure can be found in the framework of the theory of horizontal rays and vertical modes when we seek the complex modal amplitude of the sound field in the form

$$P_l(\mathbf{r}) = \sum_n A_{nl}(\mathbf{r})\exp[i\theta_{nl}(\mathbf{r})]. \quad (7)$$

Here, $A_{nl}(x, y)$ is the amplitude and $\theta_{nl}(x, y)$ is the phase shift (eikonal) of the $l$th acoustic mode $\psi_l(\mathbf{r}; z)$, which depends on the horizontal coordinate as a parameter. Note that, in the general case, not one but several horizontal rays corresponding to a given mode can arrive at the point of reception. These rays have different paths, and, therefore, they are characterized by different amplitudes and phase shifts. Hence, in Eq. (3), the summation is carried out over the horizontal rays (index $n$). For the amplitude and eikonal from Eq. (6), we can obtain conventional (two-dimensional) equations of geometric acoustics:

$$\begin{aligned}(\nabla_r\theta_{nl})^2 &= q_l^2,\\ 2\nabla_r A_{nl}\nabla_r\theta_{nl} + A_{nl}\nabla_r^2\theta_{nl} + q_l\gamma_l A_{nl} &= 0.\end{aligned} \quad (8)$$

On the right-hand side of the first equation, there is the efficient wave vector, which, for horizontal rays, can be replaced by the refractive index $n_l(\mathbf{r})$ depending on the horizontal coordinates. It is determined by the relationship

$$q_l^2(\mathbf{r}) = n_l^2(\mathbf{r})(q_l^0)^2 = (q_l^0)^2[1 + \delta n_l^2(\mathbf{r})], \quad (9)$$

where $\psi_l^0$ and $q_l^0$ are the eigenfunctions and eigenvalues of the unperturbed wave problem (without internal waves) and $k = 2\pi f/c$ is the wave vector at a fixed depth (for example, at the sea surface). The correction $\delta n_l^2$ can be determined by the perturbation theory

$$\delta n_l^2(\mathbf{r}) = \frac{1}{(q_l^0)^2}\int_0^H [\psi_l^0(z)]^2 k^2\mu(\mathbf{r}, z)dz = \nu_l\varsigma_s(\mathbf{r}), \quad (10)$$

where, using Eq. (2), the IW packet form can be singled out as a separate factor; the remaining quantities are included in the factor $\nu_l$. As can be seen from Eq. (10), the correction (factor $\nu_l$) is determined by the overlapping integral of the vertical mode and sound velocity perturbation; i.e., it is determined by the part of the modal amplitude that corresponds to the thermocline layer. In such an approximation, the space–frequency dependence of the correction for the squared refractive index of horizontal rays, $\delta n_l^2$, is determined by the form of the IW packet. Note also that, for horizontal rays (in contrast to conventional geometric acoustics), there is a frequency dependence in the eikonal and transport equations (8), or, more exactly, in the refractive index of horizontal rays (10). The frequency dependence of the part of the effective refractive index, $\nu_l$, that is related to internal waves (and that causes horizontal refraction) can be estimated on the assumption that the thermocline located at some depth $h$ has a thickness $h_t$ that is small compared to the vertical scale of mode variations:

$$\begin{aligned}\nu_l &= -\frac{Qk^2}{[q_l^0]^2}\int_0^H [\psi_l^0(z)]^2 N^2(z)\Phi(z)dz\\ &\approx -\frac{Qk^2}{[q_l^0]^2}N_0^2[\psi_l^0(h)]^2 h_t.\end{aligned} \quad (11)$$

This factor also depends on the waveguide parameters: its depth, bottom parameters, Vaisala frequency, and sound velocity profile. The frequency dependence is also related to the mode number for a horizontal ray. Subsequent calculations will be performed for the model of a shallow-water sound channel with the fol-

[2] Because the time dependence is slow, the problem can be solved in the quasistatic approximation with parameter $t$ being omitted.

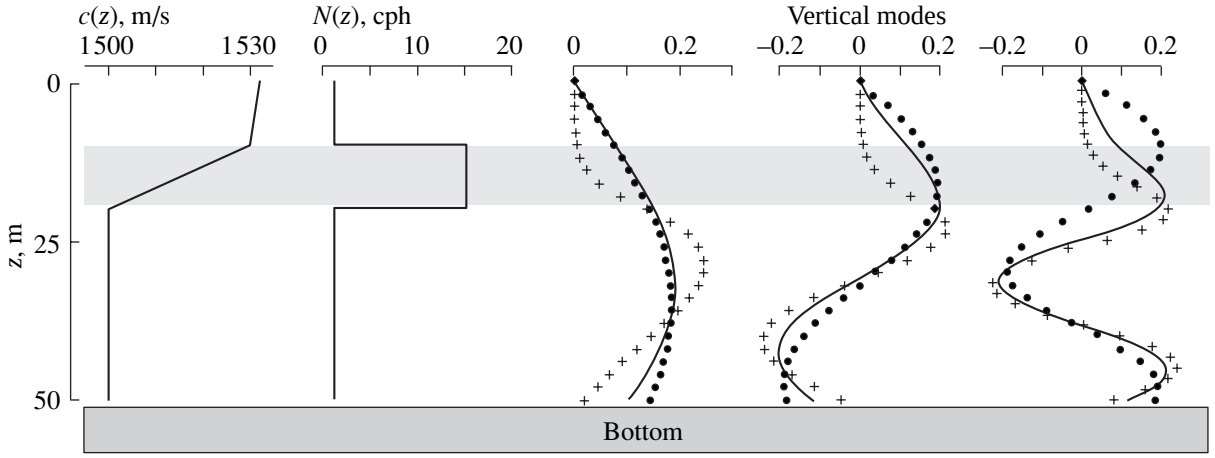


**Fig. 2.** Sound velocity profile and Vaisala frequency corresponding to the calculated model. Three first vertical modes for different sound frequencies (at the right): circles refer to frequencies of 40, 70, and 110 Hz for the first, second, and third modes; solid lines, to 80, 180, and 350 Hz for the same modes; and crosses, to 600 Hz for all modes.

lowing parameters. The sound velocity profile, $c(z)$, for the unperturbed state and the Vaisala frequency are shown in Fig. 2; the water layer depth is $H = 50$ m; the bottom has a density of $\rho_1 = 1.8$ g/cm$^3$; the sound velocity in the bottom is $c_1 = 1750$ m/s; and the absorption coefficient is $\alpha = 0.02$. As a model of the IW packet, we take a train of four internal waves with plane wave fronts shifted relative to each other:

$$\zeta_s(y, t) = \sum_{m=1}^{4} A_m \sec h^2\left(\frac{y - y_m + u_m t}{L_m}\right) \qquad (12)$$

these waves propagate, in the general case, with different velocities $u_m$ in the negative direction of the $Y$ axis. The parameters of the packet are determined by more or less typical values: $A_1 = 10$ m, $A_2 = 8.61$ m, $A_3 = 7.41$m, $A_4 = 6.38$ m; $y_1 = 300$ m, $y_2 = 800$ m, $y_3 = 1300$ m, $y_4 = 1800$ m; $L_{1,2,3,4} = 75$ m, and $u_{1,2,3,4} = 0.5$ m/s. In spite of the approximate character of formula (12), similar formulas are used for modeling IW packets (see, for example, [2, 7]). Packet (12) moves as a whole in the negative direction of the $Y$ axis, its total length is roughly 2 km, and it covers the acoustic track within 1.1 h. The position of the packet in Fig. 1 corresponds to the value of $t \sim 2000$ s.

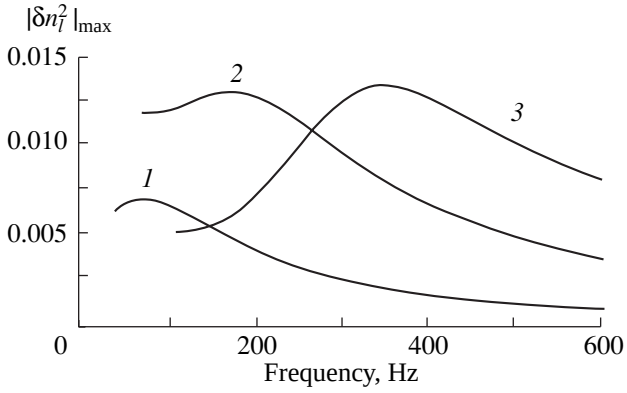


**Fig. 3.** Frequency dependence of corrections to the refractive index for horizontal rays corresponding to the first three vertical modes.

As was noted above, the addition to the squared refractive index, which determines the horizontal refraction, depends on the frequency and the transverse coordinate relative to the acoustic track (in our case, the $Y$ axis) in accordance with the form of the IW packet. It is evident that this addition has its maximum value where the quantity $\zeta_s(y, t)$ is maximum, i.e., at the wave fronts. Figure 3 shows the frequency dependences of the quantity $|\delta n_l^2|_{\max}$ for the first three modes at $\zeta = A_1 = 10$ m. Note that each vertical mode has a region where the frequency dependence is relatively steep. For example, for the first mode such a region is in the vicinity of 100 Hz. At frequencies above 200 Hz, the first mode has a small addition to the refractive index for the horizontal rays, $|\delta n_l^2|_{\max}$, which smoothly decreases with increasing frequency. It means that, if we single out the first mode in some way, then, in the frequency range above 200 Hz, its amplitude has an almost cylindrical symmetry in the horizontal plane and the frequency dispersion is almost absent. The second and third modes at such frequencies generate a system of curvilinear horizontal rays, which depends on frequency. One can see that the addition $|\delta n_l^2|_{\max}$ has a noticeable maxima in the range of ~80 Hz for the first mode, ~180 Hz for the second mode, and ~350 Hz for the third mode. This feature is explained by the fact that, in the aforementioned frequency regions, a considerable part of the mode (the region of the first maximum) is located in the thermocline zone. As the frequency increases or decreases,

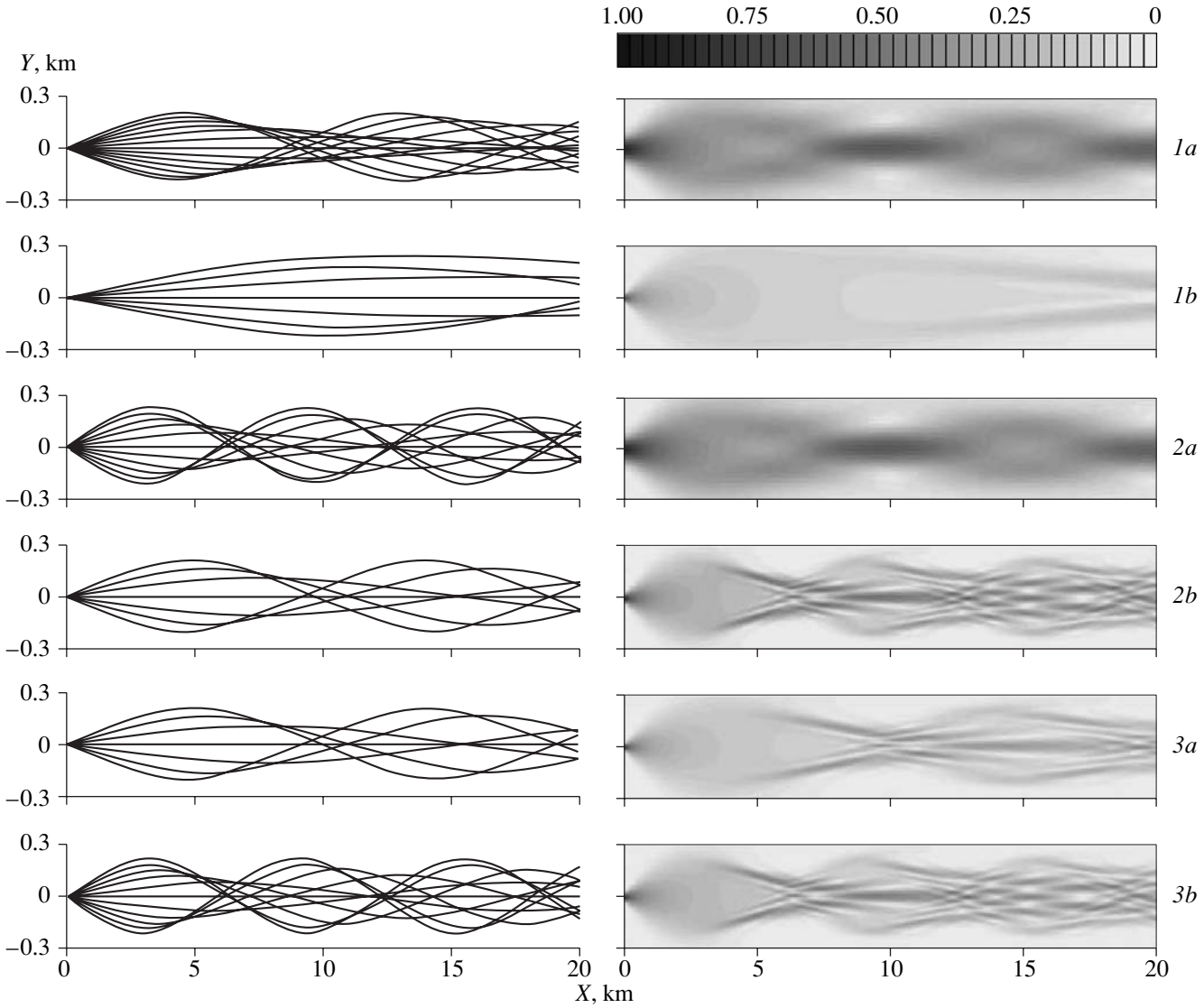


**Fig. 4.** Horizontal ray patterns (left) and the field distribution obtained in the horizontal plane by the parabolic equation method (right) for the first three modes; gradations of gray color indicate different frequencies. The scale of gradations for the intensity in relative units is shown at the top. Diagrams *1* corresponds to the first mode at $f =$ (*a*) 50 and (*b*) 350 Hz; diagrams *2* corresponds to the second mode at $f =$ (*a*) 180 and (*b*) 350 Hz; and diagrams *3* corresponds to the third mode at $f =$ (*a*) 150 and (*b*) 350 Hz.

this region of the maximum of the eigenfunction leaves the thermocline and the influence of the internal waves on it weakens in accordance with Eqs. (10) or (11). This reasoning is illustrated by Fig. 2, where vertical amplitude distributions of the first three modes are shown for several frequencies. Thus, the range of frequency features for the horizontal rays corresponding to a given mode is determined mainly by the location of the thermocline and its width.

Consider now the field structure in the horizontal plane in the ray approximation for individual modes. Figure 4 shows a set of horizontal rays for the first three modes at two frequencies, one of which corresponds to the resonance value and the other is away from it. The position of the source corresponds to the case of "focusing" in the horizontal plane; i.e., it is located in the region where the surface of constant density has its minimum deviation (minimum of the function $\zeta_s(x)$.[3] This corresponds to the instant $t$ =1000 s for our model of packet motion. At another moment, the ray pattern can be quite different.

First consider the field properties at a fixed frequency, for example, at 350 Hz. According to Fig. 3, for this frequency, the third mode has the greatest refractive index, the second mode comes next, and the first mode experiences the influence of horizontal refraction to the least extent.The ray patterns in the horizontal plane are

[3] In our case, the thermocline is located near the surface and internal waves propagate with their crests downwards.

shown in Fig. 4 (diagrams *1b*, *2b*, and *3b* at the left). One of results is that, at different points in the *XY* plane, the amplitudes (weights) of three modes at this frequency differ from their initial distribution (at the source). For example, at $y = 0$, $x = 6$ km, the third mode predominates with a focusing of horizontal rays in this region, as compared to the first two modes. At the point with the coordinates $y = 0.2$ km and $x = 6$ km, the third mode is almost in the shadow zone and the first and second modes predominate in the modal expansion. As it was noted above, this pattern also varies in time. In other words, the modal amplitudes (modal composition) change in space and time but without any mode transformation in the usual sense, i.e., without the energy transfer from one mode to another due to the interaction with inhomogeneities. Here, the main mechanism of modal amplitude variation is the redistribution of energy transferred by the modes in the horizontal plane. (Remember that all calculations are carried out in the adiabatic approximation.)

It should be noted that the aforementioned features appear in the frequency dependence of the horizontal ray pattern, which one can see in Fig. 4. Consider, for example, the horizontal rays corresponding to the first mode (diagrams *1a* and *1b*). When a source is located in the region of the minimum deviation (the case of focusing), they undergo the greatest influence of horizontal refraction in the frequency range ~80 Hz. As the frequency increases, the influence of the horizontal refraction decreases and the focusing region moves away from the source. For frequencies of 200 Hz and higher, horizontal refraction of the first mode can be neglected for distances of about 10 km. In the range >200 Hz, the effect of the frequency dependence appears mainly for the second and third vertical modes (Fig. 4, diagrams *2* and *3*). This is evident, because the first maxima of the second and third modes pass through the thermocline as the frequency changes in the vicinity of 200 and 350 Hz, respectively. In this case, the maxima in the frequency dependence are fairly sharp. Otherwise, horizontal refraction (focusing and defocusing) for sound waves with frequencies 200–400 Hz is rather pronounced for the second and third modes, as compared to the indicated effects in another frequency range.

It is possible to estimate the longitudinal distance of focusing $L_f$. Using simple geometric-acoustic considerations, we obtain

$$L_f \sim \frac{2\sqrt{2}\Lambda}{N_0 \psi_l(h)\sqrt{Qh_t\zeta_0}}, \tag{13}$$

where $\Lambda$ is some average quasi-period of the packet and $\zeta_0$ is the typical amplitude of the internal wave. The dependence on frequency and mode number is mainly described by the term $\psi_l(h)$. For example, for the third mode at a frequency of 150 Hz and the parameters corresponding to this example, we obtain $L_f \sim 10$ km. The dependence on the transverse coordinate (in our case, on $x$ in the vicinity of this distance) is rather steep. Near this distance, there is even a shadow zone (see Fig. 4, diagram *3a*). This means that when our receiver is in the shadow zone the horizontal rays corresponding to a given mode at a given frequency do not arrive at the receiver. In other words, this mode does not contribute to the sound field and, hence, the frequency dependence of the sound intensity (the spectrum of the received signal) has a dip. The depth of this dip depends on the contribution of this mode at other frequencies. The indicated ray pattern varies with time as the IW packet moves. After some time, the point of observation can come out from the shadow zone and the frequency dependence changes. Because the IW packets move slowly, with the use of short signals (for example, broadband signals) we obtain a certain sequence of spectra varying in time. Such a dependence may appear in the propagation of broadband signals when the frequency selection is realized by the indicated mechanism. The amplification or attenuation of the sound field at a given frequency and at a given point can be realized either by gathering the energy from different azimuth directions or by the energy leakage in the horizontal direction. This effect can be interpreted as the manifestation of a considerable intramode dispersion.

For a numerical calculation of the sound field characteristics (in our case, spectra) at a certain point, it is more convenient to use the parabolic equation in the horizontal plane rather then the ray approximation. To construct the main formulas of the parabolic equation method, we seek the solution to Eq. (6) in the form

$$P_l(\mathbf{r}) = F_l(\mathbf{r})\exp(iq_l^0 x). \tag{14}$$

Taking into account that the internal wave fronts are directed along the $X$ axis, we assume that $F_l(\mathbf{r})$ is a smooth function of the $x$ coordinate. As a result, in the forward scattering approximation ($\partial F_l/\partial x \ll q_l^0 F_l$) for the function $F_l(\mathbf{r})$ we obtain

$$\frac{\partial F_l}{\partial x} = \frac{i}{2q_l^0}\frac{\partial^2 F_l}{\partial y^2} + \frac{iq_l^0}{2}(n_l^2(\mathbf{r}) - 1)F_l, \tag{15}$$

where $n_l(\mathbf{r})$ is determined by Eq. (9).

The construction of the field amplitude, i.e., the solution to Eq. (15), is carried out numerically. For this purpose, we use the Split Step Fourier (SSF) algorithm:

$$\begin{aligned} F_l(x + \Delta x, y) &= \exp[-iq_l^0 \Delta x U_l(x, y)] \\ &\times FFT\{\exp[iq_l^0 \Delta x T_l(x, q)]FFT[F_l^*(x, y)]^*\}, \end{aligned} \tag{16}$$

where $FFT$ is the operator of the fast Fourier transform, $T_l(q) = \frac{1}{2}(q/q_l^0)^2$ is the operator in the Fourier space $q$, and $U(x, y) = -\lfloor n_l^2(x, y) - 1\rfloor/2$ is the operator in the space of $(x, y)$ coordinates. In the calculations, we

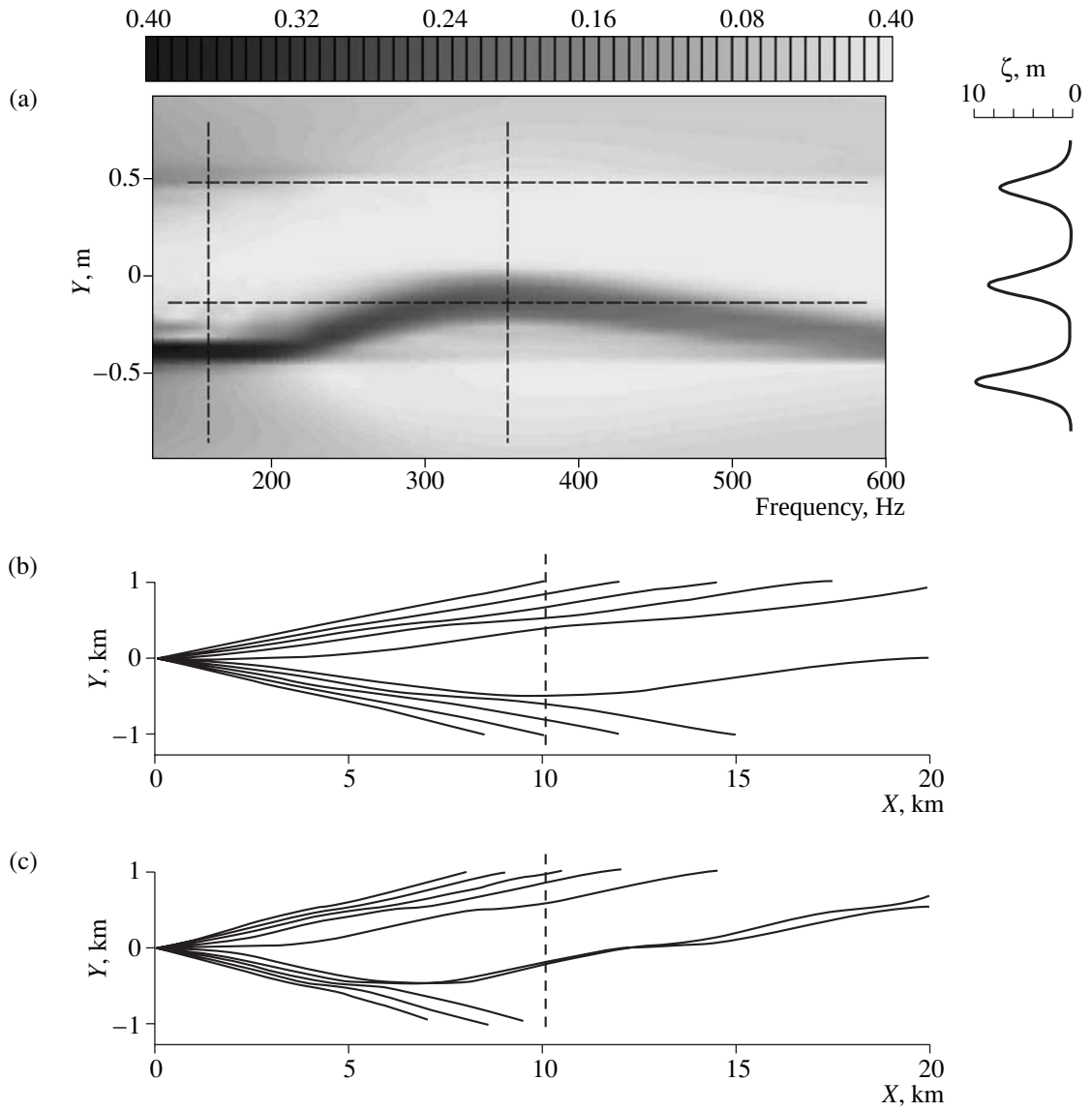


**Fig. 5.** (a) Space–frequency diagram of the modal intensity of the sound field for the third mode at a distance $x_R$ = 10 km from the source (in gradations of gray color); the location of the wave packet is shown at the right. The coordinate of the observation point (receiver), $y_R$, is represented by the vertical axis. The dotted lines show the vertical and horizontal sections. (b, c) Ray patterns in the horizontal plane for frequencies of 150 and 350 Hz; vertical sections are shown in Fig. 5a.

assumed that the source is located at the point with coordinates $x = 0$, $y = 0$. The field distribution in the Fourier space of the $l$th mode near the source has the form

$$T_l(q, 0) = a_l \exp(-q^2/2\Delta_l^2), \qquad (17)$$

where $a_l$ is the mode amplitude determined by its value at the depth of the source and $\Delta_l = q_l^0 \sin\theta_{\max}$ is the parameter that determines the angular range of source radiation, which is taken into account in calculations (the angle $\theta$ is measured with respect to the $X$ axis). It is assumed that the sound velocity profile corresponds to that shown in Fig. 2. The parameter $\theta_{\max}$ determining the angular field distribution at the source equals $\pi/18$, which corresponds to the horizontal rays with launch angles no greater than 10° in both directions. In the calculations, the digitization steps in the horizontal plane were taken to be $\Delta x$ = 50 m and $\Delta y$ = 5 m.

According to the above considerations, the amplitude $F_l(\mathbf{r})$ depends on frequency. Figure 4 (at the right) shows the distribution of the field amplitude in the horizontal plane by gradations of the gray color for the same parameters as those used for the ray patterns of vertical modes 1–3. It is seen that the qualitative pattern corresponds to the interpretation given above in the framework of the ray theory. Note that, at rather long distances from the source, even the waveguide is formed in the horizontal plane (i.e., a stable interfer-

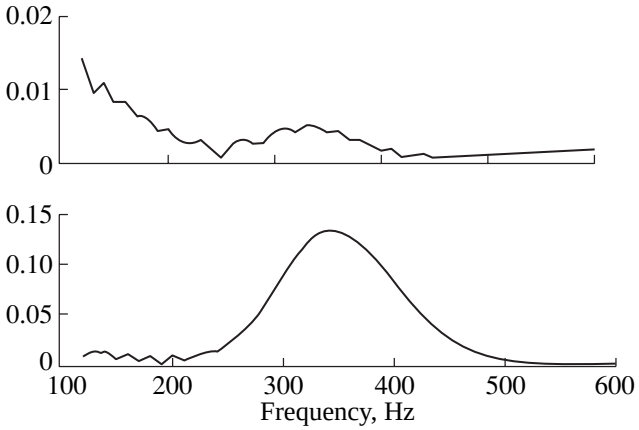


**Fig. 6.** Examples of spectra of the received signal at observation points corresponding to horizontal sections in Fig. 5a.

ence structure is formed in the horizontal plane, this structure being different for different frequencies).

For construction and analysis of the spectra of signals received at different points of the horizontal plane, we construct a space–frequency pattern (Fig. 5), where the quantity $y_R$ (the distance from the observation point) is represented by the vertical axis and the sound frequency, by the horizontal axis. In this pattern, the modal amplitude at a given point is determined by the gradation of gray color. The scale of gradations for amplitude in relative units is shown at the top of the diagram. The position of the IW packet corresponding to this pattern is shown at the right and corresponds to the moment $t = 1600$ s. The vertical section of the diagram gives the spatial distribution (across the acoustic track) of intensity at a given frequency. It is seen that a similar dependence in our case always has a maximum (the field focusing in the horizontal plane), however, this focusing occurs at different points of space. For example, comparing the field intensity distributions in the transverse section at frequencies of 150 and 350 Hz (Fig. 5, vertical lines), we see that both dependences have maxima. However, these maxima are shifted relative to each other (in our case, by about 0.5 km). To understand the origin of this shift, one should analyze the patterns of horizontal rays for the corresponding frequencies, which are shown in Figs. 5b and 5c. It is seen that such a position of the packet corresponds to a defocusing of rays in the horizontal plane and causes a dip (white color) in the region $y_R \sim 0$. However, at a frequency of 350 Hz, a maximum is observed because of certain asymmetry of the packet shifted relative to the axis at the given moment. In this case, there is a group of rays undergoing the deviation from the lower (in our figure) maximum in the direction toward the acoustic track. This ray tube determines the location of the field maximum near $y_R \sim 0$. It is clear that for another location of the IW packet this pattern changes and one can note a nontrivial time effect. From diagram *5a*, we can conclude that the maximum of modal intensity in the transverse dependence (i.e., in the dependence on $x$) should move together with the packet if the fixed frequency is higher or lower than the resonance frequency, i.e., at frequencies $f < 300$ Hz and $f > 400$ Hz. The amplitude of this maximum is approximately the same in both cases. At $f \sim 350$ Hz, the maximum is located near the waveguide axis and its amplitude varies almost simultaneously with the passage of the packet. The horizontal section at the distance $y_R$ determines the frequency spectrum of the signal received at the point $(x_R, y_R)$. Figure 6 shows two examples of amplitude spectra for the third mode. It is seen that, at different distances from the axis, the forms of these spectra are different, which can qualitatively account for the different forms observed in the experiment [8]. Note that this figure corresponds to only one mode (the third). However, since the main contribution to the sound field is made by lower modes (in our case, by three to four modes), the variation of one of them considerably changes the characteristics of the total field. In addition, it is possible to select lower modes in the experiment and study the spectrum of each of them.

We believe that the results and analysis presented above and concerned with the features of spatial and frequency dependences of acoustic signals will be useful for setting experiments and analyzing the data on acoustic probing in the shelf zone of the ocean.

## ACKNOWLEDGMENTS

This work was supported by the Ministry of Education of Russian Federation and the CRDF, project no. VZ-010-0.

## REFERENCES

1. R. H. Headrick, J. F. Lynch, J. K. Kemp, *et al.*, J. Acoust. Soc. Am. **107**, 221 (2000).
2. M. Badiey, Y. Mu, J. Lynch, *et al.*, IEEE J. Ocean Eng. **27** (1), 117 (2002).
3. J. A. Colosi, R. C. Beardsley, J. F. Lynch, *et al.*, J. Geophys. Res. **106** (C5), 9587 (2001).
4. M. K. Hsu, A. K. Liu, and C. Liu, Cont. Shelf Res. **20**, 389 (2000).
5. X. Li, P. Clemente-Colon, and K. S. Friedman, in *Johns Hopkins APL Technical Digest* (2000), Vol. 21, No. 1, pp. 130–135.
6. B. G. Katsnel'son and S. A. Pereselkov, Akust. Zh. **46**, 779 (2000) [Acoust. Phys. **46**, 684 (2000)].
7. R. Oba and S. Finette, J. Acoust. Soc. Am. **111**, 769 (2002).
8. Ji-xun Zhou and Xue-zhen Zhang, J. Acoust. Soc. Am. **90**, 2042 (1991).
9. B. G. Katsnel'son and S. A. Pereselkov, Akust. Zh. **44**, 786 (1998) [Acoust. Phys. **44**, 684 (1998)].
10. *Sound Transmission through a Fluctuating Ocean*, Ed. by S. M. Flatte (Cambridge Univ. Press, Cambridge, 1979; Mir, Moscow, 1982).

*Translated by Yu. Lysanov*

*Acoustical Physics, Vol. 50, No. 2, 2004, pp. 177–184. Translated from Akusticheskiĭ Zhurnal, Vol. 50, No. 2, 2004, pp. 220–230.*


# A Frequency-Modulated-Carrier Digital Communication Technique for Multipath Underwater Acoustic Channels

**K. G. Kebkal, A. G. Kebkal, and S. G. Yakovlev**

*State Oceanarium of Ukraine, ul. Épronovskaya 7, Sevastopol, 99024 Ukraine*

*e-mail: kebkal@ua.fm*

Received February 26, 2003

**Abstract**—Along with interferences, multipath propagation and, in particular, its instability in shallow sea is the main obstacle to increasing the digital data transfer rate in underwater acoustic communication systems. Given these conditions, the use of simple waveforms, for which the product of bandwidth by the length of the processing interval is close to unity, makes testing the quality of the communication channel much more difficult and strongly limits the possibilities of devices that compensate for current waveform distortions, such as, for example, equalizers. In multipath channels with random parameters, various complex waveforms with different spectrum spreading techniques had been used for years. Complex waveforms with a large base (time–bandwidth product) offer advantages in efficiently suppressing narrowband interferences and providing asynchronous multiple-access communications. This paper proposes a new complex waveform, which uses sequences of chirp pulses. On receiving, this waveform can be divided into individual responses through converting the delays of these individual responses to frequency offsets. After a special frequency conversion of the received signal, the multipath responses are separated in the frequency domain by conventional band-pass filtering. *© 2004 MAIK "Nauka/Interperiodica".*

## 1. INTRODUCTION

The conditions of sound propagation in a shallow sea determine the structure of the received signal. As a result of the multipath propagation typical of such underwater sound channels, the received waveform is a superposition of time shifted pulses of various intensities rather than an isolated pulse. This superposition causes intersymbol interference and reduces the communication quality of the digital data transmission.

Digital underwater communication channels employ various systems, which can be divided into two main groups. The first group uses noncoherent communication techniques, such as frequency keying. They feature a high data transmission reliability, but the data transfer rate is low. Systems of the second group use phase-coherent techniques. They are recognized as providing a higher transfer rate. However, they apply complex processing algorithms and expensive bulky equipment, for example, phased antenna arrays for shaping a narrow transmitting pattern or distributed receiving antennas for finding the signal arrival direction on reception. Below, we concisely describe the advantages and disadvantages of the highest-performance digital communication systems.

The approach developed at Northeastern University (Boston, United States) and at WHOI (United States) is detailed in [1–3]. It uses a combined technique based on the adaptive transversal filter with optimal phase synchronization for suppressing intersymbol interference. This kind of system provides underwater data transfer rates as high as 20 kbit/s [2]. An advantage of this approach is that it is capable of improving the signal-to-noise ratio (SNR) by combining the energy of the signal that arrives through all paths. The application of this approach is, however, severely limited when the channel's impulse response rapidly varies [4, 5]. The rapidly variable multipath structure also creates difficulties for synchronization of the communication systems.

Another approach relies on antennas that feature a narrow transmitting pattern. This design produces a simpler multipath structure of the received signal [6]. Equalizers are not employed. Instead of them, the receiving side uses antennas that compensate for fluctuations in the arriving signal. However, the efficiency of this approach considerably degrades with an increase in the transmission range, especially when the transmitting and receiving systems change their relative positions.

One more approach was developed at Newcastle University. It adaptively shapes the receiving pattern and separates the remaining beams through the angular filtering of the multipath components [7]. This approach adaptively places nulls on the antenna pattern in the directions of arrival of the reflected beams using the least-squares method [8, 9]. As in the previous case, the performance of this system rapidly degrades with an increase in the transmission range [10]. To improve the performance, it was proposed to supply the system with an adaptive equalizer [8]. However, in this case, the system faced the problem of convergence of the solution produced by the equalizer, especially when operating through real rapidly fluctuating channels.

1063-7710/04/5002-0177$26.00 

According to [11], it is not the multipath propagation itself that limits the performance of underwater acoustic telemetry systems, but fluctuations of individual beams. The separation of multipath signal components so that each of them contains fluctuations associated with only one propagation path may become a key to improving the quality of processing the received signal. An attempt to separate the multipath signal components and process them individually was described in [12, 13]. A system with the differential quarternary phase-shift keying (DQPSK) was used in [12] to communicate through a 100-m-long horizontal channel with a known multipath structure (the time the intervals between the arrivals of the direct signal and subsequent components were known). The special time distribution of the signals allowed the system to complete the reception of each pulse before the arrival of the first significant multipath component. The average transfer rate was 1.6 kbit/s. The system, however, stopped working when the distance was increased to 200 m, because the intervals between the arrivals became too short. Underwater communication systems that spread the spectrum by the direct sequence method to separate the multipath components of the received signal were presented in [13]. The systems applied the DQPSK and provided a transfer rate of 625 bit/s. The spectrum was spread using a 16-chip (16-element) spreading code. The data transfer rate determined the initial bandwidth, while the 16-chip (element) per bit code spread the frequency spectrum of the transmitted signal by a factor of 16. The cited paper reported that this code must provide an approximately 0.1-ms time resolution of the multipath components. However, there were no experimental results that could verify such a resolution. The use of spectrum spreading techniques for providing multiple-access and secure underwater communications was also discussed in [14]. At a 5-mile distance, a data rate of 80 bit/s was attained with 500-Hz-wide waveforms. Another trial tested a 45-mile-long channel with 375-Hz-wide waveforms showing a 37.5-bit/s data rate.

As follows from the above examples, the application of spectrum spreading codes for the suppression of multipath interference in underwater acoustic channels is associated with low data rates. Clearly, this occurs because of physical and implementation limitations on the available frequency band. In fact, if the spread-spectrum waveform should be confined within a 10- to 20-kHz-wide frequency band, usual for underwater acoustic telemetry, then the original narrowband digital waveform must occupy an order of magnitude narrower band; i.e., the data rate should not exceed 1–2 kbit/s.

In this paper, we propose an alternative spectrum spreading technique for the transmitted signal that allows a receiver to separate the multipath components. Instead of spreading the spectrum by a pseudo-random code, we use a linear frequency modulation. This technique considerably increases the data rate over the modern spectrum spreading techniques. A significant advantage is that it separates the multipath components in the frequency domain rather than in time. For underwater acoustic channels, which are usually characterized by discrete (in propagation delay) multipath and random (rather slow) variation of their parameters, this technique is capable of accurately resolving (separating) the beams without such complicated processing systems as adaptive equalizers. The beams are separated through a special preprocessing and a usual bandpass filtering. As a result, the received multipath signals, which have a complex structure and are unstable in time, are transformed into a number of separate beams. Importantly, each multipath component is separated from the others with its individual phase and time distortions that it acquires when propagating along a particular path. After being separated, some (for example, the most intense) components can be extracted from the spectrum of the multipath signal and processed in order to reconstruct the transmitted message.

In the next section, we define the frequency-modulated carrier waveform and the model of its propagation through the multipath channel. Further, the section devoted to the experiment reports results on the digital data transmission tests through the multipath underwater acoustic channels. It should be noted that these were only proof-of-the-principle tests intended to prove the feasibility of the technique and its advantages described in the second section. No complex pulse modulation techniques were applied to form the narrowband digital signal. The tests employed the differential binary phase-shift keying (DBPSK).

## 2. FREQUENCY-MODULATED CARRIER SIGNAL AND ITS PROPAGATION THROUGH MULTIPATH CHANNELS

A feature of the technique is that a digital narrowband signal (symbol) modulates a carrier, whose frequency continuously changes. Let us call it the frequency-modulated carrier (FM carrier). Since the available frequency band is limited, the carrier frequency cannot change without limit. Therefore, such a carrier will consist of a sequence of frequency-modulated segments (FM segments) limited from above and from below by the operating frequency band.

An advantage of this solution for underwater acoustic communications is as follows. Usually, when a signal of a constant frequency is transmitted through a channel characterized by long and unstable reverberation, multipath components add together in such a manner that the phase and amplitude of the received (total) signal vary randomly. Under such adverse conditions, data transmission using the phase and(or) amplitude modulation becomes much more difficult or, under certain conditions, impossible. An additional modulation of the carrier may solve this problem. If the frequency slope is sufficiently large, each multipath component arriving at the receiver with its individual delay has its individual instantaneous frequency, which is noticeably different from the instantaneous frequencies of all the

other multipath components. For example, in the classical ray propagation, the instantaneous frequency of the reflected frequency-modulated signal (FM signal) lags behind the frequency of the direct FM signal, i.e., the signal that arrives at the receiver through the direct path. Under these conditions, the interference due to the beam superposition can be removed. The greater the FM slope is, the higher the resolution of the multipath components that can be achieved. Because acoustic signals propagate in water with a relatively low speed, FM slopes that provide a sufficient beam resolution are feasible.

Below, we give a mathematical definition of the frequency-modulated carrier signal and a mathematical model of the signal received after propagation through the multipath acoustic channel.

Let the carrier signal consist of a sequence of FM segments that lie in the frequency band from $\omega_L$ to $\omega_H$ and have the duration and repetition period $T_{sw}$. Let the frequency vary within each FM segment by the linear law (Fig. 2). Then, this carrier signal can be represented as

$$c(t) = A_c \exp\left[ j\left( \omega_L\left( t - \left|\frac{t}{T_{sw}}\right| T_{sw}\right) + m\left( t - \left|\frac{t}{T_{sw}}\right| T_{sw}\right)^2\right)\right], \quad (1)$$

where $A_c$ is the amplitude; the coefficient $m = (\omega_H - \omega_L)/2T_{sw}$ determines the frequency rate; $\omega_L$ and $\omega_H$ are the lowest and highest circular frequencies, respectively; $T_{sw}$ is the length of the chirp segment; and $|t/T_{sw}|$ is the integer part of $t/T_{sw}$.

By definition, we have

$$\left( t - \left\lfloor \frac{t}{T_{sw}} \right\rfloor T_{sw}\right) = \left\{ \frac{t}{T_{sw}} \right\} T_{sw}. \quad (2)$$

Expression (2), which enters into Eq. (1), can be interpreted as the current cyclic time $t_c$ with the cycle length $T_{sw}$, i.e., $t_c = \left\{ \frac{t}{T_{sw}} \right\} T_{sw}$.

Let a signal with carrier (1) be transmitted through an underwater acoustic channel whose simplified model is illustrated in Fig. 1. The source of information generates a narrowband digital signal $s(t)$, which modulates the FM carrier so that the transmitted signal is $x(t) = s(t)c(t)$. After traveling through the channel, the received signal denoted as $y(t)$ is demodulated by multiplying it by $c(t)$ and applied to a low-pass filter (LPF). The output of the LPF provides the recipient with an estimate of the transmitted narrowband digital signal. The part of the model that represents the signal propagation in water consists of the delay components $\tau_i$, which determine the time intervals between the multipath responses, and weights, which allow for the attenuation of each of the multipath responses in the channel. In real conditions, both weights $V_i$ and delays $\tau_i$ vary in time. To simplify the analysis, consider a short time interval on which the transmission path can be regarded as stable. Let $\tau_i$ and $V_i$ be constant. To simplify the notations, we assume that the received signal is intense enough that noise can be neglected. Then, the transmitted signal, after propagating through the multipath channel, can be represented as

$$y(t) = V_0 x(t) + \sum_i V_i x(t - \tau_i), \quad (3)$$

where $x(t)$ is defined above and $x(t - \tau_i)$ has the following form:

$$x(t - \tau_i) = s(t - \tau_i) \times \exp\left[ j\left( \omega_L\left\{ \frac{t - \tau_i}{T_{sw}} \right\} T_{sw} + m\left( \left\{ \frac{t - \tau_i}{T_{sw}} \right\} T_{sw}\right)^2\right)\right]. \quad (4)$$

The term in braces in formula (4) can be written as

$$\left\{ \frac{t - \tau_i}{T_{sw}} \right\} T_{sw} = \begin{cases} t_c - \tau_{ci}, & t_c \geq \tau_{ci} \\ T_{sw} + t_c - \tau_{ci}, & t_c < \tau_{ci}, \end{cases}$$

where $t_c = \left\{ \frac{t}{T_{sw}} \right\} T_{sw}$ is the cyclic time defined in Eq. (2) and $\tau_{ci} = \left\{ \frac{\tau_i}{T_{sw}} \right\} T_{sw}$ is the fractional part of the delay determined by the ratio of $\tau_i$ to the length of the FM segment $T_{sw}$.

Therefore, each delayed response (3) can be represented as

$$x(t - \tau_i) = \begin{cases} s(t - \tau_i)\exp[j(\omega_L(t_c - \tau_{ci}) + m(t_c - \tau_{ci})^2)], \\ t_c \geq \tau_{ci} \\ s(t - \tau_i)\exp[j(\omega_L(T_{sw} + t_c - \tau_{ci}) \\ + m(T_{sw} + t_c - \tau_{ci})^2)], \quad t_c < \tau_{ci}. \end{cases} \quad (5)$$

After transforming expression (5), each delayed multipath component can be written as

$$x(t - \tau_i) = s(t - \tau_i)\exp[j(\omega_L t_c + m t_c^2)] \times \exp[j(-\Delta\omega_i t_c + \varphi_i)], \quad (6)$$

where

$$\Delta\omega_i = \begin{cases} 2m\tau_{ci}, & t_c \geq \tau_{ci} \\ -2m(T_{sw} - \tau_{ci}), & t_c < \tau_{ci} \end{cases}$$

is the frequency excursion from the intermediate frequency of each $i$th multipath response received with the

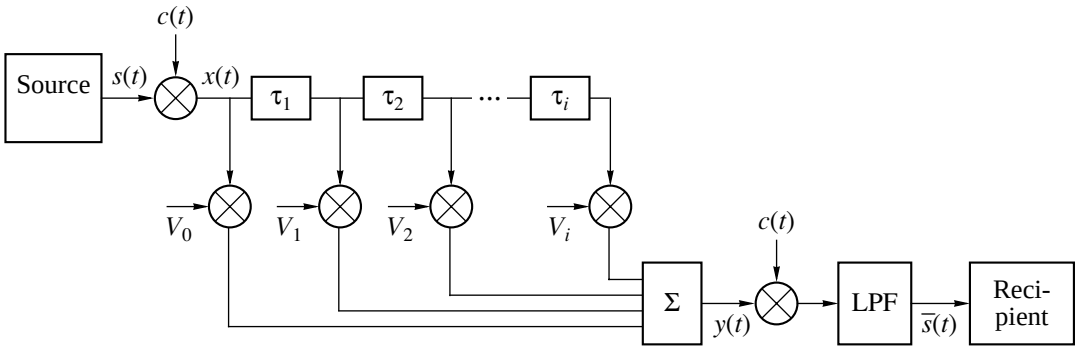


**Fig. 1.** Model of signal propagation through a multipath underwater sound channel.

delay $\tau_i$ and

$$\varphi_i = \begin{cases} (m\tau_{ci} - \omega_L)\tau_{ci}, & t_c \geq \tau_{ci} \\ (\omega_H + \omega_L - 2m\tau_{ci})\dfrac{T_{sw} - \tau_{ci}}{2}, & t_c < \tau_{ci} \end{cases}$$

is the phase of the *i*th multipath response.

The first term in formula (3) is a weighted copy of the original signal, the second is a weighted sum of the multipath components, which arrived with particular delays and, therefore, are shifted in frequency.

It should be noted that, in Eq. (6) at each instant of time, all multipath responses have different instantaneous frequencies, which differ by $\Delta\omega_i$ from the frequency of the direct signal. The technique relies on the fact that the FM carrier allows the receiver to transform the signal propagation delays through the multipath channel into frequency shifts of the multipath responses. The frequency separation (resolution) of the multipath responses having been performed, the signal distorted by the interference can be reconstructed in the frequency domain, where each spectral component (multipath response) can be extracted and processed separately [15]. Moreover, each multipath response, separable from the others, contains only the distortions that it acquires when propagating along the particular path. Clearly, each individual beam is simpler to analyze (and process) than a superposition of unseparated multipath components and, accordingly, than a superposition of distortions acquired by the signal as it propagates through different paths. When the beams are processed separately, the received multipath signal can be cleared from the noise and represented by a single multipath component or a number of components chosen for the combined processing in order to reconstruct the narrowband digital signal.

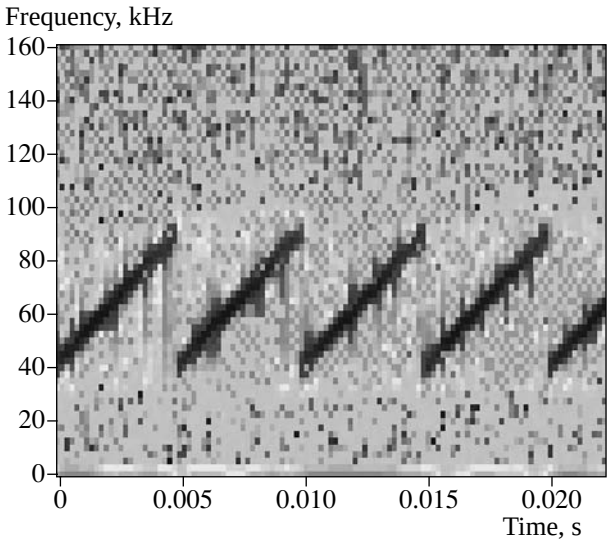


**Fig. 2.** Part of the spectrogram of the transmitted sounding signal.

## 3. EXPERIMENTAL

The material presented below was obtained in practical data transmission tests on August 24, 2001, in the inner water area of Kazach'ya bay (Sevastopol).

The acoustic channel was shallow. The depth at the test site gradually increased from 6 m on the receiver side to 8 m on the transmitter side. The transmitting and receiving transducers were carried by small-tonnage waterborne vehicles and lowered to depths of 4 and 5 m, respectively. The slant range was 210–230 m.

The operating conditions were as follows. The wind force was 6–8 m/s. The sea state was Beaufort 1.5–2. The surf at the nearby coastline, wind, and pulsed signals of a biological origin created a high noise level. The radiation intensity was 180 dB relative to 1 μPa/m. The SNR in the receiver was 11–14 dB. The transducer continuously changed its orientation in the course of transmission as a result of the rocking of the carrier vehicle. The instantaneous relative velocity of the transmitter and receiver was no higher than 2 m/s.

For the transmitter, we used a PCT Device 2 wideband piezoceramic transducer (UK). On transmission, it features a smooth amplitude-vs-frequency response with a 6-dB ripple in a 40 to 80 kHz frequency range. The transducer had a weak resonance at 57 kHz. Because of heavy damping in order to widen the oper-

ating bandwidth, the transducer had a low efficiency of no higher than 1%. To provide radiation intensity of up to about 180 dB relative to 1 μPa/m, we excited the transducer with a voltage of a peak value of up to 1200 V. To galvanically decouple the transmitting and receiving electroacoustic circuits, special electronic devices were developed.

All devices of the electroacoustic channel were mounted in a watertight container made of an aluminum–magnesium alloy. To reduce the noise level, the transducer was connected directly to the transmit–receive switch, whose other two ports were connected to the input of the preamplifier and output of the power amplifier. The power amplifier was fed from a VICOR VI-214 DC-DC dc transducers. A +24-V mains was applied through a cable from an external battery located on board the vehicle.

To form the transmitted waveforms and process the received acoustic signals, we used mobile Intel Pentium III-based computers. The computers were placed in splash-proof casings from ACME and supplied with high-speed analog I/O devices from National Instruments. The output analog signal was applied from the computer to the power amplifier through a cable. The amplified signal was fed through the transmit–receive switch to the underwater acoustic transducer to be emitted into the water. As the receiving transducer, we used a TC4034 wideband (from 5 to 350 kHz) instrument hydrophone from RESON. The hydrophone output signal was amplified and fed to an analog-to-digital converter (ADC). The sampling rate was 1 MHz. The data were preprocessed, time selected, demodulated, and recorded by a computer similar to the one used on the transmitting side.

### *3.1. Structure and Parameters of Transmitted Signals*

The data were transmitted in packets in the form of binary sequences consisting of 5000 to 10 000 information symbols. The sequences were produced by a standard quasi-random-number generator with fixed initial conditions. The DBPSK was applied to the narrowband digital signal. The carrier had the form of a sequence of frequency-modulated segments which followed without intervals. The carrier frequency was swept from 40 to 80 kHz. The length of the FM carrier segments used in our tests was 0.3 to 2 ms. Accordingly, the frequency-sweep rate was 20 to 133 kHz/ms. The symbols were 80 to 500 μs long. The data rate was 2 to 12 kbit/s.

To remove intersymbol interference, the carrier-frequency-sweep rate and the length of carrier segments were chosen so that multipath components of the current segment did not overlap with those of the next one, or the overlap was insignificant. To this end, a sounding signal consisting of ten chirp segments, used to estimate the structure of the multipath channel, was emitted immediately before transmitting the data. The sounding signal used more wideband and longer chirp segments than those used by the information carrying signal. The frequency of the sounding signal was swept from 40 to 90 kHz, and the length of the segment was 5 ms. The longer segments represented the multipath channel structure more clearly. Figure 2 shows part of the spectrogram of the emitted sounding signal. Figure 3 is a spectrogram of the same part of the received signal. Arrows in Fig. 3 indicate the most intense multipath components.

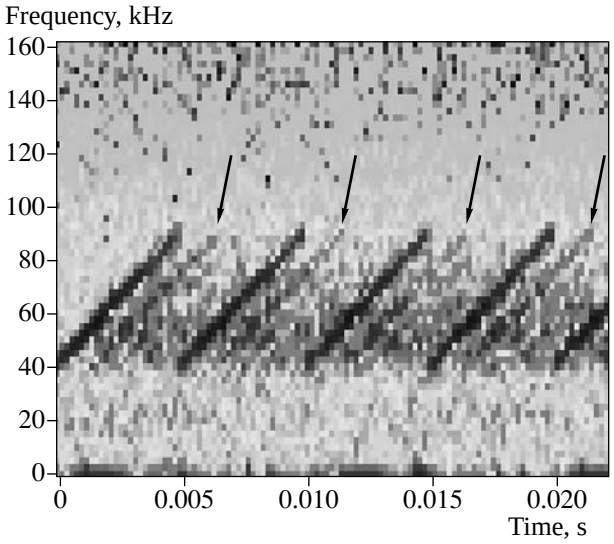


**Fig. 3.** Part of the spectrogram of the sounding signal on the receiver side.

### *3.2. Signal Processing on Reception*

After the received signal was synchronized, it was processed and demodulated, and the narrowband digital signal was subsequently estimated.

To demodulate the received signal, it was multiplied by a heterodyne frequency-modulated signal generated locally. It was identical to the carrier signal of the transmitting station. The multiplication produced two frequency bands: a high-frequency band at a double frequency with a factor of two greater chirp rate and a low-frequency band at the intermediate frequency with a zero chirp rate. If properly synchronized, the low-frequency range contained the central intermediate frequency, which is zero for the useful multipath component, and a number of spectral lines, which represent spurious multipath components shifted in time and frequency. The spurious spectral lines were filtered out by a low-pass filter.

Since we used the relative phase shift keying, the transmitted symbol was determined by the phase difference between consecutive pulses (narrowband digital signals). Phase differences within $0° \pm 90°$ referred to logical zero, while phase differences within $180° \pm 90°$ referred to logical unity.

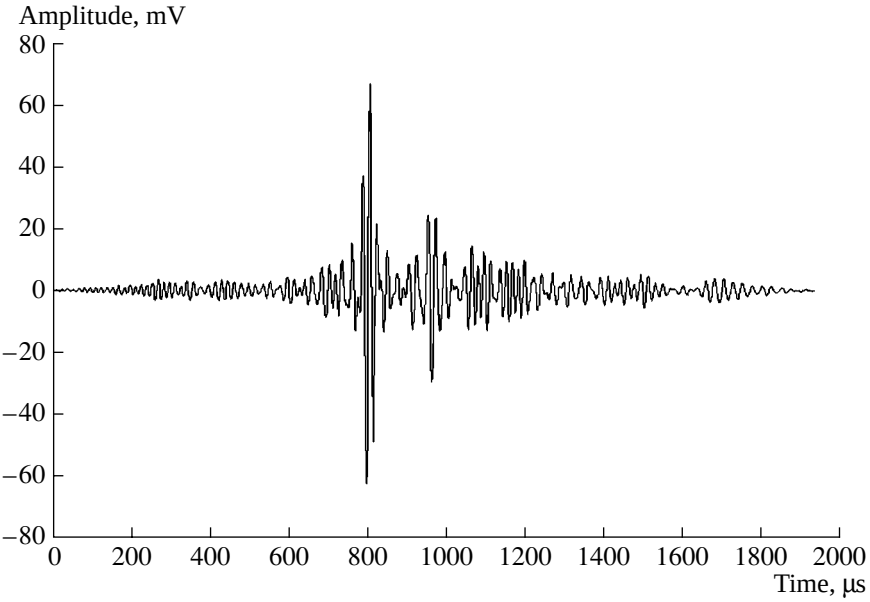


**Fig. 4.** Example of the impulse response of a multipath sound channel.

### *3.3. Channel Characteristics*

To estimate the properties of the data transmission channel, we sounded it with a test train of chirp signals. After the receiver calculated the cross-correlation function of the received and transmitted signals, the channel's multipath structure was represented as a sequence of responses whose time position, shape, and intensity could be used to estimate the channel's properties.

Figure 4 exemplifies the multipath nature of the channel through which data were transmitted immediately after the sounding sequence. The multipath propagation is represented by 3 to 4 responses. Our repeated observations have shown that power fluctuations in the multipath components were about 2 to 3 dB. The delay between the two first responses was 135 μs, which approximately agreed with the theoretical delay of the signal reflected from the surface (124 μs). The time interval occupied by the whole multipath response sequence was estimated to be 380 μs. Delays of the multipath components remained stable during the time necessary for transmitting a block of data.

### *3.4. Capacity of the Communication System*

Below, we provide an example of transmitting a sequence of binary signals through a shallow multipath underwater channel illustrated in Fig. 4. The data rate was 10.42 kbit/s. The carrier was modulated by sweeping its frequency from 40 to 80 kHz with a chirp rate of 83.3 kHz/ms. The length of the carrier segment was 480 μs. To compensate for the irregularity of the amplitude-vs-frequency response (on transmission), the amplitude of the chirp segments was corrected so that the emitted signal had approximately the same amplitude over the operating frequency range. The carrier segments were divided into five parts, each of which contained a 96-μs-long phase shift keyed symbol.

The phase angles of the received symbols are illustrated in Fig. 5. Despite the comparatively strong scatter in both angular sectors, the digital values of the phase shift keyed symbols are well distinguishable. Figure 6 shows the SNR in the course of the data transmission. As follows from this figure, the SNR deviated by 2.9 dB about its mean value of 11.5 dB. The most likely explanation of such a large deviation observed in a short data transmission time is that, in addition to a variation in the ambient noise, the fine structure of the multipath channel also changed (e.g., due to the rough sea), producing random short-term beams, which interfered with the useful signal and corrupted it.

To estimate the error level, we subtracted the known digital sequence produced by the source from the sequence processed by the receiver and supplied to the recipient. There were 9 errors almost uniformly distributed over 7200 transmitted symbols, so that the transmission error probability calculated as the ratio of the number of error symbols to the length of the transmitted sequence was 0.00125.

For the sake of comparison, other data and chirp rates were tested. Binary phase shift keying was also used. The transmitted data packets were 5000 bit long. For 165-μs-long symbols (or a data rate of 6061 bit/s) and 800-μs-long chirp segments, the error in the data transmission over 230 m was estimated as 0.00091. After the range was reduced to 100 m, the data were received without errors. In the trials at higher data rates with 90-μs-long symbols (11.1 kbit/s) and 380-μs-long chirp segments, the error probability estimate increased to 0.0109. There was no sense in further increasing the

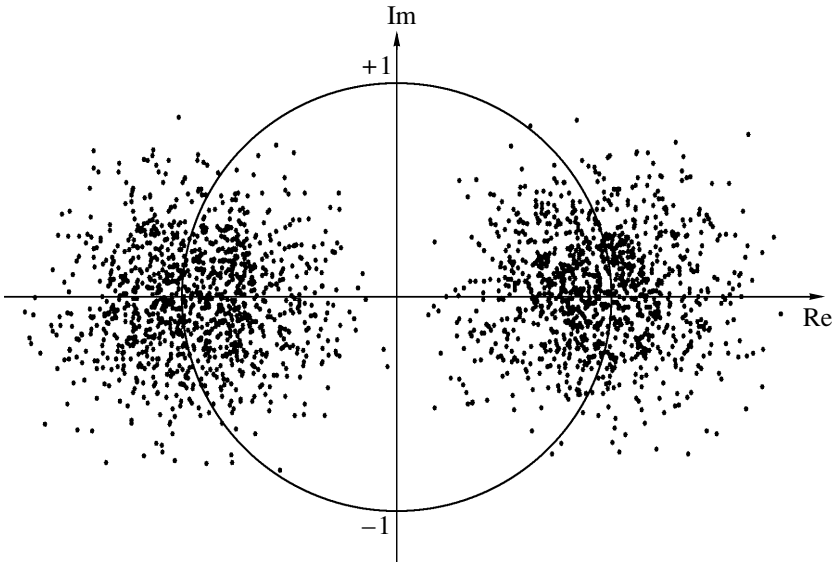


**Fig. 5.** Spread of the differential phase angles on the receiver side.

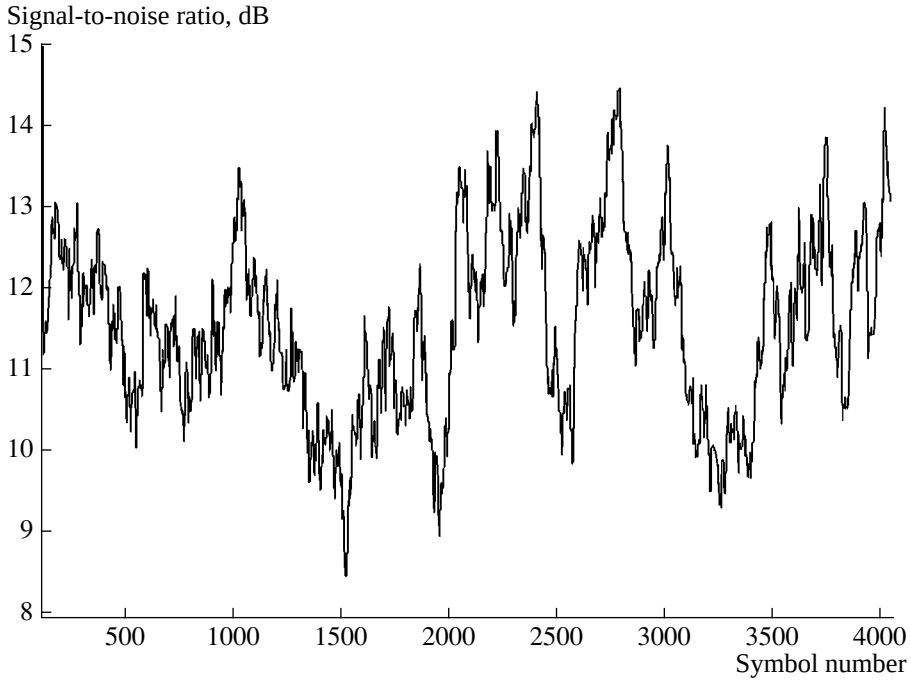


**Fig. 6.** Signal-to-noise ratio in the course of data transmission (at a data rate of 10.42 kbit/s).

data rate under these communication conditions because of the rapid increase in the error probability and emergence of group errors, which cannot be removed without special error-correcting codes.

### *3.5. Frequency Efficiency*

To estimate the results of the tests in terms of the data rate-to-bandwidth ratio, below we provide the data on the frequency efficiency of other underwater acoustic communication systems known from the literature. For noncoherent systems, this factor is usually within 0.01 to 0.15 Baud/Hz) [16]. Only one noncoherent system with a frequency efficiency as high as 0.24 Baud/Hz is known [16]. These systems are applied in the most complex (from the viewpoint of data transmission) shallow underwater channels. Partially coherent systems that use the differential phase shift keying have a frequency efficiency of 0.06 to 2 Baud/Hz. It should be noted that, although differential phase shift keying systems do not require carrier tracking, they are sensitive to intersymbol interference and their application is therefore limited with few exceptions to simple

(in terms of digital data transfer) deep vertical channels. Review [16] contains detailed information about the capacity of such systems. Only one frequency-coherent data transmission system for shallow horizontal channels, which was used in communications over a distance of 100 m, is known. Its frequency efficiency is as low as 0.16 Baud/Hz.

The highest frequency efficiency is exhibited by coherent systems. It is usually within 0.67 to 2 Baud/Hz.

Since the communication system reported in Section 2 uses differential phase shift keying, it compares with partially coherent systems. Its frequency efficiency, determined by the ratio of the achieved data rate to bandwidth, is $(11.1 \times 10^3)/(40 \times 10^3) = 0.28$ Baud/Hz. As follows from the comparison, this value is much greater than the frequency efficiency of noncoherent systems and also of frequency-coherent systems used for communications through shallow underwater sound channels.

## 4. DISCUSSION AND CONCLUSIONS

Both theoretical and experimental results demonstrated a high efficiency of the technique in reducing the effect of multipath interference in communications through shallow horizontal underwater acoustic channels.

The main distinctive feature of the technique is its complex carrier signal, which consists of sequences of chirp segments with a high chirp rate. After propagating through a shallow underwater acoustic channel, this signal, being corrupted with reverberation interference, can be separated into individual multipath components. The multipath components are separated in the frequency domain and, depending on the length of a single digital symbol (data rate), the received signal can be partially or completely cleared from the effect of multipath interference.

To estimate the advantages of this technique, we tried various parameters of carrier signal modulation and various communication ranges and data rates. Our tests of the data transmission over a range of 230 m at a data rate of 6061 bit/s with 800-μs-long chirp carrier segments demonstrated an error probability of 0.00091. In a similar test with a shorter range (100 m), no errors were observed in the transmission of a 5000-bit-long data package. In the test at a higher data rate (11.1 kbit/s) with 380-μs-long chirp segments, the error probability increased to 0.0109. This higher demodulation error can be attributed to the fact that the carrier signal became more poorly matched with the transmission channel. For example, when a current carrier segment overlapped one of the lagged replicas of the previous chirp segments, intersymbol interference was observed and the communication quality degraded.

An important index of the system's capacity is its frequency efficiency defined as the ratio of the data rate to bandwidth occupied by the transmitted signal. Its maximum value for the technique proposed here is 0.28 bit/Hz. Compared to conventional systems, the frequency-modulated carrier signal considerably increased the frequency efficiency and, accordingly, the potential data rate.

The above material relies on the analysis of data transmission using differential binary phase-shift keying. The bandwidth of these symbols is known to be the same as that necessary for the DQPSK. The hardware and software developed, which provides a data rate of 11.1 kbit/s, is thus suitable for data transmission at twice as high a rate by changing the phase modulation technique to the DQPSK. However, to keep the noise immunity of the DQPSK signal at the same level as that of the DBPSK signal, the power of the emitted signal should be increased by at least 3 dB [16, 17].

An important feature of the frequency-modulated carrier is that it provides the possibility of processing the multitude of separated multipath components in parallel. After synchronizing the beams in their propagation delay, such processing can combine the energies of the separated beams and thus increase the SNR in the receiver and improve the reliability of estimating the transmitted digital signal.

## REFERENCES

1. M. Stojanivic, J. A. Catipoivich, and J. G. Proakis, J. Acoust. Soc. Am. **94**, 1621 (1993).
2. M. Stojanivic, J. A. Catipoivich, and J. G. Proakis, IEEE J. Ocean Eng. **19** (1), 100 (1994).
3. M. Stojanivic, IEEE J. Ocean Eng. **21** (2), 125 (1996).
4. T. S. Yang and A. Al-Kurd, in *Proceedings of 16th International Congress on Acoustics* (Seattle, Washington, 1998), Vol. 1, p. 301.
5. J. L. Spiesberger and P. F. Worcester, J. Acoust. Soc. Am. **70**, 565 (1981).
6. R. Galvin and R. F. W. Coates, in *Proceedings of Oceans'94* (Brest, France, 1994), p. III.478.
7. O. R. Hinton *et al.*, in *Proceedings of EUSIPCO'94* (Edinburgh, 1994), p. 1540.
8. G. S. Howe *et al.*, in *Proceedings of Oceans'94* (Brest, France, 1994), p. I.313.
9. J. A. Neasham *et al.*, in *Proceedings of Oceans'96* (Ft. Lauderdale, Fl, 1996), p. 988.
10. S. P. D. Tarbit *et al.*, in *Proceedings of Oceans'94* (Brest, 1994), p. I.307.
11. J. A. Catipovich, IEEE J. Ocean Eng. **15** (3), 205 (1990).
12. G. S. Howe, O. R. Hinton, A. E. Adams, and A. G. J. Holt, Electron. Lett. **28**, 449 (1992).
13. J. H. Fischer, K. R. Bennet, O. R. S. A. Reible, *et al.*, presented at *Oceans'92, Newport, RI* (1992).
14. G. Loubert, V. Capellano, and R. Filipiak, presented at *Oceans'97, Halifax, Nova Scotia, Canada* (1997).
15. R. Bannasch and K. Kebkal, Patent PCT/DE99/02628.
16. D. B. Kilfoyle and A. B. Baggeroer, IEEE J. Ocean. Eng. **25** (1), 4 (2000).
17. S. U. H. Qureshi, in *Advanced Digital Communications: Systems and Signal Processing Techniques*, Ed. by K. Feher (Prentice Hall, Englewood Cliffs, N.J., 1987).

*Translated by A. Khzmalyan*

*Acoustical Physics, Vol. 50, No. 2, 2004, pp. 185–191. Translated from Akusticheskiĭ Zhurnal, Vol. 50, No. 2, 2004, pp. 231–237.*


# Photothermoacoustic Oscillations in a Solid–Piezoelectric Layered Structure

**V. V. Kozachenko and I. Ya. Kucherov**

*Department of Physics, Shevchenko National University, pr. Glushkova 2, Kiev, 03127 Ukraine*

*e-mail: victorc@univ.kiev.ua*

Received January 22, 2003

**Abstract**—Photothermoacoustic oscillations in a thin plane-layered structure consisting of an isotropic solid and a piezoelectric crystal of class 6*mm* (or piezoelectric ceramics) are studied theoretically and experimentally. Expressions for the potential difference across an arbitrary layer of the piezoelectric transducer are derived. For the case of a two-layer transducer, the amplitude–frequency and phase–frequency dependences of the signal are analyzed. It is shown that, from these experimental dependences, one can determine certain elastic and thermal parameters of a solid. An experiment is performed with samples of Cu, Zn, and TsTS-19 piezoceramics in the frequency range within 9–1000 Hz. The experimental data are used to determine the values of the reduced Young's modulus and the thermal diffusivity of the materials under study. *© 2004 MAIK "Nauka/Interperiodica".*

In the last few years, a growing interest has been expressed in acoustic studies with contactless excitation of acoustic vibrations and waves on the basis of the photothermoacoustic (PTA) effect [1–3]. The PTA effect is as follows: when a modulated light beam is incident on a material, the absorption of light leads to the heating of this material and to the excitation of thermal waves in both the material and the surrounding gas; owing to the thermoelastic effect, the temperature field formed in the material and in the gas generates acoustic vibrations and waves. A specific feature of the PTA effect is the dependence of the information obtained from it on the method used for detecting acoustic vibrations. One of the most sensitive methods for detecting a PTA signal is the piezoelectric method [1]. For acoustic studies of solids, the PTA effect in plates offers considerable promise [4–8]. The problem of the PTA effect in plates with piezoelectric detection is rather complicated in the general case and, hence, can only be solved for particular cases [4–6]. The problem considered in [6] most closely fits the experimental conditions. However, the cited publication only considers the case of a strong attenuation of thermal waves, i.e., when the thermal waves do not reach the piezoelectric transducer. This assumption imposes certain limitations on the frequency of thermal waves and on the sample thickness: the latter must be greater than the thermal diffusion length. The limitation on the thickness is especially inconvenient because, in most cases, objects of investigation are thin layered structures. In addition, most piezoelectric transducers are made of piezoceramics, and the latter is a strong pyroelectric. Therefore, if a thermal wave reaches the piezoelectric transducer, it is necessary to take into account the pyroelectric effect. Hence, a study of the PTA effect in a plate with a piezoelectric detection of acoustic vibrations and without any limitations imposed on the relation between the object thickness and the thermal diffusion length seems to be rather topical. Below, we present the results of theoretical and experimental studies of this problem.

Let us consider a layered structure formed by an isotropic solid and a piezoelectric crystal of class 6*mm* (or piezoelectric ceramics). The structure is shaped as a plate bounded by two planes $z = 0$ and $h$ ($h = h_1 + h_2$) and a cylindrical lateral surface with a closed directrix (Fig. 1). (*1*) The sample of the material under investigation has a thickness $h_1$; (*2*) the piezoelectric crystal has a thickness $h_2$ and is assumed to be isotropic in its thermomechanical properties. The polar axis of the piezoelectric crystal coincides with the $Z$ axis. The sample surface $z = 0$ is uniformly illuminated with a modulated light beam

$$P = \frac{1}{2}P_0(1 + \cos\omega t), \qquad (1)$$

where $P_0$ is the light intensity and $\omega$ is the cyclic modulation frequency.

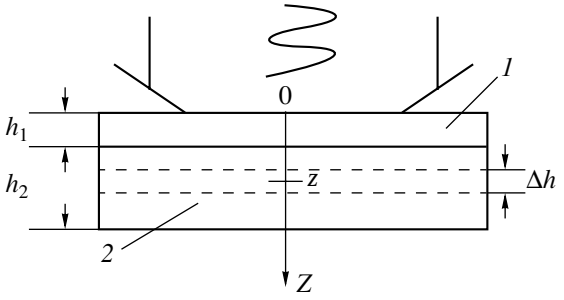


**Fig. 1.** Geometry of the problem.

1063-7710/04/5002-0185$26.00 © 2004 MAIK "Nauka/Interperiodica"

We first consider the case when light is strongly absorbed by the material under investigation ($\alpha h_1 \gg 1$, where $\alpha$ is the coefficient of light absorption in the material). The absorption of light changes the temperature of the sample surface in proportion to the absorbed light energy, which gives rise to thermal waves propagating along the $Z$ axis. Owing to the thermoelastic effect, acoustic vibrations are excited in the system. Let us consider relatively low light modulation frequencies, at which the acoustic wavelength far exceeds the characteristic dimensions of the plate (the quasi-static approximation) and the plate can be considered as thin. In this case, the nonzero components of the elastic stress tensor will be $T_{11}$ and $T_{22}$. Since the materials forming the structure are assumed to be homogeneous in their elastic and thermal properties, we have $T_{11} = T_{22} \equiv T$. Then, for the structure under consideration, we can write [9]

$$T = E_n(C_1 - C_2 z - \alpha_T \theta), \tag{2}$$

where $E_n = \dfrac{E}{1-\sigma}$, $\alpha_T$, and $\theta$ are the reduced Young's modulus ($E$ is Young's modulus and $\sigma$ is Poisson's ratio), the linear coefficient of thermal expansion, and the temperature of the sample (piezoelectric transducer), respectively, and $C_1$ and $C_2$ are constants determined from the boundary conditions.

Acoustic vibrations of the plate give rise to an electric polarization in the piezoelectric. In addition, since the piezoelectric under consideration is a pyroelectric, the thermal wave propagating in it should also produce a pyroelectric field. In the case under study, the normal component of the electric induction in the piezoelectric, $D_z$, is determined as

$$D_z = \varepsilon_{33} E_z + 2d_{31} T_n + p\theta_n, \tag{3}$$

where $\varepsilon_{33}$, $d_{31}$, and $p$ are the dielectric permittivity, piezoelectric constant, and pyroelectric constant of the piezoelectric material, respectively, and $T_n$ and $\theta_n$ are the elastic stress and temperature in the piezoelectric.

Let us calculate the potential difference $\hat{U}$ in a piezoelectric layer of thickness $\Delta h$ with a coordinate $z$ (Fig. 1). This difference is a measure of the acoustic vibrations excited in the system and is expressed as

$$\hat{U} = -\int_{z-\frac{\Delta h}{2}}^{z+\frac{\Delta h}{2}} E_z dz. \tag{4}$$

Since external electric fields are absent and the normal component of the electric induction is continuous, we have $D_z = 0$. From this condition, using Eq. (3), we obtain

$$E_z = -\frac{2d_{31}}{\varepsilon_{33}} T_n - \frac{p}{\varepsilon_{33}} \theta_n. \tag{5}$$

Now, let us determine the distribution of the alternating component of temperature $\theta$ in the structure under study. For this purpose, it is necessary to solve the heat conduction equation with the corresponding boundary conditions.

For the sample and the piezoelectric, the heat conduction equations in the complex form and the boundary conditions (the continuity of the heat flow and temperature) are as follows [1]:

the heat conduction equation for the sample is

$$\frac{\partial^2 \theta}{\partial z^2} - \frac{c\rho}{\chi}\frac{\partial \theta}{\partial t} = -\frac{\alpha P_0}{2\chi} e^{-\alpha z} e^{i\omega t}, \tag{6}$$

the heat conduction equation for the piezoelectric is

$$\frac{\partial^2 \theta_n}{\partial z^2} - \frac{c_n \rho_n}{\chi_n}\frac{\partial \theta_n}{\partial t} = 0 \tag{7}$$

and the boundary conditions (neglecting the heat flow to the surrounding medium) are

$$\left.\frac{\partial \theta}{\partial z}\right|_{z=0} = 0, \quad \chi \left.\frac{\partial \theta}{\partial z}\right|_{z=h_1} = \chi_n \left.\frac{\partial \theta_n}{\partial z}\right|_{z=h_1},$$
$$\theta|_{z=h_1} = \theta_n|_{z=h_1}, \quad \left.\frac{\partial \theta_n}{\partial z}\right|_{z=h_1+h_2} = 0. \tag{8}$$

In the above expressions, $c$, $\rho$, and $\chi$ are the specific heat, density, and thermal conductivity coefficient of the sample and $c_n$, $\rho_n$, and $\chi_n$ are the corresponding parameters of the piezoelectric. We assume that all the light energy absorbed by the sample is spent for its heating. The solution to Eq. (6) has the form

$$\theta = (\theta_{11} e^{\gamma z} + \theta_{12} e^{-\gamma z} - \theta_{13} e^{-\alpha z}) e^{i\omega t},$$
$$\theta_{13} = \frac{\alpha P_0}{2\chi(\alpha^2 - \gamma^2)}, \tag{9}$$

and the solution to Eq. (7) is

$$\theta_n = (\theta_{21} e^{-\gamma_n (z-h_1)} + \theta_{22} e^{\gamma_n (z-h_1)}) e^{i\omega t}. \tag{10}$$

The coefficients $\theta_{11}$, $\theta_{12}$, $\theta_{21}$, and $\theta_{22}$ are determined from boundary conditions (8). They depend in a complex way on the thermal and geometric parameters of the structure and on the modulation frequency of light. When heat does not reach the surface $z = h_1 + h_2$, i.e., when the thermal wave completely attenuates in the structure ($\theta_n(h_1 + h_2) = 0$); this case is considered below), the expressions for $\theta_{mn}$ are simplified and take the form

$$\theta_{11} = \frac{\alpha(1-b)e^{-\gamma h_1}}{2\gamma s}\theta_{13}, \quad \theta_{12} = \frac{\alpha(1+b)e^{\gamma h_1}}{2\gamma s}\theta_{13},$$
$$\theta_{21} = \frac{\alpha\theta_{13}}{\gamma s}, \quad \theta_{22} = 0, \tag{11}$$

$$b = \frac{\gamma_n \chi_n}{\gamma \chi}, \quad s = \sinh(\gamma h_1) + b\cosh(\gamma h_1),$$

$$\gamma = \sqrt{\frac{c\rho\omega}{2\chi}}(1+i), \quad \gamma_n = \sqrt{\frac{c_n\rho_n\omega}{2\chi_n}}(1+i).$$

Substituting Eq. (10) into Eq. (5) with allowances for Eqs. (2) and (11), we obtain the potential difference $\hat{U}$ across a piezoelectric layer of thickness $\Delta h$:

$$\hat{U} = \frac{2d_{31}E_{nn}}{\varepsilon_{33}}\left\{(C_1 - C_2 z)\Delta h - \frac{2\alpha_{Tn}\theta_{21}}{\gamma_n}\left(1 - \frac{p}{2d_{31}E_{nn}\alpha_{Tn}}\right)e^{-\gamma_n(z-h_1)}\sinh\left(\gamma_h\frac{\Delta h}{2}\right)\right\}, \quad (12)$$

where $E_{mn}$ and $\alpha_{Tn}$ are the reduced Young's modulus and linear coefficient of thermal expansion of the piezoelectric, respectively. Here and below, the time factor is omitted.

Constants $C_1$ and $C_2$ are determined from the following boundary conditions: the resultant force and the resultant moment per unit length of the structure contour should be equal to zero [9], i.e.,

$$\int_0^h T dz = 0, \quad \int_0^h T z dz = 0. \quad (13)$$

Substituting Eq. (2) into Eqs. (13) with allowance for Eqs. (9)–(11) and the relation $\alpha \gg \gamma$, we obtain

$$C_1 - C_2 z = \frac{\alpha_T E_0 h P_0 (Z - Z_p)\left(\frac{2q}{\gamma h}n - \psi\right)}{2\chi s(\gamma h)^2 (Z_p - Z_u)[1 + (E_0 - 1)H_1]}, \quad (14)$$

$$Z_p = \frac{2}{3}\frac{1 + (E_0-1)H_1^3}{1 + (E_0-1)H_1^2}, \; Z_u = \frac{1}{2}\frac{1 + (E_0-1)H_1^2}{1 + (E_0-1)H_1}, \quad (15)$$

$$q = b\sinh(\gamma h_1) + \cosh(\gamma h_1) - 1 - b\gamma h_1 + \frac{\alpha_0 D_0}{E_0}(\gamma_n h_1 + 1),$$

$$\psi = \sinh(\gamma h_1) + b\cosh(\gamma h_1) - b + \frac{\alpha_0\sqrt{D_0}}{E_0},$$

$$n = \frac{Z - Z_u}{2Z_u(Z - Z_p)}, \; E_0 = \frac{E_n}{E_{nn}}, \; \alpha_0 = \frac{\alpha_{Tn}}{\alpha_T}, \; D_0 = \frac{D_{Tn}}{D_T},$$

$$Z = \frac{z}{h}, \quad H_1 = \frac{h_1}{h},$$

where $D_T = \dfrac{\chi}{c\rho}$ and $D_{Tn} = \dfrac{\chi_n}{c_n\rho_n}$ are the thermal diffusivities of the sample and the piezoelectric, respectively. One can easily show that the geometric parameters $Z_p$ and $Z_u$ actually represent the coordinates of neutral planes after normalization to $h$: $Z_p$ corresponds to the neutral plane of the structure under surface tension and $Z_u$, to the neutral plane of the structure under pure bending.

Substituting Eq. (14) into expression (12) for $\hat{U}$, we finally obtain

$$\hat{U} = U_m\{G_1 + G_2\}, \quad (16)$$

$$G_1 = (Z - Z_p)\left(\frac{2q}{\gamma h}n - \psi\right)\Delta H,$$

$$G_2 = \frac{\sqrt{D_0}Z_0}{\alpha_T E_n}\left(\frac{p}{d_{31}} - 2\alpha_{Tn}E_{nn}\right)e^{-\gamma_n(z-h_1)}\sinh\left(\gamma_n\frac{\Delta h}{2}\right),$$

$$Z_0 = (Z_p - Z_u)[1 + (E_0 - 1)H_1], \quad \Delta H = \frac{\Delta h}{h},$$

$$U_m = \frac{d_{31}\alpha_T E_n P_0}{\varepsilon_{33}\chi\gamma^2 Z_0[\sinh(\gamma h_1) + b\cosh(\gamma h_1)]}.$$

The first term in Eq. (16), $G_1$, is associated with the thermoelastic deformation of the piezoelectric (the piezoelectric component), and the second term, $G_2$, with the heating (the pyroelectric component).

An analysis of expression (16) shows that, when the thermal wave completely attenuates in the sample $\gamma h_1 \gg 1$ (i.e., does not reach the piezoelectric transducer), the first term in Eq. (16) predominates and the voltage $\hat{U}$ is proportional to the thermoelastic coefficient ($\alpha_T E_n$) of the material under study. This means that, at fixed parameters of light ($P_0$, $\omega$), the amplitude of acoustic vibrations in the given structure is mainly governed by the thermoelastic properties of the sample.

The pyroelectric part of the voltage consists of two components: the first is caused by the true pyroelectric effect and the second, by the secondary pyroelectric effect.

Depending on the relation between coordinate $Z$ of the layer from which the electric signal is taken and coordinate $Z_p$, the piezoelectric component of the signal may be as follows: $G_1 > 0$ when $Z > Z_p$, $G_1 < 0$ when $Z < Z_p$, and $G_1 = 0$ when $Z = Z_p$. In the latter case, the PTA signal is determined by the pyroelectric effect alone.

Consider the case of a two-layer piezoelectric transducer proposed in [6]. Assuming that the layers of the transducer have the same thickness $\dfrac{h_2}{2}$, we obtain the following expression for the ratio between the voltages

taken from these layers:

$$\frac{\hat{U}_1}{\hat{U}_2} = \frac{(Z_1 - Z_p)\left(\frac{2q}{\gamma h}n_1 - \psi\right)\frac{H_2}{2} + G_0\left(1 - e^{-\frac{\gamma_n h_2}{2}}\right)}{(Z_2 - Z_p)\left(\frac{2q}{\gamma h}n_2 - \psi\right)\frac{H_2}{2} + G_0 e^{-\frac{\gamma_n h_2}{2}}}, \quad (17)$$

$$G_0 = \frac{\sqrt{D_0}Z_0}{2\alpha_T E_n}\left(\frac{p}{d_{31}} - 2\alpha_{Tn}E_{3n}\right), \quad H_2 = \frac{h_2}{h},$$

where $\hat{U}_1$, $\hat{U}_2$, $Z_1$, $Z_2$, $n_1$, and $n_2$ are the respective quantities for the first layer, which lies next to the sample, (subscript 1) and the second layer (subscript 2) of the piezoelectric transducer.

Formula (17) takes into account that the thermal wave completely attenuates in the structure under study (i.e., does not reach the surface $z = h$). From this formula one can see that, at relatively high modulation frequencies, when the thermal wave does not reach the piezoelectric transducer, the second terms in the numerator and denominator tend to zero and $q = \psi = 1$. Then, expression (17) takes the form

$$\frac{\hat{U}_1}{\hat{U}_2} = \frac{(Z_1 - Z_p)\left(\frac{2n_1}{\gamma h} - 1\right)}{(Z_2 - Z_p)\left(\frac{2n_2}{\gamma h} - 1\right)}, \quad (18)$$

which coincides with the results reported in [6], where only this particular case was considered. At relatively low modulation frequencies, when the thermal wave does reach the piezoelectric transducer, The PTA signal is influenced by the pyroelectric effect and the ratio $\left(\frac{\hat{U}_1}{\hat{U}_2}\right)$ varies noticeably with the frequency.

From Eq. (16), one can see that, in the case under consideration, the ratio $\left(\frac{\hat{U}_1}{\hat{U}_2}\right)$ depends on the parameters of the structure and on the light modulation frequency in a complex way, which is difficult to analyze. However, for a specific structure, the amplitude–frequency and phase–frequency dependences of the PTA signal can be calculated by numerical methods.

Let us analyze some particular cases.

(i) We assume that the material under study is a heat-conducting material (like a metal) and $\gamma\chi \gg \gamma_n\chi_n$; i.e., the thermal wave is almost completely reflected from the piezoelectric transducer (the heat almost does not penetrate into the transducer). In this case, Eq. (17) takes the form

$$\frac{\hat{U}_1}{\hat{U}_2} = \frac{(Z_1 - Z_p)\left(\frac{2(\cosh(\gamma h_1) - 1)}{\gamma h}n_1 - \sinh(\gamma h_1)\right)}{(Z_2 - Z_p)\left(\frac{2(\cosh(\gamma h_1) - 1)}{\gamma h}n_2 - \sinh(\gamma h_1)\right)}. \quad (19)$$

From Eq. (19), we determine the amplitude ratio $\left(\frac{U_1}{U_2}\right)$ of signals taken from individual layers of the piezoelectric transducer and the phase difference $\Delta\varphi = \varphi_1 - \varphi_2$ between these signals:

$$\frac{U_1}{U_2} = \frac{Z_1 - Z_p}{Z_2 - Z_p}\sqrt{\frac{(m\sinh\beta - n_1)^2 + (m\sin\beta - n_1)^2}{(m\sinh\beta - n_2)^2 + (m\sin\beta - n_2)^2}}, \quad (20)$$

$$\tan(\Delta\varphi) = \frac{m(\sinh\beta - \sin\beta)(n_1 - n_2)}{2n_1n_2 + m^2(\sinh^2\beta + \sin^2\beta) - m(\sinh\beta + \sin\beta)(n_1 + n_2)}, \quad (21)$$

where

$$m = \frac{(\cosh\beta - \cos\beta)\sqrt{F}}{(\cosh\beta\cos\beta - 1)^2 + (\sinh\beta\sin\beta)^2}, \quad \beta = H_1\sqrt{F},$$

$F = \frac{\pi h^2}{D_T}f$ is the dimensionless frequency, and $f = \frac{\omega}{2\pi}$.

An analysis of Eqs. (20) and (21) shows that, at relatively high frequencies satisfying the condition $\frac{1}{\sqrt{F}} \ll 1$ ($\beta \gg 1$), the amplitude ratio $\left(\frac{U_1}{U_2}\right)$ and the tangent of the phase difference $\tan(\Delta\varphi)$ are approximately linear functions of $\frac{1}{\sqrt{F}}$:

$$\frac{U_1}{U_2} = \frac{(Z_1 - Z_p)}{(Z_2 - Z_p)}\left(1 - (n_1 - n_2)\frac{1}{\sqrt{F}}\right), \quad (22)$$

$$\tan(\Delta\varphi) = \frac{n_1 - n_2}{\sqrt{F}}. \quad (23)$$

These high-frequency properties of the amplitude–frequency, $\frac{U_1}{U_2}\left(\frac{1}{\sqrt{F}}\right)$, and phase–frequency, $\tan(\Delta\varphi)\left(\frac{1}{\sqrt{F}}\right)$, dependences of the PTA signal can be used to determine some elastic and thermal parameters of the sample material, including the reduced Young's modulus $E_n$ and the thermal diffusivity $D_T$. Indeed, by extrapolating the experimental dependence $\frac{U_1}{U_2}\left(\frac{1}{\sqrt{F}}\right)$ to the region

$\frac{1}{\sqrt{F}} \longrightarrow 0$, we determine the quantity $\frac{(Z_1 - Z_p)}{(Z_2 - Z_p)}$ and, hence, the quantity $Z_p$. From expression (15) for $Z_p$, using the known geometric parameters of the structure and the known reduced Young's modulus of the piezoelectric transducer, we determine $E_n$. Knowing $E_n$, from the slope of dependence (22) or dependence (23), we determine the thermal diffusivity $D_T$ of the sample material.

(ii) Now, we assume that the thermal and elastic properties of the material under study are close to those of the transducer material (such sample materials are mainly dielectrics): $D_0$, $\alpha_0$, $E_0 \approx 1$. In this case, expression (17) takes the form

$$\frac{\hat{U}_1}{\hat{U}_2} = \frac{\left(Z_1 - \frac{2}{3}\right)\left(\frac{2n_1}{\gamma h} - 1\right)\frac{H_2}{2} - G_{i0}\left(1 - e^{-\frac{\gamma h_2}{2}}\right)e^{-\frac{\gamma h_1}{2}}}{\left(Z_2 - \frac{2}{3}\right)\left(\frac{2n_2}{\gamma h} - 1\right)\frac{H_2}{2} + G_{i0}e^{-\gamma\left(h_1 + \frac{h_2}{2}\right)}}, \quad (24)$$

where $G_{i0} = \frac{1}{6}\left(\frac{p}{2d_{31}\alpha_{Tn}E_{3n}} - 1\right)$.

In the particular case when both sample and transducer are made of TsTS-19 piezoceramics, which is often used in practice (PZT-type ceramics), with both the sample thickness and the transducer layer thickness are about 1 mm, the quantities $e^{-\gamma h_{1,2}}$ are negligibly small for frequencies beginning from several hertz. In this case, we obtain

$$\frac{\hat{U}_1}{\hat{U}_2} = -\left(\frac{4}{\gamma h} - 1\right)^{-1}. \quad (25)$$

From Eq. (25), we derive

$$\frac{U_1}{U_2} = -\sqrt{\frac{F}{4 + (2 - \sqrt{F})^2}}, \quad (26)$$

$$\tan(\Delta\varphi) = \frac{2}{2 - \sqrt{F}}. \quad (27)$$

From expressions (26) and (27), one can see that, if the sample and the piezoelectric transducer are made of the same material and the layers of the transducer and the sample have the same thickness, the amplitude–frequency (26) and phase–frequency (27) dependences do not depend on the elastic parameters of the material and are governed by thermal diffusivity alone. Hence, only this parameter can be determined experimentally.

In the case of relatively high frequencies, $\left(\frac{1}{\sqrt{F}} \ll 1\right)$, expressions (26) and (27) take the form

$$\frac{U_1}{U_2} = -\left(1 + \frac{2}{\sqrt{F}}\right), \quad (28)$$

$$\tan(\Delta\varphi) = -\frac{2}{\sqrt{F}}. \quad (29)$$

Experimental studies were performed with samples made of Cu, Zn, and TsTS-19 piezoceramics. The piezoelectric transducer consisted of two identical layers of TsTS-19 piezoceramics, each of them being 0.6 mm thick. The samples and the transducer had the form of circular plates 15 mm in diameter. The thickness of different samples was as follows: 0.97 and 1.64 mm for Cu, 1.13 mm for Zn, and 0.6 mm for TsTS-19. The sample surface was uniformly illumi-

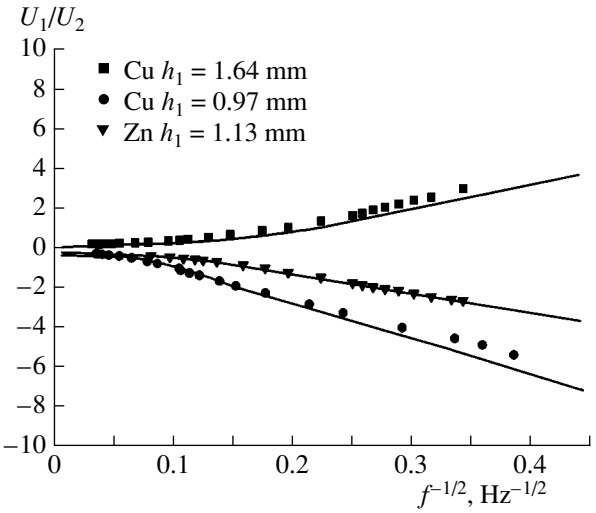


**Fig. 2.** Amplitude ratio $\left(\frac{U_1}{U_2}\right)$ of signals taken from individual layers of the piezoelectric transducer versus the inverse square root of frequency ($f^{-1/2}$) for Cu and Zn: dots represent the experiment and solid lines, the theory.

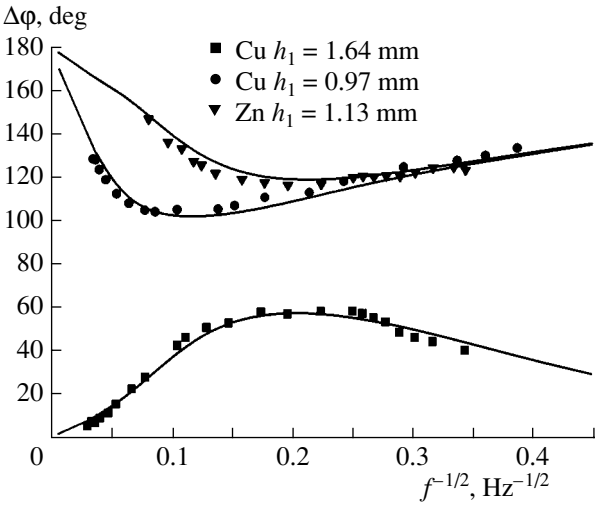


**Fig. 3.** Phase difference (Δφ) between signals taken from individual layers of the piezoelectric transducer versus the inverse square root of the frequency ($f^{-1/2}$) for Cu and Zn: dots represent the experiment and solid lines, the theory.

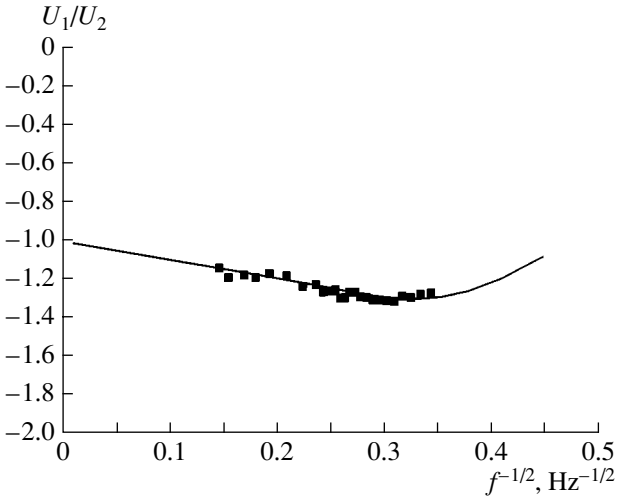


**Fig. 4.** Amplitude ratio $\left(\frac{U_1}{U_2}\right)$ of signals taken from individual layers of the piezoelectric transducer versus the inverse square root of frequency ($f^{-1/2}$) for TsTS-19: dots represent the experiment and solid lines, the theory.

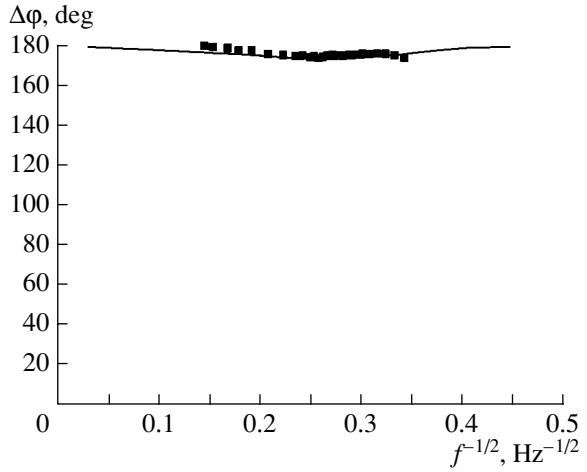


**Fig. 5.** Phase difference (Δφ) between signals taken from individual layers of the piezoelectric transducer versus the inverse square root of the frequency ($f^{-1/2}$) for TsTS-19: dots represent the experiment and solid lines, the theory.

nated with modulated light. In the experiment with low modulation frequencies (up to 100 Hz), the light was produced by 25 light-emitting diodes (LEDs) (λ = 700 nm) distributed over a parabolic surface, and in the experiment with high modulation frequencies, the source of light was a laser (λ = 687 nm). The light from the LEDs was modulated by varying the current flowing through them, and the laser light was modulated by an electromechanical chopper. The studies were performed in the frequency range within 9–1000 Hz. The quantities determined from the experiment were the amplitude ratios $\left(\frac{U_1}{U_2}\right)$ and the phase differences $\Delta\varphi = \varphi_1 - \varphi_2$ of signals taken from individual layers of the transducer as functions of the light modulation frequency $f$. The informative signal was measured by a lock-in nanovoltmeter. The relative measurement error was different for different modulation frequencies: it increased with frequency and did not exceed 10% in the high-frequency region of the frequency range used in the experiments.

**Table**

| Material | Reduced Young's modulus, $\times 10^{10}$ N/m$^2$ | | Thermal diffusivity, $\times 10^{-6}$ m$^2$/s | |
|---|---|---|---|---|
| | experiment | literature | experiment | literature |
| Cu | 22 | 12–20 | 100 | 117 |
| Zn | 11 | 11–12 | 40 | 37–42 |
| TsTS-19 | – | – | 0.4 | – |

The results of the experimental studies are represented by dots in Figs. 2–5. From these experimental data, by the method described above, we determined the reduced Young's modulus $E_n$ and the thermal diffusivity $D_T$ for Cu and Zn; for TsTS-19 piezoceramics, we determined only $D_T$. The resulting values are presented in the table. For comparison, the table also shows data taken from the literature [10, 11]. Using the experimental values of $E_n$ and $D_T$, we calculated the theoretical dependences $\left(\frac{U_1}{U_2}\right)(f)$ and $(\Delta\varphi(f))$ from Eq. (17) for Cu and Zn and from Eqs. (26) and (27) for TsTS-19. These dependences are shown in Figs. 2–5 by solid lines. The elastic, piezoelectric, and pyroelectric parameters of TsTS-19 were taken from [12, 13]. From Figs. 2–5, one can see that the experimental data agree well with the theoretical calculations.

Thus, we derived expressions for the potential difference across an arbitrary layer of a piezoelectric transducer in the presence of PTA oscillations in a solid–piezoelectric layered structure. For the case of a two-layer piezoelectric transducer, we analyzed the amplitude–frequency and phase–frequency dependences of signals taken from individual layers of the transducer. We showed that, in the high-frequency region, the amplitude ratio $\left(\frac{U_1}{U_2}\right)$ and the tangent of the phase difference $\tan(\Delta\varphi)$ of signals taken from individual layers of the transducer depend almost linearly on the inverse square root of the frequency $\left(f^{-\frac{1}{2}}\right)$. This feature made it possible to determine some elastic and thermal parameters of solids from experimental data. For samples whose material has the same elastic and thermal parameters as the piezoelectric transducer and whose thickness is greater than the thermal diffusion length, the amplitude–frequency and phase–frequency dependences of the PTA signal are only determined by

the thermal diffusivity, which can be found from the experiments. Experimental data were obtained for samples of Cu, Zn, and TsTS-19 piezoceramics and proved to agree well with the theoretical calculations. These data were used to determine the thermal diffusivities for all samples; for Cu and Zn, we also determined the reduced Young's moduli.

## REFERENCES


1. A. Rozencwaig, *Photoacoustics and Photoacoustic Spectroscopy* (Wiley, New York, 1980).
2. L. M. Lyamshev, *Laser Thermooptical Excitation of Sound* (Nauka, Moscow, 1989).
3. V. É. Gusev and A. A. Karabutov, *Laser Optical Acoustics* (Nauka, Moscow, 1991).
4. W. Jachson and N. M. Amer, Appl. Phys. **51**, 3343 (1980).
5. Yu. V. Gulyaev, A. I. Morozov, and V. Yu. Raevskiĭ, Akust. Zh. **31**, 469 (1985) [Sov. Phys. Acoust. **31**, 278 (1985)].
6. D. A. Andrusenko and I. Ya. Kucherov, Zh. Tekh. Fiz. **69** (12), 1 (1999) [Tech. Phys. **44**, 1397 (1999)].
7. M. L. Lyamshev, Akust. Zh. **46**, 844 (2000) [Acoust. Phys. **46**, 743 (2000)].
8. S. A. Vinokurov, Inzh.–Fiz. Zh. **45**, 570 (1984).
9. A. D. Kovalenko, *Thermoelasticity* (Vishcha Shkola, Kiev, 1975).
10. G. W. C. Kaye and T. H. Laby, *Tables of Physical and Chemical Constants and Some Mathematical Functions*, 16th ed. (Longman, New York, 1995; Fizmatgiz, Moscow, 1962).
11. *Tables of Physical Data: Reference Book*, Ed. by I. K. Kikoin (Atomizdat, Moscow, 1976).
12. *Piezoceramic Transducers*, Ed. by S. I. Pugachev (Sudostroenie, Leningrad, 1984).
13. A. Lukashyavichus, P. Sladki, and V. Kubechek, Nauchn. Tr. Vyssh. Uchebn. Zaved. LitSSR, Ul'trazvuk **16**, 37 (1984).


*Translated by E. Golyamina*

*Acoustical Physics, Vol. 50, No. 2, 2004, pp. 192–194. Translated from Akusticheskiĭ Zhurnal, Vol. 50, No. 2, 2004, pp. 238–241.*


# Absorption of Bending Waves in a Plate Driven by a Normal Force Source Encircled with Monopole–Dipole Resonators

**A. D. Lapin**

*Andreev Acoustics Institute, Russian Academy of Sciences, ul. Shvernika 4, Moscow, 117036 Russia*
*e-mail: mironov@akin.ru*

Received June 17, 2003

**Abstract**—The field produced by a harmonic point source of normal force in a plate with resonators is studied. The origin of the force is encircled with a ring of closely spaced identical monopole–dipole resonators responsive to both the displacement and tilt of the plate. For these resonators, parameters are determined that ensure the complete absorption of the divergent cylindrical bending wave generated in the plate by the point source of normal force. © *2004 MAIK "Nauka/Interperiodica".*

Previously, the simplest resonator for bending waves in a rod was studied, this resonator being responsive to both the displacement and tilt (the derivative of the displacement) of the rod axis [1]. The resonator consists of two spring-mass systems attached to the rod, along which a bending wave propagates via a hard (unbendable) bar common to both systems. One of these spring-mass systems is oriented perpendicularly to the rod and serves as a monopole resonator responsive to the rod displacements, and the other is oriented along the rod and serves as a dipole resonator responsive to the tilt of the rod. Under the action of an incident bending wave, monopole and dipole resonators begin to oscillate and produce, via the hard bar, a point normal force and a point bending moment applied to the rod. In the rod, the scattered field is the sum of the monopole and dipole fields generated by these point sources. It was shown that, in the rod, a single monopole–dipole resonator completely absorbs the incident bending wave of resonance frequency if the dissipative loss coincides with the radiation loss. Note that a single monopole resonator with the optimal friction can absorb no more than half the energy of the incident bending wave. Theoretical and experimental investigations of vibration insulation for bending waves with the use of monopole resonance systems was carried out in [2–8].

In practice, the issue of the day is the problem of the absorption of bending waves generated by a point source in a plate. This problem can be solved with the use of a system of monopole–dipole resonators attached to the plate. Let us encircle the origin of force on the plate with a ring of closely spaced identical monopole–dipole resonators and orient the horizontal spring-mass systems along the ring radius. One can expect that monopole–dipole resonators with an appropriate friction will completely absorb the divergent cylindrical bending wave generated in the plate by the point source at resonance frequency.

Let an unbounded think plate lie in the *xy* plane and a harmonic normal force $f(t) = f_0\exp(-i\omega t)$ act on it at the point (0, 0). If the plate had no resonators, the bending waves excited by this point source would have the displacements

$$w_0(r, t) = \frac{if_0}{8k^2D}\{H_0^{(1)}(kr) - H_0^{(1)}(ikr)\}\exp(-i\omega t), \quad (1)$$

where $k = \sqrt[4]{\frac{\rho\omega^2}{D}}$ is the wave number of the bending wave; $H_0^{(1)}(kr)$ is the Hankel function of the first kind; $r = \sqrt{x^2 + y^2}$; and ρ and $D$ are the surface density and flexural rigidity of the plate, respectively. In Eq. (1), the first and second terms describe the propagating and evanescent (damped) cylindrical waves, respectively. Let us attach closely spaced identical monopole–dipole resonators to the plate along the circle $r = r_0$. By "spreading" these resonators over the circumference, it is possible to characterize the circular resonance system by the parameters determined per unit length of the circumference. The figure shows the section of the plate with attached resonators by the plane passing through the vertical axis *z*; in the figure, marker *1* points to the vertical spring-mass system with linear elastic stiffness $\kappa_1(1 - i\varepsilon_1)$, marker *2* points to the horizontal spring-mass system with linear elastic stiffness $\kappa_2(1 - i\varepsilon_2)$, $\varepsilon_1$ and $\varepsilon_2$ are the linear dissipation coefficients), $m_1$ and $m_2$ are the linear masses of the monopole and dipole resonators, marker *3* points to the hard bar of length *H*, and marker *4* points to the plate. Under the action of harmonic cylindrical waves (1), the resonators oscillate

1063-7710/04/5002-0192$26.00 © 2004 MAIK "Nauka/Interperiodica"

and create a linear normal force $F(t)$ and a linear bending moment $M(t)$ applied to the plate. The equation of motion of the plate with the attached resonators can be written in the form

$$\rho\frac{\partial^2 w}{\partial t^2} + D\Delta^2 w = F(t)\delta(r-r_0) - M(t)\delta'(r-r_0), \quad (2)$$

where $\Delta$ is the Laplace operator and $\delta(r-r_0)$ and $\delta'(r-r_0)$ are the delta-function and its derivative.

We denote $\xi_1(t)$ the displacement of mass $m_1$ from the equilibrium position along the $z$ axis and $\xi_2(t)$ the displacement of mass $m_2$ from the equilibrium position in the radial direction. Then, the equations of motion of the resonators have the form

$$m_1\ddot{\xi}_1(t) = -F(t), \quad m_2\ddot{\xi}_2(t) = -g(t), \quad (3)$$

where the forces $F(t)$ and $g(t)$ are given by the formulas

$$F(t) = \kappa_1(-i\varepsilon_1)[\xi_1(t) - w(r_0, t)], \quad (4)$$

$$g(t) = \kappa_2(1-i\varepsilon_2)\left[\xi_2(t) + H\left(\frac{\partial w}{\partial r}\right)_{r=r_0}\right] = -M(t)/H, \quad (5)$$

and $w(r, t)$ is the total field in the plate, which is equal to the sum of the incident and scattered fields.

In the case of harmonic incident field (1), the normal force and bending moment can be represented as $F(t) = F_0\exp(-i\omega t)$ and $M(t) = M_0\exp(-i\omega t)$, where $F_0$ and $M_0$ are the complex amplitudes of the force and the moment, respectively. In accordance with Eq. (2), the scattered field in the plate is the sum of the monopole ($w_1$) and dipole ($w_2$) fields determined by the formulas

$$w_1(r, t) = \frac{i\pi r_0 F_0}{4k^2 D}\{H_0^{(1)}(kr_0)J_0(kr) - H_0^{(1)}(ikr_0)J_0(ikr)\}\exp(-i\omega t), \quad r < r_0, \quad (6)$$

$$w_1(r, t) = \frac{i\pi r_0 F_0}{4k^2 D}\{J_0(kr_0)H_0^{(1)}(kr) - J_0(ikr_0)H_0^{(1)}(ikr)\}\exp(-i\omega t), \quad r > r_0, \quad (7)$$

$$w_2(r, t) = -\frac{i\pi r_0 M_0}{4kD}\{H_1^{(1)}(kr_0)J_0(kr) - iH_1^{(1)}(ikr_0)J_0(ikr)\}\exp(-i\omega t), \quad r < r_0, \quad (8)$$

$$w_2(r, t) = -\frac{i\pi r_0 M_0}{4kD}\{J_1(kr_0)H_0^{(1)}(kr) - iJ_1(ikr_0)H_0^{(1)}(ikr)\}\exp(-i\omega t), \quad r > r_0, \quad (9)$$

where $J_0(kr)$ and $J_1(kr)$ are the Bessel functions. The total field in the plate is $w = w_0 + w_1 + w_2$.

Let us choose the amplitudes $F_0$ and $M_0$ so as to satisfy relationships (4) and (5). In accordance with Eq. (3), the displacements of the masses will be

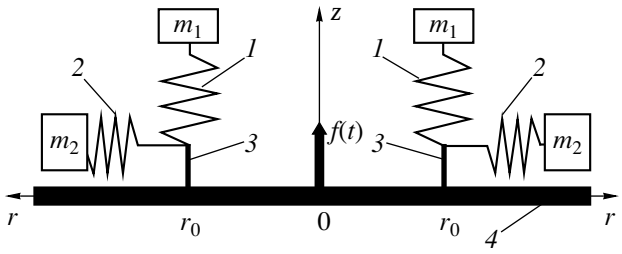


Monopole–dipole absorber of bending waves generated by a point source of normal force in a plate.

$$\xi_1(t) = \frac{F_0}{m_1\omega^2}\exp(-i\omega t), \qquad \xi_2(t) = -\frac{M_0}{Hm_2\omega^2}\exp(-i\omega t). \quad (10)$$

Substituting Eqs. (1), (7), (9), and (10) into Eqs. (4) and (5), we obtain equations for the force and moment amplitudes:

$$(Y_{10} + Y_{11})F_0 + GM_0 = i\omega w(r_0),$$
$$H^2 GF_0 + (Y_{20} + Y_{22})M_0 = i\omega H^2\left(\frac{\partial w_0}{\partial r}\right)\Big|_{r=r_0}, \quad (11)$$

where

$$Y_{10} = i\left[\frac{1}{\omega m_1} - \frac{\omega}{\kappa_1(1-i\varepsilon_1)}\right], \qquad Y_{20} = i\left[\frac{1}{\omega m_2} - \frac{\omega}{\kappa_2(1-i\varepsilon_2)}\right], \quad (12)$$

$$Y_{11} = -i\omega\frac{w_1(r_0, t)}{F(t)} = \frac{\pi\omega r_0}{4k^2 D}[J_0(kr_0)H_0^{(1)}(kr_0) - J_0(ikr_0)H_0^{(1)}(ikr_0)], \quad (13)$$

$Y_{10}$ and $Y_{20}$ are the conductivities of the monopole and dipole resonators,

$$Y_{22} = -i\omega H^2\frac{1}{F(t)}\left(\frac{\partial w_2}{\partial r}\right)_{r=r_0} = \frac{\pi\omega r_0 H^2}{4D}[J_1(kr_0)H_1^{(1)}(kr_0) + J_1(ikr_0)H_1^{(1)}(ikr_0)], \quad (14)$$

$$G = -i\omega\frac{w_2(r_0 t)}{M(t)} = -\frac{\pi\omega r_0}{4kD}[J_1(kr_0)H_0^{(1)}(kr_0) - iJ_1(ikr_0)H_0^{(1)}(ikr_0)], \quad (15)$$

and $w_0(r) \equiv w_0(r, t)\exp(+i\omega t)$ is the complex amplitude of the displacement in the incident wave.

Solutions to Eqs. (11) have the form

$$F_0 = i\omega\frac{\left[(Y_{20}+Y_{22})w_0(r_0) - GH^2\left(\frac{\partial w_0}{\partial r}\right)_{r=r_0}\right]}{[(Y_{10}+Y_{11})(Y_{20}+Y_{22}) - H^2G^2]},$$

$$M_0 = i\omega H^2\frac{\left[(Y_{10}+Y_{11})\left(\frac{\partial w_0}{\partial r}\right)_{r=r_0} - Gw(r_0)\right]}{[(Y_{10}+Y_{11})(Y_{20}+Y_{22}) - H^2G^2]}.$$

Substituting these expressions for $F_0$ and $M_0$ into Eqs. (6)–(9), we obtain the scattered fields of monopole and dipole types.

Now, we determine the resonator parameters ensuring that the cylindrical wave diverging from the point source $f(t) = f_0\exp(-i\omega t)$ is completely absorbed. For this purpose, we find the force and moment amplitudes that satisfy the following requirements:

(i) the divergent homogeneous cylindrical wave is absent in the total field $w = w_0 + w_1 + w_2$ outside the ring (for $r > r_0$),

(ii) homogeneous (propagating) cylindrical waves are absent in the scattered field $w_1 + w_2$ inside the ring (for $r < r_0$).

Using the relationships that express these requirements and taking into account Eqs. (1) and (6)–(9), we obtain the following expressions:

$$F_0 = -\frac{i}{4}kf_0H_1^{(1)}(kr_0), \quad M_0 = -\frac{i}{4}f_0H_0^{(1)}(kr_0). \quad (16)$$

Let us choose the conductivities $Y_{10}$ and $Y_{20}$ so that expressions (16) satisfy Eqs. (11). The desired conductivities are

$$Y_{10} = -\frac{i\omega}{2k^3DH_1^{(1)}(kr_0)} \times\left\{\left[1 - i\frac{2}{\omega}k^2DG\right]H_0^{(1)}(kr_0) - H_0^{(1)}(ikr_0)\right\} - Y_{11}, \quad (17)$$

$$Y_{20} = \frac{i\omega H^2}{2kDH_0^{(1)}(kr_0)} \times\left\{\left[1 + i\frac{2}{\omega}k^2DG\right]H_1^{(1)}(kr_0) - iH_1^{(1)}(ikr_0)\right\} - Y_{22}, \quad (18)$$

where the quantities $Y_{11}$, $Y_{22}$, and $G$ are given by formulas (13), (14), and (15), respectively. Resonators with conductivities (17) and (18) completely absorb the divergent cylindrical wave of frequency $\omega$.

Assume that the radius of the ring is much greater than the wavelength of the bending wave ($kr_0 \gg 1$). In this case, formulas (17) and (18) are simplified and take on the form

$$Y_{10} = \frac{\omega}{4k^3D}(1-i), \quad Y_{20} = \frac{\omega H^2}{4kD}(1+i).$$

Separating the real and imaginary parts in these approximate formulas, we obtain the expressions

$$\varepsilon_1 = \frac{\kappa_1}{4k^3D}, \quad \frac{1}{\omega m_1} - \frac{\omega}{\kappa_1} + \frac{\omega}{4k^3D} = 0,$$

$$\varepsilon_2 = \frac{\kappa_2H^2}{4kD}, \quad \frac{1}{\omega m_2} - \frac{\omega}{\kappa_2} - \frac{\omega H^2}{4kD}.$$

These expressions mean that the dissipative losses in the monopole and dipole resonators are equal to the radiation losses and that the natural frequencies of these resonators coincide. The ring consisting of such monopole–dipole resonators completely absorbs the divergent cylindrical wave in a thin plate. In a thicker plate, two such resonator rings attached to the plate from above and from below will completely absorb the divergent bending wave generated by a point source, because no scattered longitudinal wave will be generated in the plate owing to the symmetry of the problem.

## REFERENCES

1. A. D. Lapin, Akust. Zh. **50**, 99 (2004) [Acoust. Phys. **50**, 77 (2004)].
2. I. I. Klyukin, Akust. Zh. **6**, 213 (1960) [Sov. Phys. Acoust. **6**, 209 (1960)].
3. I. I. Klyukin and Yu. D. Sergeev, Akust. Zh. **10**, 60 (1964) [Sov. Phys. Acoust. **10**, 49 (1964)].
4. V. V. Tyutekin and A. P. Shkvarnikov, Akust. Zh. **18**, 441 (1972) [Sov. Phys. Acoust. **18**, 369 (1972)].
5. M. A. Isakovich, V. I. Kashina, and V. V. Tyutekin, Akust. Zh. **23**, 384 (1977) [Sov. Phys. Acoust. **23**, 214 (1977)].
6. *Acoustics Handbook*, Ed. by Malcolm J. Crocker (Wiley, New York, 1997).
7. M. Gurgoze and H. Batan, J. Sound Vibr. **195** (1), 164 (1996).
8. M. Gurgoze, J. Sound Vibr. **223** (4), 667 (1999).

*Translated by A. Vinogradov*

*Acoustical Physics, Vol. 50, No. 2, 2004, pp. 195–200. Translated from Akusticheskiĭ Zhurnal, Vol. 50, No. 2, 2004, pp. 242–248.*


# Diffraction Focusing of Acoustic Fields in Oceanic Waveguides Smoothly Varying along the Track

**Yu. V. Petukhov**

*Institute of Applied Physics, Russian Academy of Sciences, ul. Ul'yanova 46, Nizhni Novgorod, 603950 Russia*
*e-mail: petukhov@hydro.appl.sci-nnov.ru*

Received November 27, 2002

**Abstract**—With the use of adiabatic and WKB approximations for the mode representation of an acoustic field excited by a tone source in an oceanic waveguide smoothly varying along the track, dependences of the characteristic spatial scales of the phenomenon of diffraction focusing are obtained. Conditions that should be satisfied for the formation of zones of diffraction focusing of the acoustic field in such a waveguide are formulated.


As is known from the literature [1–3], by analogy with the formation of diffraction images of periodic structures in optics [4], the phenomenon of diffraction focusing can be observed for acoustic waves propagating in some waveguide media. The formation of the zones of diffraction focusing of acoustic fields in range-independent oceanic waveguides was considered in detail in [5–11].

The purpose of this paper is to study the effect of a smooth horizontal variability of the parameters of an oceanic waveguide on the formation of zones of diffraction focusing of an acoustic field.

To solve the above-stated problem, let us use the adiabatic approximation for the mode representation of the acoustic field in a waveguide smoothly varying along the track by assuming that the conditions of applicability of this approximation are satisfied [12–16]. Then, the dependence of the acoustic field intensity $J(r, z)$ on the horizontal distance $r$ and reception depth $z$ is expressed by the formula

$$J(r,z) = 2\pi p_0^2 \frac{R_0^2}{r}\left\{\sum_{l=1}^{L}|A_l(r,z)|^2 + \sum_{l\neq l'\,l'=1}^{L}\sum^{L} A_l(r,z)A_{l'}(r,z)\cos\left[\frac{2\pi r}{\bar{R}_{l,l'}}\right]\right\}. \quad (1)$$

Here,

$$A_l(r,z) = \psi_l(z_s,0)\psi_l(z,r)/\sqrt{k_l(r)} \quad (2)$$

is the amplitude of the mode of number $l$, $k_l(r)$ is the wave number of this mode, $\psi_l(z, r)$ is the corresponding orthonormal eigenfunction determined for the reference waveguide, $L = \max\{l\}$ is the number of modes excited at the cyclic frequency of transmission $\omega$, $z_s$ is the source depth, and $p_0$ is the amplitude of pressure perturbation produced by a point source in the corresponding homogeneous medium at a spherical surface of radius $R_0$. Expression (1) also involves the quantity

$$\bar{R}_{l,l'}(r) = r/\int_0^r \frac{dr}{R_{l,l'}(r)}, \quad (3)$$

which corresponds to the spatial scale of interference of modes with numbers $l$ and $l'$, where

$$R_{l,l'}(r) = \frac{2\pi}{k_l(r)-k_{l'}(r)}. \quad (4)$$

Using the results reported in [5], by analogy with range-independent oceanic waveguides, we introduce the following quantity that is necessary for subsequent consideration:

$$\bar{R}_g(l,l';n,n';r) = \frac{\bar{R}_{l,l'}(r)\bar{R}_{n,n'}(r)}{|\bar{R}_{l,l'}(r)-\bar{R}_{n,n'}(r)|} = \frac{r}{\left|\int_0^r \frac{dr}{R_g(l,l';n,n';r)}\right|}. \quad (5)$$

This quantity characterizes the spatial scale of the rearrangement of the interference structure formed by the field of two pairs of modes with numbers $l$, $l'$ and $n$, $n'$, where

$$R_g(l,l';n,n';r) = \frac{R_{l,l'}(r)R_{n,n'}(r)}{|R_{l,l'}(r)-R_{n,n'}(r)|}. \quad (6)$$

Evidently, dependences $R_{l,l'}(r)$ and $R_g(l, l'; n, n'; r)$ (Eqs. (4) and (6)) can be interpreted as the periods of interference of modes with numbers $l$ and $l'$ and the periods of rearrangement of interference structure formed by different pairs of modes with numbers $l$, $l'$ and $n$, $n'$ for the reference waveguide.

As in [5], in the range-dependent oceanic waveguides under consideration, the constructive interference of different pairs of constructively interfering modes is characterized by the quantity $\bar{R}_g(l, l'; n, n'; r)$ given by Eq. (5), which determines the possibility of a noticeable manifestation of the diffraction focusing of an acoustic field in spatial regions

$$m\bar{R}_{\min}(r) \le r \le m\bar{R}_{\max}(r) \quad (m = 1, 2, \ldots). \tag{7}$$

The changes that occur with distance in the characteristic minimal

$$\bar{R}_{\min}(r) = \min\{\bar{R}_g(l, l'; n, n'; r)\} \tag{8}$$

and maximal

$$\bar{R}_{\max}(r) = \max\{\bar{R}_g(l, l'; n, n'; r)\} \tag{9}$$

spatial scales of diffraction focusing lead not only to displacements of the zones of diffraction focusing along the $r$ axis but also to changes in the width of these zones:

$$\begin{aligned} \Delta R_m(r) &= m\Delta\bar{R}(r), \\ \Delta\bar{R}(r) &= \bar{R}_{\max}(r) - \bar{R}_{\min}(r). \end{aligned} \tag{10}$$

However, the absolute values of the changes that occur in the width of diffraction focusing zones $\Delta\bar{R}_m(r)$ cannot uniquely characterize the changes in the efficiency of diffraction focusing. This is caused by the fact that, even for two similar range-independent oceanic waveguides with different scales of vertical inhomogeneity, a comparative estimate of the efficiency of diffraction focusing implies (all other factors being the same) a comparison of the relative variations of all quantities characterizing this phenomenon in the diffraction focusing zones of corresponding numbers. The use of relative values allows one to eliminate the differences in the positions of these zones, as well as in the conditions of excitation and reception of modes. Therefore, the efficiency of diffraction focusing in oceanic waveguides smoothly varying along the track can be estimated by the ratio

$$\sigma(r) = \Delta\bar{R}(r)/\bar{R}_{\max}(r), \tag{11}$$

which characterizes the relative width of each given zone. Naturally, the efficiency of diffraction focusing increases with decreasing $\sigma(r)$.

Here, it should be noted that, in the general case, the acoustic field in an oceanic waveguide is formed by different types of modes, namely, by purely water-path modes, modes interacting only with the surface or with the bottom, and by modes interacting with both surface and bottom. In this connection, by analogy with [5], the diffraction focusing may manifest itself most strongly for a certain group of maximum-energy-carrying modes with numbers $l_s(r) \le l \le l_b(r)$ (belonging to one of the aforementioned types), for which the quantity $\bar{R}_g(l, l'; n, n'; r)$ (Eq. (5)) exhibits minimal variations as a function of $l$, $l'$, $n$, and $n'$. The greater the number of modes $L_m(r) = l_b(r) - l_s(r)$ in such a group, the more pronounced the diffraction focusing of acoustic field is in the corresponding intervals of horizontal distances:

$$m\bar{R}_s(r) \le r \le m\bar{R}_b(r), \tag{12}$$

where

$$\begin{aligned} \bar{R}_s(r) &= \min\{\bar{R}_g(l, l'; n, n'; r)\}, \\ \bar{R}_b(r) &= \max\{\bar{R}_g(l, l'; n, n'; r)\} \\ &(l_s(r) \le l, l', n, n' \le l_b(r)). \end{aligned} \tag{13}$$

In addition to the number of modes $L_m(r)$, the width of these zones for the corresponding group of modes,

$$\begin{aligned} \Delta R_m(r) &= m\Delta\bar{R}_{bs}(r), \\ \Delta\bar{R}_{bs}(r) &= \bar{R}_b(r) - \bar{R}_s(r), \end{aligned} \tag{14}$$

also determines the efficiency of diffraction focusing. The latter proves to be more pronounced for smaller values of the ratio

$$\delta(r) = \Delta\bar{R}_{bs}(r)/\bar{R}_b(r), \tag{15}$$

characterizing the relative width of the zones. This suggests that the efficiency of diffraction focusing of the acoustic field in an oceanic waveguide smoothly varying along the track may exhibit no decrease with increasing $\sigma(r)$ (Eq. (11)): it may even grow if the increase in $\sigma(r)$ is accompanied by a decrease in $\delta(r)$ (Eq. (15)) and an increase in the number of modes $L_m(r)$ in the corresponding group.

Below, as in [5–11], we consider the most stable and actually predictable large-scale interference structure of an acoustic field formed in an oceanic waveguide by different pairs of adjacent modes. Then, assuming that the conditions of applicability of the WKB approximation are satisfied (see [16]) and applying the transformations analogous to those given in [5] and relations derived in the same paper [5], from Eqs. (3) and (5) we obtain the expressions

$$\bar{R}_{l, l+1}(r) = r/\int_0^r \frac{dr}{R_{l, l+1}(r)}, \tag{16}$$

$$\begin{aligned} R_{l, l+1}(r) \approx D_l/\Bigg\{1 + \frac{\pi}{kD_l^2}\frac{dD_l}{d\beta_l} \\ - \frac{2\pi^2}{3k^2D_l^3}\left[\frac{d^2D_l}{d\beta_l^2} - \frac{2}{D_l}\left(\frac{dD_l}{d\beta_l}\right)^2\right]\Bigg\}; \end{aligned} \tag{17}$$

$$\begin{aligned} &\bar{R}_g(l, l+1; l+1, l+2; r) \\ &= r/\left|\int_0^r \frac{dr}{R_g(l, l+1; l+1, l+2; r)}\right|, \end{aligned} \tag{18}$$

$$R_g(l, l+1; l+1, l+2; r) \approx \frac{kD_l^3}{2\pi} \times \left(1 - \frac{2\pi}{kD_l^2}\frac{dD_l}{d\beta_l}\right) \Big/ \left\{\frac{dD_l}{d\beta_l} - \frac{2\pi}{kD_l}\left[\frac{d^2D_l}{d\beta_l^2} - \frac{2}{D_l}\left(\frac{dD_l}{d\beta_l}\right)^2\right]\right\}. \quad (19)$$

Here,

$$D_l = 2\beta_l(r)\int_{z_1(r)}^{z_2(r)} \frac{dz}{\sqrt{n^2(z, r) - \beta_l^2(r)}} \quad (20)$$

is the cycle length of the Brillouin ray with a corresponding grazing angle $\chi_l(r)$ at a depth $z = z_0(r)$ of the channel axis where the velocity of sound $c(z, r)$ takes its minimal value $c_0(r)$, $n(z, r) = c_0(r)/c(z, r)$ is the refraction index of acoustic waves, and $\beta_l(r) = k_l(r)/k(r) = \cos\chi_l$ is the ray parameter. The latter is determined from the dispersion relation in the WKB approximation:

$$k(r)\int_{z_1(r)}^{z_2(r)} \sqrt{n^2(z, r) - \beta_l^2(r)}\,dz = \pi(l - \nu), \quad (21)$$

where $k(r) = \omega/c_0(r)$. Depending on whether $z_1(r)$ and $z_2(r)$ are the turning or reflection depth of Brillouin rays, the values of parameter $\nu$ in Eq. (21) vary in a relatively narrow interval: $\frac{1}{4} \le \nu \le \frac{1}{2}$ (see [5, 16]).

From Eqs. (8), (9), (18), and (19) for $kD_l \gg 1$, we obtain fairly simple expressions for the minimal and maximal spatial scales of diffraction focusing:

$$\bar{R}_{\min}(r) = \frac{1}{2\pi}\min\left\{r \Big/ \left|\int_0^r \frac{dD_l}{d\beta_l}\frac{dr}{kD_l^3}\right|\right\}, \quad (22)$$

$$\bar{R}_{\max}(r) = \begin{cases} \dfrac{1}{2\pi}\max\left\{r/\left|\displaystyle\int_0^r \frac{dD_l}{d\beta_l}\frac{dr}{kD_l^3}\right|\right\}, & \dfrac{dD_l}{d\beta_l} \ne 0 \\ \dfrac{1}{4\pi^2} r/\left|\displaystyle\int_0^r \left(\frac{d^2D_l}{d\beta_l^2}D_l^{-4}\right)\right|_{\beta_l = \beta_c(r)} \\ \times \dfrac{dr}{k^2}\left|\dfrac{dD_l}{d\beta_l}\right|_{\beta_l = \beta_c(r)} = 0. \end{cases} \quad (23)$$

The presence of two fundamentally different dependences for $\bar{R}_{\max}(r)$ (see Eq. (23)) is caused by the possibility of the formation of weakly divergent beams along the track at certain values of the parameter $\beta_l = \beta_c(r)$, which correspond to relatively smooth minima of the function $D_l(\beta_l)$ [17, 18].

As noted in [5], in range-independent oceanic waveguides, the diffraction focusing is more pronounced for smaller intervals of variation of the quantity

$$R_g(l, l+1; l+1, l+2) \equiv \bar{R}_g(l, l+1; l+1, l+2; r_0) \quad (24)$$

as a function of $l$ for all $1 \le l \le L$ or for a certain group of modes $l_s \le l \le l_b$. Here, $r_0$ is an arbitrarily fixed distance, on which the quantities under consideration do not depend in this case. Under the conditions of multimode propagation of acoustic waves, the interval of variation of the parameter $\beta_g \le \beta_l \le 1$ that is acceptable for propagating modes (this interval is bounded from below by $\beta_g$, corresponding to the excitation of reradiating modes at $\beta_l < \beta_g$) is separated into small segments $\Delta\beta_l = \beta_l - \beta_{l+1}$:

$$\Delta\beta_l/(1 - \beta_g) \ll 1.$$

In this case, the condition for an efficient manifestation of diffraction focusing of acoustic field in a range-independent oceanic waveguide can be formulated as the requirement that the derivative $dR_g/dl$ be small. Since the strongest diffraction focusing is observed at $R_g = \text{const}$ (see [5]), in this situation, in the case of multimode propagation, the corresponding differential equality is satisfied for a certain group of modes $l_s \le l \le l_b$:

$$\frac{dR_g}{dl} = 0. \quad (25)$$

Now, let us return to considering the possibility of the enhancement or weakening of diffraction focusing for the same group of modes in an oceanic waveguide smoothly varying along the propagation track. In this case, the behavior of the derivative $d\bar{R}_g/dl$, analogous to that given by Eq. (25) as a function of distance, is no longer an informative feature. The point is that, as in the formulation of expressions (11) and (15) for the quantities $\sigma(r)$ and $\delta(r)$, the essential characteristics prove to be not absolute but relative variations of the quantity $\bar{R}_g(r)$ (with respect to $\bar{R}_{\max}$). Therefore, in oceanic waveguides smoothly varying along the track, the efficiency of diffraction focusing for the given group of modes $l_s \le l \le l_b$ should be characterized by the derivative

$$\Phi(l, r) = \frac{d}{dl}(\bar{R}_g/\bar{R}_{\max}). \quad (26)$$

Naturally, the strongest diffraction focusing of acoustic field is achieved in the limiting situation

$$\Phi(l, r) = 0. \quad (27)$$

From Eq. (21), we derive the relation

$$\frac{d\beta_l}{dl} = -\frac{2\pi}{k(r)D_l}. \quad (28)$$

Using this relation and assuming that condition $kD_l \gg 1$ is satisfied, from Eqs. (18), (19), and (27) we obtain the

approximate equation

$$\frac{d^2\bar{D}_l}{d\beta_l^2} - \frac{3}{\bar{D}_l}\left(\frac{d\bar{D}_l}{d\beta_l}\right)^2 = 0, \quad (29)$$

for the dependence $\bar{D}_l(\beta_l)$, which should be satisfied for the given group of modes. Here, $\bar{D}_l = D_l/\{(D_l)|_{l=l_a}\}$ and $l_a$ is the mode number corresponding to the maximal value of $\bar{R}_g$.

It should be noted that, if the solution $\bar{D}_l = a_1(r)$ to Eq. (29), where $a_1(r)$ is an arbitrary function of $r$, does not depend on the ray parameter $\beta_l$ at a fixed distance, it should be rejected, because it corresponds to an infinitely large value of $\bar{R}_g$ (Eq. (18)), which actually means the absence of diffraction focusing of the acoustic field for the given group of modes.

Equation (29) can be reduced to a simpler form more convenient for analysis:

$$\frac{d^2}{d\beta_l^2}(\bar{D}_l^{-2}) = 0. \quad (30)$$

This equation allows one to determine the intervals of the ray parameter variation, $\beta_b \le \beta_l \le \beta_s$, within which the linear dependence (following from Eq. (30))

$$\bar{D}_l^{-2} = a_1(r)\beta_l + a_2(r) \quad (\beta_b \le \beta_l \le \beta_s) \quad (31)$$

corresponds to the maximal possible effect of the diffraction focusing of the acoustic field. In Eq. (31), the arbitrary function $a_2(r)$ taken at a fixed distance also does not depend on the ray parameter $\beta_l$ for the given group of modes.

With the use of dependence (31), expression (18) is reduced to the form

$$\bar{R}_g(l, l+1; l+1, l+2; r) = \frac{\omega}{\pi} r \Big/ \int_0^r a_1 c_0 dr = \bar{R}_s = \bar{R}_b \quad (l_s \le l \le l_b). \quad (32)$$

As one would expect (see Eq. (32)), the efficiency of diffraction focusing for the given group of modes does not depend on the behavior of the functions $a_1(r)$ and $a_2(r)$. In this case, only one of them, $a_1(r)$, influences the values of the characteristic spatial scales $\bar{R}_s$ and $\bar{R}_b$ (Eqs. (13)). From Eq. (32) it also follows that, in the special case of a possible mutual compensation of $a_1(r)$ and $c_0(r)$ variations, i.e., at $a_1 c_0 = \text{const}$, the spatial scale of diffraction focusing of the field of the given group of modes does not depend on horizontal distance. Therefore, in such range-dependent oceanic waveguides smoothly varying along the track, the phenomenon under consideration will be of a purely periodic character:

$$\bar{R}_b = \frac{\omega}{\pi c_0 a_1}. \quad (33)$$

It is quite natural that the efficiency of the diffraction focusing of the acoustic field is completely determined by the width of the corresponding interval of the ray parameter variation, $\Delta\beta(r) = \beta_s(r) - \beta_b(r)$, and the rate of its displacement along the $\beta_l$ axis. An increase in the interval $\Delta\beta(r)$ with distance, which accompanies an increase in the number of modes in the given group $L_m(r) = l_b(r) - l_s(r)$, will necessarily lead to an increase in the efficiency of diffraction focusing for $\beta_b(0) \ge \beta_b(r)$ and $\beta_s(0) \le \beta_s(r)$. However, in some situations, an increase in $\Delta\beta(r)$ with distance may be accompanied by a considerable displacement of this interval along the $\beta_l$ axis. The latter may result in that when one of the conditions

$$\left.\begin{aligned}\beta_s(r) \le \beta_b(0)\\ \beta_b(r) \ge \beta_s(0)\end{aligned}\right\} \quad (r < \bar{R}_b), \quad (34)$$

are satisfied, when the initial interval $\Delta\beta(0)$ does not overlap with a similar interval $\Delta\beta(r)$ at distances smaller than the maximal spatial scale of the effect, the diffraction focusing of acoustic field will not manifest itself.

After the above-stated general conclusions concerning the phenomenon of diffraction focusing of acoustic fields in oceanic waveguides smoothly varying along the track, let us proceed to considering the possibility of using the simplest waveguide model that allows the determination of the approximate analytical dependences for the quantities of interest.

For this purpose, we consider a waveguide model in the form of an isovelocity water layer whose depth $H(r)$ smoothly varies with distance and assume that this layer overlies a perfectly rigid half-space:

$$n^2(r, z) = 1 \quad (0 \le z \le H(r)). \quad (35)$$

With the use of an adiabatic approximation in the framework of this model, we obtain a fairly simple analytical dependence for the horizontal wave numbers of modes [16, 19]:

$$k_l(r) = k(r)\sqrt{1 - x_l(r)}, \quad x_l(r) = \left(\frac{\pi\left(l - \frac{1}{2}\right)}{k(r)H(r)}\right)^2, \quad (36)$$

where $x_l(r) \le 1$. For the case of interest, i.e., for multimode propagation with $kH \gg 1$, we limit our consideration to the low-number modes with small grazing angles ($x_l(r) \ll 1$). Then, using the expression following from Eq. (36) and obtained by a series expansion in $x_l(r)$ to the second-order terms inclusive, by analogy

with [7, 8] we obtain the dependence for $R_g$ (see Eq. (6)) at $l' = l + 1$, $n = l'$, and $n' = n + 1$:

$$R_g(l, l+1; l+1, l+2; r) \approx S/\left[1 + \frac{\pi}{4kS}(12l^2 + 12l + 5)\right], \quad S = \frac{2}{\pi}kH^2. \tag{37}$$

Consider the situation when $k(r) = k_0 = \text{const}$ and the depth of the water layer varies with distance according to the law

$$H(r) = H_0/\sqrt{1 - r/R_H}, \tag{38}$$

where $H_0 = H$ ($r = 0$) and the characteristic horizontal scale of inhomogeneity $R_H$ is sufficiently large:

$$\bar{R}_{l, l+1}(r)/R_H \ll 1, \quad r/R_H \ll 1. \tag{39}$$

Then, from Eq. (5) with the use of Eq. (37), we determine the following dependence for $\bar{R}_g$ at $l' = l + 1$, $n = l'$, and $n' = n + 1$:

$$\bar{R}_g(l, l+1; l+1, l+2; r) \approx \frac{S_0/\left(1 - \frac{r}{2R_H}\right)}{1 + \frac{\pi}{4k_0S_0}(12l^2 + 12l + 5)\left(1 - \frac{r}{2R_H}\right)}, \quad S_0 = \frac{2}{\pi}k_0H_0^2. \tag{40}$$

As seen from Eq. (40), variations of $\bar{R}_g$ as a function of $l$ are minimal for low-number modes, and, therefore, it is these modes that form the most intense field maxima in the diffraction focusing zones (see [7, 8]). Naturally, the maximal value $\bar{R}_{\max}(r)$ of $\bar{R}_g$ is achieved in expression (40) at $l = l_a = l_s = 1$. The minimum of $\bar{R}_g$ is achieved at a certain value of $l = l_u$, the determination of which by approximate expression (40) is inappropriate (see [7, 8]). However, if we only consider the group of modes with $1 \le l \le l_b$, which make the main contribution to the formation of the diffraction focusing zones, then, instead of $l_u$, we can use the boundary value $l_b$, which can approximately be determined from the condition of equality between the width of the first diffraction focusing zone and the period of interference of adjacent modes:

$$\Delta R_{bs}(r) = \bar{R}_{l_b, l_b+1}(r). \tag{41}$$

For the following consideration, the knowledge of the value of $l_b$ is of no significance. Therefore, without solving Eq. (41), we proceed to the determination of dependences (14), (15), and (26) for $\Delta\bar{R}_{bs}(r)$, $\delta(r)$, and $\Phi(l, r)$, which characterize the phenomenon of diffraction focusing of an acoustic field in an ideal waveguide given by Eq. (35).

From Eqs. (14), (15), (26), and (37), we obtain

$$\Delta\bar{R}_{bs} \approx \frac{3\pi}{k_0}\frac{(l_b^2 + l_b - 2)}{1 + \frac{\pi}{2k_0S_0}(6l_b^2 + 6l_b + 17)\left(1 - \frac{r}{2R_H}\right)}, \tag{42}$$

$$\delta(r) \approx \frac{3\pi}{k_0S_0}\frac{(l_b^2 + l_b - 2)\left(1 - \frac{r}{2R_H}\right)}{1 + \frac{\pi}{4k_0S_0}(12l_b^2 + 12l_b + 5)\left(1 - \frac{r}{2R_H}\right)}, \tag{43}$$

$$\Phi(l, r) \approx -\frac{3\pi}{k_0S_0}\frac{\left(1 + \frac{29\pi}{4k_0S_0}\left(1 - \frac{r}{2R_H}\right)\right)\left(1 - \frac{r}{2R_H}\right)(2l + 1)}{1 + \frac{\pi}{2k_0S_0}(12l^2 + 12l + 5)\left(1 - \frac{r}{2R_H}\right)}. \tag{44}$$

As seen from Eqs. (37) and (42)–(44), an increase in the depth of the water layer with distance leads to a noticeable increase in the maximal and minimal scales of diffraction focusing,

$$\bar{R}_{\max}(r) = \bar{R}_g\big|_{l=1} \approx S, \quad \bar{R}_{\min}(r) = \bar{R}_g\big|_{l=l_b} \approx S - \frac{3\pi}{k}\left(l_b^2 + l_b + \frac{5}{12}\right), \quad S = S_0/\left(1 - \frac{r}{2R_H}\right), \tag{45}$$

and to a small increase in the absolute width of each of the corresponding zones. However, a decrease in the relative width $\delta(r)$ of the diffraction focusing zones with distance, as well as a decrease in the absolute value of the characteristic derivative $|\Phi(l, r)|$, should lead to an enhancement of the effect under discussion in such a waveguide. It should be noted that the quantity $|\Phi(l, r)|$, considerably increasing with the mode number, exhibits the fastest decrease with distance for the low-number modes, which govern the formation of the zones of diffraction focusing of an acoustic field.

Let us now consider an isovelocity waveguide in which not only the depth $H(r)$ (Eq. (38)) but also the sound velocity $c_0(r)$ and, hence, the wave number $k(r)$ vary with distance while the quantity $kH^2 = k_0H_0^2$ remains constant. In this case, from Eqs. (5) and (37), we obtain the dependence

$$\bar{R}_g(l, l+1; l+1, l+2; r) \approx S_0/\left[1 - \frac{\pi}{4k_0S_0}(12l^2 + 12l + 5)\frac{R_H}{r}\ln\left(1 - \frac{r}{R_H}\right)\right]. \tag{46}$$

With an allowance for the smallness of the ratio $r/R_H \ll 1$ (see Eq. (39)), we transform expression (46) to the more convenient form

$$\bar{R}_g(l, l+1; l+1, l+2; r) \approx S_0 \Big/ \left[1 + \frac{\pi}{4k_0 S_0}(12l^2 + 12l + 5)\left(1 - \frac{r}{2R_H}\right)\right]. \quad (47)$$

From the comparison of dependences (40) and (47), it follows that, in the second case, the maximal (at $l = l_s = 1$) and minimal (at $l = l_b$) spatial scales of diffraction focusing increase much more slowly with distance. As a result, the dependence

$$\Delta\bar{R}_{bs} \approx \frac{3\pi}{k_0} \frac{(l_b^2 + l_b - 2)\left(1 - \frac{r}{2R_H}\right)}{1 + \frac{\pi}{2k_0 S_0}(6l_b^2 + 6l_p + 17)\left(1 - \frac{r}{2R_H}\right)} \quad (48)$$

which follows from Eqs. (14) and (47), decreases with distance in contrast to the ascending dependence (42) at $k = k_0$. However, the corresponding decrease in the width of each diffraction focusing zone $\Delta R_m(r)$ with distance is not accompanied by an enhancement of the effect as compared to the first case (where $k = k_0$), since the dependences $\delta(r)$ and $\Phi(l, r)$ following from Eqs. (15), (26), and (47) and characterizing this process fully coincide with the analogous dependences (43) and (44). Therefore, in the situations considered above, the efficiency of diffraction focusing of an acoustic field in the corresponding spatial regions increases with distance at the same rate.

In closing, let us formulate the main results of this study and the conclusions derived from them.

Conditions are formulated that are necessary for the diffraction focusing of an acoustic field to occur in an oceanic waveguide smoothly varying along the track. Using the adiabatic and WKB approximations for the mode representation of acoustic field in such waveguides, it is shown that the highest efficiency of diffraction focusing is achieved for the intervals of ray parameter variation, within which the inverse square of Brillouin ray cycle length linearly depends on the ray parameter. It is noted that the diffraction focusing manifests itself only when the initial interval of ray parameter variation overlaps with a similar interval at distances exceeding a certain number of maximal spatial scales of the phenomenon under consideration.

Characteristic features of the enhancement of diffraction focusing in an oceanic waveguide smoothly varying along the track are studied analytically for the model of an isovelocity waveguide with an increasing depth of the water layer and a perfectly rigid bottom.

A numerical simulation of the processes considered above will be the subject of a subsequent publication.

Presumably, the quasi-periodic character of diffraction focusing should be taken into account in the case of sound focusing in oceanic waveguides with the use of wave conjugation, because, in this case (see [19–21]), even in oceanic waveguides that are inhomogeneous along the track, the formation of several pronounced focal regions is possible.

## ACKNOWLEDGMENTS

This work was supported by the Russian Foundation for Basic Research (project no. 00-05-64604).

## REFERENCES

1. L. A. Rivlin and V. S. Shil'dyaev, Izv. Vyssh. Uchebn. Zaved., Radiofiz. **11**, 572 (1968).
2. E. E. Grigor'eva and A. T. Semenov, Kvantovaya Élektron. (Moscow) **5**, 1877 (1978).
3. D. E. Weston, J. Acoust. Soc. Am. **44**, 1706 (1968).
4. R. F. Edgar, Opt. Acta **16** (3), 281 (1969).
5. Yu. V. Petukhov, Akust. Zh. **46**, 384 (2000) [Acoust. Phys. **46**, 327 (2000)].
6. D. I. Abrosimov and Yu. V. Petukhov, Akust. Zh. **46**, 149 (2000) [Acoust. Phys. **46**, 113 (2000)].
7. D. I. Abrosimov and Yu. V. Petukhov, Akust. Zh. **46**, 5 (2000) [Acoust. Phys. **46**, 1 (2000)].
8. E. L. Borodina and Yu. V. Petukhov, Akust. Zh. **47**, 313 (2001) [Acoust. Phys. **47**, 262 (2001)].
9. E. L. Borodina and Yu. V. Petukhov, Akust. Zh. **47**, 451 (2001) [Acoust. Phys. **47**, 384 (2001)].
10. E. L. Borodina and Yu. V. Petukhov, Akust. Zh. **47**, 590 (2001) [Acoust. Phys. **47**, 511 (2001)].
11. E. L. Borodina and Yu. V. Petukhov, Preprint No. 555, IPF RAN (Nizhni Novgorod Inst. of Applied Physics, Russian Academy of Sciences, 2001); Akust. Zh. **48**, 602 (2002) [Acoust. Phys. **48**, 529 (2002)].
12. B. Z. Katsenelenbaum, Akust. Zh. **7**, 201 (1961) [Sov. Phys. Acoust. **7**, 159 (1961)].
13. V. V. Shevchenko, Akust. Zh. **7**, 484 (1961) [Sov. Phys. Acoust. **7**, 392 (1961)].
14. B. Z. Katsenelenbaum, *Theory of Irregular Waveguides with Slowly Varying Parameters* (Akad. Nauk SSSR, Moscow, 1961).
15. V. V. Shevchenko, *Continuous Transitions in Open Waveguides* (Nauka, Moscow, 1969; Golem, Boulder, Colo., 1971).
16. L. M. Brekhovskikh and Yu. P. Lysanov, *Fundamentals of Ocean Acoustics* (Gidrometeoizdat, Leningrad, 1982; Springer, New York, 1991).
17. Yu. V. Petukhov, Akust. Zh. **41**, 807 (1995) [Acoust. Phys. **41**, 712 (1995)].
18. Yu. V. Petukhov, Akust. Zh. **43**, 230 (1997) [Acoust. Phys. **43**, 196 (1997)].
19. F. M. Ismagilov and Yu. A. Kravtsov, Akust. Zh. **37**, 294 (1991) [Sov. Phys. Acoust. **37**, 148 (1991)].
20. D. R. Dowling and D. R. Jackson, J. Acoust. Soc. Am. **89**, 171 (1991).
21. T. Akal, C. Ferla, D. R. Jackson, *et al.*, J. Acoust. Soc. Am. **105**, 1597 (1999).

*Translated by E. Golyamina*

*Acoustical Physics, Vol. 50, No. 2, 2004, pp. 201–211. Translated from Akusticheskiĭ Zhurnal, Vol. 50, No. 2, 2004, pp. 249–260.*


# Stochastic Resonance at the Periphery of Auditory System: A Simulation Experiment

**L. K. Rimskaya-Korsakova**

*Andreev Acoustics Institute, Russian Academy of Sciences, ul. Shvernika 4, Moscow, 117036 Russia*

*e-mail: lkrk@akin.ru*

Received April 14, 2003

**Abstract**—An auditory nerve fiber model is studied. The model includes the formation of the response of the basilar membrane, formation of the receptor potential of the internal hair cell, formation of the synaptic potential of the auditory nerve fiber, and transformation of the synaptic potential into a sequence of spikes. The role of this transformation, as well as the role of changes in the excitability of the fiber after the spike generation in the coding of amplitude-modulated signals is revealed for the cases of signals of medium (i.e., corresponding to the sloping part of the curve representing the mean firing rate of an auditory nerve fiber as a function of the stimulus level) and subthreshold levels. Simulated experiments show that the coding of the envelope of a medium-level amplitude-modulated signal is a dynamic process, which includes fine tuning (adaptation) of the threshold of the auditory nerve fiber to the stimulus level. The coding of the signal envelope is little affected by the slope of the dependence of the mean firing rate on the stimulus level. However, fibers with steep input–output characteristics may exhibit stochastic resonance properties. Owing to these properties, such fibers are capable of reproducing the envelope of a subthreshold modulated signal when weak noise is added to it. Ways are considered for extending the range of subthreshold signal and noise levels within which the envelope of a modulated signal is reproduced (or the phenomenon of stochastic resonance is observed). © *2004 MAIK "Nauka/Interperiodica".*

It has been known that auditory nerve fibers, according to their spontaneous activity (SA), i.e., the ability of a fiber to spontaneously generate spikes in the absence of stimulus, possess not only different physiological and morphological properties [1–12] but, presumably, also different functional properties [13].

Depending on the level of SA, auditory nerve fibers are classed into three groups: fibers with low, medium, and high SA [1, 2, 10]. The time of recovery of the response thresholds after the end of a stimulus presentation (short-term adaptation) is known to be greater for auditory nerve fibers with lower SA [4, 14]. After the beginning of the stimulus presentation, the firing rate decreases to a certain stationary level. According to the data reported in [11, 12], this decrease occurs faster for fibers with lower SA, while according to [4, 14], it is faster for fibers with higher SA.

Fibers with higher SA are known to have steep and narrow characteristics that represent the mean firing rate as a function of the signal level (the input–output characteristics), as well as low response thresholds. Fibers with low SA have gently sloping and wide input–output characteristics and high response thresholds. However, fibers with low SA and sloping input–output characteristics reproduce the envelope of a sine-amplitude-modulated signal (SAMS) much better than fibers with high SA and steep input–output characteristics [3, 7–9, 11, 12, 16, 17]. Fibers with medium SA have intermediate properties.

Auditory nerve fibers have one synaptic input from the internal receptor hair cell, and they exhibit SA [1, 2, 10]. Each internal receptor hair cell innerves 10–20 afferent fibers with different SAs, while these fibers are assumed to be affected by the same receptor potential. Fibers with different SAs are connected to a receptor cell on different sides and, at the points of connection, have different sizes of synaptic knobs; in addition, they have different diameters within the distance from the hair cell to the cochlear nuclei and different numbers of synaptic terminals at the cells of these nuclei [15]. The mechanism of SA is believed to be related to spontaneous outbursts of mediator portions from the receptor cell into the synaptic cleft. Evidently, the formation of synaptic potentials of auditory nerve fibers with different SAs from the receptor potential of a single internal hair cell should be related to SA. This relation may be responsible for the dependence of the steepness of the input–output characteristic of auditory nerve fiber on the level of SA.

Using a model of auditory nerve fiber, it was shown that the reproduction of the envelope of a SAMS in fibers is closely related not to the profile of the input–output characteristic but to the adaptation properties, which presumably provide the tuning (adaptation) of the fiber response threshold to the level of the acting stimulus. For auditory nerve fibers that have high SA levels, low response thresholds, steep input–output characteristics, and poorly reproduce the envelope of

1063-7710/04/5002-0201$26.00 © 2004 MAIK "Nauka/Interperiodica"

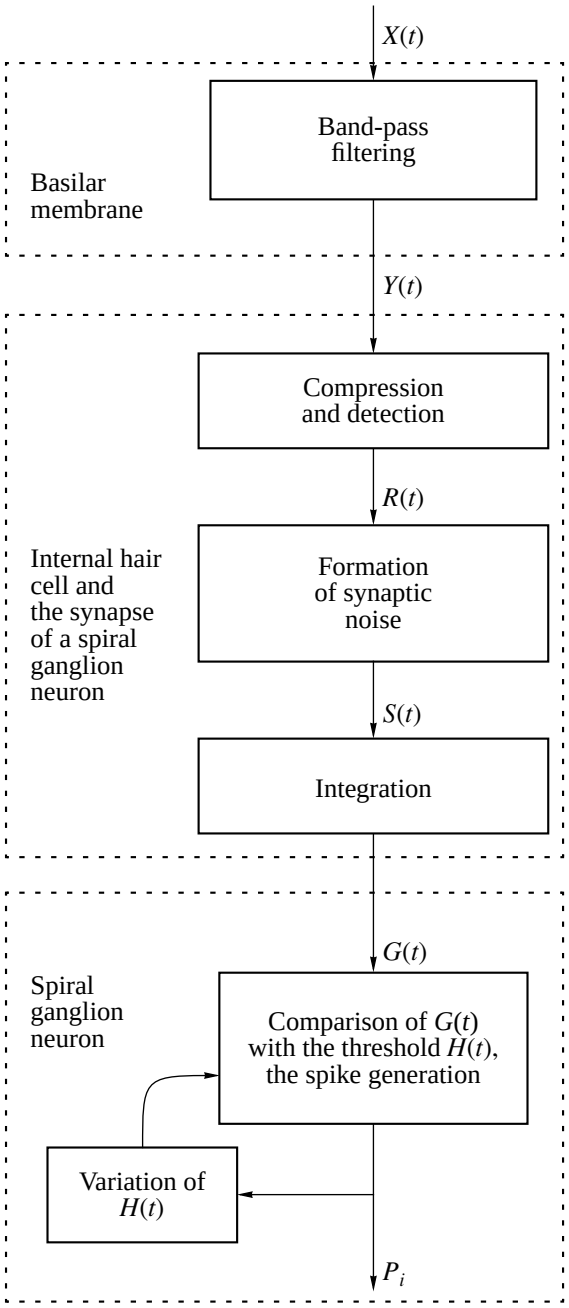


**Fig. 1.** Flow chart representing the model of the periphery of the auditory system. (For explanation, see the main body of the paper.)

a SAMS, it was found that such fibers may exhibit stochastic resonance properties. Owing to the stochastic resonance, these fibers are capable of extracting the envelope of a SAMS of a subthreshold level when weak noise is added to the signal. A stochastic resonance occurs in nonlinear systems transforming a signal to a Poisson sequence of events [19–21]. Precisely this kind of sequence of events is formed by the evoked activity of real [22] and model [23–25] auditory nerve fibers.

The purpose of this study is to determine the conditions for the best reproduction of the envelopes of SAMSs of medium (corresponding to the sloping part of the input–output characteristic) and subthreshold levels in the firing rate of auditory nerve fibers with different SAs. Conditions for the appearance of a stochastic resonance in auditory nerve fibers in the presence of an additive mixture of subthreshold SAMSs and broadband noise are estimated. Ways of extending the range of subthreshold SAMS levels, within which the extraction of the SAMS envelope is possible, are considered.

The study was carried out using a phenomenological model of auditory nerve fiber (Fig. 1) [23–25]. The model includes several stages of stimulus transformation: first, formation of the response of the basilar membrane; second, formation of the receptor and synaptic potentials of an internal hair cell; and, third, formation of a sequence of short pulses, i.e., spikes, by the spiral ganglion neurons. The adequacy of the model was verified by comparing the responses of model and real auditory nerve fibers.

At the first stage corresponding to the formation of the pulsed response of the basilar membrane $y(t)$, a convolution of the input signal $x(t)$ with the pulsed characteristic of the filter of the basilar membrane $h(t)$ takes place [26]:

$$y(t) = \int h(t-t')x(t')dt', \quad (1)$$

$$h(t) = (\omega t)^{\beta}\exp[-\alpha(\omega t)]\sin(\omega t), \quad (2)$$

where $t$ is time; $\omega$ is the central frequency of the filter, i.e., the tuning frequency of the model of auditory nerve fiber; and $\alpha$ and $\beta$ are constants.

The nonlinear transformation of the signal, which reproduces the stage of mechanoreception, is often realized by one of the sigmoid functions [27–30]. Such functions adequately reproduce the variations of the receptor potentials of internal hair cells [31, 32] and are capable of providing a better amplification for weak signals than for stronger ones. The model under consideration uses a nonlinear transformation realized by a modified sigmoid function $R(t)$. It was assumed that the mechanism of the synaptic potential formation from the receptor potentials is related to the mechanism responsible for the appearance of SA. Therefore, in the model of auditory nerve fiber, the slope of the sigmoid functions (parameter Sl in Eq. (3)) depends on the level of SA in approximately the same way as the slope of the input–output characteristic of real fiber depends on the level of SA [7]:

$$R(t) = R_{\max}[2.0/(1.0 + e^{(\mathrm{Dis} - y(t))/\mathrm{Sl}}) - 1.0], \quad (3)$$

where $R_{\max}$ is the maximum synaptic potential and the parameter Dis determines the displacement of the function; this parameter was equal to 0.05 in all cases.

Then, synaptic noise $S(t)$ was formed as a random process whose mean value and variance were proportional to the demodulated function $R(t)$. To reproduce

the SA, the rms deviation of the random process was increased by a quantity $\xi$. In the absence of the signal $x(t)$, the synaptic noise $S(t)$ had a zero mean and an rms deviation proportional to $\xi$. The formation of the synaptic potential $G(t)$ was terminated by integrating the quantity $S(t)$:

$$G(t) = \int \exp(-t/\tau)S(t)dt, \quad (4)$$

where $\tau$ is a time constant equal to 0.2 ms. Expression (4) takes into account the inertial properties of the signal transformation at the mechanoreceptor level and (or) at the membrane of the spiral ganglion neuron.

The stage of the transformation of the synaptic potential to the firing rate of the fiber $P_i$ included the comparison of the synaptic potential $G(t)$ with the time-dependent threshold $H(T)$. If $G(t)$ exceeded the threshold, a short pulse, i.e., a spike, was generated by a neuron. Each spike caused a temporal threshold increase in the neuron model. Within a time interval equal to the sum of the periods of the absolute and relative refractorinesses, the threshold decreased to the initial level $H_0$. At the stage of the relative refractoriness, the threshold $H(t)$ had a rapid and a slow component [33] and could increase by quantities equal to the remainders of the rise of each of the threshold components before the spike generation. The variation of the threshold $H(t)$ with time after the spike generation has the form

$$H(t) = H_0 + H_f \exp[-(t-\tau_a)/\tau_f + \Omega \operatorname{sgn}(\tau_a - t)] + H_s \exp[-(t-\tau_a)/\tau_s + \Omega \operatorname{sgn}(\tau_a - t)], \quad (5)$$

where $H_f = H_{0f} + dH_f$ and $H_s = H_{0s} + dH_s$; $H_{0f}$, $H_{0s}$, $H_f$, and $H_s$ are the constant and varying values of the rapid and slow components of the neuron threshold at the stage of relative refractoriness; $dH_f$ and $dH_s$ are the remainders of the rise of each of the threshold components at the instant preceding the spike generation; $\tau_a$ is the time of absolute refractoriness; $\tau_f$ and $\tau_s$ are the time constants of the two threshold components at the stage of relative refractoriness; $\Omega$ is a constant that determines the threshold value at the stage of absolute refractoriness; and sgn is the function determined as $\operatorname{sgn}(t) = 1$ for $t < 0$ and $\operatorname{sgn}(t) = 0$ for $t > 0$.

The threshold function $H(t)$ given above allows one to preset different adaptation and refractoriness properties in the fiber model. Remember that refractoriness is characterized by a change in the excitability of a neuron immediately after the appearance of a response while adaptation is characterized by a decrease in the firing rate of the response during the action of a prolonged stimulus.

The central frequency of the filter of the basilar membrane was taken to be equal to 10 kHz. The threshold value was $H_0 = 0.02$. The period of the absolute refractoriness was $\tau_a = 0.5$ ms. It was assumed that smaller values of parameter $\xi$, which determines the frequency of synaptic potential fluctuations with respect to the spike generation threshold in the absence of a stimulus, correspond to greater values of the parameter Sl, which determines the slope of the transformation function $R(t)$. The smaller the parameters $\xi$, $\tau_f$, $\tau_s$, $H_{0f}/H_0$, and $H_{0s}/H_0$, the lower the level of SA. The quantity $R_{max}$ determines the mean firing rate in the saturation regime. The value of this quantity was chosen so that the firing rate did not exceed 380–400 spikes per second. The parameters chosen for the fiber models with different SAs are presented in the table at the bottom of Fig. 2.

The stimuli had the form of a SAMS, broadband noise, and an additive mixture of the SAMS and noise. The carrier frequency of the SAMS was equal to 10 kHz, the modulation depth $m$ was equal to 0.2, and the modulation frequency was 100 Hz. The duration of a stimulus was 100 ms. The time step used in the calculations was 0.001 ms, and the time step (bin) in calculating the histograms of the responses of fiber models was 0.1 ms.

To estimate the statistical properties of the responses of fiber models, the following characteristics were determined (by analogy with electrophysiological experiments):

(i) The post-stimulus histogram determining the probability of firing for auditory fiber before, during, and after stimulus presentation;

(ii) The dependence of the mean firing rate $n$ of the fiber during the stimulus presentation on the input signal level (the input–output characteristic);

(iii) The phase histogram determining the probability of firing corresponding to a given phase of the SAMS. For the phase histogram, the synchronization coefficient $r$ was calculated. This quantity characterized the degree of reproduction of modulations in the response of the auditory nerve fiber, so that $r = 0$ when the density of spike distribution over the modulation period was constant and $r = 1$ when all spikes were localized in one bin;

(iv) The dependence of the synchronization coefficient $r$ on the level of the SAMS carrier;

(v) The dependence of the principal component of the Fourier transform of the phase histogram, $r1$, on the noise level for the case of a stimulus in the form of an additive mixture of SAMS and noise: $r1 = 2nr$. The quantity $r1$ allows one to estimate the modulation of the instantaneous firing rate of the fiber and can be interpreted as the energy characteristic of the envelope reproduction in the response of the fiber at the modulation frequency [34].

Let us consider the responses of the models of auditory nerve fibers with different SAs to an SAMS in the absence of noise (Fig. 2). Figure 2a presents post-stimulus histograms of the responses of different fiber models. The histograms were obtained at SAMS levels at which the mean firing rate was equal to about 200 spikes per second. The character of adaptation varied

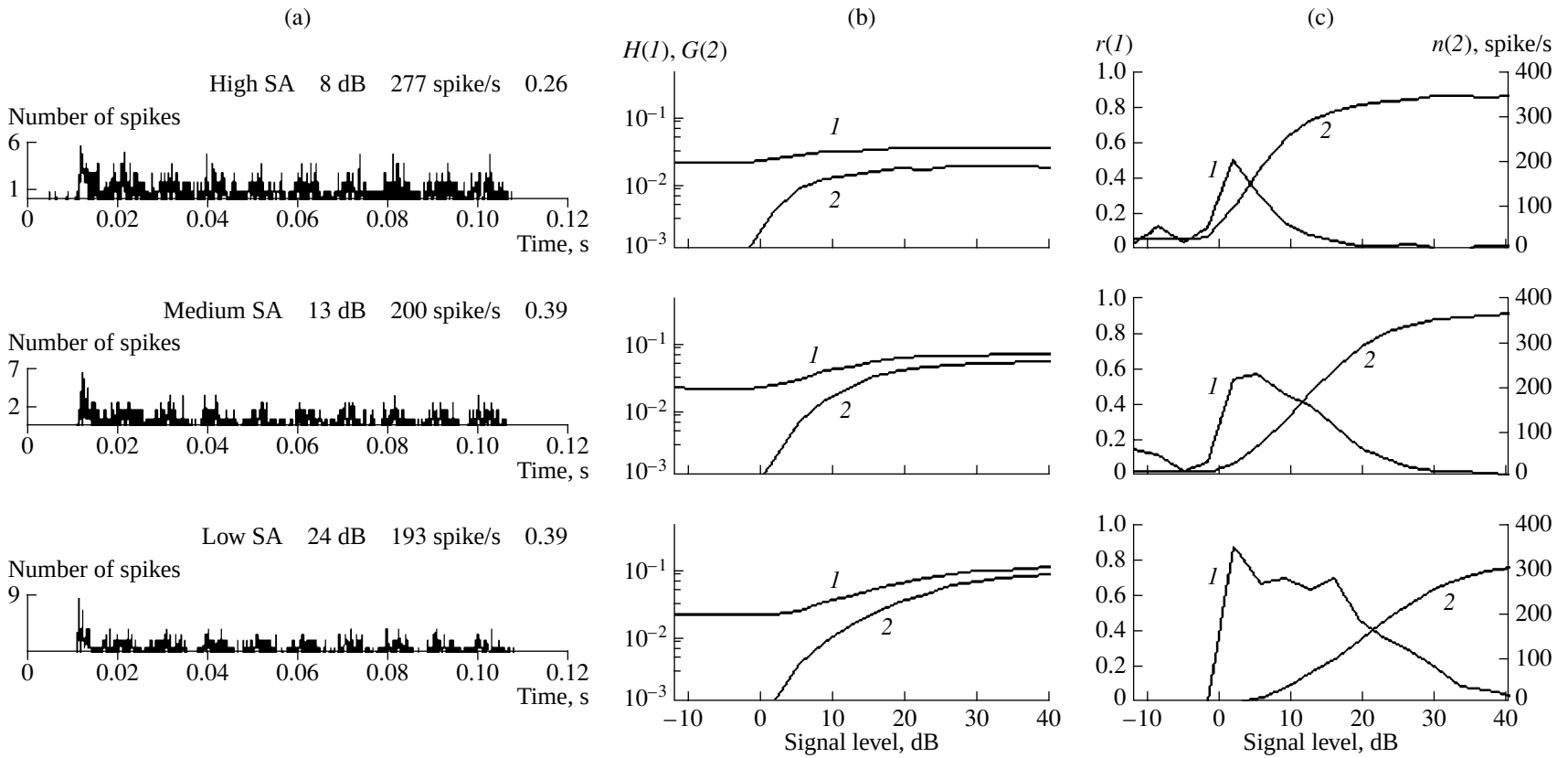


| Type of model | SA, spike/s | ξ | $R_{max}$ | Sl | $\tau_f$, ms | $H_{0f}/H_0$ | $\tau_s$, ms | $H_{0s}/H_0$ |
|---|---|---|---|---|---|---|---|---|
| High SA | 25 | 0.016 | 0.05 | 0.025 | 2 | 0.3 | 20 | 0.1 |
| Medium SA | 9 | 0.012 | 0.12 | 0.150 | 3 | 0.7 | 30 | 0.2 |
| Low SA | 0 | 0.005 | 0.22 | 0.700 | 4 | 1.2 | 40 | 0.3 |

**Fig. 2.** Responses of the models of auditory nerve fibers with different SAs to a SAMS in the absence of noise: (a) post-stimulus histograms (30 stimulus presentations), (b) dependences of (*1*) the threshold *H* averaged over the time of stimulus presentation and (*2*) the synaptic potential *G* on the SAMS level, and (c) dependences of (*1*) the synchronization coefficient *r* and (*2*) the mean firing rate *n* in spikes per second on the SAMS level. The first row from the top represents the responses of the model of a fiber with high SA, the second row corresponds to fiber with medium SA, and the third row, to fiber with low SA. The level of 0 dB corresponds to the threshold of the response to SAMS (without noise) in the model of fiber with high SA. The parameters given over the histograms (Fig. 2a) indicate the corresponding type of model, the SAMS level for which the histogram was obtained, and the values of *n* and *r*. The table presented at the bottom shows the parameters of the models of fibers with different SAs.

for different models because of the difference in the parameters of the threshold function $H(t)$. The difference between the mean firing rates recorded at the beginning and at the end of the SAMS presentation was greater and the time interval within which this change occurred was smaller in the model of fiber with low SA, compared to the model with high SA.

Figure 2b displays the threshold values averaged over the stimulus duration (curves *1*) and the synaptic potentials (curves *2*) as functions of the SAMS level. Curve *2* is called the amplitude characteristic of synaptic transmission of the fiber. The steepness of this curve (determined by parameter Sl of the function $R(t)$) is greater and the SAMS level interval, within which the steepness grows, is smaller for fiber with high SA, compared to fiber with low SA. The dependences of the mean threshold values (curves *1*) on the SAMS level exhibit pronounced differences in the temporal summation of the thresholds for different fibers. The summation is smaller for models of fiber with high SA. The greater the parameters of the threshold function $H(t)$ and the smaller the SA (parameter $\xi$ of the function $S(t)$), the greater the change in the threshold value (curve *1*), finer the tuning (adaptation) of the threshold to the synaptic potential level (curve *2*), and longer the time of recovery of the mean threshold value after the end of the SAMS presentation (not shown in the plots).

Figure 2c shows the dependences of the synchronization coefficients $r$ on the SAMS level (curves *1*) and the input–output characteristics (curves *2*) of the models of auditory nerve fibers. The steepness of the input–output characteristic is determined by the steepness of the amplitude characteristic of synaptic transmission (curve *2* in Fig. 2b) but can also flatten. The flattening of a steep characteristic will be stronger the greater the adaptation parameters of the threshold function are and the greater the SA is. The range of variation of the quantity $r$ (curve *1* in Fig. 2c) is determined by the width of the range within which the input–output characteristic exhibits a growth (curve *2* in Fig. 2c). The maximum values of $r$ and the widest range of SAMS levels, within which the SAMS is synchronized with the response of the fiber, is observed for the fiber model with low SA, sloping input–output characteristic, and high values of the parameters of the threshold function. In the fiber model with high SA, which has the steepest input–output characteristic and small values of the parameters of the threshold function, the minimum values of $r$ are obtained along with the smallest range of SAMS levels, within which the SAMS is synchronized with the fiber response.

From calculations it follows that both the synchronization coefficient $r$ and the steepness of the input–output characteristic depend on the steepness of the amplitude characteristic of synaptic transmission of the fiber (parameter Sl in $R(t)$), on the SA (parameter $\xi$ in $S(t)$), and on the tuning (adaptation) of the threshold to the level of the synaptic potential (the parameters of $H(t)$). In the fiber models with different SAs, these processes occur in different ways and lead to the same relation between the steepness of the input–output characteristic and the values of the synchronization coefficient $r$ as in real fibers with different SAs [3, 7–9, 11, 12, 16, 17]. It is significant that the reproduction of the SAMS envelope in the responses of auditory nerve fibers occurs via the transformation of the synaptic potential $G(t)$ into a sequence of spikes $P_i$. Such a transformation is only weakly affected by the steepness of the input–output characteristic but strongly affected by the tuning (adaptation) of the threshold to the level of the acting SAMS. In fact, the tuning realizes a kind of amplification control by means of the threshold variation.

However, the steepness of the input–output characteristic of auditory nerve fiber may play an important role in the reproduction of the envelopes of subthreshold SAMSs when the latter are combined with weak noise. Figures 3–5 show the responses of the models of fibers with different SAs to noise and to an additive mixture of SAMS and noise. The curves nearest to the abscissa axes in Figs. 3–5 correspond to the responses of fiber models to noise alone.

Figure 3 shows the responses of the fiber models whose parameters are given in Fig. 2. Evidently, if an SAMS of over-threshold level is presented in combination with low-level noise, any fiber provides a good synchronization of its response with the SAMS (the first row in Fig. 3). An increase in the noise level reduces the synchronization. However, when the SAMS level is gradually decreased below the response threshold, at some of the subthreshold SAMS levels the dependence of the synchronization coefficient $r$ (of the response with the SAMS envelope) on the noise level exhibits an increase in synchronization in a local region near the response threshold. As in Fig. 2c, the maximum values of the synchronization coefficient $r$ are observed for the model of auditory nerve fiber with low SA.

An analysis of the data presented in the second row of Fig. 3 shows that a combination of SAMS with noise increases the mean firing rate in the initial part of the profile of the input–output characteristic, compared to the profile of the characteristic obtained in the presence of noise alone. The steeper the input–output characteristic, the greater the aforementioned increase in the firing rate and the wider the range of noise levels within which this increase is observed. Since the greatest increase in the firing rate occurs in the fiber model with high SA, the lowest subthreshold SAMS level at which the fiber response is synchronized with the SAMS envelope is also observed for this model (the first row in Fig. 3).

Now, let us consider the principal component of the Fourier transform of the phase histogram, $r1$, as a function of the noise level under the presentation of an additive mixture of SAMS and noise (the third row in Fig. 3; this row is obtained as a result of the multiplica-

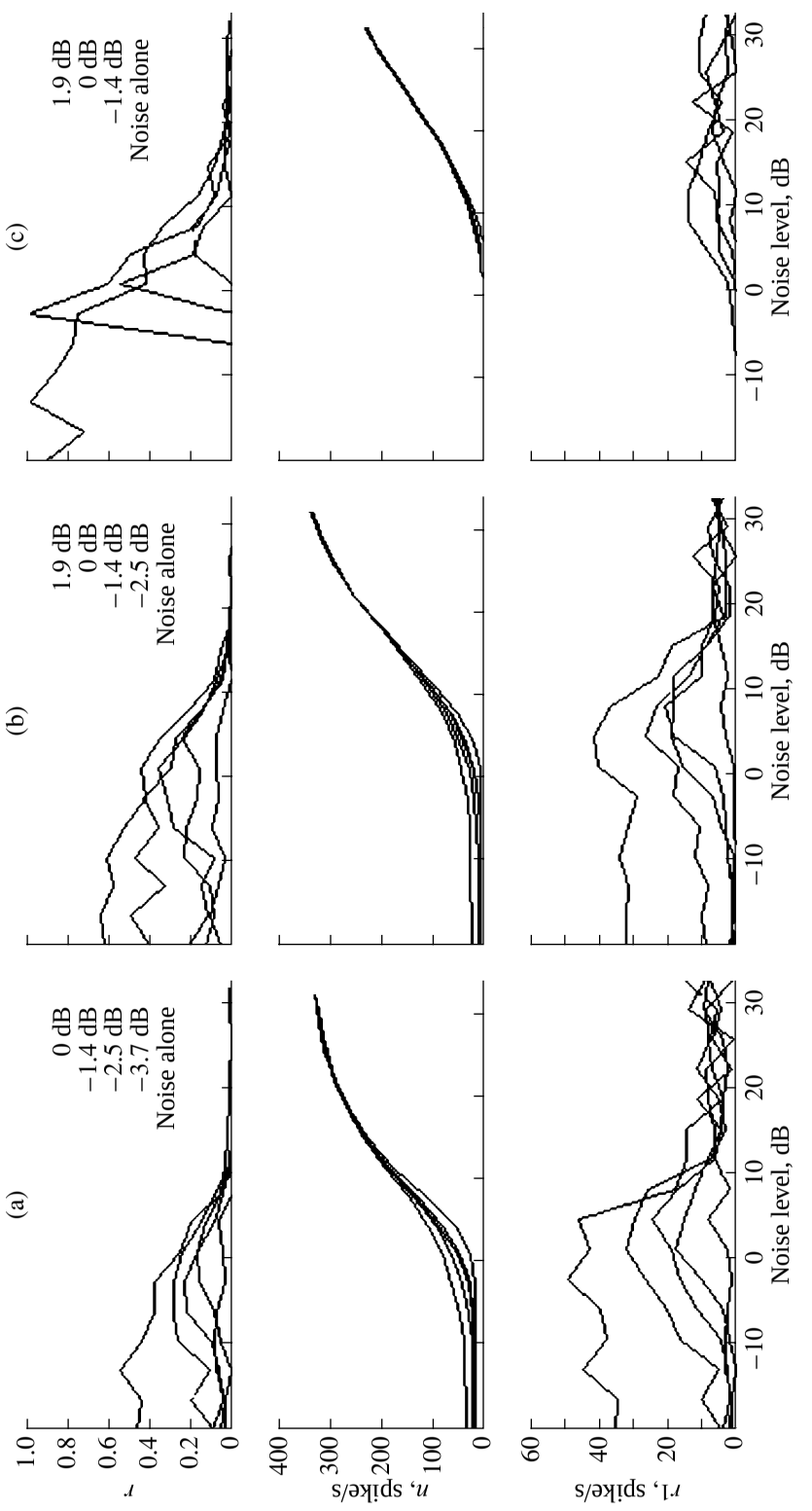


**Fig. 3.** Families of responses to noise or to an additive mixture of SAMS and noise for models of auditory nerve fibers with different SAs: (a) model of auditory nerve fiber with high SA, (b) model with medium SA, and (c) model with low SA. The three rows numbered from top to bottom correspond to the following responses of the model fibers as functions of the noise level: the first row shows the synchronization coefficient *r*, the second row shows the mean firing rate *n*, and the third row represents the principal component of the Fourier transform of the phase histogram *r*1 (in spikes per second). The parameters given in the plots indicate the SAMS levels in decibels with respect to the threshold of the response to SAMS presented in the absence of noise in the model of auditory nerve fiber with high SA. In all plots, the SAMS levels are indicated for the curves in order from top to bottom. The abscissa axis represents the rms deviation of noise in decibels, where 0 dB corresponds to the threshold of the response to noise in the fiber model with high SA.

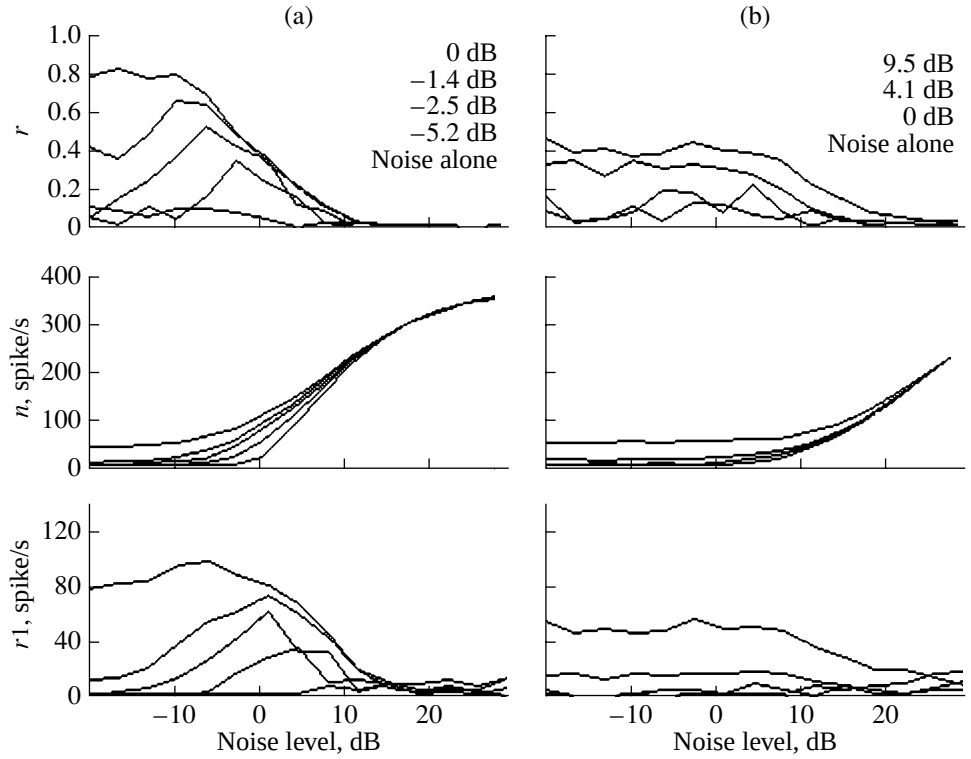


| Column | SA, spike/s | ξ | $R_{max}$ | Sl | $\tau_f$, ms | $H_{0f}/H_0$ | $\tau_s$, ms | $H_{0s}/H_0$ |
|---|---|---|---|---|---|---|---|---|
| a | 13 | 0.015 | 0.12 | 0.025 | 3 | 0.7 | 30 | 0.2 |
| b | ″ | ″ | ″ | 0.5 | ″ | ″ | ″ | ″ |

**Fig. 4.** Families of responses to noise or to an additive mixture of SAMS and noise for models of auditory nerve fibers with different SAs. The effect to be estimated is that of the steepness of the curve representing the mean firing rate versus the noise level (i.e., parameter Sl of the function $R(t)$) on the range of noise and signal levels within which the SAMS envelope can be extracted. The parameters of the fiber models are given in the table at the bottom. The rest of the description corresponds to that of Fig. 3.

tion of the first two rows). In the models of fibers with low and medium SA and with steep input–output characteristics, a certain local increase in $r1$ is observed at some noise levels (the third row in Figs. 3a and 3b). The response of the fiber model with low SA and with a gently sloping input–output characteristic does not exhibit such a local region (the third row in Fig. 3c). From the value of $r1$, it is possible to estimate the modulation of the instantaneous firing rate of the fiber, i.e., to estimate a certain energy characteristic showing the reproduction of the envelope of the SAMS in the output response of the fiber at the modulation frequency. Using the values that were obtained for the principal component of the Fourier transform of the phase histogram $r1$ when the SAMS was mixed with noise and when noise was presented alone, it is possible to estimate the signal-to-noise ratio at different noise levels. Analyzing the data shown in Fig. 3 (the third row in Figs. 3a and 3b), one can see that the signal-to-noise ratio as a function of noise level exhibits an extremum, which occurs in the same optimal range of noise levels as that observed for $r1$. This extremum corresponds to the region of the appearance of stochastic resonance [19–21]. The stochastic resonance occurs when the SAMS levels are within –3.7 to 0 dB for the fiber model with high SA and from –2.5 to 0 dB for the fiber model with medium SA. In the case of the fiber model with low SA and a sloping input–output characteristic, stochastic resonance is absent (the third row in Fig. 3c).

Is it possible to detect subthreshold SAMSs with even lower levels? Remember that the model of auditory nerve fiber includes several stages of nonlinear transformation of the signal, namely: compression of the signal at the receptor or synapse level ($R(t)$), formation of synaptic noise and SA ($S(t)$), transformation of the synaptic potential ($G(t)$) to a sequence of spikes ($P_i$), and adaptation and refractoriness ($H(t)$). These processes affect the property of extracting the SAMS envelope in the response of auditory nerve fiber in the absence of noise. Now, let us consider how these properties affect the value of the subthreshold SAMS level, at which the extraction of the envelope of SAMS is still possible, in the presence of weak noise.

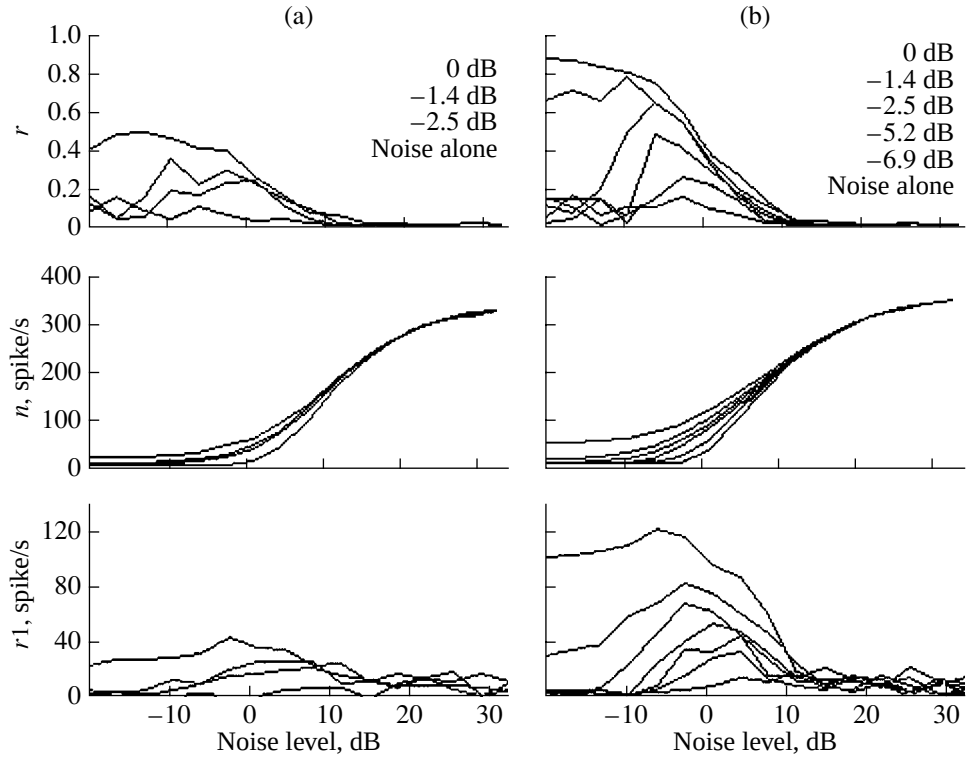


| Column | SA, spike/s | ξ | $R_{max}$ | Sl | $\tau_f$, ms | $H_{0f}/H_0$ | $\tau_s$, ms | $H_{0s}/H_0$ |
|---|---|---|---|---|---|---|---|---|
| a | 15 | 0.014 | 0.054 | 0.025 | 2 | 0.3 | 15 | 0.1 |
| b | " | 0.020 | 0.250 | " | 4 | 1.2 | 45 | 0.3 |

**Fig. 5.** Families of responses to noise or to an additive mixture of SAMS and noise for models of auditory nerve fibers with different SAs. The effect to be estimated is that of the refractoriness and adaptation on the range of noise and signal levels within which the SAMS envelope can be extracted. The parameters of the fiber models are given in the table at the bottom. The minimum (corresponding to the SA level) and maximum values of the mean firing rate were fixed. Because of the changes in the parameters of the threshold function, parameter ξ of the function $S(t)$ and parameter $R_{max}$ of the function $R(t)$ also varied. The rest of the description corresponds to that of Fig. 3.

Figure 4 illustrates the effect of parameter Sl of the function $R(t)$ on the range of signal and noise levels within which the stochastic resonance is observed. All other parameters of the fiber models were identical. The steepness of the amplitude characteristic of synaptic transmission is crucial for the appearance of stochastic resonance. The greater the steepness, the lower the subthreshold SAMS levels at which a stable extraction of the SAMS envelope is possible and the wider the range of noise levels within which stochastic resonance manifests itself.

Fiber models with lower SA (i.e., with a smaller parameter ξ of the function $S(t)$ and with all other parameters of the fiber model being the same) have lower subthreshold SAMS levels at which the SAMS envelope can be extracted in the presence of noise and a wider range of noise levels within which stochastic resonance takes place. However, this decrease in the subthreshold SAMS levels is very small (not shown in the plots).

Other parameters that are crucial for the appearance of stochastic resonance are the parameters of the threshold function $H(t)$. Figure 5 shows the responses of the models of auditory nerve fibers with identical SAs and with the same steepness of the amplitude characteristics of synaptic transmission. The models of fibers with greatest parameters of the threshold function and steep amplitude characteristics of synaptic transmission (Fig. 5b) exhibit the lowest subthreshold SAMS level equal to –6.9 dB, at which the extraction of the SAMS envelope is observed in the presence of weak noise. The simulation experiment shows that the parameters of the threshold function (the adaptation and refractoriness properties) and the SA (the synaptic noise properties) influence the position of the operating point of the amplitude characteristic of synaptic transmission, i.e., the point at which the spikes synchronized

with the SAMS envelope are generated in a given fiber model.

Owing to the great volume of data characterizing the firing rates of auditory nerve fibers of different animals, it is possible to compare the model responses with real responses. It was noted above that real auditory nerve fibers are classed into three groups according to both the SA levels and the response thresholds. The lower the SA of a given auditory nerve fiber, the higher its response threshold is. The scatter of the thresholds depending on SA has been much discussed in the literature [1, 3, 35, 36]. It is well known that the experimental values of the response thresholds of auditory nerve fibers strongly depend on the criterion of the threshold determination. Using the statistical criterion [3], it was found that the response thresholds of auditory nerve fibers with different SAs differ from each other by only a few decibels. Taking these data as a basis, we fixed parameter Dis in the function $R(t)$ and parameter $H_0$ in the function $H(t)$ but varied parameter $\xi$ in the function $S(t)$ determining both the synaptic noise and SA. Because of the change in the synaptic noise level, the response thresholds for the fiber model with high SA were found to be approximately 5 dB lower than those for the fiber model with low SA.

The parameters that determine the refractoriness and adaptation properties (the parameters of the threshold function $H(t)$) of the fiber models were selected so as to reproduce the profiles of the post-stimulus histograms of the responses obtained from auditory nerve fibers with different SAs [11, 12]. Therefore, in the fiber models with high SA, the parameters of the threshold function were the smallest ones. Hence, after the stimulus termination, the response thresholds of these fiber models recovered faster than the response thresholds of other models (this effect is not shown in the figures). This result agrees well with the known fact: the time of the response threshold recovery after the stimulus presentation is greater for fibers with low SA [4, 14].

It has been shown [3, 7, 9, 11, 16] that real auditory nerve fibers with low SA exhibit wider and less steep input–output characteristics than fibers with high SA. The models of auditory nerve fibers with different SAs adequately reproduce these properties (Fig. 2). The input–output characteristic will be flatter when the amplitude characteristic of synaptic transmission is less steep and when the adaptation and refractoriness are more pronounced. The influence of SA is much weaker: the steepness of the characteristic is smaller for higher SA. Therefore, in the model of auditory nerve fiber with low SA, the input–output characteristic is wider and less steep than the corresponding characteristic in the model with high SA.

If the stimulus is a SAMS alone (without noise), real auditory nerve fibers with low SA, in spite of the profile of their input–output characteristic, reproduce the SAMS envelope more adequately than fibers with high SA [7, 9, 11, 12]. In addition, the range of signal levels, within which the envelope is reproduced, is wider for fibers with low SA. An explanation was found for the discrepancy between the profiles of the input–output characteristics of fibers with different SAs and the measured values of the synchronization coefficient $r$ (Fig. 2). Calculations by the model showed that the reproduction of the SAMS envelope in the responses of auditory nerve fibers critically depends on the property of tuning (adaptation) of the threshold to the level of the acting synaptic potential. Since in fibers with low SA such an adaptation occurs more quickly [11, 12], we believe that the synchronization of the response with the SAMS envelope should be better in these fibers.

Different authors investigated the responses of auditory nerve fibers to SAMSs in the presence of broadband noise [9, 11, 37]. As a rule, the presence of high-level noise shifts the mean firing rate of auditory nerve fiber to the region of higher stimulus levels. Such a shift does not affect the reproduction of the SAMS envelope [11]. The physical properties of an additive mixture of signal and noise, as well as the nonlinear properties of the transformation, which manifest themselves at the periphery of the auditory system, may shift the input–output characteristic of the fiber toward lower signal levels [38].

An improvement in the extraction of the stimulus envelope is actually observed in the auditory system for a mixture of a threshold-level signal and broadband noise [39]. In measuring the microphone potentials from the round window of the cochlea, the amplitudes of the envelope of the summary response produced by auditory nerve fibers were estimated under the variation of either noise level or stimulus level. The amplitude of the response increased when the threshold signal was mixed with broadband noise whose level was below 10–15 dB. The amplitude remained unchanged at intermediate noise levels and decreased at high noise levels. The increase in the amplitude of the response of the summary microphone potential was explained by the author of the cited publication by the phenomenon of stochastic resonance. Most likely, under the effect of the additive mixture of the threshold-level signal and noise, the summary microphone potential was formed from the responses of low-threshold auditory nerve fibers with steep input–output characteristics. Hence, the results reported in paper [39] can be qualitatively compared with the results of the above calculations (Fig. 3). From the model calculations, it follows that an improvement in the extraction of the signal envelope for subthreshold SAMSs in the presence of weak broadband noise occurs in the low-threshold models of auditory nerve fiber with high SA owing to their steep input–output characteristics and the stochastic resonance property. This result agrees well with the conclusions of [31, 40].

Model studies show that the region of the stochastic resonance manifestation can be different. Therefore,

the range of subthreshold SAMS and noise levels may be broader if the adaptation and refractoriness properties of the fiber are clearly pronounced (Fig. 5). At this point it is unclear which of the properties of real fibers change in the course of adaptation. Let us assume that adaptation provides not only the tuning of the synaptic potential to the response threshold of a spiral ganglion neuron but also leads to a change in the profile of the transient amplitude characteristic of synaptic transmission by increasing the steepness of the profile. In this case, the effect of stochastic resonance may play an important role in the analysis of hearing data at the periphery and at higher levels of the auditory system.

It is also necessary to note the important role of synaptic noise. Owing to noise, the spike sequence obeys a Poisson distribution. It is well known that noise provides the desynchronization of responses in different fibers. Noise can prevent the correlation that may appear between interspike intervals at high-level stimuli because of the refractoriness. Such a correlation leads to the appearance of chopper-type responses, which are characteristic of the neurons of cochlear nuclei rather than of auditory nerve fibers [24, 25].

Evidently, the coding of the SAMS envelope at the periphery of the auditory system depends on the properties of nonlinear transformations. The periphery model considered in this study includes the following nonlinear transformations: (i) compression and detection of the signal at the receptor level, (ii) formation of the synaptic potential in the form of a random process, (iii) transformation of the synaptic potential into a sequence of spikes, (iv) change in the excitability of the fiber after the generation of a spike (refractoriness), and (v) decrease in the firing rate during the presentation of a prolonged stimulus (adaptation).

The simulation experiments revealed the role of these processes in the extraction of the envelopes of SAMSs of medium (corresponding to the sloping part of the input–output characteristic) and subthreshold levels.

The coding of the envelopes of SAMSs with any levels at the periphery of the auditory system is a dynamic process, which occurs with the transformation of synaptic potentials into a spike sequence and provides the tuning (adaptation) of the system to the level of the acting SAMS. This tuning plays a positive role in all cases. It serves as a kind of amplification control. It changes the position of the operating point on the amplitude characteristic of synaptic transmission, i.e., the point at which the generation of spikes synchronized with the SAMS envelope takes place.

When a SAMS of intermediate level is presented, the steepness of the input–output characteristic weakly affects the degree of reproduction of the SAMS envelope in the fiber response. The SAMS envelope is reproduced and pronounced more strongly when the SA is lower and the adaptation and refractoriness are greater, i.e., when the tuning of the threshold of the fiber response to the level of the synaptic potential is better. For low-threshold auditory nerve fibers, the role of the steepness of the input–output characteristic drastically increases when the coding of subthreshold SAMS envelopes occurs in the presence of weak noise. The region of the stochastic resonance manifestation can be greater if the tuning of the response threshold of the fiber to the signal level is finer. The existence of the tuning of the system to the level of an acting stimulus is recognized by many researchers [1, 5, 6, 9, 12, 17]. This study reveals its important role.

Further studies of both the dynamic coding of the SAMS envelope and the stochastic resonance are necessary for understanding the mechanisms of signal processing not only at the periphery but also at higher levels of the auditory system.

## ACKNOWLEDGMENTS

I am grateful to V.N. Telepnev for useful discussions and for his interest in this study. The work was supported by the Russian Foundation for Basic Research, project nos. 00-04-49311 and 03-04-48746.

## REFERENCES

1. M. C. Liberman, J. Acoust. Soc. Am. **63**, 442 (1978).
2. M. C. Liberman and M. E. Oliver, J. Comp. Neurol. **223**, 163 (1984).
3. C. D. Geisler, L. Deng, and S. Greenberg, J. Acoust. Soc. Am. **77**, 1102 (1985).
4. W. S. Rhode and P. H. Smith, Hear. Res. **18**, 159 (1985).
5. N. G. Bibikov, *Description of Sound Features by Neurons of the Auditory System of Land Vertebrates* (Nauka, Moscow, 1987), pp. 16–49.
6. N. G. Bibikov, in *Mechanisms of Functioning of the Peripheral Elements of Auditory Pathway*, Ed. by M. A. Ostrovskiĭ (VINITI, Moscow, 1988), Itogi Nauki Tekh., Vol. 39, p. 122.
7. I. M. Winter, D. Robertson, and G. K. Yates, Hear. Res. **45**, 191 (1990).
8. P. X. Joris and T. C. T. Yin, J. Acoust. Soc. Am. **91**, 215 (1992).
9. W. S. Rhode and S. Greenberg, J. Neurophysiol. **71**, 1797 (1994).
10. A. Merchan-Perez and M. C. Liberman, J. Comp. Neurol. **371**, 208 (1996).
11. R. D. Frisina, K. J. Karcich, T. C. Tracy, *et al.*, J. Acoust. Soc. Am. **99**, 475 (1996).
12. R. D. Frisina, Hear. Res. **158**, 1 (2001).
13. J. J. Eggermont, Hear. Res. **157**, 1 (2001).
14. E. M. Relkin and J. R. Doucet, Hear. Res. **55**, 215 (1991).
15. D. K. Ryugo and E. M. Rouiller, J. Comp. Neurol. **271**, 130 (1988).
16. R. Patuzzi and P. M. Sellick, J. Acoust. Soc. Am. **74**, 1734 (1983).
17. G. K. Yates, Hear. Res. **27**, 221 (1987).

18. L. K. Rimskaya-Korsakova, V. N. Telepnev, and N. A. Dubrovsky, Ross. Fiziol. Zh. **89**, 700 (2003).
19. S. M. Bezrukov, Phys. Lett. A **248**, 29 (1998).
20. J. Tougaard, Biol. Cybern. **87**, 79 (2002).
21. L. M. Ward, A. Neiman, and F. Moss, Biol. Cybern. **87**, 91 (2002).
22. D. H. Johonson and A. Swami, J. Acoust. Soc. Am. **74**, 493 (1983).
23. L. K. Rimskaya-Korsakova, Akust. Zh. **35**, 887 (1989) [Sov. Phys. Acoust. **35**, 516 (1989)].
24. N. A. Dubrovskiĭ and L. K. Rimskaya-Korsakova, Akust. Zh. **43**, 492 (1997) [Acoust. Phys. **43**, 421 (1997)].
25. N. A. Dubrovskiĭ and L. K. Rimskaya-Korsakova, Akust. Zh. **44**, 213 (1998) [Acoust. Phys. **44**, 173 (1998)].
26. J. L. Flanagan, *Speech Analysis, Synthesis and Perception*, 2nd ed. (Springer, Berlin, 1972; Svyaz', Moscow, 1968).
27. S. A. Shamma and K. A. Morrish, J. Acoust. Soc. Am. **81**, 1486 (1987).
28. M. B. Sachs, R. L. Winslow, and B. H. A. Sokolowski, Hear. Res. **41**, 61 (1989).
29. M. Zagaeski, A. R. Cody, I. J. Russell, and D. C. Mountain, J. Acoust. Soc. Am. **95**, 3430 (1994).
30. X. Zhang, M. G. Heinz, I. C. Bruce, and L. H. Carney, J. Acoust. Soc. Am. **109**, 648 (2001).
31. R. Patuzzi and P. M. Sellick, J. Acoust. Soc. Am. **74**, 1734 (1983).
32. A. Rees and A. R. Palmer, J. Acoust. Soc. Am. **85**, 1978 (1989).
33. N. G. Bibikov and G. A. Ivanitskiĭ, Biofizika **30** (1), 141 (1985).
34. D. O. Kim, J. G. Sirianni, and S. O. Chang, Hear. Res. **45**, 95 (1990).
35. N. Y. Kiang, Ann. Otol. Rhinol. Laryngol. **77**, 656 (1968).
36. G. K. Yates, Hear. Res. **57**, 57 (1991).
37. D. J. Gibson, E. D. Young, and J. A. Castalupes, J. Neurophysiol. **53**, 940 (1985).
38. E. R. Lewis and K. R. Henry, Hear. Res. **92**, 1 (1995).
39. K. R. Henry, J. Comp. Physiol. A **184**, 577 (1999).
40. F. Jaramillo and K. Wiesenfeld, Nat. Neurosci. **1**, 384 (1998).

*Translated by E. Golyamina*

*Acoustical Physics, Vol. 50, No. 2, 2004, pp. 212–221. Translated from Akusticheskiĭ Zhurnal, Vol. 50, No. 2, 2004, pp. 261–271.*


# Spherical Focusing of Acoustic Pulses in a Liquid

**G. N. Sankin**

*Lavrent'ev Institute of Hydrodynamics, Siberian Division, Russian Academy of Sciences, pr. Akademika Lavrent'eva 15, Novosibirsk, 630090 Russia*

*e-mail: sankin@hydro.nsc.ru*

Received March 27, 2003

**Abstract**—Nonlinear processes accompanying the focusing of a microsecond acoustic pulse produced by an electromagnetic source shaped as a spherical segment are investigated. The processes are considered to be far from the boundaries of a liquid, in the absence of cavitation. Detailed measurements of the pressure field by a fiber-optic sensor and high-speed photography of the shock front are performed. The pressure field is found to be determined by the nonlinear effects that occur in the course of the propagation of the initial converging compression wave and an edge rarefaction wave. The peak pressure amplitudes at the focus are 75 and –42 MPa for the compression and rarefaction waves, respectively, at the maximum voltage of the pulse generator in use. The measured length of the compression wave front is equal to the response time of the sensor (8 ns). The pressure amplitude is shown to be limited by the irregularity of the propagation of a shock wave in the form of Mach's disk. At the focus, the pressure gradient across the radiator axis reaches 0.5 atm/μm, while the diameter of the focal spot is 2.5 ± 0.2 mm. The focus of the edge rarefaction wave formed due to diffraction is located closer to the radiator than the focus of the compression wave, which may facilitate the study of the biological effect of cavitation independently of the shear motion of the medium. © *2004 MAIK "Nauka/Interperiodica".*

## INTRODUCTION

Starting from the mid-1980s and up to now, systems for focusing shock waves have been much used in medicine for lithotripsy (stone destruction in kidneys) [1] and therapy of malignant tumors [2]. The pressure gradient in the compression phase and the cavitation in the rarefaction phase seem to be the two most important factors in the mechanisms of stone and cell destruction that are not yet understood [3]. Thus, to develop medical applications of shock-wave generators, it is necessary to know the pressure field and, especially, its negative component. The location of the focus of the negative pressure phase is quite important: it is almost always reached before the geometrical focus of the radiator [4], and, according to theoretical estimates, the coefficient of volume expansion of a gas-vapor cavity in the case of cavitation is maximal at this point [5]. This rule was suggested to increase the efficiency of destruction of kidney stones in lithotripsy [6].

In the approximation of linear geometrical acoustics, the amplitude of both positive and negative pressure pulses at the focus theoretically grows without limit. However, in practice, pressure at the focus is limited by the diffraction laws and the irregular (Mach's) character of propagation of a shock front near the focus [7, 8]. Therefore, investigations [9] of focusing of a rarefaction wave, whose form in a liquid can be calculated using the Khokhlov–Zabolotskaya–Kuznetsov model proposed in [10, 11], are conducted in a limited pressure range. The results of experimental and theoretical studies in this case agree well in the precavitation conditions [12].

Here, we present the results of an experimental study of nonlinear processes and measurement of a detailed space–time distribution of pressure in the case of focusing of an acoustic pulse produced by a source shaped as a spherical segment. The results of pressure field measurements belong to the precavitation conditions of acoustic pulse propagation (the influence of cavitation on pressure measurements is excluded).

## 1. BRIEF THEORY

To develop a theory of shock waves, an equation of state and conservation laws are necessary. The key points of this study were interpreted using the approximation of weak shock waves in water, which can be described by the following equation of state:

$$p/p_c = (\rho/\rho_0)^\gamma(1 + p_0/p_c) - 1, \quad (1)$$

where $\rho_0$ is the density of water at atmospheric pressure $p_0$ and $p_c$ and $\gamma$ are characteristic functions that are usually selected from the experiment, but in the pressure and temperature ranges under consideration they can approximately be considered as constants. The values of $p_c = 2955$ atm and $\gamma = 7.44$ are chosen so as, with the given equation of state, to obtain the correct value of sound velocity $c_0 = 1483$ m/s at room temperature from the expression

$$c_s^2 \equiv (\partial p/\partial\rho)_s = \gamma(p + p_c)/\rho. \quad (2)$$

Using the approximation of an infinitely small thickness of a shock front and proceeding from the laws of conservation of mass and momentum, we obtain

equations for calculating the velocity of a plane shock wave $c$ and the velocity of motion of the medium behind the front $u_1$:

$$c^2 = p_1/\rho_0[1 - (1 + p_1/p_c)^{-1/\gamma}]^{-1}, \quad (3)$$

$$u_1 = (p_1 - p_0)/\rho_0 c \quad (4)$$

or, in terms of the Mach number $M = c/c_0$ and dimensionless density $r = \rho_1/\rho_0$,

$$M^2 = (r/\gamma)(r^\gamma - 1)/(r - 1). \quad (5)$$

Since the compressibility of water is small, its density does not change significantly in the case of weak shock waves if the pressure is $p \le p_c$. Therefore, the equations obtained can be simplified by decomposition with respect to a small parameter $r - 1$. Holl demonstrated [13] that the equations of gas dynamics can be used to describe weak shock waves in a liquid by introducing the effective pressure $p' = p + p_c$ and index $\gamma$ instead of the adiabatic exponent $\gamma_{gas}$ into the equations of gas dynamics. For example, the expression for the Mach number in a liquid takes the form

$$M = \{[(\gamma + 1)(p_1 + p_c)/(p_0 + p_c) + \gamma - 1]/2\gamma\}^{1/2} \quad (6)$$

and $M = 1.07$ for $p_1 = 72$ MPa.

Thus, in the case of the focusing of weak shock waves in water, one can expect effects analogous to those observed in [14] in the case of reflection and focusing in a gas.

The dependence of the refraction index of water

$$n(p_1) = 1 + (n_0 - 1)[1 + (p_1 - p_0)/(p_0 + p_c)]^{1/\gamma}, \quad (7)$$

which is expressed through the relationship of density and pressure, is used in optical diagnostics of shock waves.

This means that shock waves can be detected by the deflection of an illuminating beam or by the reflection of light from a shock front with possibility of a quantitative determination of shock wave parameters.

A converging shock wave in the form of a spherical segment has an axial symmetry. Therefore, the velocity of the medium at the axis does not have a component normal to the axis. In other words, the symmetry axis plays the role of a solid boundary. An oblique incidence of an shock wave front on a solid surface is examined in [7] and schematically represented in Fig. 1. A solution for the reflection angle $\alpha'$ as a function of the angle of incidence $\alpha$ has two roots. This fact indicates a special reflection mode that is known as the irregular or Mach's reflection. The critical reflection angle $\alpha_{extr}$ can be calculated proceeding from simple conditions for reflection and the laws of conservation of mass and momentum at the fronts of the incident and reflected waves. For example, for the pressure $p = 65$ MPa, we obtain $\alpha_{extr} = 57°$ and $\alpha'_{extr} = 73°$ [7]. As the Mach's foot does not obey the $D$–$U$ equation [15] for regular shock waves, its velocity depends on the angle of incidence $\alpha$.

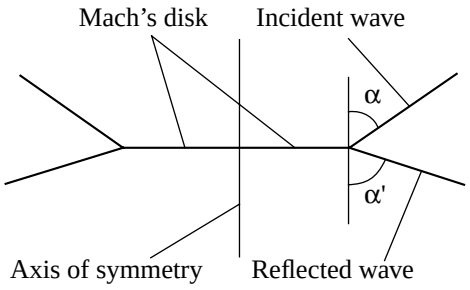


**Fig. 1.** Mach's disk formation in the focusing process.

## 2. MATERIALS AND METHODS

### *2.1. Electromagnetic Generator of Shock Waves*

The generator of acoustic pulses used in the experiment consists of a generator of intense current pulses [16] and a removable spherical radiator. In the generator, a low-inductance ($L < 5$ nH) capacitance $C = 1$ and 2 μF was connected with a high-voltage charging unit. The capacitance was charged up to the voltage set by a voltage comparator with the help of high-voltage pulses of 10 kV with a frequency of 10–20 kHz. After attaining a preset voltage, charging was interrupted until the voltage at the capacitance became lower than the preset one. An accumulating capacitance was connected to the output terminals of the generator of current pulses through an RU-62 gas-discharge switch. The operating voltage $U_c$ of the generator was 5 to 10 kV.

To obtain short pulses and, therefore, a high coefficient of conversion of electric energy to acoustical energy, the inductance of the circuit capacitance–switch–shunt circuit must be smaller than the radiator inductance. Radiators were connected to the generator output with the help of a strip line. A high-power pulse of current is formed as a result of the capacitance discharge through the coil of the radiator. It is evident that periodic damped oscillations are excited in the circuit [17]. The maximum possible pulse frequencies for different charging voltages are given in Table 1.

**Table 1.** Frequency of "fast" pulses of the generator for $C = 2$ μF

| $U_g$, kV | Time between pulses, s | Pulse frequency $f_f$, Hz |
|---|---|---|
| 5 | 4.0 | 0.25 |
| 6 | 4.5 | 0.22 |
| 7 | 5.2 | 0.19 |
| 8 | 6.3 | 0.16 |
| 9 | 7.5 | 0.13 |
| 10 | 8.1 | 0.12 |

The spherical radiator (schematically represented in Fig. 2) had an aperture $D$ = 70 mm and a curvature radius $R$ = 55 mm. It contained (*1*) an electromagnetic coil and (*2*) an aluminum membrane, which were separated by an insulating foil. The coil consisted of eleven winds laid in an Archimedes spiral onto a caprolan substrate with the help of adhesive tape. The wind density of the coil was uniformly distributed over the substrate surface, and, therefore, the coil provided the most homogeneous magnetic field at its surface. The coil made of a 0.6-mm copper wire, a mylar insulating film with a thickness of 0.04 mm, and an aluminum membrane with a thickness of 0.3 mm were tightly pressed to each other. The membrane screens the magnetic field of the coil and, therefore, the magnetic pressure pushes the membrane into a liquid. A compression wave with its focus at the point $F_+$ and an edge rarefaction wave with its focus at the point $F_-$ propagate in the liquid [18].

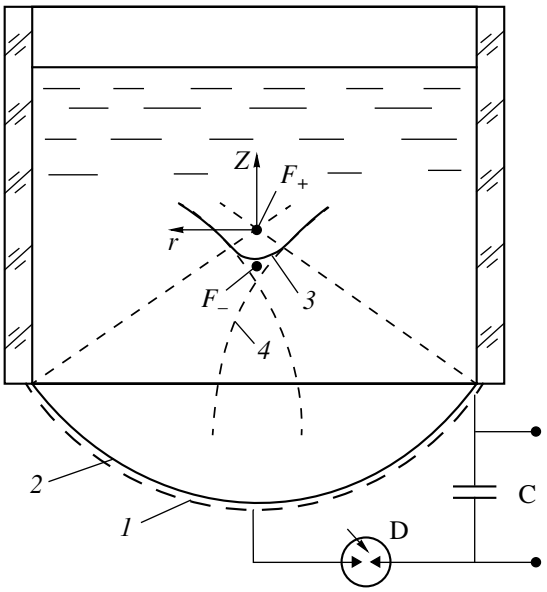


**Fig. 2.** Radiator of acoustic pulses: (*1*) single-layer inductance coil, (*2*) membrane, (*3*) focused acoustic pulse, (*4*) edge rarefaction wave, (C) accumulating capacitor, (S) switch, ($F_+$) focus of the compression wave, and ($F_-$) focus of the rarefaction wave.

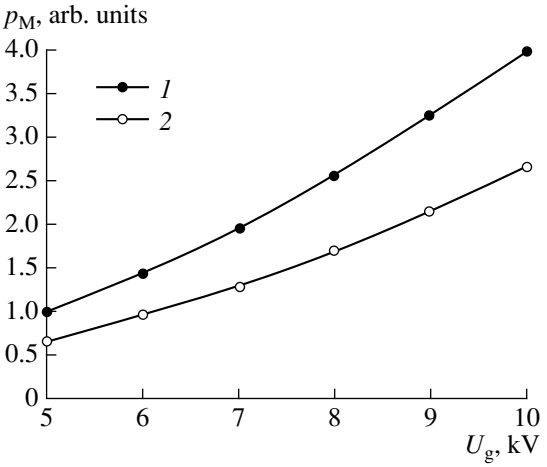


**Fig. 3.** Relative pressure values at the radiator membrane. $T$ = (*1*) 4 and (*2*) 3 μs.

The generator design provides an opportunity to shape the radiator as a spherical segment to obtain a converging acoustic pulse without a lens. Utilization of an acoustic lens for focusing is undesirable, since it leads to a temperature dependence of the focal distance of the radiator [19], to a complex pattern of pressure field because of the interference of waves reflected from the lens surfaces [20], and to a possible triboluminescence of the lens.

It was found experimentally that the pressure amplitude of an acoustic pulse in the positive and negative phases near the membrane changes proportionally to the square of charging voltage $U_g$ [17]. When the capacitance was reduced by half, the period $T$ changed from 4 to 3 μs, which led to an approximately 30% reduction of pressure at the membrane [21]. The pressure at the radiator was calculated on the basis of observations, according to the approximating function preset with the help of Fig. 3.

In the approximation of linear diffraction, the diameter $d$ of the focal region is determined by the diffraction relation $d \sim Fc_0\tau_M/D$, where $D$ is the radiator aperture, $F$ is the focal distance, $c_0$ is the sound velocity, and $\tau_M$ is the length of a pressure pulse at the membrane. The pulse amplitude at the focus is approximately inversely proportional to the diameter $d$ of the focal spot. This means that to increase the pressure gain it is necessary to reduce the pulse length $\tau_M$ and the ratio $F/D$ as follows from the diffraction relation.

### *2.2. Measurement of the Velocity of a Shock Front*

High-speed cameras and pressure sensors were used to investigate the pressure field. A setup for studying the propagation dynamics of converging shock waves is similar to that described in [22]. Experiments were conducted in water at room temperature.

The time profile of pressure was measured by an FOPH 300 sensor [23], which operates on the basis of the determination of the variation of the reflection coefficient at the end of optical fiber because of the change in the refraction index of the medium (Eq. (7)). The measurement error in the pressure measurement is determined by the conditions at the optical fiber surface (2.5%), by temperature instability (1%), by the error of measurement of the oscilloscope signal (about 2%), and by the error in positioning the optical fiber of the sensor. In the case of a wave with a shock front, the measurement error is also connected with the limited time resolution of the sensor, which reduces the amplitude of the measured signal. The time resolution becomes lower if the optical fiber is installed incorrectly. In the case of an inclination of 5°–7°, the pres-

sure rise time becomes comparable with the time resolution of the sensor because of the oblique incidence of shock waves. The front speed for regular waves was determined by Eq. (3) according to the measured pressure amplitude.

To estimate the propagation velocity of waves, we also used the formula

$$V = (z_1 - z_2)/(t_1 - t_2), \quad (8)$$

where $z_1$ and $z_2$ are two positions of the sensor and $t_1$ and $t_2$ are the times corresponding to the pressure maximum. This formula makes it possible to evaluate the velocity from two measurements by the sensor. The value of the velocity obtained in this way belongs to the time moment $t_i = (t_1 + t_2)/2$ and the coordinate $z_i = (z_1 + z_2)/2$. The measurement error was introduced in the process of sensor positioning and determining the position of the pressure maximum. The coordinate was controlled with an accuracy of 20 μm, which constitutes 0.4% of the base $|z_1 - z_2| = 5$ mm.

The time error was determined by the sharpness of the pressure peak for a wave without a shock front, whose principal spectral component had a frequency of 250 kHz (a time error of 80 ns). In the case of a wave with a shock front, the error was determined by the time resolution of the measuring system, which was equal to 8 ns or 125 MHz, and the start-up system using an antenna pickup with a signal front shorter than 4 ns. Therefore, a delay between the generator start and the arrival of a wave at the sensor is measured with a scatter of less than 12 ns. The systematic error of measurement was 0.4% for shock fronts and 2.5% for pulses without shock fronts.

Film shots present a time-resolved general pattern of waves in the $x$, $z$ coordinates. The determination of the velocity of a wave front according to film shots was performed using Eq. (8). In this case, the coordinates of the darkest points in a film shot were taken as the values of $z_1$ and $z_2$, and delays for two frames were taken as the values of $t_1$ and $t_2$. The measurement error $z$ was determined by the height of a digital matrix, which was 50 μm in the object plane, and the time error of 10 ns was determined by the time of exposure of each frame. The root-mean-square error of measurement in this case was 1.5%.

## 3. RESULTS

Since the membrane is shaped as a spherical segment, a converging acoustic pulse is generated in water. As a result of nonlinear distortion, a sinusoidal pulse is transformed to a pulse with a shock front.

Figure 4a presents an oscillogram of a signal from a pressure sensor. The sensitive surface of the sensor was positioned at the focus $z = r = 0$ of a spherical radiator in water, which was determined as the maximum of pressure amplitude for $p_M = 3.0$ MPa. This method provided an opportunity to determine the focus position

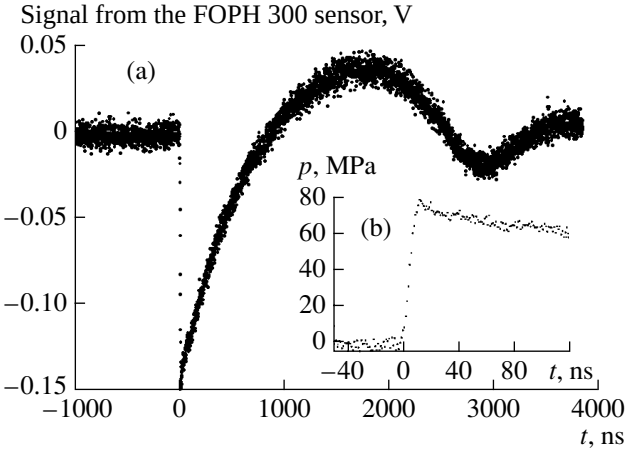


**Fig. 4.** (a) Signal from a fiber-optical sensor and (b) the reconstructed pressure at the focus ($z = r = 0$ mm) for $p_M$ = 4.3 MPa. The digitizing rate is 1 ns.

across the axis with an accuracy of 0.25 mm. The parallelism of the sensor to the shock front was monitored according to the film shots obtained using a microscope. We achieved an alignment precision of 1°. Figure 4b demonstrates the front of a reconstructed inverted and calibrated signal. The time of its rise from 10 up to 90% of the maximum value was 8 ns and did not change when the pressure at the membrane $p_M$ varied from 3.0 to 9.7 MPa; i.e., this time was determined by the sensor lag.

High-speed microscopic photography of a shock front was performed near the focus of the radiator. The results are given in Fig. 5. One can see a transition from a front geometry that is concave towards the membrane (a spherically converging wave) to a geometry convex from the membrane (a spherically divergent wave). A visible transition near the focus point is accompanied by the formation of a Mach type wave pattern. At the instant of 36.5 μs for $p_M = 3.0$ MPa (Fig. 5a), a disk-like front is observed, which is connected with two fronts inclined with respect to it. The incident wave front makes a smaller angle ($\alpha_{3.0\ \mathrm{MPa}} = 71.0° \pm 0.8°$) to the axis than the reflected wave front. Thus, the disk perimeter is the place of connection of three fronts, by analogy with the triple point (Fig. 1), and the disk is the Mach's foot in the case of a Mach's or irregular reflection.

At the same setting of the generator parameters, the time and space reproducibility of the pressure field from one experiment to another provided an opportunity to investigate it in detail, including the case of precision positioning of the sensor with the help of a microscope (a displacement in the direction perpendicular to the generator axis that is smaller than 1/4 of the sensor diameter corresponds to 50 μm).

Figure 6 gives the pattern of pressure field for $p_M$ = 3.0 MPa. Time dependences of pressure at some points are given (Figs. 6f–6m). At $z = -24.5$ mm, at the axis,

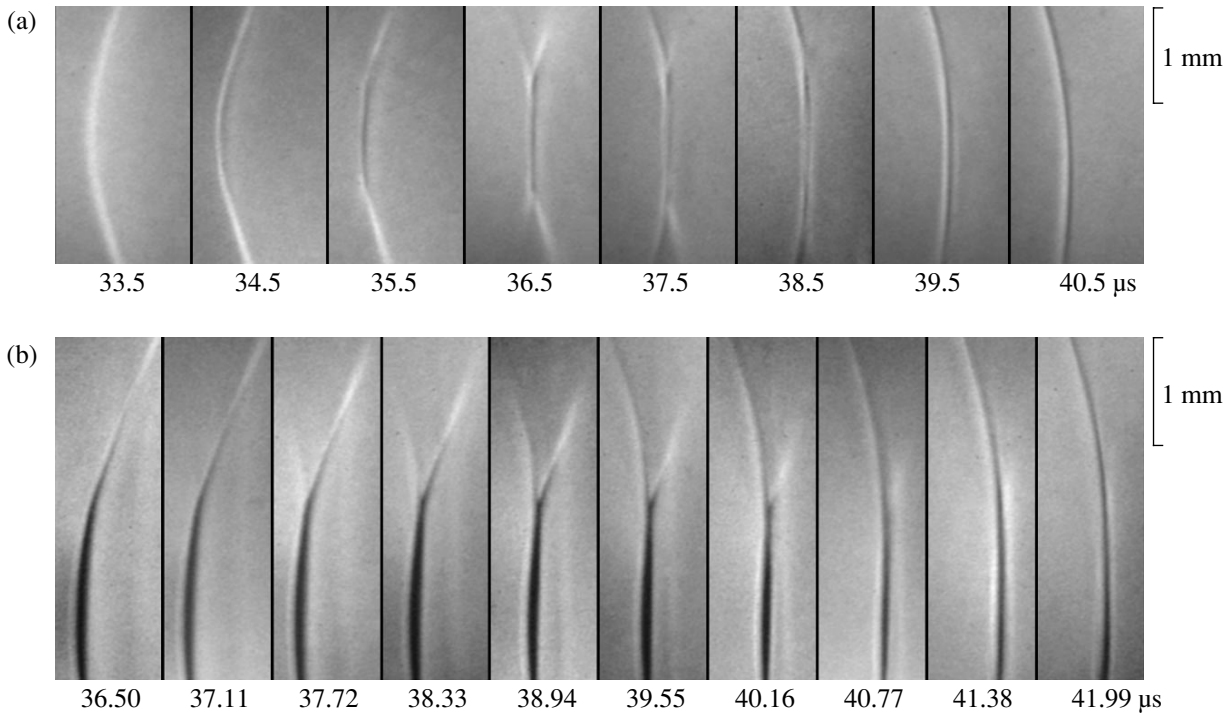


**Fig. 5.** Microscopic image of the compression wave front (propagating from left to right) near the focus for $p_M$ = (a) 3.0 and (b) 5.9 MPa (the radiator axis is shifted from the center toward the lower boundary of the frame).

the positive phase of pressure consists of two peaks (Fig. 6l, indicated by arrows) corresponding to two half-periods of the discharge current of the capacitor. At $r$ = 2 mm, for the same $z$, in the negative phase the sensor detects a double passage of the rarefaction wave from opposite edges of the radiator in the form of two minima in the oscillogram (indicated by arrows in Fig. 6m) with the distance between them decreasing down to zero at the axis.

After that, the pressure profiles were linearly interpolated taking into account the weight, and the resulting isobars were plotted in the $t$, $r$ coordinates for different $z$. Figures 6a–6d present the result of the interpolation. For $z$ = –8, –2, 0, 2, and 8 mm, the sensor coordinate $r$ varied from 0 to 9 mm with a step of 1 mm (Figs. 6a, 6b). For $z$ = –24.5 mm, the measurements were conducted for $r$ from 0 to 14 mm with a step of 2 mm (Fig. 6d). The isobars have artefacts in the form of "microscopic islands" of increased pressure because of the large step.

Figure 6c shows the results of pressure measurements at the focus for $z$ = 0 mm and for $r$ = –1 to 1.5 mm with a step of 250 μm (160% of the sensor diameter). The focal zone width measured at a level of –6 dB (the 50%-level for pressure) was 2.5 mm for $p_M$ = 3.0 MPa.

The region of the medium with a pressure amplitude greater than half the maximum one has a form close to axisymmetric and is elongated along the axis. Some characteristics of pressure in this region that are measured for a spherical generator as functions of pulse length and amplitude at the membrane are given in Tables 2 and 3. The region length along the axis (the focus depth $L_{+/-}$), the region diameter $D_{+/-}$, the pressure gain $K_{p+}$, the position of space–time extrema of pressure $\Delta z_{+/-}$, the peak flux of acoustic energy at the center of the region

$$I = \frac{p_{max}^2}{\rho c}, \quad (9)$$

**Table 2.** Geometrical characteristics of the focal region

| $p_M$, MPa/$T$, μs | $L_+$, mm | $L_-$, mm | $D_+$, mm | $D_-$, mm | $K$ | $\Delta z_+$, mm | $\Delta z_-$, mm |
|---|---|---|---|---|---|---|---|
| 1.5/3 | 9 ± 2 | 20 ± 5 | 1.6 ± 0.2 | 4.0 ± 0.5 | 36.7 ± 1.5 | 0 ± 0.5 | –3 ± 1 |
| 3.0/4 | 18 ± 1 | 25 ± 5 | 2.5 ± 0.2 | 6.0 ± 0.5 | 23.3 ± 0.5 | 0 | –5 ± 1 |
| 4.3/4 | 22 ± 1 | 25 ± 5 | 3.0 ± 0.5 | – | 15.9 ± 0.5 | 0 ± 0.5 | –5 ± 1 |

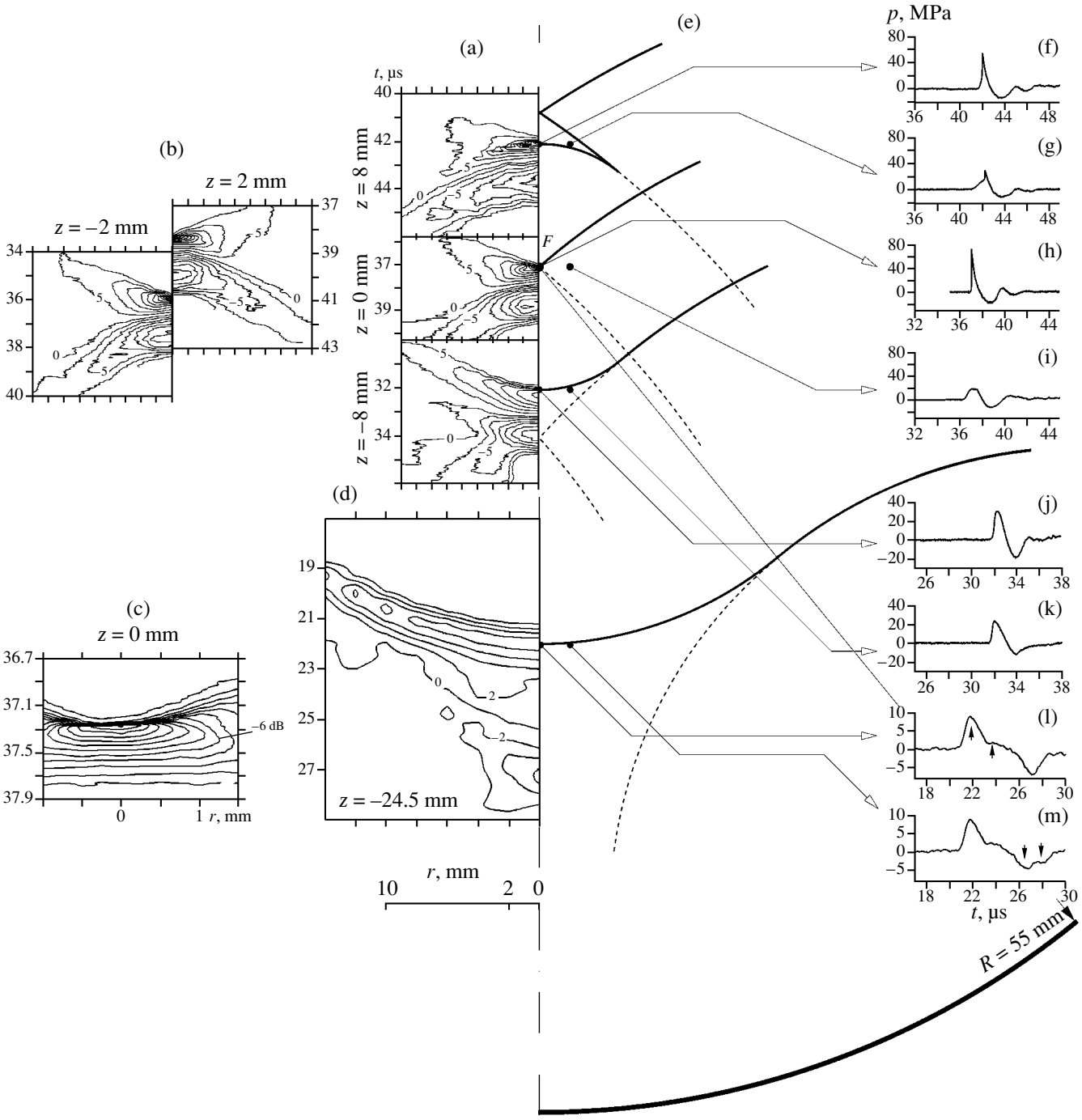


**Fig. 6.** Pressure pattern of a focused wave for $p_M$ = 3.0 MPa. (a–d) Experimental data for a fiber-optical sensor. Isobars are given at a step of (a, b) 5 MPa for positive pressure, 2.5 MPa for negative pressure, and (d) 2 MPa. (c) Pressure distribution near the focus: the distance between isobars is 5 MPa, the maximum pressure is 70 MPa, and the level is –6 dB (35 MPa for pressure). (e) Wave fronts in the approximation of linear geometrical acoustics. (f–m) Oscillograms of pressure for certain positions of the sensor.

the area of the section $S_{-6\,\mathrm{dB}}$ of the indicated region by the focal plane, and the total energy transmitted through the indicated area

$$E_{-6\,\mathrm{dB}} = \int_{t\,r|_{p<0.5p_{\max}}} \int \frac{p^2(r,t)}{\rho c} 2\pi r\,dr\,dt \qquad (10)$$

are given in these tables as functions of the pressure at the membrane. The subscripts + and – correspond to the positive and negative maxima, respectively.

Figure 6e presents the comparison of the results of pressure measurements with the model of linear acoustics, where solid lines show the front of a compression

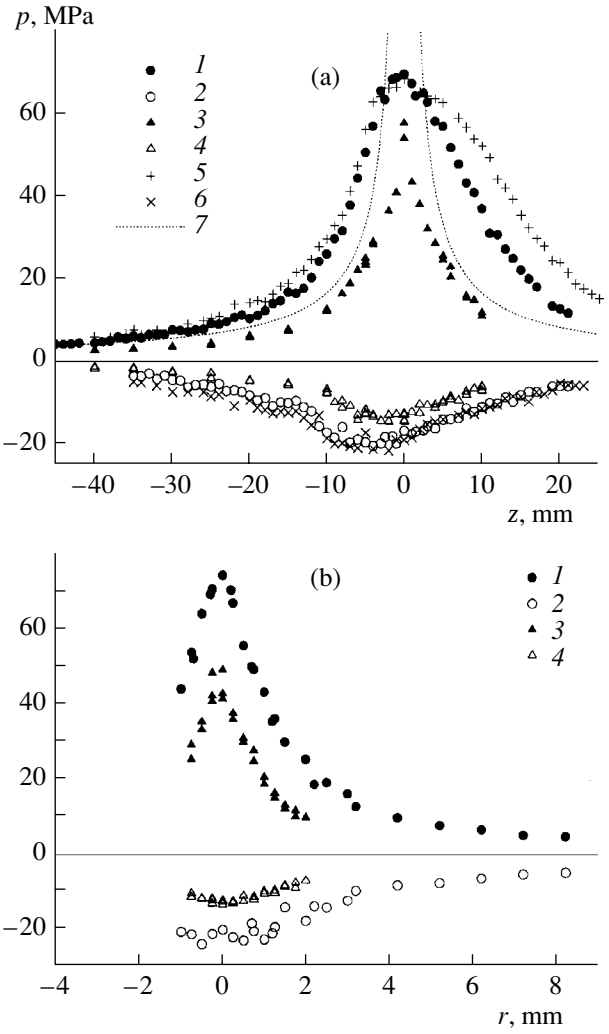


**Fig. 7.** (a) Pressure amplitude at the radiator axis for (*1*, *3*, *5*) the compression and (*2*, *4*, *6*) rarefaction waves: (*1*, *2*) $p_M$ = 3.0 MPa and $T$ = 4 μs; (*3*, *4*) $p_M$ = 2.0 MPa and $T$ = 3 μs; and (*5*, *6*) $p_M$ = 4.3 MPa and $T$ = 4 μs; (*7*) the approximation of linear geometrical acoustics for $p_M$ = 3.0 MPa ($p = p_M R/|z|$). (b) Pressure amplitude in the focal plane for (*1*, *3*) the compression and (*2*, *4*) rarefaction waves: (*1*, *2*) $p_M$ = 3.0 MPa and $T$ = 4 μs; (*3*, *4*) $p_M$ = 2.0 MPa and $T$ = 3 μs.

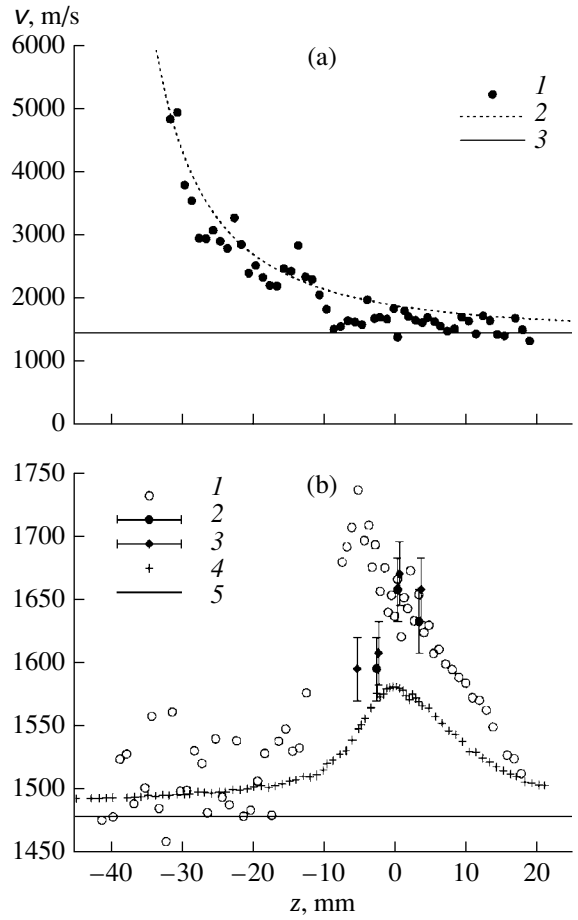


**Fig. 8.** Wave velocity along the radiator axis: (a) the phase velocity of an edge rarefaction wave (*1*) measured by the FOPH 300 sensor for $p_M$ = 3.0 MPa and (*2*) calculated according to Eq. (11) and (*3*) the sound velocity; (b) the velocity of the compression wave measured (*1*) by the FOPH 300 sensor for $p_M$ = 3.0 MPa, (*2*, *3*) measured according to high-speed photography for $p_M$ = (*2*) 3.0 and (*3*) 5.9 MPa, and (*4*) calculated according to Eq. (3) and (*5*) the sound velocity.

wave and broken lines, the front of a rarefaction wave at different time moments. One can see from the figure that experimental isobars near the focus do not coincide with the approximation of linear geometrical acoustics, because the velocities of different parts of fronts differ due to an inhomogeneity of the pressure, which leads to a deviation of the front shape from a spherical one, and because the direction of the velocity of the wave front is not parallel to the generator axis. Therefore the pulse front propagates along the axis with a phase velocity exceeding the sound velocity. The deviation is more significant the higher the pressure is.

**Table 3.** Energy characteristics of the generator ($T$ = 4 μs)

| $p_M$, MPa | $I$, W/m$^2$ | $S_{-6\,dB}$, m$^2$ | $E_{-6\,dB}$, J |
|---|---|---|---|
| 3.0 | $(2.9 \pm 0.2) \times 10^9$ | $(4.9 \pm 0.3) \times 10^{-6}$ | $\sim 8 \times 10^{-4}$ |
| 4.3 | $(3.2 \pm 0.2) \times 10^9$ | $(7.1 \pm 0.3) \times 10^{-6}$ | $\sim 18 \times 10^{-4}$ |
| 5.9 | $(3.8 \pm 0.2) \times 10^9$ | $(12.6 \pm 6) \times 10^{-6}$ | $\sim 70 \times 10^{-4}$ |

The pressure was measured systematically in the focal plane as a function of the radius $r$ and along the $z$ axis as a function of the distance to the focus $z$. Figure 7 shows positive and negative pressure amplitudes estimated from pressure oscillograms along the axis (Fig. 7a) and in the focal plane (Fig. 7b) for a spherical radiator for different voltages and capacities of the charging capacitor. An amplification of pressure amplitude at the focus was determined for compression and rarefaction waves on the basis of these measurements.

If we reduce the length of the current pulse by 50%, the amplitude at the membrane, which is determined by the approximation, decreases by 30% (Fig. 7a), which agrees well with the previous numerical estimate (Fig. 3). In the case of a shorter pulse, the half-height width of pressure distribution becomes smaller (Figs. 7a, 7b), and the amplification coefficient of positive pressure increases (Table 2).

The velocity of the compression wave was determined according to the delays of the wave front measured by both the sensor and high-speed photography. To determine the velocity, the signal from the sensor was filtered at the frequency $f_1 = 150$ MHz for the data at $t > 29$ μs, where a shock front exists. In the case of $t < 29$ μs, the filtration frequency was reduced to $f_2 = 2$ MHz. The velocities of a compression wave and a rarefaction wave coming from the membrane edges with the delay caused by the geometric dimensions of the membrane were measured. The results of velocity measurements at the radiator axis are given in Fig. 8.

The axial component of the phase velocity of a rarefaction wave was measured at the $z$ axis. Its value varies from the sound velocity (at $z \longrightarrow \infty$) up to 5000 m/s (Fig. 8a, $z = -30$ mm) as the observation point was shifted towards the radiator. Since the normal to the rarefaction half-wave is inclined to the axis, its phase velocity $v_{ph}$ along the axis at negative $z$ is higher than the velocity of the compression wave and the sound velocity. An estimate of the velocity of this wave can be performed according to the following expression from geometrical acoustics under the assumption that the source is located at the membrane edges:

$$v_{ph}/c_0 = [1 + \{(4F^2/D^2 - 1)^{1/2} + 2z/D\}^{-2}]^{1/2}. \quad (11)$$

Here, $F$ is the focal distance, $D$ is the diameter of the radiator aperture, and $c_0$ is the sound velocity.

Theoretical estimates (dots *4* in Fig. 8b) by Eq. (3) for a plane wave coincide within the experimental error (±2.5%) with the data measured for $z$ smaller than −10 mm and greater than 20 mm, for which we can ignore the curvature of the shock front. Near the focus, the experimental data for the velocity of the positive pressure phase lie higher than those calculated proceeding from the equations of hydrodynamics (the difference reaches 4.7 ± 0.7%), since they are determined by the velocity of motion of the Mach's disk. An analogous effect is observed in the measurements with an electrochemical sensor [24].

As the data in Fig. 8b (curve *1*) from a FOPH sensor refer to the velocity of motion of the pressure maximum, they deviate from the data measured according to high-speed photography records (curve *2*), where the maximum gradient of pressure is detected.

Figure 9 demonstrates the dependences of amplitudes in the compression and rarefaction phases at the focus of the radiator with increasing initial pressure at the membrane. The growth of the peak pressure in a shock wave slowed down for both values of the generator pulse length and did not exceed 75 MPa, and the gain did not exceed 36.7 ± 1.5 for the compression phase (Table 2). Within the pressure range of $p_M$ from 2.0 to 7.7 MPa, the amplitude of the negative phase at the focus ($z = r = 0$) obeys the dependence

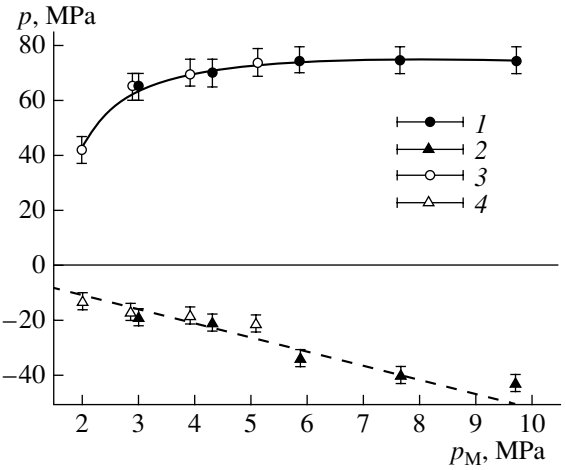


**Fig. 9.** Pressure amplitudes at the focus as functions of the pressure at the membrane: (*1*, *3*) the compression wave and (*2*, *4*) the rarefaction wave. $T$ = (*1*, *2*) 4 and (*3*, *4*) 3 μs.

$$p = -5.1p_M. \quad (12)$$

At the focus of an edge wave of rarefaction, its amplitude is no less than 10% higher than at $z = 0$ in the absolute value (Fig. 7a); i.e., the coefficient in Eq. (11) is about −5.7 at $z = -5$ mm. The values obtained for $p_M > 5.5$ MPa correspond to the case of developed cavitation [25, 26], however cavitation weakly affects the amplitude of a rarefaction wave because of the focusing and the small length of a cavitation pulse.

With this geometry of spherical focusing, the rarefaction wave moving along the axis with a phase velocity exceeding the sound velocity overtakes the compression wave and forms a so-called N-wave. At the same time, the compression wave becomes a shock wave about 30 μs after the generator discharge, which occurs due to the dependence of sound velocity on pressure. The pressure amplitude of a positive pulse for negative $z$ increases as $1/|z|^{1.25}$ up to the moment when the Mach's disk begins to form.

## 4. CONCLUSIONS

The generation of a localized region of reduced pressure, which can be used to excite cavitation away from the boundaries of a liquid, is obtained by the method of focusing a compression wave and an edge rarefaction wave arising due to diffraction at the edges of a radiating membrane. The pressure at the focus varies from −22 to −42 MPa, which exceeds the threshold of developed cavitation. The pressure amplitude depends linearly on pressure at the membrane (quadratically on the charging voltage of the capacitor). This

can be used to determine the cavitation strength of a liquid. Negative pressures of higher absolute values and an intensification of cavitation luminescence can be obtained by focusing a compression wave at a free surface [18, 26].

Despite the inhomogeneity of pressure distribution over the membrane [17] and, probably, a small inaccuracy in the radiator manufacture, we obtained the mode of generation of a spherically converging wave when pressure at the compression focus is determined by the pressure in the Mach's disk and is likely to be limiting for this value of the ratio of the aperture to the focal distance of the radiator. This statement is supported by the reduction of pressure gain and growth of the diameter of the focal region with increasing pressure amplitude at the membrane, which was also noted in [27, 28]. The growth in the pressure gain is obtained by reducing the discharge time. This assumption is confirmed experimentally by a comparison of the pressure fields of the radiator with discharge periods of 3 and 4 μs.

The values of negative pressure measured by a piezoelectric transducer [18] turned out to be lower in their moduli than the values obtained with a fiber-optical sensor. Thus, an FOPH sensor is suitable for measuring large tensile stresses.

Pressure gradients near the focus can reach 50 GPa/m, which is very important for the survival of biological cells under lithotripsy. One may expect that high gradients of shear liquid motion can cause the destruction of cells without the effect of cavitation [29]. Therefore, this problem needs further investigation. In this respect, it may be important that, for a spherically focused acoustic pulse, the focuses of compression and rarefaction waves are spaced apart, which provides an opportunity to study separately the processes connected with each of these waves. One can expect that the maximum cavitation activity will occur at the focus of the negative phase, i.e., below the geometrical focus of the radiator.

At present, a pulsed mode of cavitation excitation with an analogous setup is being used for a complex investigation of collective properties of clusters (bubble dynamics, pressure fields, and luminescence) under the conditions of formation of a cavitation zone [30, 31].

## ACKNOWLEDGMENTS

This work was supported by the German Academic Exchange Service (Deutscher Akademischer Austauschdienst), DAAD grant no. A/00/01480; the Acoustical Society of America, CRDF grant no. 1210/1; and the Russian Foundation for Basic Research, project nos. 00-02-17992, 03-02-17682, 01-02-06444-mas, 02-02-06838-mas, and 03-02-06212-mas.

I am sincerely grateful to V.S. Teslenko for formulating the problem, to V.A. Maier for developing the GIT-2 generator of high-power current pulses, and to A.P. Drozhzhin for his assistance in servicing the generator. I am also grateful to the employees of the Third Physical Institute, Goettingen University (Drittes Physikalisches Institut, Univesitaet Goettingen), Germany: W. Lauterborn for the opportunity to conduct this study, R. Mettin and R. Geisler for their assistance in familiarizing me with the diagnostic equipment (FOPH 300 pressure sensor and high-speed microscopic photography) and for their interest in the study. I am grateful to S.V. Stebnovskii and V.F. Klimkin for valuable remarks and M.E. Topchiyan for discussions, which critically improved the manuscript.

## REFERENCES

1. H. Reichenberger, Proc. IEEE **76**, 1236 (1988).
2. V. S. Teslenko, N. G. Kolosova, I. V. Mastikhin, and V. P. Nikolin, Dokl. Ross. Akad. Nauk **369**, 698 (1999).
3. W. Eisenmenger, Ultrasound Med. Biol. **27**, 683 (2001).
4. A. J. Coleman, M. Whitlock, T. Leighton, and J. E. Saunders, Phys. Med. Biol. **38**, 1545 (1993).
5. C. C. Church, J. Acoust. Soc. Am. **86**, 215 (1989).
6. D. L. Sokolov, M. R. Bailey, L. A. Crum, *et al.*, J. Endourol. **16**, 709 (2002).
7. R. H. Cole, *Underwater Explosions* (Princeton Univ. Press, Princeton, N.J., 1948; Inostrannaya Literatura, Moscow, 1950).
8. M. Müller, Dissertation (Reinisch-Westfalischen Technischen Hochschule, Aachen, Germany, 1987).
9. A. J. Coleman and J. E. Saunders, Ultrasound Med. Biol. **15** (3), 213 (1989).
10. E. A. Zabolotskaya and R. V. Khokhlov, Akust. Zh. **15**, 40 (1969) [Sov. Phys. Acoust. **15**, 35 (1969)].
11. V. P. Kuznetsov, Akust. Zh. **16**, 548 (1970) [Sov. Phys. Acoust. **16**, 467 (1970)].
12. M. A. Averkiou and R. O. Cleveland, J. Acoust. Soc. Am. **106**, 102 (1999).
13. R. Holl, Dissertation (Reinisch-Westfalischen Technischen Hochschule, Aachen, Germany, 1982).
14. B. Sturtevant and V. A. Kulkarny, J. Fluid Mech. **73**, 651 (1976).
15. R. F. Trunin, Usp. Fiz. Nauk **171**, 387 (2001) [Phys. Usp. **44**, 371 (2001)].
16. V. V. Mitrofanov, V. S. Teslenko, V. A. Maĭer, and A. I. Kudryashov, Report under Contract No. 43/89 (Inst. Gidrodin., Sib. Otd. Akad. Nauk SSSR, Novosibirsk, 1990).
17. G. N. Sankin, Prib. Tekh. Éksp. **46** (3), 145 (2003).
18. V. S. Teslenko, G. N. Sankin, and A. P. Drozhzhin, Fiz. Goreniya Vzryva **35** (6), 125 (1999).
19. P. Augat and L. Claes, Ultrasound Med. Biol. **21** (1), 89 (1995).
20. Yu. V. Andriyanov, A. A. Li, and V. S. Teslenko, Vopr. Kurortol. Fizioter. Lech. Fiz. Kult., No. 4, 42 (1992).
21. W. Eisenmenger, Acustica **12**, 185 (1962).
22. D. V. Voronin, G. N. Sankin, V. S. Teslenko, *et al.*, Prikl. Mekh. Tekh. Fiz. **44** (1), 22 (2003).
23. J. Staudenraus and W. Eisenmenger, Ultrasonics **31**, 267 (1993).
24. G. N. Sankin, Prib. Tekh. Éksp. **46** (1), 136 (2003).

25. G. N. Sankin, R. Mettin, V. Lauterborn, and V. S. Teslenko, in *Physical Acoustics, Wave Propagation and Diffraction: Proceedings of XI Session of the Russian Acoustic Society* (GEOS, Moscow, 2001), Vol. 1, p. 32.

26. G. Sankin, R. Mettin, R. Geisler, *et al.*, in *Fortschritte der Akustik—DAGA 2001, Harburg–Hamburg, Germany*, Ed. by Otto von Estorff (DEGA, Oldenburg, 2001), p. 258; CDROM, ISBN 3-9804568-9-7.

27. O. A. Sapozhnikov, Akust. Zh. **37**, 760 (1991) [Sov. Phys. Acoust. **37**, 395 (1991)].

28. A. G. Musatov, O. V. Rudenko, and O. A. Sapozhnikov, Akust. Zh. **38**, 502 (1992) [Sov. Phys. Acoust. **38**, 274 (1992)].

29. M. Lokhandwalla, J. McAteer, J. Williams, Jr., and B. Sturtevant, Phys. Med. Biol. **46**, 1245 (2001).

30. G. N. Sankin and V. S. Teslenko, Dokl. Akad. Nauk **393** (6), 665 (2003).

31. G. N. Sankin, Akust. Zh. (in press).

*Translated by M. Lyamshev*

*Acoustical Physics, Vol. 50, No. 2, 2004, pp. 222–231. Translated from Akusticheskiĭ Zhurnal, Vol. 50, No. 2, 2004, pp. 272–282.*


# Heating of Biological Tissues by Two-Dimensional Phased Arrays with Random and Regular Element Distributions

**E. A. Filonenko*, L. R. Gavrilov**, V. A. Khokhlova*, and J. W. Hand*****

** Moscow State University, Vorob'evy gory, Moscow, 119899 Russia*
*e-mail: vera@acs366.phys.msu.su*
*** Andreev Acoustics Institute, ul. Shvernika 4, Moscow, 117036 Russia*
*e-mail: gavrilov@akin.ru*
**** Hammersmith Hospital, Imperial College, London, W12 0HS United Kingdom*
Received May 28, 2003

**Abstract**—The effect of an irregularity of the element distribution in a two-dimensional phased array upon the efficiency of heating of biological tissue is studied in an ultrasonic surgery regime. Two arrays of 256 piston elements, which either form a regular square pattern or are positioned randomly on the surface of a spherical segment, are considered as a model. The formation and the steering of a set of nine foci along the array axis and in the direction perpendicular to it are investigated. The theoretical model includes the algorithm of determining a phase set at the array elements that is optimal for the formation of foci with equal intensities and a preset geometry, as well as the calculation of acoustic and temperature fields in a tissue. The results of numerical simulation are presented for the spatial distributions of ultrasonic intensity, temperature, and the corresponding thermal dose in tissue. It is demonstrated that an irregularity of the element distribution reduces the level of secondary intensity peaks in the field produced by the array. This provides an opportunity to avoid the overheating and ablation of tissue outside the target volume, even in the case of steering with the set of foci away from the array axis within a distance of ±7 mm. A nine-foci regime is studied with the parameters necessary to produce uniform thermal ablation in a volume that is evaluated on the basis of the thermal dose distribution. © *2004 MAIK "Nauka/Interperiodica".*

Opportunities to use phased arrays capable of focusing ultrasonic energy and electrically steering the focus within a preset volume of a biological tissue have been actively investigated in connection with the development of new noninvasive surgery methods [1–9]. An advantage of phased arrays is their capability to simultaneously produce several foci in tissue and in this way increase the volume of the affected region, which essentially reduces the treatment time [2]. However the discrete structure of an array can give rise to undesirable sidelobes and secondary peaks in the acoustic field produced by the array [3–6]. It is known that the steering of foci in the direction perpendicular to the axis of a regular array within a distance of 7–10 mm leads to the appearance of secondary peaks with an intensity level reaching 50–60% of the maximum intensity in the major foci [8]. In the case of greater distances, the secondary intensity peaks may be still higher. The problem of secondary peaks in the field of phased arrays is especially important for ultrasonic surgery, where high intensity values (500–3000 W/cm$^2$) are used, which lead to a fast temperature rise in the focal region (above 60–80°C) within several seconds. This regime can be used for the ablation of tumors in soft tissues and also to stop internal bleeding [10]. A series of papers [2–6] are devoted to discussing the problem of secondary peaks in the acoustic field of therapeutic arrays and the ways to minimize the overheating of tissue along the path of ultrasound propagation to the target region.

One of the approaches used to reduce the level of secondary peaks is based on the utilization of arrays with elements positioned randomly on their surfaces [7–9]. This approach is also known in radar [11], where, however, the effect of randomization does not manifest itself as noticeably as in the case of powerful acoustic arrays. This can be explained by the fact that the velocity of light is greater than the velocity of sound, and, therefore, it is much simpler to manufacture an electromagnetic array with a distance between the centers of neighboring elements not exceeding the half-wavelength $\lambda/2$. Manufacturing such an acoustic array, which in addition has an acoustic power not smaller than 300–500 W, requires an extremely large number of elements and channels feeding them. Therefore, the development of theoretical models and numerical algorithms for calculating and analyzing the acoustic field and the corresponding temperature distribution in tissue in the case of the utilization of arrays of various configurations is important for designing therapeutic arrays and planning an experiment. Numerical simulation and comparative analysis of acoustic [8, 9] and temperature [12] fields produced by two-dimensional phased arrays for the case of steering a single focus with the help of arrays with regular and random distri-

1063-7710/04/5002-0222$26.00 

butions of 256 elements demonstrated that irregularity in the element distribution noticeably improves the quality of intensity and temperature distributions. A randomization of the element distribution suppresses the secondary intensity and temperature peaks in the field produced by the array and provides an opportunity to bring the size of the elements up to five sound wavelengths while still retaining an acceptable intensity level for the secondary peaks (approximately 10% of the principal peak in the case of steering a single focus up to 15 mm away from the array axis) [8, 9, 12]. An increase in the size of elements leads to a sharp decrease in the effect of randomization of element distribution. For example, elements with a diameter of $11.2\lambda$ were used in [7], and the effect of randomization was insignificant.

Here, we investigate the regime of simultaneous formation and steering of nine foci ($N = 9$) by a powerful acoustic array with random and regular element distributions on the array surface shaped as part of a sphere (Fig. 1). The theoretical model presented below includes an algorithm for calculating the coordinates of element positions for a random array, for choosing the phases at the elements to produce foci of equal intensities, and for calculating the acoustic and temperature fields in tissue, as well as the distribution of the thermal dose. Modeling and analysis of the acoustic field and thermal sources and the spatial distributions of temperature and thermal dose are performed for arrays with regular and random element distributions in the case of steering the focal volume along the array axis and in the direction perpendicular to it. The necessary parameters of irradiation and focus geometries that provide tissue ablation not only locally, in each focal region, but also uniformly in the whole volume between them are revealed.

Let us consider the problem of obtaining nine foci at a preset distance $z$ at the array axis, so that these foci form a square pattern in the $(x, y)$ plane perpendicular to the $z$ axis and that the distance between the focus centers is, foe example, 3 mm (Fig. 2). To estimate the array capability to steer the set of foci along the array axis and in the direction perpendicular to it, we set the shift of the central focus along the array axis ($z$ axis) to be equal to 2 cm from the geometrical focus toward the array and equal to 0.7 cm in the $y$ direction away from the axis. It is assumed that ultrasound propagates in a tissue with the following acoustic parameters: density $\rho_0 = 1000$ kg/m$^3$, sound velocity $c_0 = 1500$ m/s, and attenuation coefficient $\alpha_0 = 5$ m$^{-1}$ at a frequency of 1 MHz, with the attenuation coefficient increasing linearly with frequency.

We use an acoustic array of $M = 256$ circular piston elements with diameters $d = 5$ mm and operating frequency $f_0 = 1.5$ MHz. The elements are distributed over the surface of a spherical segment 13 cm in diameter with a curvature radius $F = 12$ cm. The maximum distance between the centers of the outermost elements is 12 cm.

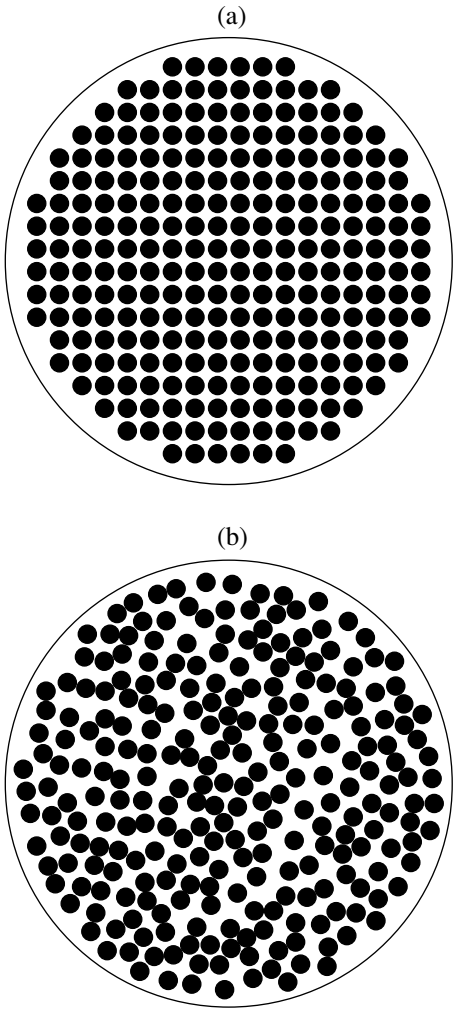


**Fig. 1.** Schematic diagrams of ultrasonic arrays containing 256 elements 5 mm in diameter: (a) a regular arrangement of elements in a square pattern and (b) a random distribution of elements over the array surface.

In the case of a regular array, the elements are positioned in squares with a distance of 6 mm between the centers of neighboring elements (Fig. 1a). A distribution in the form of a square pattern was selected because it is the most popular one among the designs of powerful therapeutic arrays discussed in the literature [4, 5].

In the case of a randomized array (Fig. 1b), the element coordinates are selected as follows. A large (tens of thousands) two-dimensional array of independent random coordinates $(x, y)$ is formed with the help of a random-number generator (uniform distribution) in the interval from –6 to 6 cm. The coordinates within a circle with a radius of 6 cm are selected from it. The first point is chosen arbitrarily from this array at the beginning, and then all other 255 points (element coordinates) are chosen so as to be located no closer than 5.5 mm from all preceding ones. Coordinates inconsistent with this condition are rejected. In one of the realizations of element distributions obtained in this way

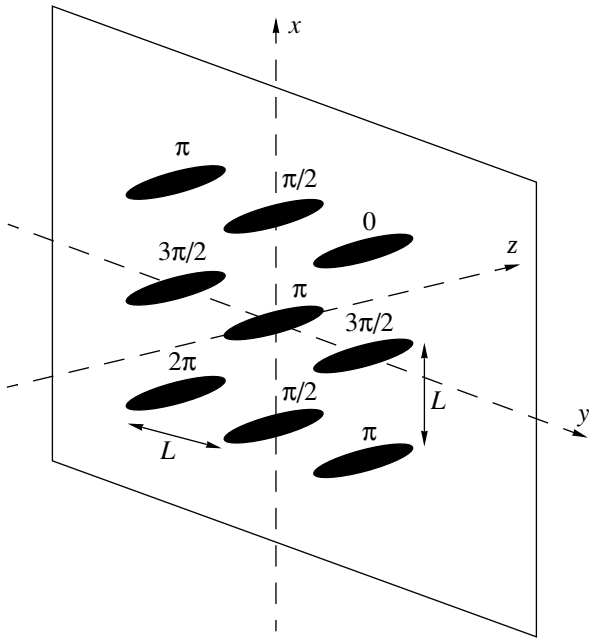


**Fig. 2.** Schematic diagram of nine foci in the *xy* plane and the method of rotation of the pressure phase at the foci. The distance between the foci $L$ is equal to 3 mm.

and examined here (Fig. 1b), the distances between the centers of neighboring elements vary within the interval from 5.5 to 8.45 mm. It is necessary to note that the utilization of different sets of random coordinates of the 256 elements can affect the fine structure of the field produced by the array but does not influence in any way the main result: the use of randomized arrays leads to a considerable reduction of secondary intensity peaks caused by the regular discrete structure of the array.

Calculation of the acoustic field produced by an array in a tissue in the case of a preset element distribution and a set of control points (foci) in space can be conditionally divided into three stages: the calculation of the field of a single array element, the determination of the optimal phase set with a subsequent matching of the absolute values of amplitudes at the elements, and the determination of the array field by summation of all fields of all elements with the amplitude-phase distribution determined at the previous stages. At the first stage the acoustic field of one circular element of the array is calculated with the help of the Rayleigh–Sommerfeld integral [1, 13],

$$p(\mathbf{r}_i) = \frac{j\rho_0 c_0 k u_0}{2\pi}\int\limits_S \frac{\exp((jk-\alpha)|\mathbf{r}-\mathbf{r}_i|)}{|\mathbf{r}-\mathbf{r}_i|}dS, \qquad (1)$$

where $p$ is the complex pressure amplitude, $k = 2\pi f_0/c_0$ is the wave number, $\alpha = 7.5\ \mathrm{m}^{-1}$ is the attenuation coefficient at the operating frequency of the array, $u_0$ is the amplitude of particle velocity at the element surface, $|\mathbf{r}-\mathbf{r}_i|$ is the distance from a point $\mathbf{r}$ of the radiating surface $S$ of the circular piston element to the $i$th point in the space $\mathbf{r}_i$.

The Rayleigh–Sommerfeld integral (Eq. (1)) is calculated numerically at the nodes of a sufficiently dense spatial grid. The following values of simulation parameters are used: the integration region along the longitudinal coordinate is $2 < z < 16$ cm, the spatial window along the transverse coordinate is $0 < r < 10$ cm, and the grid step along both directions is $hz = hr = 0.2$ mm, which is 1/5 of the wavelength. For numerical integration, the element surface was divided into 7849 square regions with a side of 0.05 mm ($\lambda/20$), which provided the necessary precision of the solution. The solution obtained is further used to determine the phases at the elements and also in calculating the total field produced by the array.

At the second stage, the values of the complex amplitude of the particle velocity at each element are determined so as to obtain a set of $N = 9$ physical foci (control points) with preset coordinates in space. Additional conditions are imposed upon the selection of pressure amplitudes and phases at each control point: phases rotate uniformly clockwise with respect to the axis of the given set of foci with a step of $\pi/2$ (Fig. 2), and the values of the pressure amplitude at the control points are equal. The basis of the technique for calculating the complex amplitude of particle velocity at the elements was proposed in [1]. However, the brevity of its description makes it difficult to use it in practice. Therefore, below we give the basic components of this approach in two modifications. In one of them, the acoustic field of a piston element (Eq. (1)) is used for calculating the amplitude and phase of particle velocity at the elements [1]. In the second modification, the piston field is replaced by the field of a point source located at the element center [8, 9]. Both modifications are considered here to compare the resulting sets of phases and the acoustic fields produced by the array.

In the approximation of the linear propagation of an acoustic wave, the pressure $p(\mathbf{r}_n)$ at each $n$th control point ($n = 1, \ldots, N$) is the superposition of $M$ partial pressures $p_m$ produced by each of the $M$ elements of the array, $p(\mathbf{r}_n) = \sum_{m=1}^{M} H_{nm}u_m$, or, in the matrix form,

$$P = H \times U. \qquad (2)$$

Here, $u_m$ is the complex amplitude of particle velocity at the surface of the $m$th element ($m = \{1, \ldots, M\}$), $U$ is the vector of the $M$ values of the particle velocity amplitudes $u_m$, $P$ is the vector of pressures $p(\mathbf{r}_n)$ at $N$ control points, and the matrix $H$ with the dimension $(N \times M)$ determines the operator of direct propagation from the $m$th element at the array to the $n$th control point in space. If the field of a piston element with a uniform distribution of particle velocity is used to solve Eq. (2), the elements of the matrix $H_{nm}$ are determined by solution (1) that is calculated for the $m$th element of the

array at the *n*th control point:

$$H_{nm} = \frac{j\rho_0 c_0 k}{2\pi}\int_{S_m}\frac{\exp((jk-\alpha)|(\mathbf{r}_m-\mathbf{r}_n)|)}{|\mathbf{r}_m-\mathbf{r}_n|}dS_m. \quad (3)$$

It should be noted that, to determine the values of the elements of the matrix $H_{nm}$ (Eq. (3)), it is necessary to calculate the Rayleigh–Sommerfeld integral $NM$ times (in $N$ foci from $M$ elements of the array). However, it is possible to use field (1) calculated for one of the elements to determine the matrix elements (3) from an arbitrary element $m$ at an arbitrary control point $n$. To do this, we determine the position of the control point with respect to the cylindrical coordinate system connected with the selected element and determine the weighted mean value of the field at the closest nodes if the point lies within the intervals *hz* or *hr* of the grid. Multiplying the result by the complex amplitude of the particle velocity of the element, it is possible to obtain the value of the pressure field produced by the element $m$ at the control point $n$.

However, if we use the field of a point source with the coordinate $\mathbf{r}_n$, the matrix elements $H_{nm}$ have a simpler form:

$$H_{nm} = C\frac{\exp((jk-\alpha)|(\mathbf{r}_m-\mathbf{r}_n)|)}{|\mathbf{r}_m-\mathbf{r}_n|}, \quad (4)$$

where the coefficient of proportionality $C = j\rho_0 c_0 kS/2\pi$ is the same for all $n$ and $m$ and $S = \pi d^2/4$ is the area of the array element.

In the case of equal quantities of array elements and foci ($N = M$), the matrix $H$ is quadratic, and there is a unique solution to the set of equations (2); i.e., $U = H^{-1} \times P$, where $H^{-1}$ is the matrix inverse with respect to matrix $H$. Within the framework of this problem, an underdetermined system of equations ($N < M$) exists, which has an infinite number of solutions in the general case [14]. Therefore, the principal goal is to determine the "best" solution, i.e., a vector $\hat{U}$ with the elements $\hat{u}_m$ that provides the minimum acoustic power at the array (the minimum norm of vector $\hat{U}$) with the given values of complex pressure at the control points. From a physical point of view, this condition guarantees that the control points are local peaks of the field. Here, we use the singular value decomposition method and the technique of minimization of the norm to construct a solution [14]. The method of decomposition of a singular quantity provides an opportunity to obtain a matrix pseudo-inverse to $H$, while the technique of minimization of the norm allows us to choose the "best" pseudo-solution $\hat{U}$. In this case, a solution to Eqs. (2) can be written down as

$$\hat{U} = H^{*T}(H\,H^{*T})^{-1}P. \quad (5)$$

Here, $H^{*T}$ is the matrix conjugate to $H$, for which the transposition procedure is performed. The solution given by Eq. (5) provides the minimum norm of the vector $U$ of matrix equation (2) [14]. The matrix $H^{*T}(M \times N)$ determines the operator of inverse propagation of an acoustic wave from the $n$th control point in space to the $m$th element at the array surface. The physical significance of the operator $(H\,H^{*T})^{-1}$ (the $N \times N$ matrix inverse of the matrix $H\,H^{*T}$) lies in the fact that it introduces a correction to the directivity of the element's field before the procedure of reconstructing the field at the control points [1, 14]. If we ignore this operator in Eq. (5), the field at the control points is reconstructed inaccurately.

It is necessary to note that a certain limiting admissible value of the amplitude of particle velocity (or intensity) exists at the surface of the piezoelectric array elements, which makes its operation safe. In the solution given by Eq. (5), the modulus of the complex amplitude $\hat{u}_m$ is not the same for different elements; i.e., if the velocities at some elements are close to the maximum admissible value, they can be very small at other elements. In this case, the array efficiency [1]

$$\eta_A = 100\% \times \sum\nolimits_{m=1}^{M}|\hat{u}_m|^2/Nu_{\max}^2,$$

where $u_{\max}$ is the maximum amplitude of particle velocity at its elements, can be from 20 to 35% in the case of the generation of nine foci. It is clear that the maximum efficiency of the array can be obtained when all elements have the same amplitude. Therefore, this condition of the minimum norm of the vector $U$ is relaxed, and the iteration procedure of amplitude equalizing is performed to increase the efficiency of (to optimize) the acoustic array. The notion of a weighted norm is introduced to perform such an optimization [14]:

$$\|\hat{U}\|_W = (\hat{U}^{*T}\,W\,\hat{U})^{1/2}, \quad (6)$$

where $W$ is a positively defined diagonal matrix with the dimension $M \times M$. The condition of amplitude equality is realized by calculating the diagonal matrix elements of matrix $W$ in the iterative procedure [1]. If $W$ is a unit matrix, the determination of a weighted norm (6) exactly reproduces the determination of the Euclidean norm [14]. A solution to matrix equation (2) taking into account weighted norm (6) is written down in the form

$$\hat{U} = W\,H^{*T}(H\,W\,H^{*T})^{-1}P. \quad (7)$$

At the first step of the iterations, the diagonal matrix elements of the weight matrix $W$ in Eq. (7) are assumed to be equal to unity, and the velocity vector $\hat{U}$ (Eq. (5)) is determined. The solution obtained is verified for uniformity of the distribution of velocity amplitude using the criterion of array efficiency. If solution $\hat{U}$ satisfies the condition $\eta_A \geq 99\%$, the iterations are stopped. If the condition is not satisfied, a redetermination of the

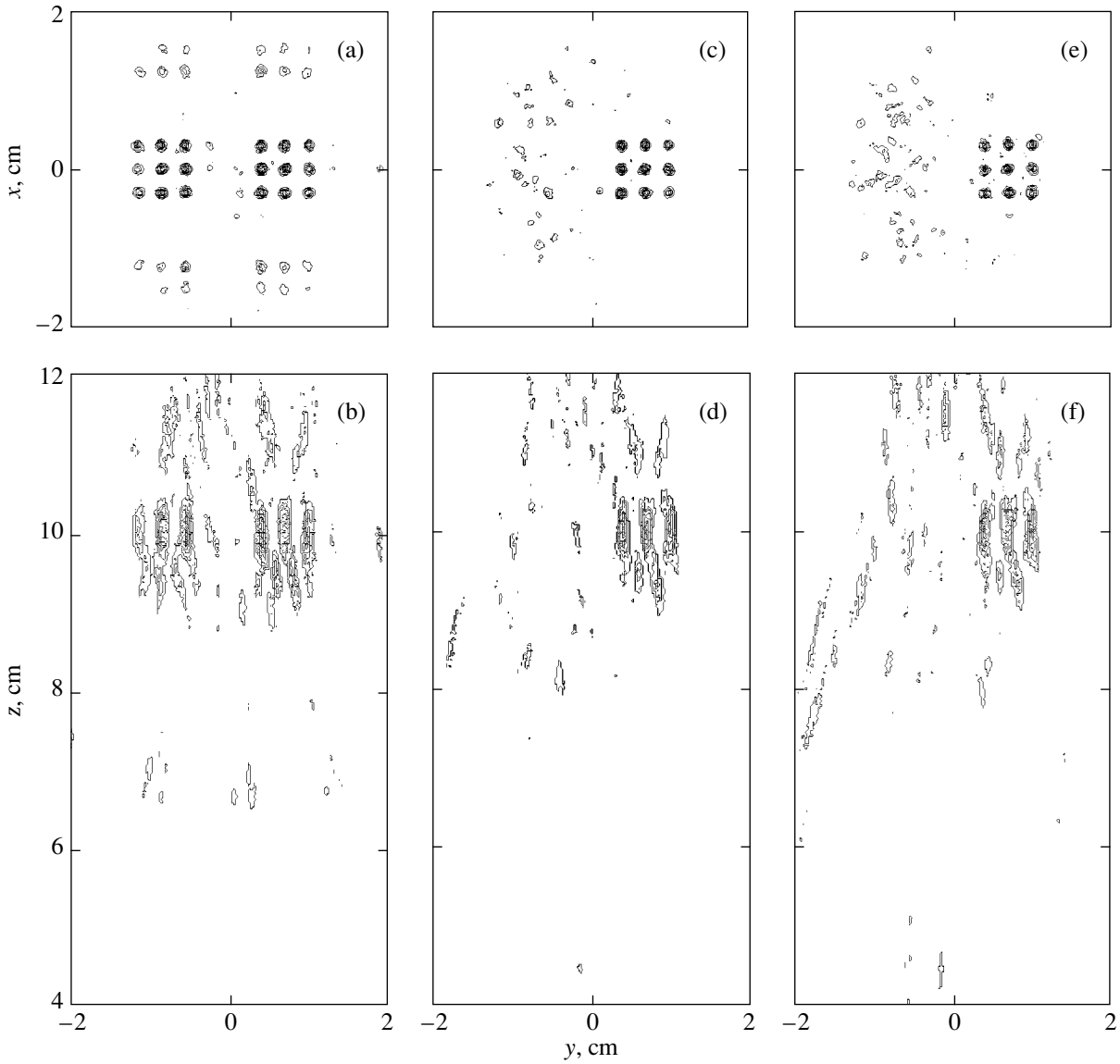


**Fig. 3.** Spatial intensity distributions in the *xy* plane (from above) and in the *yz* plane (from below) (a, b) for a regular array and (c, d) for two random arrays with a different choice of phases at the elements. Stirring with the set of foci is performed along the array axis to a distance of 2 cm from the geometrical focus towards the radiator and to 7 mm away from the axis. The intensity is normalized to the corresponding maximum value reached in the focus region.

diagonal elements of the weight matrix $W$ takes place, so that $W_{mm} = u_{\max}/|\hat{u}_m|$ ($m = 1, \ldots, M$). Then, Eq. (7) is used again to calculate the vector of the complex amplitudes of particle velocity $\hat{U}$, taking into account the redetermined elements of the weight matrix. After that, the result is again tested to make sure it satisfies the condition $\eta_A \geq 99\%$. The described iteration technique provides an opportunity to conduct an equalization of the amplitude values of particle velocity at different elements on the array surface [1].

At the second stage, the pressure field in a tissue $\breve{p}(\mathbf{r})$ produced by the whole array is calculated for a selected value of amplitude and a preset distribution of phases of particle velocity at the elements. The calculation is performed in the nodes of a rectangular grid $\mathbf{r}_i$ with a step $hz = hy = hx = 0.2$ mm in the region $4 < z < 13$ cm along the array axis and $-2 < y < 2$ cm and $-2 < x < 2$ cm along the transverse coordinates. For this purpose, pressures from each element are determined analogously to the calculation of pressure at control points, which was described above, and the procedure of summation is performed (for details, see [8, 9]). The resulting pressure field is used to calculate the intensity field at the same grid in the plane wave approximation: $I(\mathbf{r}_i) = |\breve{p}(\mathbf{r}_i)|^2/2\rho_0 c_0$, and the field of thermal sources:

$$Q(\mathbf{r}_i) = 2\alpha I(\mathbf{r}_i), \tag{8}$$

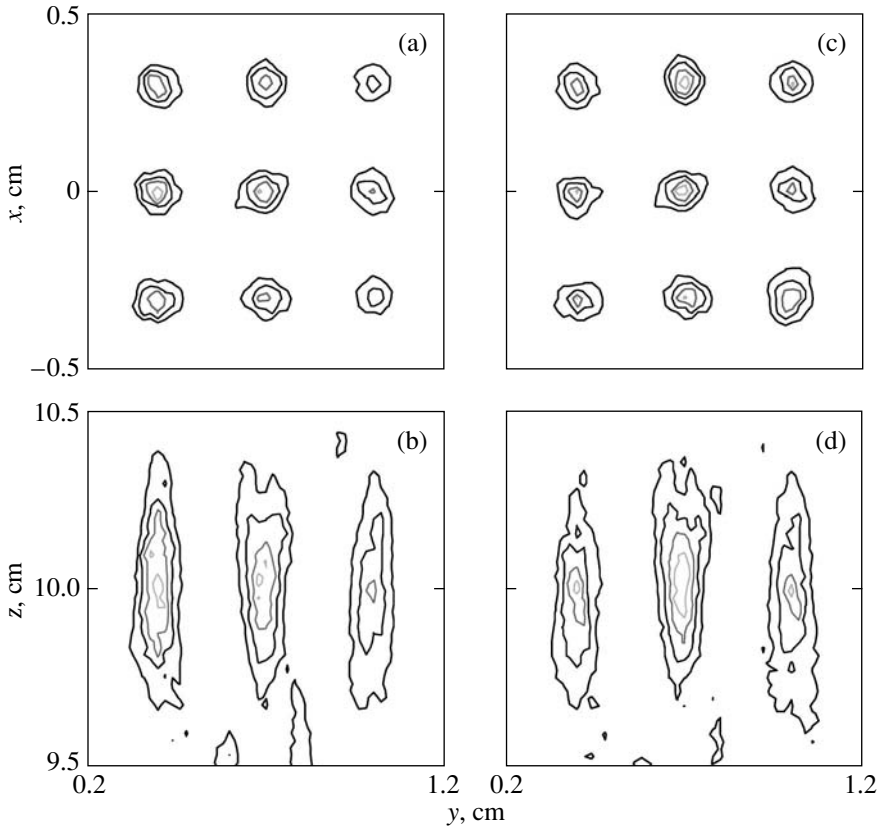


**Fig. 4.** Spatial intensity distributions (Fig. 3) for two random arrays on an extended scale. The phases of particle velocity at the elements are determined using either (a, b) the field of a point source or (c, d) the field of a piston element.

where the absorption coefficient at the operating frequency of the array is assumed to be equal to the attenuation coefficient $\alpha$.

The inhomogeneous Pennes equation of heat conduction [15] is used to calculate the temperature field in a tissue:

$$\frac{\partial T}{\partial t} = k\Delta T - \frac{T - T_0}{\tau} + \frac{Q(\mathbf{r})}{c_v}, \qquad (9)$$

where $T = T(x, y, z, t)$ is the temperature in the tissue, $T_0 = 36.6$°C is the equilibrium temperature, $\Delta = \partial^2/\partial x^2 + \partial^2/\partial y^2 + \partial^2/\partial z^2$ is the Laplacian, $c_v = 3.81 \times 10^6$ W s/m$^3$ °C is the volumetric heat capacity, and $k = 1.33 \times 10^{-7}$ m$^2$/s is the thermal diffusivity. The perfusion time $\tau$ was selected to be sufficiently large, $\tau = 250$ s, so that the process of perfusion almost did not influence the heating of the tissue [16]. Equation (9) was solved numerically in the Cartesian coordinates $(x, y, z)$ by the finite-difference method on the same spatial grid with the nodes where the acoustic field was calculated and the thermal sources $Q$ were located. An algorithm developed earlier for a cylindrically symmetrical problem [17] and generalized here for the case of an arbitrary three-dimensional spatial distribution of a temperature field was used. The field was calculated within the region $4 < z < 13$ cm along the array axis and $-2 < y < 2$ cm and $-2 < x < 2$ cm along the transverse coordinates. At each time step of the grid $ht = 0.05$ s, the results for the temperature field were used to calculate the thermal dose [18]:

$$td_{T_{\text{ref}}} = \int_0^t R^{(T_{\text{ref}} - T_t)} dt, \qquad (10)$$

where the integration is performed over the total time of heating and subsequent cooling $t = t_{\text{heat}} + t_{\text{cool}}$ and $T_{\text{ref}}$ is the temperature with respect to which the thermal dose necessary for thermal ablation of the tissue is calculated [18, 19]. In the hyperthermia regimes, the thermal dose usually corresponds to the temperature $T_{\text{ref}} = 43$°C maintained in the tissue during 120–240 min [20]. For heating regimes used in acoustic surgery, it is convenient to use $T_{\text{ref}} = 56$°C; then, the thermal dose $td_{T_{\text{ref}}} = 1$ s is equivalent to $td_{T_{\text{ref}}} = 140$ min at a temperature of 43°C [2, 18].

The results of the simulation given below provide an opportunity to investigate the influence of irregularity in the element distribution on the spatial distributions of thermal sources and the evolution of the temperature field and thermal dose in a tissue. As indicated above, the stirring of a set of nine foci was performed along the

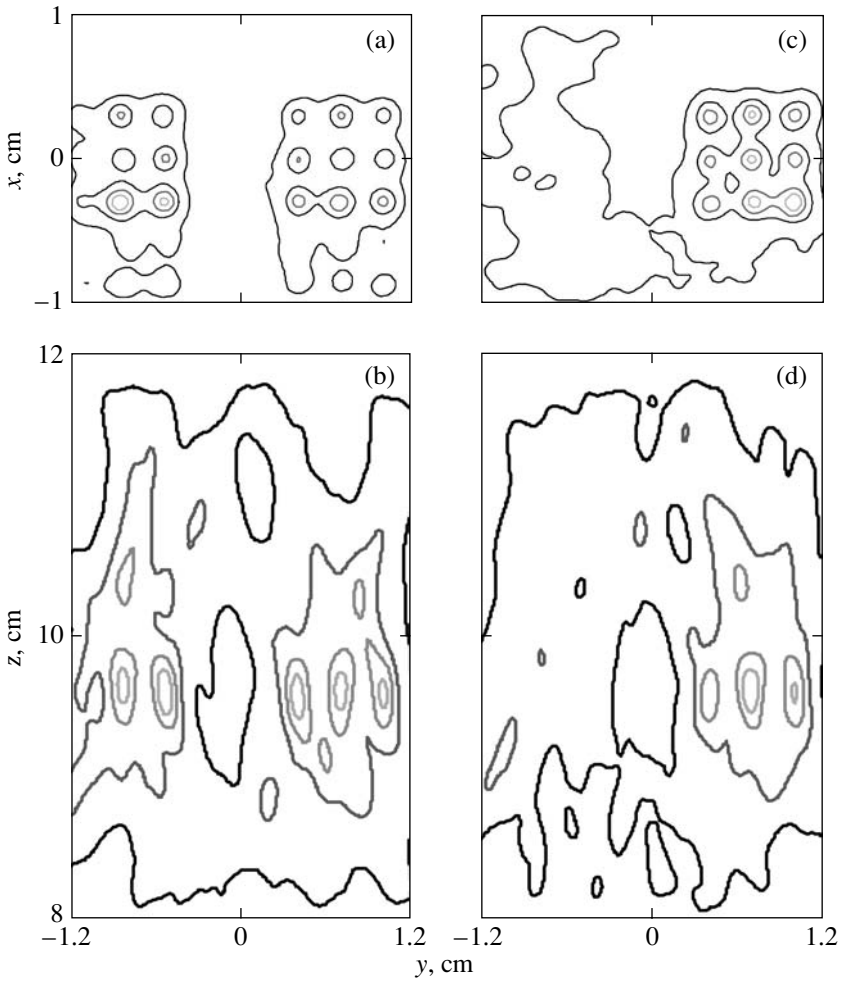


**Fig. 5.** Spatial temperature distributions after 8 s of heating in ultrasonic field (Fig. 3) with (a, b) regular and (c, d) random arrays. The phases at the elements are chosen with the help of the field of a piston element.

array axis to 2 cm from the geometrical focus towards the radiator and to 7 mm away from the array axis. Figure 3 demonstrates the spatial intensity distributions for regular (left) and random (in the middle and at the right of the figure) distributions of elements. The intensity was normalized to its maximum value $I_{max}$ in the volume of the region of foci, and nine levels of contours in the figures correspond to an intensity change from $0.1I_{max}$ to $0.9I_{max}$. In the case of a regular array, the phases of particle velocities at the elements were reconstructed using the field of a point source located at the element center [8, 9]. In the case of a random array, both approaches were used, i.e., the approximation of a point source (the results are given in the middle of the figure) and the approximation of a piston element (at the right of the figure). The distributions are shown in two sections: *xy* at $z = 10$ cm (section from above) and *yz* at $x = 0$ (section from below). One can see that, in the case of using a regular array, an incidental set of pronounced secondary peaks with an intensity level exceeding 80% of $I_{max}$ is observed together with the main set of physical foci (Figs. 3a and 3b). The presence of these secondary peaks is inadmissible, because they can lead to unpredictable heating of tissue outside the target region. If a randomized array is used, the intensity of the secondary peaks is considerably reduced down to a level below 30% of $I_{max}$ (Figs. 3c–3f), which is more acceptable in practice. Figure 4 shows the same intensity distributions (on an extended scale) in the region of nine foci for a randomized array and for two approaches to the determination of phases at the elements. Four contours from $0.2I_{max}$ to $0.8I_{max}$ with the step between them equal to $0.2I_{max}$ are chosen for illustration.

The major differences in the intensity distributions obtained for a randomized array in the cases of choosing the phases at the elements in the approximations of point (Figs. 4a, 4b) or piston (Figs. 4c, 4d) sources are as follows. As can be seen from Fig. 3, in the first case (the approximation of a point source), the field does not contain any great number of secondary peaks with an intensity within 10–20% of $I_{max}$. In the second case (the

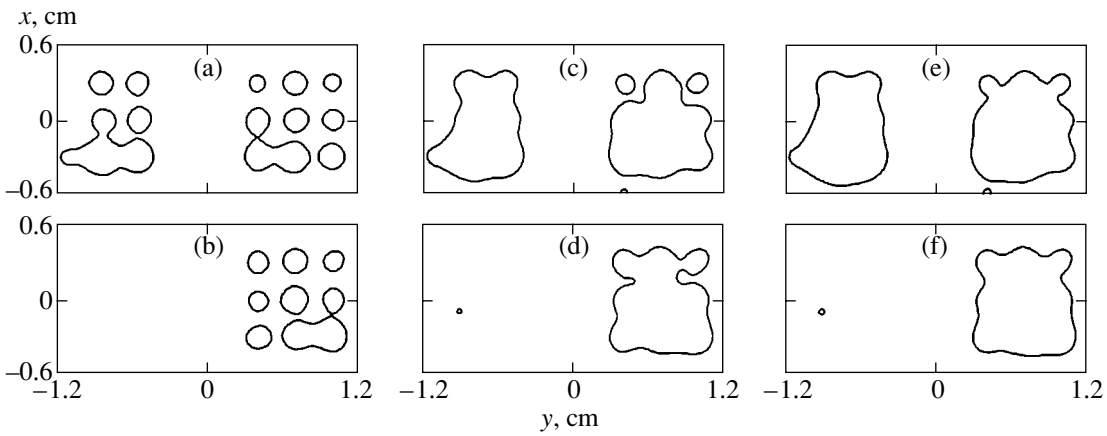


**Fig. 6.** Section in the *xy* plane for the thermal dose field (a, b) after 8 s of heating and later, after (c, d) 5 and (e, f) 10 s of cooling, for regular (above) and random (below) element distributions. The contour is drawn at a thermal dose level of $td_{T_{ref}} = 1$ s at a temperature of $T_{ref} = 56°C$ and encloses the region of thermal necrosis of tissue.

approximation of a piston element), a greater number of such peaks with the higher intensity of 10–30% of $I_{max}$ is observed both along the array axis and in the transverse direction. However, the approach of a piston element is still preferable, because it provides an opportunity to obtain a set of nine foci with very close values of maximum intensity (Fig. 4). In the case of using the approximation of a point source, the intensity levels in the foci noticeably decrease with the distance from the array axis and constitute from 60–80% of $I_{max}$ at the nearest foci to 40–60% of $I_{max}$ at the foci most distant from the axis. Further calculation for a randomized array is conducted for the case of phase setting using the field of a piston element.

The simulation was performed for different intensities obtained at the foci, different distances between the foci, and different durations of treatment with the aim to determine a regime that provides a thermal necrosis of tissue after 5–10 s of treatment not only in the discrete number of regions around the foci but also in all intervals between them. Below, we present the results for a 8-s-long treatment and the geometry of focus arrangement already determined earlier, in determining the intensity fields (Figs. 2 and 3). The intensity at the radiator was selected to be 25 W/cm$^2$, which corresponded to a maximum intensity of 754 W/cm$^2$ in the focus region for a random array and an intensity of 845 W/cm$^2$ for a regular array. It is necessary to note that this high intensity value at the radiator is obtained under the assumption that ultrasound propagates in tissue through the whole distance from the array to the target depth of 10 cm. If the water–tissue boundary is located within 5 cm from the array, which is quite reasonable for many practical applications, the intensity at the radiator is 10.5 W/cm$^2$.

Figure 5 shows the spatial distributions of temperature in the same sections, *xy* and *yz*, as in Figs. 3 and 4 after 8 s of irradiation for regular (Figs. 5a, 5b) and random (Figs. 5c, 5d) distributions of elements. Four contours are presented, where the outer contour corresponds to the temperature exceeding the equilibrium value $T_0 = 36.6°C$ by $\Delta T = 0.2(T_{max} - T_0)$. The step between the contours is also equal to $\Delta T$. Here, $T_{max}$ is the maximum temperature value in the focal region, $T_{max} = 92.6°C$ and $\Delta T = 11.2°C$ for a regular array, and $T_{max} = 80.3°C$ and $\Delta T = 8.74°C$ for a random one. One can see that, in the temperature field of a regular array, the temperature increment in the incidental set of foci is not smaller but actually greater (Fig. 5a) than in the principal one, which is inadmissible for practical purposes. At the same time, in the case of a random array (Figs. 5c, 5d), one may expect that the ablation of tissue will occur only in the region where the set of nine foci is focused, because the temperature increment outside this region is much smaller.

Figures 6 and 7 demonstrate the evolution of thermal dose distributions for the same sections, *xy* and *yz*, selected above. The distributions are calculated for the time of 8 s corresponding to the moment of switching on ultrasound (Figs. 6a, 6b, 7a, 7b) and after 5 (Figs. 6c, 6d, 7c, 7d) and 10 s (Figs. 6e, 6f, 7e, 7f) after switching it off. The thermal dose fields obtained with regular (left) and random (right) arrays are compared. Contours in the figures correspond to the level of $td_{56} = 1$ s and surround the region of a thermal necrosis of tissue. As one can see, the role of thermal diffusion can be considerable even after the irradiation is switched off. Within 5 and 10 s after switching off the source, the outflow of heat from the strongly heated regions of foci to less heated regions occurs due to a high temperature gradient, which provides in this way the uniformity of ablation in the region between the foci. In the case of cooling times exceeding 10 s, no considerable changes in the thermal dose field are observed.

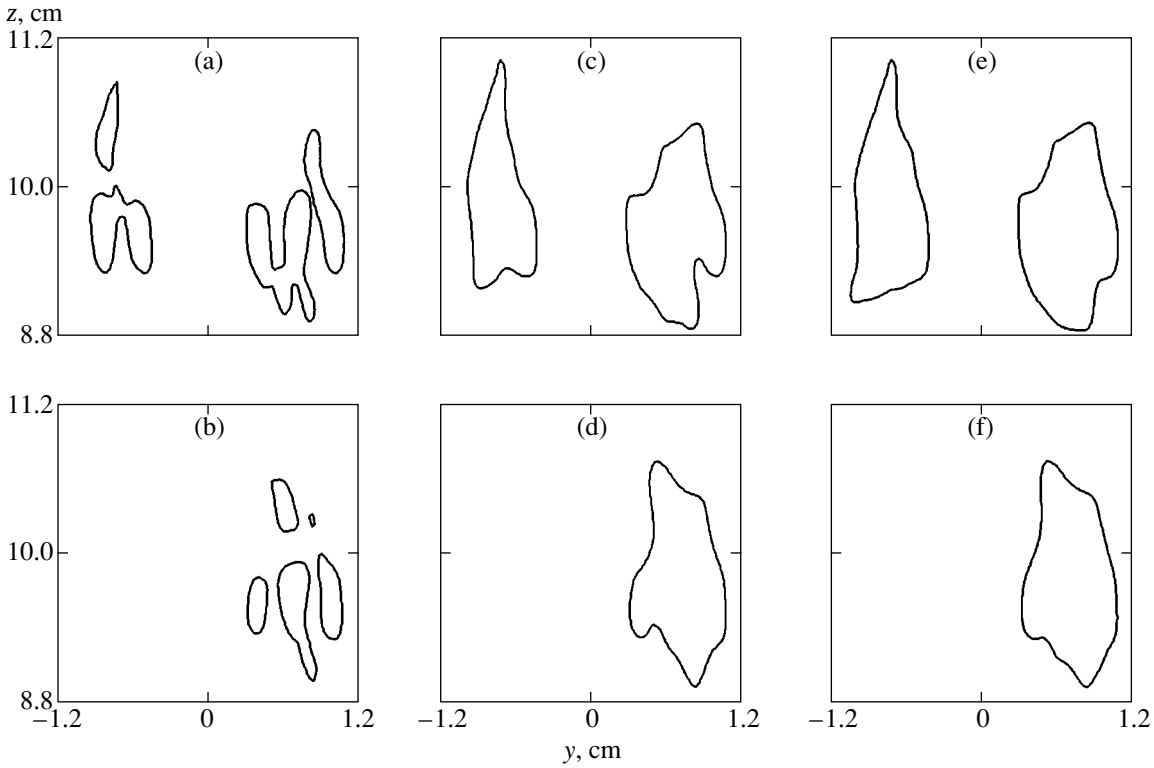


**Fig. 7.** Section in the *yz* plane for the thermal dose field (a, b) after 8 s of heating and later, after (c, d) 5 and (e, f) 10 s of cooling, for regular (above) and random (below) element distributions. The contour is drawn at a thermal dose level of $td_{T_{\mathrm{ref}}} = 1$ s at a temperature of $T_{\mathrm{ref}} = 56°\mathrm{C}$ and encloses the region of thermal necrosis of tissue.

To reduce the acoustic power of the array and the intensity values at the elements, the above-mentioned nine-foci regime can be modified to a regime with two sequentially switched sets of four and five foci formed at the same coordinates. The frequency of switching the sets can be selected within 10–20 Hz, as in [20]. The results of our calculation of the spatial distributions of acoustic and temperature fields, which correspond to this regime, show that, for obtaining the same thermal effect within the heated region, the array power and average intensity can be reduced almost twice (for brevity, we do not present here the corresponding graphical representation). The advantage of this regime is the much better quality of spatial distributions of acoustic and temperature fields, and its disadvantage is the more than twofold increase in the duration of ultrasonic treatment that is necessary for obtaining the same thermal effect.

The results presented above show that arrays with random element distributions provide a noticeably better quality of intensity and temperature distributions in the case of the steering of several foci than arrays with regular element distributions. We determined the parameters of a random array, the geometry of the arrangement of nine foci, and the heating regime that provide a uniform thermal ablation of tissue within the volume surrounding the foci. At the same time, in the field of a regular array, the ablation is observed in both the region of focusing of the set of nine foci and in the region of secondary intensity peaks, which is inadmissible for practical use.

## ACKNOWLEDGMENTS

This work was supported by the Russian Foundation for Basic Research, project nos. 02-02-16999 and 03-02-16232, and by the Civil Research and Development Foundation, grant no. PR2-2384-MO-02.

## REFERENCES

1. E. S. Ebbini and C. A. Cain, IEEE Trans. Ultrason. Ferroelectr. Freq. Control **36** (5), 540 (1989).
2. X. Fan and K. Hynynen, Ultrasound Med. Biol. **22** (4), 471 (1996).
3. E. Ebbini and C. A. Cain, Int. J. Hyperthermia **7** (6), 951 (1991).
4. X. Fan and K. Hynynen, Phys. Med. Biol. **41** (4), 591 (1996).
5. H. Wan, P. VanBaren, E. S. Ebbini, and C. A. Cain, IEEE Trans. Ultrason. Ferroelectr. Freq. Control **43** (6), 1085 (1996).
6. C. Damianou and K. Hynynen, Ultrasound Med. Biol. **19** (9), 777 (1993).

7. S. A. Goss, L. A. Frizell, J. T. Kouzmanoff, *et al.*, IEEE Trans. Ultrason. Ferroelectr. Freq. Control **43** (6), 1111 (1996).
8. L. R. Gavrilov and J. Hand, IEEE Trans. Ultrason. Ferroelectr. Freq. Control **47** (1), 125 (2000).
9. L. R. Gavrilov and J. W. Hand, Akust. Zh. **46**, 456 (2000) [Acoust. Phys. **46**, 390 (2000)].
10. G. R. ter Haar, Phys. Today **54** (12), 29 (2001).
11. M. I. Skolnik, *Introduction to Radar Systems* (McGraw-Hill, New York, 1962; Mir, Moscow, 1965).
12. E. A. Filonenko, V. A. Khokhlova, and L. R. Gavrilov, in *Proceedings of XI Session of the Russian Acoustical Society* (GEOS, Moscow, 2001), p. 19.
13. H. T. O'Neil, J. Acoust. Soc. Am. **21**, 516 (1949).
14. G. Strang, *Linear Algebra and Its Applications* (Academic, New York, 1980).
15. H. H. Pennes, J. Appl. Physiol. **1**, 93 (1948).
16. J. P. Bensted, Phys. Med. Biol. **38**, 1661 (1993).
17. E. A. Filonenko and V. A. Khokhlova, Akust. Zh. **47**, 541 (2001) [Acoust. Phys. **47**, 468 (2001)].
18. S. A. Sapareto and W. C. Dewey, Radiat. Oncol. Biol. Phys. **10**, 787 (1984).
19. C. Damianou, K. Hynynen, and X. Fan, in *Proceedings of IEEE International Ultrasonics Symposium* (1993), p. 1199.
20. D. R. Daum and K. Hynynen, IEEE Trans. Ultrason. Ferroelectr. Freq. Control **46** (5), 1254 (1999).

*Translated by M. Lyamshev*

*Acoustical Physics, Vol. 50, No. 2, 2004, pp. 232–234. Translated from Akusticheskiĭ Zhurnal, Vol. 50, No. 2, 2004, pp. 283–285.*


**SHORT COMMUNICATIONS**

# Velocity of Ultrasound in High-Viscosity Oils in a Wide Range of State Variables

**A. S. Magomadov**

*Kuban State Technological University, ul. Moskovskaya 2, Krasnodar, 350042 Russia*

*e-mail: magomadovas@mail.ru*

Received March 18, 2003

It is well known that sound vibrations find increasing application in the intensification of such processes as mass transfer, combustion, separation, and precipitation; in measurement technology; and so on [1]. The data on the velocity of ultrasound in substances give additional information on their thermodynamic properties. A combined processing of data on thermal properties of materials and data on the velocity of ultrasound makes it possible to determine their thermodynamic properties [2]. Evidently, this approach increases the reliability of investigations. The study of the velocity of ultrasound propagation in substances in a wide range of state variables in combination with other thermal physical properties allows one also to develop new approaches for predicting the thermal physical properties of these substances [3, 4].

The problem of exploitation of deposits of heavy high-viscosity oils (HVOs) by using thermal methods requires a calculation of the heat and mass transfer processes in the disperse flows of oil pools. In its turn, such a calculation requires a prediction of the effective thermal physical properties of fluids (oils and their aqueous emulsions) in the pools.

To study the velocity of ultrasound in HVOs, a special system was developed that allowed us to perform the measurements in the temperature range from 20 to 200°C under pressures from 0.1 to 60 MPa [4].

A flow chart of this system is shown in Fig. 1. A rectangular pulse with a width of about half the resonance wavelength of the transducers is fed from pulse generator *2* to radiator *Rad*. Under the shock action of the electric pulse, the radiator is excited and transmits oscillations to receiver *Rec* in the form of a decaying pulse. The shape of the pulse can be observed on the screen of oscilloscope *5*. The oscilloscope is synchronized by pulse generator *2*. The latter is excited by audio-frequency generator *3*, whose frequency is monitored by digital frequency meter *4*.

Varying the pulse repetition frequency by generator *3*, we reach a frequency equal to the reciprocal of the doubled time of pulse propagation along the distance *l*, and the transmitted and twice reflected pulses become superimposed. In this case, a resonance increase in the pulse amplitude is seen on the screen of the oscilloscope.

The formula for calculating the sound velocity has the simple form

$$c = 2lf, \tag{1}$$

where $c$ is the velocity of sound propagation, $l$ is the distance between radiator and receiver, and $f$ is the frequency of pulse repetition.

As a radiator, we used quartz plates 20 mm in diameter with a resonance frequency $f = 1$ MHz.

Thermostatting of an autoclave with a measuring cell was realized in a special thermostat. The temperature was measured using a platinum thermometer, accurate to ±0.05°C.

The pressure in the autoclave was produced and measured by an MP-600 dead-weight pressure gauge of accuracy class 0.05.

The measuring system described above provided the measurements of ultrasonic velocity in HVOs with a relative error not exceeding, on the average, ±0.1% with a confidence level of 0.95. This was confirmed by calibration tests with distilled water and pure hydrocarbons with various values of state variables.

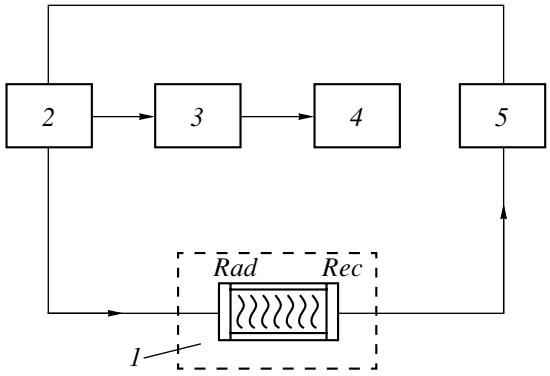


**Fig. 1.** Flow chart of the system for measuring the velocity of ultrasound in a liquid: (*1*) measuring cell, (*2*) pulse generator, (*3*) audio-frequency generator, (*4*) digital frequency meter, and (*5*) oscilloscope.

1063-7710/04/5002-0232$26.00 © 2004 MAIK “Nauka/Interperiodica”

A total of 12 samples of HVOs from various deposits of Russia and Kazakhstan were investigated. The physical chemical properties of the oils studied were presented in [5]. As an example, Fig. 2 illustrates the dependence of the velocity of ultrasound in HVO from the Zybza–Glubokii Yar deposit (well no. 304) on both temperature and pressure. As can be seen from this figure, the isobars of ultrasonic velocity vary linearly and the isotherms vary curvilinearly. The rate of the ultrasonic velocity variation with pressure increases at high temperatures. Similar dependences were observed for other HVOs.

For mathematical processing of the data on the velocity of ultrasound in oils, we used the results presented in [6]. In the cited paper, for describing and developing the procedure of calculating thermal physical properties of hydrocarbon mixtures, elements of information theory were used along with the methods of thermodynamic similarity of the properties of materials. As applied to describing the velocity of ultrasound in HVOs, the equation derived in [4] can be written as

$$c_{\tau,\pi} = c_0 \exp[c_1(\tau) + c_2(\tau, \pi)], \quad (2)$$

where $c_0$ is the velocity of ultrasound (in m/s) in oil at a fixed temperature of $T = 0.45\,T_{cr}$ (in K) and a fixed pressure of $p = p_{cr}$ (in Pa), $c_1(\tau)$ is the function depending on the reduced temperature $\tau = T - 0.45T_{cr}$ at the critical isobar $p = p_{cr}$, and $c_2(\tau, \pi)$ is the function depending on $\tau$ and $\pi = p_{cr}$.

In Eq. (2), the pseudocritical temperature $T_{cr}$ and pseudocritical pressure $p_{cr}$ are calculated using the procedure described in [5].

The values of $c_0$ for the oils under investigation were determined by the extrapolation of experimental data on sound velocity. In the absence of these data, $c_0$ can be found from the equation

$$c_0 = AT_{\hbar p}^{\alpha} p_{\hbar}^{\beta} \mu^{\gamma}, \quad (3)$$

where $\mu$ is the molar mass of the oil and $A$, $\alpha$, $\beta$, and $\gamma$ are constants: $A = 13999.5$, $\alpha = -0.747510$, $\beta = 0.454857$, and $\gamma = -1.787843 \times 10^{-2}$.

The mean relative error of calculating $c_0$ from Eq. (3) was ±0.16% with a confidence level of 0.95; the maximum error was –0.41%.

The function $c_1(\tau)$ in Eq. (2) was found by processing the experimental data on the ultrasonic velocity in HVO at the pseudocritical isobar; this function has the form

$$c_1(\tau) = -0.00246609\tau - 8.437174 \times 10^{-7}\tau^2. \quad (4)$$

Figure 3 displays the dependence supporting the validity of Eq. (4). The function $c_1(\tau)$ is represented as $\ln\frac{c_{\tau,0}}{c_0}$, where $c_{\tau,0}$ are the values of the velocity of ultrasound in HVO at the pseudocritical isobar.

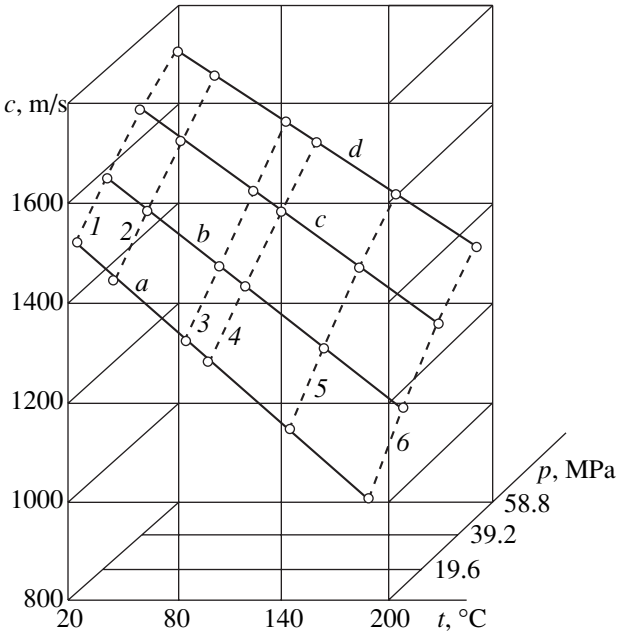


**Fig. 2.** Dependence of the velocity of ultrasound propagation in HVO from the Zybza–Glubokii Yar deposit (well no. 304) on temperature and pressure. Isobars: (*a*) 0.098, (*b*) 19.6, (*c*) 39.7, and (*d*) 58.8 MPa. Isotherms: (*1*) 21.0, (*2*) 43.3, (*3*) 82.7, (*4*) 99.7, (*5*) 145.0, and (*6*) 190.0°C.

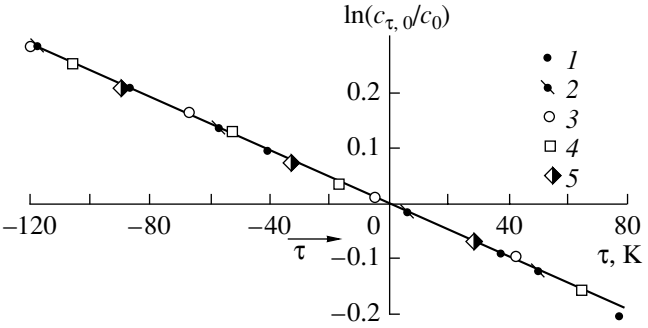


**Fig. 3.** Dependence of the velocity of ultrasound in HVOs in reduced coordinates at the critical isobar: (*1–3*) Zybza–Glubokii Yar (well nos. 688, 304, 849), (*4*) Karazhanbas (well no. 2), and (*5*) Russkoe (well no. 42).

For determining the function $c_2(\tau, \pi)$, experimental data were processed in the coordinates $\ln\frac{c_{\tau,\pi}}{c_{\tau,0}} - \pi$. Here, $c_{\tau,\pi}$ is the value of ultrasonic velocity as a function of reduced temperature $\tau$ and reduced pressure $\pi$. The function $c_2(\tau, \pi) = \ln\frac{c_{\tau,\pi}}{c_{\tau,0}}$ mentioned above is described by the equation

$$c_2(\tau, \pi) = M\pi + L\pi^2, \quad (5)$$

where $M$ and $L$ are the quantities depending on the reduced temperature $\tau$.

The quantity $M$ is described by the equation

$$M = F_0 + F_1\tau + F_2\tau^2, \quad (6)$$

where $F_0 = 0.00493874$, $F_1 = 2.482396 \times 10^{-5}$, and $F_2 = 3.464068 \times 10^{-8}$.

The quantity $L$ is described by the equation

$$L = J_0 + J_1\tau + J_2\tau^2, \quad (7)$$

where $J_0 = -2.111854 \times 10^{-5}$, $J_1 = -1.768529 \times 10^{-7}$, and $J_2 = -4.195657 \times 10^{-10}$.

Equations (2)–(7) make it possible to determine the velocity of ultrasound in HVOs with a mean error of ±0.22% at a confidence level of 0.95 and with a maximum error of +0.57%.

## REFERENCES

1. *Ultrasound. Small Encyclopedia*, Ed. by I. P. Golyamina (Sovetskaya Éntsiklopediya, Moscow, 1979).
2. V. F. Nozdrev, *Application of Ultrasonics in Molecular Physics* (Fizmatlit, Moscow, 1958).
3. B. B. Badmaev and B. B. Damdinov, Akust. Zh. **47**, 561 (2001) [Acoust. Phys. **47**, 487 (2001)].
4. O. F. Susekov, A. S. Magomadov, M. V. Bondarenko, and V. A. Krivonos, in *Ultrasound and Thermodynamic Properties of Substances* (Kursk. Pedagog. Inst., Kursk, 1984), pp. 164–192.
5. A. S. Magomadov and I. Yu. Sanzharovskiĭ, in *Proceedings of XIII School–Seminar on Physical Fundamentals of Experimental and Mathematical Modeling of the Processes of Gas Dynamics and Heat and Mass Transfer in Power Plants* (St. Petersburg, 2001), Vol. 2, p. 276.
6. A. S. Magomadov, *Thermal Physical Properties of High-Viscosity Oils* (Kuban. Gos. Tekh. Univ., Krasnodar, 2000).

*Translated by A. Svechnikov*

*Acoustical Physics, Vol. 50, No. 2, 2004, p. 235. Translated from Akusticheskiĭ Zhurnal, Vol. 50, No. 2, 2004, p. 286.*


**INFORMATION**

# Review of the Book *Modulated Waves* by L. Ostrovsky and A. Potapov

## (Fizmatlit, Moscow, 2003; J. Hopkins Univ. Press, Baltimore, 1999)

The book that has finally appeared in Russian can be considered a textbook on the theory of linear and nonlinear waves, as well as a monograph, because it describes a wide variety of wave processes on the basis of a unified approach. Namely, the authors make an attempt to consider complex dynamic wave structures in terms of modulated waves, i.e., quasi-plane waves whose amplitude, frequency, and phase vary in the course of their propagation. This approach makes the monograph logically complete, and the aforementioned attempt can be characterized as rather successful, although the authors also had to consider some structures that did not in the least resemble plane waves, such as, for example, soliton solutions to the Korteweg–de Vries equation.

The book is written in an easy and vivid manner. It does not contain a "clinical sequence" of lemmas and theorems, which, according to R. Feynman, would be a disadvantage. At the same time, it contains sufficiently rigorous derivations of the main statements of the theory of modulated waves. This fact makes the monograph under review suitable for being used as a textbook for students and postgraduates specializing in physics; moreover, mature scientists can also find it interesting and useful. The book analyzes wave processes in a wide variety of media: waves on the water surface, acoustic waves in fluid and elastic media, and electromagnetic modulated waves in dielectric structures.

Note that the Russian edition, which was prepared by the authors after the appearance of the American version, is more complete. The theory of solitons is presented in two separate chapters. This is all the more appropriate because it includes the results of a series of original works by L.A. Ostrovsky with students, which were carried out in the 1970s. One should especially note Chapter 14, *Interaction of Topological Solitons*, where a set of exact solutions to the sine-Gordon equation is presented and the efficiency of approximate solutions is analyzed. By the width of the scope and the rigor and clarity of the presentation, the book under review can be compared to the well-known monograph by Whitham, *Linear and Nonlinear Waves*, published more than thirty years ago. The book by Ostrovsky and Potapov contains some recent results, for example: results obtained for waves in nonequilibrium media and negative-energy waves in continuous media, an asymptotic analysis of modulated waves, and results for waves in nonstationary media. An efficient approach is used by the authors for describing the nonlinear evolution equations, which for a number of years were studied by Russian scientists: R.V. Khokhlov, O.V. Rudenko, S.I. Soluyan, K.A. Naugol'nykh, L.A. Ostrovsky, and E.N. Pelinovskiĭ.

An important advantage of the book is that it contains historical notes and comments for every chapter, as well as tasks and exercises, which contribute to a better understanding of the material.

Evidently, every professional has his own favorite topics, while some of the problems seem to be somewhat briefly described. However, such deviations are inevitable. On the whole, one can be sure that the reader will find sufficiently full and, often, original answers to the problems of the evolution of modulated waves in nonstationary inhomogeneous media.

The monograph under review is the result of long-term scientific and pedagogical activities of the authors. Its publication, supported by the Russian Foundation for Basic Research, is timely and topical.

**S.A. Rybak**

*Translated by E. Golyamina*

1063-7710/04/5002-0235$26.00 © 2004 MAIK "Nauka/Interperiodica"

*Acoustical Physics, Vol. 50, No. 2, 2004, p. 236. Translated from Akusticheskiĭ Zhurnal, Vol. 50, No. 2, 2004, p. 287.*


**INFORMATION**

# XV Session of the Russian Acoustical Society

The XV Scientific Session of the Russian Acoustical Society, dedicated to the 80th birthday of Corresponding Member of the Russian Academy of Sciences Vitaliĭ Anatol'evich Zverev, will be held November 15–18, 2004, at the Institute of Applied Physics, Russian Academy of Sciences, in Nizhni Novgorod.

The program of the session includes lectures, oral presentations, and poster sessions that cover the following fields of acoustics:

Ocean acoustics
Speech acoustics
Acoustic measurements and standardization
Acoustics in higher education
Acoustical problems of applied linguistics
Architectural acoustics and acoustics of buildings
Atmospheric acoustics
Aeroacoustics
Geoacoustics
Medical acoustics and bio- and psychoacoustics
Musical acoustics
Photoacoustics
Propagation and diffraction of waves
Physical acoustics
Noise and vibration
Ultrasound and ultrasonic technologies
Electroacoustics.

The session will be accompanied by an exhibition of instruments with demonstrations of experimental models and computer programs.

May 15, 2004, is the deadline for submitting papers: six pages for plenary lectures and four pages for regular oral presentations.

Information concerning participation in the session is available from the Russian Acoustical Society, Andreev Acoustics Institute, ul. Shvernika 4, Moscow, 117036 Russia

Tel: (095) 126 9835; (095) 126 9823
Fax: (095) 126 0100
e-mail: ras@akin.ru; yudina@akin.ru
Web: http://www.akin.ru/rao.htm

1063-7710/04/5002-0236$26.00 © 2004 MAIK "Nauka/Interperiodica"

*Acoustical Physics, Vol. 50, No. 2, 2004, p. 237. Translated from Akusticheskiĭ Zhurnal, Vol. 50, No. 2, 2004, p. 288.*


# Congratulations to Academician Fedor Vasil'evich Bunkin

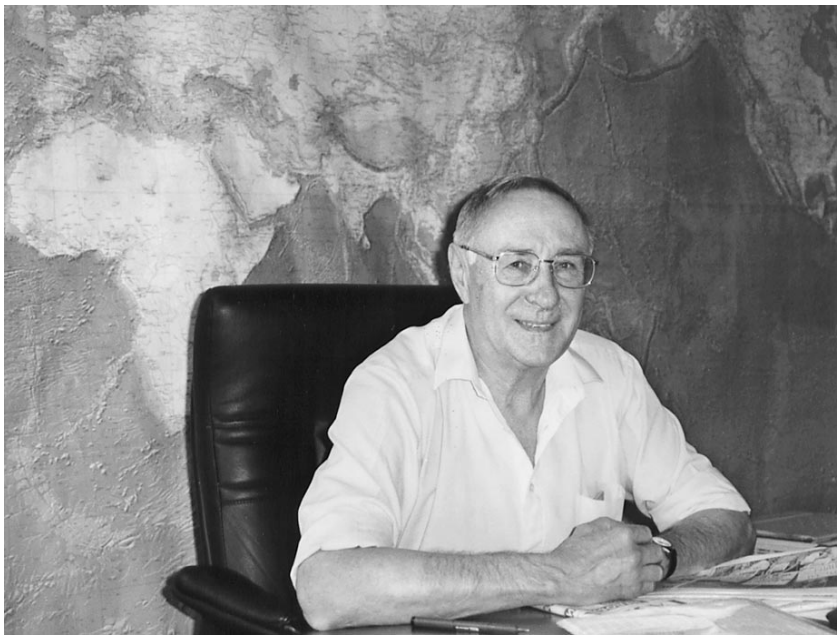

The Editorial Board of *Acoustical Physics* and colleagues-acousticians cordially congratulate Academician Fedor Vasil'evich Bunkin, Director of the Wave Research Center of the General Physics Institute, Russian Academy of Sciences, on his 75th birthday. Academician Bunkin is the author of many important basic and applied studies in radio-wave physics, laser physics, and acoustics. We are grateful to Bunkin for his long-term fruitful work as a member of the Editorial Board and Editorial Council and as Deputy Editor-in-Chief of our journal.

We wish Fedor Vasil'evich Bunkin many happy years to come and new scientific achievements.

*Editorial Board*

1063-7710/04/5002-0237$26.00 © 2004 MAIK "Nauka/Interperiodica"